The Climate of Mars from Assimilations of Spacecraft Data

Tao Ruan

Lincoln College

University of Oxford

A thesis submitted for the degree of Doctor of Philosophy in

Atmospheric, Oceanic and Planetary Physics, Department of Physics

Hilary 2015

Abstract

The Mars climate has been explored using two reanalysis datasets based on combining spacecraft observations of temperature and dust with the UK version of the LMD[1] Mars GCM. The semiannual oscillation (SAO) of zonal-mean zonal wind was studied using the existing *Mars Analysis Correction Data Assimilation* reanalysis during Mars Years (MYs) 24-27. The SAO of zonal-mean zonal wind was shown to exist and extend over a wide range of latitudes. The dynamical driving processes of the SAO in the tropics were investigated, and the forcing due to meridional advection appeared to be the main contributor to the SAO. The study also highlighted some phenomena associated with perturbations of the global circulation during the MY 25 global dust storm (GDS). The meridional advection term was shown to be weaker in the first half of GDS year MY 25 than in the following year, but the forcing due to meridional advection and westward thermal tides both appeared to intensify during the MY 25 GDS.

The capabilities of the Mars data assimilation system were also extended in this thesis, 1) to represent dynamic dust lifting and dust transport during the assimilation and 2) to assimilate measurements of the dust vertical distribution. The updated reanalysis was then used to study several major dust events during MY28-29. It proved able to reproduce a southward-moving regional dust storm without the overwhelming assistance of the assimilation. Dust devil lifting was found to at least partly provide the initial pattern of dust of this moving dust storm. The cold anomaly of the cooling zone beneath this dust storm could be as large as ~ 2 K similar to the magnitude of what was found during the MY 25 GDS. Using the reanalysis, the life cycle of the planet-encircling global dust storm in MY28 was also studied. The Noachis dust storm that occurred just before the MY 28 GDS was found to be the joint result of a travelling Chryse storm, enhanced by dust lifting along its path and local dust lifting in Noachis itself. The adiabatic heating associated with the north polar warming that occurred during MY 28 GDS was up to ~ 3 times as large as that found during the non-GDS year MY 29. The wind stress dust lifting was shown to in strong correlation with the global average dust loadings, and significantly decreased when the GDS decayed.

[1] Laboratoire de Météorologie Dynamique du CNRS.

Acknowledgements

My greatest thanks go to my supervisors, Peter Read and Stephen Lewis, for their advice and criticism on the work of this thesis; Peter in particular for his thoughtful suggestions and enormous time spending on scrutiny of my thesis, and Stephen for his advice on the modeling work and sharing the codes. I thank Luca Montabone for his assistance of initiating the new assimilation, producing the observation data, as well as interesting ideas. I also thank David Mulholland for the discussion of choosing the dust lifting parameters. I am grateful to David Andrews for the discussion of the formulation of Transform Euler Mean equation, and Liam Steele for sharing his codes fixing the bugs inside the model.

I am very grateful to my parents Xiangdong Ruan and Lan Yu for encouraging me to relocate to Oxford, as well as their full support to my life in Oxford. Last, but not the least, I owe great thanks to my wife, Yi, for her endless support by my side and willing to stay with me in Oxford giving up her working opportunity in China.

Contents

Chapter 1 Introduction

1.1. Background

The most famous events reminding people of Mars in the last century were probably the Viking missions of the 1970s and 1980s. In spite of the failure of the Mars Observer mission in 1993, and the loss of both Mars Climate Orbiter and Mars Polar Lander spacecraft in 1999, which were significant setbacks to the recent exploration of Mars [Euler et al., 2001], it is lucky that our passion of exploring the other planets in our solar system is still thriving. A series of instruments on different orbital missions have been operating successfully to provide relatively complete observational datasets for Martian researches. These include Mars Global Surveyor (MGS) / Mars Orbiter Camera (MOC), MGS / Thermal Emission Spectrometer (TES), Mars Odyssey (MO) / Thermal Emission Imaging System (THEMIS), Mars Reconnaissance Orbiter (MRO) / Mars Climate Sounder (MCS) and so forth. Apart from these aspects of observations, plenty of modelling studies have also been conducted using different models developed in different institutions [e.g., Forget et al., 1999; Basu et al. 2004; Montabone et al., 2005; Lewis et al., 2005; Lewis et al., 2007; Wilson et al., 2008a; Kuroda et al., 2008].

	Earth	Mars
Mean orbital radius (10^{11} m)	1.50	2.28
Distance from Sun (AU)	0.98-1.02	1.38-1.67
Orbital eccentricit	0.017	0.093
L_s of perihelion	281°	251°
Planetary obliquity	23.93°	25.19°
Rotation rate, Ω (10^{-5} s^{-1})	7.294	7.088
Solar day, sol (s)	86,400	88,775
Year length (sol)	365.24	686.6
Year length (Earth days)	365.24	686.98
Equatorial radius (10^6 m)	6.378	3.396
Surface gravity, g(ms^{-2})	9.81	3.72
Surface pressure (Pa)	101,300	600(variable)
Atmospheric constituents (molar ratio)	N_2 (77%)	CO_2(95%)
	O_2 (21%)	N_2(2.7%)
	H_2O(1%)	Ar(1.6%)
	Ar(0.9%)	O_2(0.13%)
Gas constant, R($m^2s^{-2}K^{-1}$)	287	192
c_p/R	3.5	4.4
Mean Solar Constant (Wm^{-2})	1367	589
Bond Albedo	0.306	0.25
Equilibrium temperature, T_e (K)	256	210
Scale height, $H_p=RT_e/g$ (km)	7.5	10.8
Surface temperature (K)	230-315	140-300
Dry adiabatic lapse rate ($K\cdot km^{-1}$)	9.8	4.5
Buoyancy frequency, N(10^{-2} s^{-1})	1.1	0.6
Deformation radius, $L = NH_p/\Omega$ (km)	1100	920

Table 1.1 Parameters for Earth and Mars (adapted from Read and Lewis [2004]).

Most people are likely to be more familiar with the Earth than with Mars, so it is better to start to describe some main characteristics of Mars as a planet along with the Earth. Our nearest neighbour, Mars, is a rocky body with half the size of Earth in diameter and at a somewhat greater distance to the sun (1.38 – 1.67 AU) compared to that of the Earth (0.98 – 1.02 AU). The rotation period (Martian day, i.e. sol) around its axis is approximately 40 minutes longer than the length of day on Earth and the planetary obliquities of both planets are also close to each other at the present time (25.19° for Mars while 23.93° for the Earth). This implies that their tropics are both

heated by the sun stronger than the polar regions and seasonal variations can be observed on both planets as they orbit the Sun. The length of a year on Mars is nearly 83% longer than that of Earth, (668 days compared to 365 days), which results from the greater distance from Mars to the Sun, and the Martian calendar is defined such that the first Mars year (MY) began from 11 April 1955, following the convention established by Clancy et al. [2000]. The surface gravity on Mars is around one third ($3.72\, m \cdot s^{-2}$) of the Earth's ($9.81\, m \cdot s^{-2}$). It seems that in both planets the atmospheric circulation prefers to transport heat from the equator to the high latitudes, and the Coriolis force has a similar effect on the atmospheric motions. This results, for example, in the development of baroclinic instabilities at mid-latitudes and similar phenomena of Rossby and inertial wave propagation. The much more elliptical orbit of Mars leads to some significant asymmetrices between the seasons in the two hemispheres compared to the Earth. The details of the parameters for both planets are shown in Table 1.1.

Compared to the Earth, the Martian atmosphere is thin and composed mainly of CO_2 with small amounts of nitrogen (N_2), argon (Ar) and very little free oxygen (O_2). The total pressure of the atmosphere at the surface on Mars is only 0.5%-1% that of the Earth. On Earth, the water vapor makes up ~1% of the atmospheric mass, corresponding to precipitable cm of liquid water, while the concentrations of water vapor on Mars are measured in precipitable microns, which means if all the water contained in a vertical column of the atmosphere were condensed to a liquid state, it would form a layer typically only a few tens of microns thick. Therefore, the Martian atmosphere has a very low absolute humidity. Actually, because of the low mean pressure of the Martian atmosphere, close to that of the triple point of water, ice could not melt into liquid water in most places but would sublime directly into water vapor

regardless of its temperature below the normal freezing point of water (i.e., around 273 K at 1 bar). These lead to a very dry climate on Mars. It is obvious, therefore, that a desert-like landscape can be found easily in regions outside the icy polar caps.

Various landscapes can be found on Mars, including extensive sand-covered deserts in the northern tropics, through the mid-latitudes up to the arctic ice fields, with rugged mountainous terrain in the southern hemisphere and so on. Each landscape has its own characteristic local weather in terms of wind patterns, temperature and occasional clouds. Figure 1.1 shows the spatial and topographic layout of Mars based on the measurements of the Mars Orbiter Laser Altimeter (MOLA). The surface altitude is referenced to an equipotential surface of Mars, i.e. areoid, analogous to the terrestrial sea level, corresponding to a mean equatorial radius, 3396200 ± 160 m [Smith D. E. et al., 2001]. In order to facilitate the future discussion of various studies on dust events, the names of topographic place are labeled on this map.

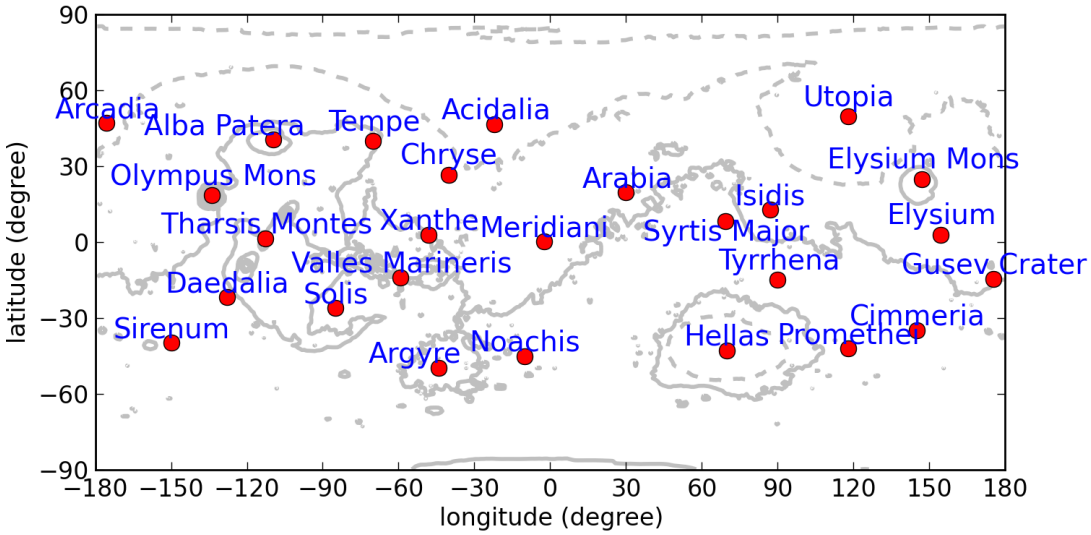

Figure 1.1 The locations of topography mentioned in this work. The solid grey lines are the topography above the standard areoid, and the dashed grey lines are the topography below the standard areoid. The contours are from -4 to 20 km with 4 km interval.

Apart from the similarities between Mars and Earth, dust is an extremely important

environmental component on Mars. Martian atmospheric dust itself can affect the atmospheric radiation by scattering and absorption. The key physical parameters concerning the radiative properties of an individual particle includes the size and shape of the particle, as well as the particle composition through the associated component refractive indices [e.g. Sanchez-Lavega, 2011]. The extinction aerosol optical depth is equal to the sum of the scattering optical depth and the absorption optical depth. According to Mie theory, when the aerosol radius is comparable to the wavelength of the radiation, the aerosol extinction per unit aerosol mass is largest [e.g. Bohren and Huffman, 1998; Stier et al., 2007]. The effective radius of dust particles on Mars is generally reported as around 1.5 μm based on retrievals [e.g. Pollack et al., 1995; Lemmon et al., 2004]. Therefore, the dust particles interact strongly with solar radiation (shortwave radiation, normally ranging in wavelength from 0.3 to 4 μm), but also have capability to interact with long-wave surface radiation (normally ranging in wavelength from 4 μm to over 25 μm).

There is a strong potential to develop dust storms on Mars both locally and globally. Dust particles can be lifted by the near-surface wind stress and the dust devils [Newman et al., 2002a; Read and Lewis, 2004], so that large numbers of dust particles can be entrained into the dust cycle, and then subsequently settle back on the Martian surface by sedimentation under gravity. The source areas for dust have been evaluated by assessing the change of the surface albedo [e.g. Lee, 1986; Szwast et al., 2006]. The possible source regions can be Syrtis Major, Solis Planum, Daedalia Planum, south of Tharsis and so on. However, the sources of dust are very variable, and some areas that were observed to be the source of dust early in a storm might not necessarily being the net source integrated over the whole storm period [Szwast et al., 2006].

Since the airborne dust particles are usually entrained in the atmospheric circulation, Martian dust has a considerable impact on the thermal and dynamical state of the atmosphere. For instance, during the Martian global dust storm happened in Earth year 2001, Cantor [2007] found that the intense dust loading led to an global average cooling on the surface on the order of 1-2 K. The presence of atmospheric dust have also been mentioned and showed that it would lead to intensified polar warming in the winter pole [e.g., Deming et al., 1986; Medvedev and Hartogh, 2007].

In the process of near-surface wind stress lifting, once the wind speed reaches a threshold wind speed, the drag force can be sufficient to lift the large particles temporarily from the surface, but then quickly the particles fall out by sedimentation in the saltation. When the large particles impact with the surface, however, they may lift smaller particles into the air which can remain suspended in the atmosphere [Greeley and Iversen, 1985; Read and Lewis, 2004]. In the dust devil lifting process, a dust devil is an atmospheric convective vortex associated with low-pressure center and strong updraft. The convection in its center is able to lift dust particles into the air efficiently in a localized area. This process is generally believed to be mild, but important to maintain the background dust loadings in the Martian atmosphere [Read and Lewis, 2004]. By conducting the numerical experiments, these two dust lifting mechanisms are found to have different radiative feedbacks [Newman et al., 2002a]. The near-surface wind stress lifting exhibits a strongly positive non-linear feedback, in that large amount of dust being lifted into the atmosphere by the wind stress, the radiative-dynamical feedback will enhance the further lifting. This is because the increased dust thermal forcing leads to a stronger circulation and stronger near-surface wind, which in turn causes further lifting [Leovy et al., 1973]. On the contrary, the dust devil lifting exhibits a negative feedback. The reason for this is that

the dust lifted in the atmosphere can warm the surrounding air, but tend to cool the ground, which reduces the thermal contrast between the air and the ground, hence, the strength of convection in dust devils. Eventually, the dust devils can no longer sustain.

As the main concern of this study is on observing and understanding various dust events, the classification of dust storms defined by Cantor et al. [2001] is described here. According to this classification, based on a size-duration relationship [Cantor et al., 2001], the types of dust storm can fall into three categories, a *local dust storm*, a *regional storm* and a *planet-encircling storm*. The *local dust storm* is defined by the size of the affected area lying between 10^2 km^2 and 1.6×10^6 km^2 and with a duration of less than 3 sols. The term *'regional dust storm'* is applied when the size of the affected area is larger than 1.6×10^6 km^2 and of duration more than 3 sols. The *planet-encircling dust storm* refers to those multi-regional storm events which spread dust in the atmosphere across most longitudes. Thus they have an effect at a global scale and last a relatively long time (often several tens of sols) until most dust settles by getting entrained into the global dust transport cycle or eventually dropping back to the Martian surface. In this thesis study, for convenience, I have used the archaic term *global dust storm* (GDS) when referring to this kind of planet-encircling storm.

Dust cycle is generally considered as the key process of controlling the Martian climate at intraseasonal and interannual time scales, as well as the short and medium time scales corresponding to the "weather" variability. The frequent GDS event (roughly one in every three MYs) is one of the most intriguing scientific topics [Cantor, 2007; Wang and Richardson, 2013]. To improve the understanding of these global-scale events, complete 3-D dust climatology is required. Dust climatology can help study the spatio-temporal distribution of dust during GDSs, when the dust observation in general has reduced coverage during strong dust events. With the dust

climatology including the vertical distribution of dust, the lifecycle of individual GDS event can be investigated in more detail than observation-based studies [Cantor, 2007; Smith, 2009; Wang and Richardson 2013]. It is also possible to improve the simulation of the polar warming in the GCMs [McCleese et al., 2008], so as to study in detail the enhanced polar warming during dusty conditions [Medvedev and Hartogh, 2007].

Through complete 3-D dust climatology, the details and lifecycle of individual regional storm may be of interest to explore under what circumstances they may develop into global scale, and an estimate of cross-equatorial dust transport may be obtained for future analysis of surface dust supply.

1.2. Observations

Observations not only contribute to our understanding of the Martian atmosphere directly, but also provide important inputs and constraints for model studies, especially for analyses employing data assimilation. Since the objectives of my DPhil project concerns both the use of data assimilation and its technical development and implementation, it is necessary to address the main observations involved in this project, including both satellite and ground based measurements. Thanks to the presence of various spacecraft in orbit around Mars since 1997, intensive measurements of atmospheric temperature and dust extending over nearly 8 MYs are now available with unprecedented spatial and temporal coverage. After retrieving atmospheric temperature, certain kinds of dust observations could also be retrieved, depending on the instruments onboard the spacecraft concerned.

1.2.1. TES

A lack of complete sets of observational data significantly impedes the detailed study of the Martian atmosphere. The operational mapping of Martian atmospheric properties by the MGS spacecraft began on 1 March 1999 ($L_s \approx 104°$ in MY 24). The details can be found in the work of Smith [2004]. The retrievals from the infrared spectra returned by the on-board Thermal Emission Spectrometer (TES) are capable of providing detailed information on atmospheric and surface temperature, dust and water ice aerosol optical depth, and water vapor column abundance.

MGS is in a Sun-synchronous, nearly polar orbit. The atmospheric retrievals are based on 3x2 pixels of each TES footprint, and the corresponding spatial resolution is 9 km in the east-west direction and 10-20 km in the north-south direction by considering the impact of spacecraft motion. MGS provides two sets of twelve such strip-like datasets each day, one of which set is taken near a local time of 1400 hours and the other of which is taken near a local time of 0200 hours. A constrained linear inversion of spectrally-resolved radiance in the 15-μm CO_2 band [Conrath et al., 2000] is used to retrieve atmospheric temperature as a function of pressure. The uncertainty on temperature retrievals is ~ 2 K in the middle atmosphere (~ 10-30 km), and larger both in the lowest scale height and at the highest altitudes where limb observation are used [Smith, 2004].

After completing the retrieval of atmosphere temperature, the TES data team started to retrieve aerosol optical depth in a separate second step. The first attempt to obtain dust opacity retrievals from TES measurements was conducted by Smith et al. [2000]. TES datasets used in this thesis are obtained using an updated retrieval algorithm that was based on the same method of his previous work [Smith et al., 2000] but with further improvements [Smith, 2004]. The values of surface temperature, dust and

water ice optical depth that simultaneously provide the best fit between computed and observed radiance spectra are taken to be the results of the retrieval algorithm for aerosol optical depth and the other variables. The details of the algorithm were described in the work of Smith [2004].

An overview of the available retrievals of dust optical depth is shown in Figure 1.2 obtained from the analysis of Smith [2004]. The values shown in Figure 1.2 are the zonal means of daytime (local time ~ 1400 hours) measurements as a function of solar longitude (L_s) and latitude. In order to obtain adequate thermal contrast between the surface and the atmosphere, the retrieval algorithm is restricted to only inverting those spectra from regions of the atmosphere overlying a surface temperature greater than 220K.

In general, northern spring and summer ($L_s = 0° - 180°$) were relatively clear of dust, while southern spring and summer ($L_s = 180° - 360°$) were relatively dusty. MY 24 represented a typical year without a major global dust storm. The background amount of dust in southern spring and summer was nearly double compared to that of the northern spring and summer. The moderately active dust storms in MY 24 were distinctive in the dusty season. The largest dust storm activity was at $L_s \sim 225° - 245°$, which resulted from two principal storm centers. Later in the year, another strong regional storm was noticed in the polar region, but still did not grow into a global scale event. An intensive GDS occurred in MY 25, beginning as a local dust storm at $L_s \approx 185°$, and expanding to global scale by $L_s \approx 193°$. The dust optical depth at 1075 cm^{-1} reached ~ 2 over wide areas during this MY 25 GDS, and some parts of the atmosphere were evidently warmed by > 40 K [Smith, 2004].

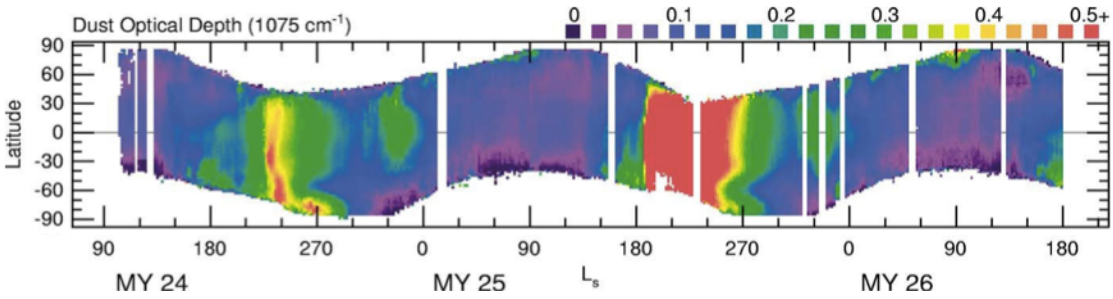

Figure 1.2 An overview of TES daytime (local time ~ 1400) dust optical depth. The zonal average of dust optical depth is shown as a function of latitude and season (L_s). The dust optical depth at 1075 cm^{-1} was scaled to an equivalent 610 Pa pressure surface (to remove the effect of topography). The largest data gaps were caused by solar conjunction and various times when the MGS spacecraft went into contingency (safing) mode. (Adapted from the work of Smith [2004]).

1.2.2. THEMIS

Apart from the TES instrument, the Thermal Emission Imaging System (THEMIS) is another instrument that provides relatively consistent measurements of column-integrated dust opacity in the infrared [Smith et al., 2003; Smith, 2008]. The THEMIS instrument is on-board the MO spacecraft, and was principally designed for the identification of various features of geological and meteorological interest [Christensen et al., 2003]. It began its scientific mapping in February 2002 ($L_s \approx 330°$ in MY 25), and is still continuously working at the time of writing. The THEMIS instrument consists of two separate focal planes. One covered visible wavelengths with 5 spectral filters ranging from 450 to 850 nm, while the other takes images at thermal infrared wavelengths between 6.5 to 15 μm with 10 spectral filters [Christensen et al., 2003]. The data used to retrieve column-integrated dust opacities are taken only from the images taken in the thermal infrared [Smith et al., 2003]. The features of geological interest, for instance, involving mineralogy and local environments of possible landing sites, in general requires localized information. THEMIS therefore has a spatial resolution as high as 100 m/pixel at the surface, and its infrared images are 320 pixels wide. The actual retrieval of dust opacity is

performed based on a block of 320×256 pixels that is equivalent to 32×26 km in space. The retrieval algorithm was described in detail in the work of Smith et al. [2003] and Smith [2004]. The uncertainties of the THEMIS retrieval come from a number of sources [Smith, 2009]. However, the uncertainties of the THEMIS retrieval are not well evaluated, and they are based on the previous experience with TES retrievals and the comparison of THEMIS dust retrieval with TES. For the typical dust condition, the estimate of the uncertainty for a single THEMIS observation is larger of a constant value of 0.04 or 10% of the total thermal infrared absorption optical depth. Smith [2009] pointed out that the associated uncertainty could be greater than 20% during the most intense dust storms.

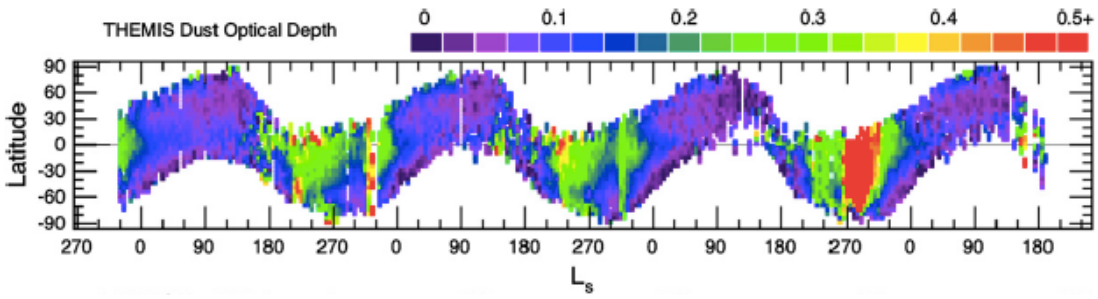

Figure 1.3 An overview of THEMIS retrieved dust optical depth at 1075 cm^{-1} between $L_s = 330°$ of MY 25 to $L_s = 183°$ of MY 29. The dust opacity depth was scaled to an equivalent 610 Pa pressure surface to remove the effect of topography. (Adapted from the work of Smith [2009]).

Figure 1.3 shows an overview of THEMIS retrieved dust optical depth over 3.5 MYs. Compared to the TES dataset, the latitudinal coverage of THEMIS dataset had a larger seasonal variation. In the relatively "dust-free" season ($L_s = 0° - 180°$), the observations mainly covered Northern Hemisphere, while the observations were mainly available in Southern Hemisphere in the dusty season ($L_s = 180° - 360°$). Although the THEMIS dataset could not provide continuous pole-to-pole measurements, the coverage of the available observations was still able to capture the

main yearly pattern of dust activity, as well as the signature of the MY 28 GDS.

1.2.3. Mars Climate Sounder (MCS)

The MCS instrument is currently operational onboard on the MRO spacecraft [McCleese et al., 2007]. The aim of MCS is to measure the Martian surface and atmosphere at high vertical resolution using limb, nadir and off-nadir viewing geometries. The data started being taken by MCS on 24 September 2006 ($L_s \approx 110°$ in MY 28). A mechanical anomaly happened between 9 February and 14 June 2007 which interrupted data coverage, however, the details of which can be found in the paper of Kleinbohl et al. [2009]. Pressure and vertical profiles of atmospheric temperature, dust opacity and water ice opacity can be retrieved from the MCS instruments. A series of analyses have been conducted based on these datasets, which include investigating the temperature maximum in the polar middle atmosphere during southern hemisphere winter [McCleese et al., 2008], the atmospheric thermal tides [Lee et al., 2009], seasonal variations in zonal mean temperature, dust and water ice aerosols [McCleese et al., 2010], ice and dust layering in the Martian atmosphere [Benson et al., 2011] and many other topics.

Channel	Band Pass (cm^{-1})	NER ($mWm^{-2}sr^{-1}/cm^{-1}$)	Main Absorbers
A1	595-615	0.0557	CO_2
A2	615-645	0.0399	CO_2
A3	635-665	0.0419	CO_2
A4	820-870	0.0287	H_2O ice
A5	400-500	0.0278	Dust
B1	290-340	0.0453	Dust
B2	220-260	0.0568	H_2O vapor, H_2O ice
B3	230-245	0.174	H_2O vapor, H_2O ice

Table 1.2 Bandpasses of the MCS Infrared Channels, their Noise Equivalent Radiances for a 2-s integration, and the main absorbers in the Martian atmosphere at these frequencies (adapted from the work of Kleinbohl et al. [2009]).

MRO is also in a polar, Sun-synchronous orbit around Mars. This orbit globally covers the day and night sides of the atmosphere, allowing diurnal and seasonal atmospheric trends to be separated. The channels used for the infrared radiometer are summarized in Table 2. The pressure can be retrieved very precisely with an uncertainty of 1%-2%, and it is frequently used as a vertical coordinate for atmospheric profiles. The retrieval of temperature profiles are over a range from 5-10 km to 80-90 km altitude, and the typical vertical resolution is 4-6 km with a precision 0.5-2 K over most of this altitude range. The profiles of dust and water ice opacity also achieve similar vertical resolution to the temperature profiles, about 5 km, and their typical precisions are $\pm 10^{-4}$-10^{-5} km^{-1} at wavenumbers of 463 cm^{-1} and 843 cm^{-1}, respectively [Kleinbohl et al., 2009]. The precisions are calculated from the uncertainty due to noise and the quality of the fit. However, the estimate of uncertainty ignore potential cross correlations like the uncertainty in temperature influencing pressure, or the uncertainty in aerosol influencing temperature. The accuracy of the data also includes the systematic errors, which may include measurement errors, errors in geometry, uncertainties of spectroscopic parameters and size distributions and so on.

McCleese et al. [2010] have used MCS data to analyze the structure and dynamics of the Martian lower and middle atmosphere in terms of temperature, dust, water ice and even the zonal gradient wind outside the tropics derived from zonal average temperatures. In their study, McCleese et al. [2010] indicated that the Martian atmospheric thermal structure typically has two modes: a symmetrical equinoctial structure with middle atmosphere polar warming, and a solstitial structure with an intense middle atmosphere polar warming overlying a deep, cold winter polar vortex. The zonal average dust opacities in MY 29 retrieved from MCS data are shown in

Figures 1.4 and 1.5, respectively for both nightside and dayside. In general, the night side retrievals could extend to lower altitudes than the dayside retrievals. It was obvious that the latitudinal vertical distribution of dust also exhibited equinoctial and solstitial modes. For the equinoctial mode, the dust penetrates to high altitudes over the tropics but lower penetrations could be found near the poles (Figure 1.4a and e, Figure 1.5a and e). For the solstitial mode, the dust penetrated to high altitudes over the tropics, and a region of nearly dust-free air in the mid-latitudes of the winter hemisphere could be observed clearly (Figure 1.4c, Figure 1.5c). However, the quantitative aspects of these features could differ between both solstices [McCleese et al., 2010].

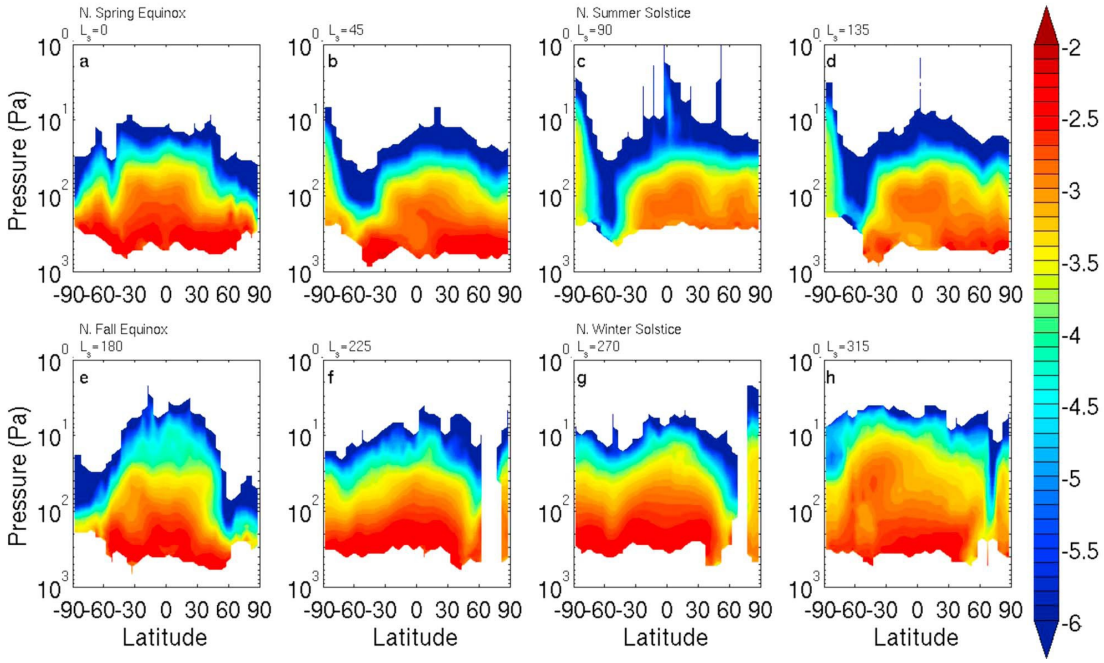

Figure 1.4 Log_{10} of the zonal average dust opacity (km^{-1}) nightside retrievals of MY 29 for the L_s bins labeled at the top of each panel. Contours are shown every 0.1 log units. Note the pressure scale is between 1000 and 1 Pa. (from the work of McCleese et al. [2010]).

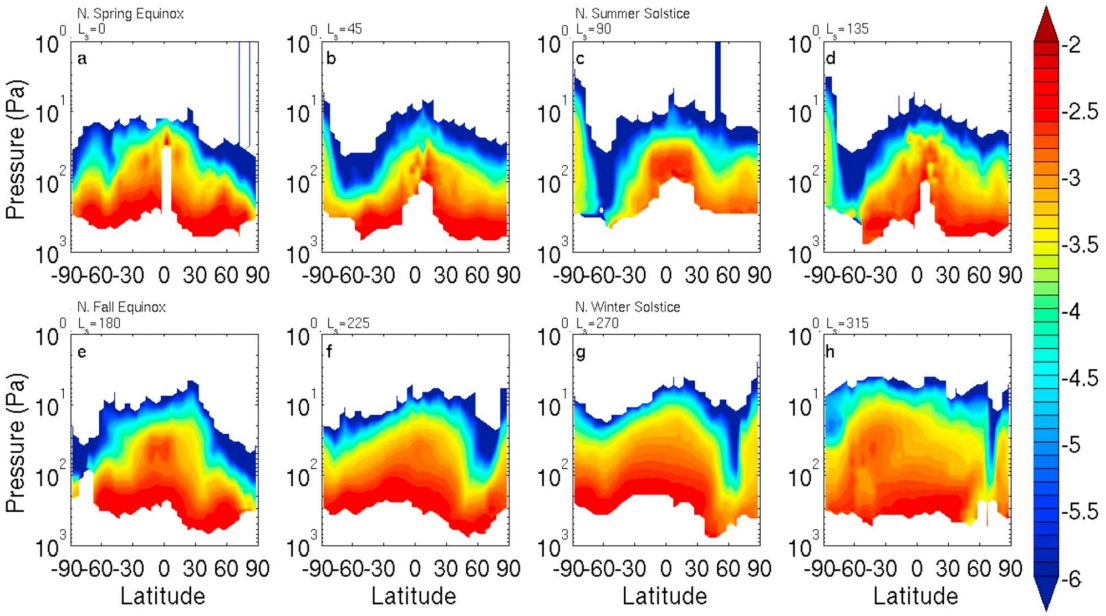

Figure 1.5 Log_{10} of the zonal average dust opacity (km^{-1}) dayside retrievals of MY 29 for the L_s bins labeled at the top of each panel. Contours are shown every 0.1 log units. Note the pressure scale is between 1000 and 1 Pa. (from the work of McCleese et al. [2010]).

1.2.4. Mars Exploration Rovers

Apart from these satellite-based measurements, some ground-based measurements are also utilized in this thesis. They are able, for example, to provide a bottom-up view of column-integrated dust opacity that is independent of satellite-based datasets, though they normally only observe over a limited area. Among limited ground-based observations, the measurements from two rover spacecraft (i.e., "Spirit" and "Opportunity") during the Mars Exploration Rovers (MERs) mission were available within the chosen study period for this thesis. The "Spirit" rover landed at Gusev Crater (-14.57° latitude, 175.48° longitude) on 4 January 2004 ($L_s \approx 328°$ in MY 26), and about three weeks later the "Opportunity" rover landed at Meridiani (-1.95° latitude, -5.53° longtiude) on 25 January 2004 ($L_s \approx 339°$ in MY 26) [Lemmon et al., 2004]. The locations of Gusev Crater and Meridiani can be seen with reference to Figure 1.1. Nine cameras were carried by each rover. The solar filters, at the wavelengths of 440 nm and 880 nm were designed for the Pancam camera that was

used to image the Sun [Lemmon et al., 2004]. According to Lemmon et al. [2004], potentially larger sources of uncertainty included the absolute radiometric response, at 30% uncertainty for the two solar filters, and variations in response with temperature. A red leak consistently contaminated the filter at the wavelength of 440 nm [Lemmon et al., 2014]. The estimates of effective radius of dust particles based on these rovers' observations were 1.47 ± 0.21 μm for "Spirit" and 1.52 ± 0.18 μm for "Opportunity". [Lemmon et al., 2004].

1.3. Modeling studies

The comprehensive general circulation modelling of the Martian atmosphere can be traced back to the work of Leovy and Mintz [1969], in which a two-level terrestrial Global Climate Model (GCM), originally developed at the University of California, Los Angeles (UCLA), was applied to study Martian wind systems, thermal structure and energetics. Atmospheric condensation of CO_2 and the presence of transient baroclinic waves in the winter mid-latitudes were simulated by this model. From the early 1970s, further model development was conducted continually at NASA's Ames Research Center, resulting in a model known as the NASA Ames Mars GCM (Ames MGCM). With the topographic data released from Mariner 9 measurements, the Ames MGCM started to include spatially varying surface elevation at the model's lower boundary. The first 3-D simulations of a global dust storm were conducted with the Ames MGCM incorporating a tracer transport scheme [Murphy et al., 1995]. The important role of dust transport by atmospheric eddies and the seasonal and topographic effects resulting in differences between each hemisphere were illustrated in their work, as well as the Martian polar warming and the relationship between CO_2 column loading and the onset of major dust storms.

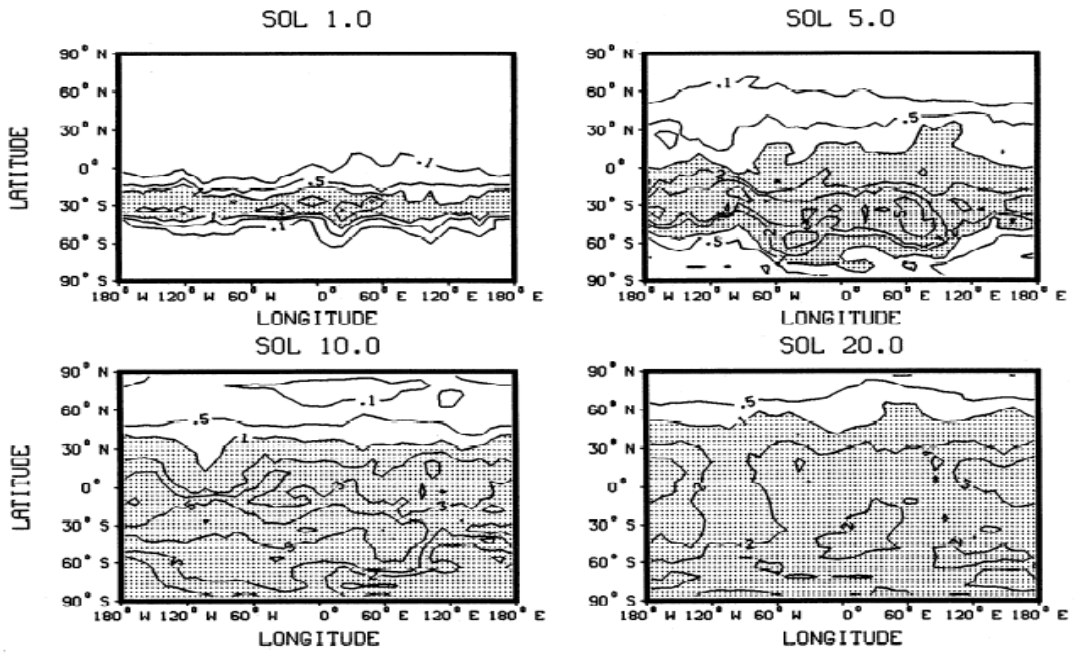

Figure 1.6 Instantaneous visible (0.67 μm wavelength) dust opacity after sols 1, 5, 10 and 20 of the baseline simulation (zonally symmetric dust source); contours at 0.1, 0.5, 1.0, 2.0, 3.0, 5.0, 10.0. Opacities greater than unity are shaded. (from the study of Murphy et al. [1995]).

The baseline simulation in the study of Murphy et al. [1995] started with a 30-sol dust-free spin-up at northern winter solstice (solar latitude L_s = 273°). Initial surface pressure was specified with respect to altitude at each grid point, with initial global average values of 760 Pa. After spin-up, the MGCM was coupled interactively with an aerosol model (described in detail in their work). They prescribed a uniform dust source in their aerosol model across the entire surface between 15°S and 37.5°S [Murphy et al., 1995]. The source magnitude was 1.54×10^{-7} kg m^{-2} s^{-1} for 10 sols with a prescribed size distribution and a particle material density of 3000 kg m^{-3} [Toon et al., 1977]. The simulation was conducted for an additional 40 sols after 10-sol of steady dust injection. In their baseline simulation (see Figure 1.6), the dust spread all over the domain at a rapid pace except in the northern polar region (by 20 sols). The $\tau_{vis} = 1$ line moved to 10°N by sol 5, then to about 40°N by sol 10. By sol 20, the dust had reached 50°N and the spread of dust was much faster moving to the south

from the original dust source region prescribed in this study. Optical depths higher than $\tau_{vis} = 1$ could be seen to almost cover the southern hemisphere by sol 20. The dust distribution developed very asymmetrically within the region south of the dust input corridor and they claimed that this strong southward transport was due primarily to a strong standing eddy that developed rapidly during the dust input phase of the simulation and rapidly diminished after sol 5. However, in their parallel simulation, the same as this baseline simulation but with spatially invariant topography, thermal inertia and albedo fields, this southward dust transport was not so strong as in the baseline simulation. However, at that time, there was not enough observational data to verify their model simulations directly.

In 1989, the grid-based LMD (Laboratoire de Météorologie Dynamique) Mars GCM was developed, based on the LMD terrestrial climate model which was used on Earth for weather forecasting or climate change studies [Forget et al., 1999]. A new radiative transfer code and a self-consistent parameterization for the condensation and sublimation of CO_2 were developed to adapt to the Martian atmospheric conditions. Reasonable seasonal and transient pressure variations were able to be reproduced by this model, the first to simulate a full Martian year without any forcing other than insolation. [Hourdin et al., 1995; Collins et al., 1996].

Around that time, a GCM with a physical package similar to the Ames model was developed at NOAA's Geophysical Fluid Dynamics Laboratory (GFDL) at Princeton, USA. The GFDL Mars GCM (GFDL MGCM) was adapted from the GFDL SKYHI terrestrial GCM [Hamilton, 1995; Wilson and Hamilton, 1996]. The model has since been used to study many different phenomena on Mars, such as Martian thermal tides [Wilson and Hamilton, 1996], surface winds [Fenton and Richardson, 2001] and the dust cycle [Basu et al., 2004]. In the study of Basu et al. [2004], they mainly

investigated the capability of simulating the dust cycle and related temperature fields by the GFDL MGCM with a similar approach to treating dust lifting as described in the work of Newman et al. [2002a]. Through their model experiments, they obtained a set of parameters to provide a "best fit" model climate based on dust devil lifting responsible for the seasonal haze cycle and wind stress lifting responsible for dust storms. For a year without a major dust storm, the comparison between observations and temperature fields predicted by their model in terms of "best fit" tuning is shown in Figure 1.7. Comparing the top panel with the middle panel in Figure 1.7, it indicates that not only had "global mean" temperatures been produced reasonably, but also the meridional gradients. Specifically, the double-peaked feature of air temperatures in the mid-latitudes in both hemispheres, and local minimum in the tropics during summer could be observed in their model results. The difference between the MGCM output and the TES observations suggested that their model predicted the air temperature in the mid-latitudes and tropics quite well except for the relatively large discrepancy at roughly $L_s = 200°$ and $L_s = 235°$. However, for the polar region, a large discrepancy (> 20 K) could be seen in both hemispheres, especially for the Southern Hemisphere.

Almost at the same time, in the 1990s, a three-dimensional MGCM was developed jointly with Universities of Reading and Oxford in the United Kingdom (UK MGCM). The spectral solver used in this MGCM was originally adapted from a simplified Earth GCM at the University of Reading [Hoskins and Simmons, 1975]. But in the vertical direction, levels were still defined in terms of the terrain-following σ coordinate system using a standard finite difference approach. Besides simulating the standard atmospheric properties, the UK MGCM, more recently with contributions from The Open University, also has the capability (via a shared physics

package with the LMD MGCM since the mid 1990s) of treating the CO_2, water and dust cycles, CO_2-ice transformations, as well as data assimilation for temperature and dust [Montabone et al., 2005; Lewis et al., 2005; Montabone et al., 2006a; Montabone et al., 2006b; Lewis et al., 2007; Wilson et al., 2008a; Rogberg et al. 2010]. Hereafter,

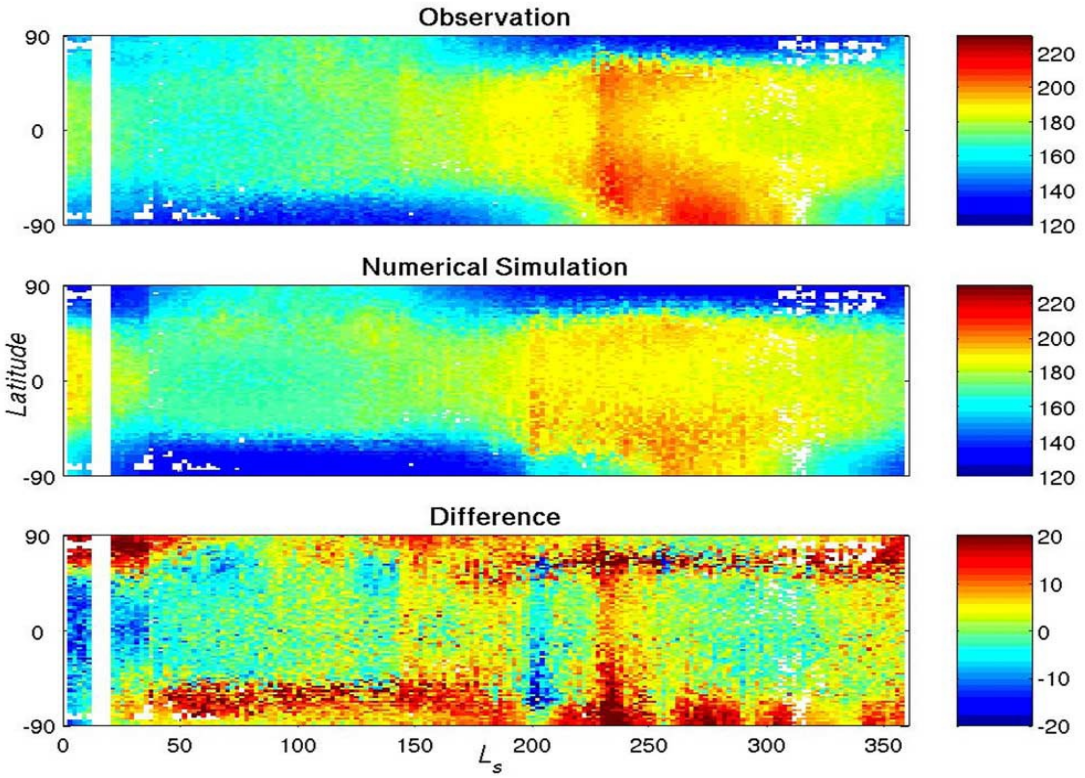

Figure 1.7 A comparison of zonal-mean 15 μm channel temperatures derived from MGS TES spectra and from the GCM. The GCM output was sampled using the TES observational pattern to maximize comparability. A full annual cycle was shown for each, along with the difference between the model and observations. The results were for a non-global dust storm year (the first MGS mapping year from northern summer and rolling around into the second) and from the ‘‘best fit’’ GCM simulation. (from the work of Basu et al. [2004])

the version of the UK MGCM with the complete physics package is denoted as the UK-LMD MGCM in this thesis. In the work of Montabone et al. [2005], data assimilation for temperature profiles and column-integrated dust opacity was employed to provide the model outputs consistent with the observation. Not only was the interannual variability of different atmospheric properties described, but also first

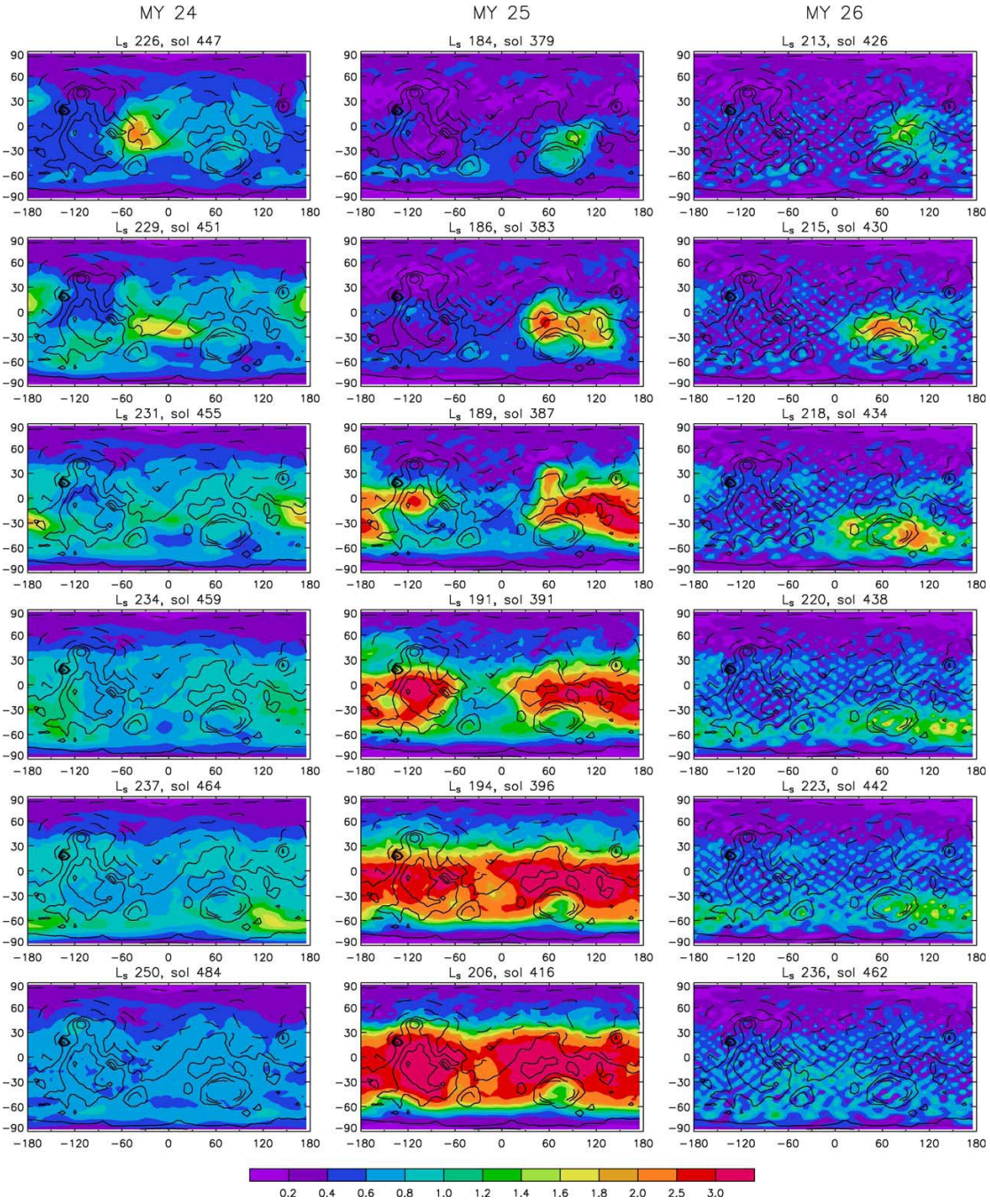

Figure 1.8 Evolution of dust storms in MY 24-26 in a Martian reanalysis dataset. All the snapshots show the latitude-longitude distribution of the dust total optical depth normalized to 700 Pa. Note the dramatic growth of the regional storm between Hellas and Isidis Planitia up to planetary scale on a short time scale in MY 25: it took just 18 sols to encircle the entire planet with an average dust loading three times larger than that in the other two years. (from the work of Montabone et al. [2005]).

step in capturing the evolution of dust storms in MY 24-26 (see Figure 1.8), including the 2001 planet-encircling dust storm (i.e. MY 25 GDS). In their study, they pointed out that the localization of major dust storms varied with season. The MY 25 GDS

started as a regional storm but developed into a planetary-scale dust storm within only 18 sols because of the eastward migration and the consequent contribution of dust from the Tharsis region and the plains south of the Tharsis ridge. This probably resulted from the positive feedback to the strength of wind stress lifting due to radiative interactions with the dust cloud, which would enhance the dust lifting in turn. In fact, in MY 26, some regional storms built up in the same place as at the start of the MY 25 GDS, but did not develop strongly enough to form a planetary-scale dust storm.

1.4. Motivation and objectives

A reasonable dust treatment is now included in almost all current state-of-the-art MGCMs in some form. The dust in the Martian model simulations is generally treated in one of several different ways, either

1) treating the dust as prescribed in seasonal and latitudinal dust distribution scenarios in terms of available observations and then repeated in other years, such as the TES scenario in one of the experiments of Kuroda et al. [2008]. Some of the special scenarios assume a horizontally and temporally uniform dust distribution [e.g. Kahre and Haberle, 2010]. In either case, the dust will be distributed vertically according to a prescribed vertical profile, such as the one originally described by Conrath [1975],

2) giving an initial prescribed injection of dust in space and time before transporting the dust according to the wind and temperature fields predicted by Martian GCM itself [e.g. Murphy et al., 1995],

3) simulating dust transport using the wind fields and temperature predicted by the MGCM itself, but with runtime dust sources, i.e. near-surface wind stress lifting and

dust devil lifting [e.g. Newman et al., 2002a; Basu et al., 2004; Mulholland et al., 2013],

4) data assimilation for observed column-integrated dust opacity without dust transport, distributing the dust vertically by scaling of a prescribed (e.g. Conrath) profile [e.g. Montabone et al., 2005; Lewis et al., 2007], or,

5) simulating dust transport with a spatially uniform dust lifting rate, then to enforce the MGCM results to match the observationally-derived daily maps of column-integrated dust opacity [e.g. Madeleine et al. 2011].

The methods mentioned above have their own advantages and disadvantages. Method 1) only has reliable information for the column dust opacity according to the limitations of TES observations. Even if vertical information is available in the observed datasets, such as in MCS limb data, it will rapidly still lose detailed information in space, as well as through continuous seasonal variability. The special treatment of dust assuming horizontally and temporally uniform dust opacity is mainly used on various idealised experiments, so it is almost impossible to represent real instantaneous atmospheric conditions.. In the method 2) a totally artificial dust source is added at the start of the simulation so that it lacks any representation of dust lifting mechanisms on Mars and can only produce some reasonable short-term dust transport patterns through tuning the initial dust injection. In this case the dust would either spread across most of the planet (as shown in the results of Murphy et al. [1995]) which may not be realistic, or quickly settle out by sedimentation. Method 3) implements reasonable parameterizations of physical mechanisms to represent the unique dust behaviour on Mars and can therefore produce long-term dust climate results in acceptable agreement with real observations. However, no simulation has

yet quite produced the observed amount of interannual variability [Newman et al., 2002b; Mulholland et al. 2013]. Recent results [Wilson and Kahre, 2009; Mulholland et al., 2013; Newman et al., 2015] suggest that a finite dust reservoir is likely needed to reproduce a more realistic interannual variability of dust climatology, in addition to better dust lifting parameterizations. Method 4) is able to provide a complete and balanced state that is constrained to be consistent with the observations, but the dust transport has not been enabled so far, partly because of a lack of vertical information on dust opacity from TES. Thus, the dust would be distributed by scaling an arbitrary (and probably incorrect) Conrath profile in the vertical, and current implementations force the dust distribution to remain static when no observation is available to correct the dust fields. Finally, method 5) is in fact a similar process of assimilation, and is practicable to reproduce a reasonable simulation of long term dust climatology. However, the assumption of a spatially uniform dust lifting rate is far from reality. This results in imperfect predictions of the regional details of the dust spatial distribution [Madeleine et al. 2011]. Another concern is that this method in general requires a daily-map of column-integrated dust opacity [e.g. Montabone et al., 2015] to guide the model, which has to be interpolated from intermittent observations. Regardless of additional work for producing the "mosaic" map of column-integrated dust opacity, the model prediction may therefore be regulated by large intervals of uncertain information when observations are not consistently available. There are also methods in which the model can advect the dust that is added/removed from the boundary layer in terms of the differences between predicted and observed dust column opacity [e.g. Wilson et al. 2008b]. This could be considered as a hybrid of method 4) - 6).

As discussed above, method 4) should be the most reasonable way of doing dust

simulation on Mars in terms of its physical representation. However, in the light of limitations in both the data and model [Newman et al., 2002a; Newman et al., 2002b], it is difficult to capture the dust behaviour precisely, which results in a failure to simultaneously produce some significant features of observed dust storms, (e.g. the development of the MY 25 GDS), as well as the regular interannual variability of dust. Without producing daily-maps of dust distribution from incomplete information, Method 5), on the other hand, in practice generates results that reconstruct atmospheric states that are close to real observations through the data assimilation technique. The absence of a dust transport scheme, however, often leads to unrealistic vertical distributions of dust. This impedes the capability of providing a realistic reconstruction of the dust storm structures, especially for GDS event, such as MY 25 GDS and more recent MY 28 GDS.

Therefore, it is extremely important to improve the capabilities of the data assimilation technique on Mars. As MCS datasets become available which contain vertical information on dust opacity, it is important to incorporate the dust transport scheme into the data assimilation in order to provide a three-dimensional structure of dust storms, corrected by the real observational data. It is also notable that none of the above MGCM studies have so far reported substantial success in reproducing the observed elevated dust layers, first discussed by Heavens et al. [2011a] using MCS observations. More recently, Spiga et al. [2013] reported that “rocket dust storms” and detached dust layers were possible to be simulated in a mesoscale model. Further implementation in a MGCM however requires a sophisticated parameterization due to the inadequate temporal and spatial resolution of MGCM. Navarro et al. [2014] have shown that a data assimilation system that only assimilates MCS temperature profiles allows the dust field to be adjusted according to its correlations with temperature. In

their work, the feature of an elevated dust layer during a regional dust storm could be reproduced. However, their data assimilation system failed to reproduce the elevated dust layers that are close to equator and in Northern Hemisphere, due to their unapparent thermal signature. The assimilation of time-varying MCS dust profiles is an alternative to at least reconstruct part of the feature of elevated dust layers. Further diagnosis of the assimilation (and its pattern of increments), together with sensitivity experiments with a standalone version of the model, can possibly provide increased understanding of the source of model systematic error.

The ultimate aim of this DPhil project is to investigate the Martian climate (in particular involving the role of suspended dust) using the reanalysis produced by a data assimilation system based on the UK-LMD MGCM. The key questions that are explored and answered in this thesis can be summarised as follows,

1. Is there a semiannual oscillation (SAO) of zonal-mean zonal wind on Mars and can it be observed in a reanalysis dataset? If so, what are the driving forces behind this SAO in the tropics?
2. How did a major southward moving dust storm in MY 29 evolve along its moving path from its origin to cross equator, and to what extent can the physical processes implemented in the UK-LMD MGCM reproduce the required pattern of spontaneous dust lifting to account for this?
3. How did the possible precursor event of the MY 28 GDS develop? Is the UK-LMD MGCM capable of spontaneously producing such associated events, and what was the overall impact of the MY 28 GDS on the evolving dust distribution in the atmosphere and the warmings observed over either pole?

The first of these was inspired by the tropical SAO study of Kuroda et al. [2008]

based on their free-running MGCM. As this was an early work of my DPhil project, the data used for diagnosing the Martian SAO from observations consisted of the assimilated results from the Mars Analysis Correction Data Assimilation (MACDA) [Montabone et al., 2011b]. This dataset assimilated retrieved TES temperature profiles and column-integrated dust opacities, corresponding to the dust treatment method 5) discussed above. The results are presented in Chapter 3.

The rest of the work described in this thesis focuses on extending the data assimilation methodology to assimilate MCS retrieved dust profiles with dust lifting and transport activated during the corresponding model simulations. The upgrades of data assimilation system are described in Chapter 4, and the validation of the reanalysis from this updated data assimilation system is presented in Chapter 5. In Chapter 6, this new reanalysis is used to document the evolution of a major southward moving dust storm in MY 29. The capability of the UK-LMD MGCM to reproduce this moving dust storm is also discussed. Chapter 7 studies the precursor event of the MY 28 GDS and the impacts of the MY 28 GDS on the dust distribution and zonal temperature structure. The impacts of these MY 28 events are studied by comparing with the same time window of MY 29, during which no GDS was observed. The enhanced north polar warming during the MY 28 GDS is also discussed. Through analysing individual dust events in Chapters 6 and 7, the ability of reanalysis to reproduce the observations are also assessed for specific dust conditions. Finally, Chapter 8 summarises the results of the project and suggests some possible future improvements of the reanalysis methodology and possible extensions of the research presented in this thesis.

In the content of this thesis, different symbols/names for the different dust quantities are used to reflect the subtle difference of each term. This may sometimes lead to

confuse from the reader's point of view. To avoid ambiguity, the symbols/names related to dust quantity in this thesis are explained in the Table 1.3.

Symbol/ acronym	Quantity represented
CIDO	column-integrated dust opacity, varying with the atmospheric path from nadir view (dimensionless)
tauref	CIDO rescaled to a standard pressure level (dimensionless)
dust opacity	the average dust opacity along the optical path (km^{-1})
LIDO	dust opacity integrated vertically across a layer (dimensionless)

Table 1.3 The summary of the acronyms used in the following chapters for different dust quantities.

Chapter 2 Martian Global Climate Model

The UK version of a three-dimensional Martian Global Climate Model (UK-LMD MGCM) [Forget et al., 1999] is used in this project to study some aspects of the climate of Mars. Based on this UK-LMD MGCM, for the work described in this thesis I have implemented a more sophisticated data assimilation scheme into the model to extend the capabilities of the Oxford reanalysis system to include the available observations of three-dimensional dust distributions with transport. The details of the new data assimilation system will be addressed in Chapter 4. This UK-LMD MGCM used in the current study combines a spectral dynamical solver, a tracer transport scheme and dust lifting routines, developed in the UK, with a full range of physical parameterizations developed by the Laboratoire de Météorologie Dynamique (LMD; Paris, France) in collaboration with Oxford, The Open University and Instituto de Astrofisica de Andalucia (Granada, Spain). Early attempts at data assimilation, based on this UK-LMD MGCM and observations of temperature and total column dust amount, have been applied in several studies [Montabone et al., 2005; Lewis et al., 2005; Montabone et al., 2006a; Montabone et al., 2006b; Lewis et al., 2007; Wilson et al., 2008a; Rogberg et al. 2010] as an effective tool with which to analyze spacecraft observations of meteorological phenomena (e.g., atmospheric tides,

transient wave behavior, effects of clouds in the tropics, weather predictability, etc.) in the Martian atmosphere.

Another branch of this Martian Global Climate Model has been developed at LMD with the same physics package but a different dynamical core. This LMD-MGCM is a grid-point model based on the discretization of the horizontal model fields on a latitude-longitude grid, while in the UK-LMD MGCM the horizontal model fields are represented by a truncated series of spherical harmonics. The advantages and disadvantages of both formulations were discussed in the work of Forget et al. [1999].

In this chapter, only the details of the UK-LMD MGCM will be described, including the model dynamics and physics parameterizations. In addition, the existing data assimilation scheme developed prior to this project, upon which the new scheme is based, will be reviewed.

2.1. Model dynamics

The dynamical core of the UK-LMD MGCM is based on a spectral solver which was adapted from the University of Reading [Hoskins and Simmons, 1975], and later developed at Oxford [Collins and James, 1995; Collins et al., 1996]. With further extension, the total wavenumber 31 for triangular truncation is used in my project, corresponding to a 96×48 real space grid in longitude and latitude in terms of dynamical fields.

In the vertical direction, levels are defined in terms of the terrain-following σ coordinate system using a standard finite difference approach. The first three of 25 vertical levels close to surface are at heights of 4, 19 and 44 m above surface, and this enhanced vertical resolution near the surface provides the capability of resolving detailed surface processes represented in the model. The model top is typically at an

approximate altitude of 100 km. Some advantages coming with this extension are that it enables us to explore meteorological phenomena at higher altitudes and such a deep model domain allows the unconstrained development of the Hadley circulation which is important to obtain a better simulation [Forget et al., 1999]. At the three uppermost levels, sponge layers are used with the purpose of reducing spurious reflections of vertically propagating waves at the top of the model, within which a linear drag is added to the eddy components of the vorticity and divergence fields.

The basic equations for a hydrostatic, adiabatic and inviscid gas surrounding a rotating spherical planet are cast in vorticity-divergence form following Hoskins and Simmons [1975],

Vorticity equation

$$\frac{\partial \zeta}{\partial t} = \frac{1}{1-\mu^2}\frac{\partial F_v}{\partial \lambda} - \frac{\partial F_u}{\partial \mu} \tag{2.1}$$

Divergence equation

$$\frac{\partial D}{\partial t} = \frac{1}{1-\mu^2}\frac{\partial F_u}{\partial \lambda} + \frac{\partial F_v}{\partial \mu} - \nabla^2\left(\frac{U^2+V^2}{2\left(1-\mu^2\right)} + \varphi + \overline{T}\ln p_*\right) \tag{2.2}$$

First law of thermodynamics

$$\frac{\partial T'}{\partial t} = -\frac{1}{1-\mu^2}\frac{\partial (UT')}{\partial \lambda} - \frac{\partial (VT')}{\partial \mu} + DT' - \dot{\sigma}\frac{\partial T}{\partial \sigma} + \kappa\frac{T\omega}{p} \tag{2.3}$$

Continuity equation

$$\frac{\partial \ln p_*}{\partial t} = -V \bullet \nabla \ln p_* - D - \frac{\partial \dot{\sigma}}{\partial \sigma} \tag{2.4}$$

Hydrostatic balance

$$\frac{\partial \phi}{\partial \ln \sigma} = -T \tag{2.5}$$

Here,

$$F_U = V\zeta - \dot{\sigma}\frac{\partial U}{\partial \sigma} - T'\frac{\partial \ln p_*}{\partial \lambda},$$

$$F_V = -U\zeta - \dot{\sigma}\frac{\partial V}{\partial \sigma} - T'\left(1-\mu^2\right)\frac{\partial \ln p_*}{\partial \mu}.$$

The notation used for the variables in the equations above are listed in Table 2.1.

ζ	absolute vorticity
D	divergence
$T = \bar{T}(\sigma) + T'$	temperature
p_*	surface pressure
p	pressure
ϕ	geopotential
$\sigma = p/p_*$	sigma vertical coordinate
λ	longitude
θ	latitude
μ	$\sin\theta$
u	zonal velocity
v	meridional velocity
U	$u\cos\theta$
V	$v\cos\theta$
R	specific gas constant
c_p	specific heat capacity of dry air at constant pressure
κ	R/c_p

Table 2.1. Notation used in the basic equations.

2.2. Radiative transfer

The radiative transfer scheme included in the UK-LMD MGCM [Forget et al., 1999] is called every 10 dynamics time steps in the original setting. In the version used in this thesis, it calculates the atmospheric absorption and emission only due to the carbon dioxide and dust at every 5 dynamics time steps to better resolve the radiative transfer, but the water cycle is not included in my study. In the latest version beyond

the project described here, a full water cycle has been included which also takes account of the radiative effects of water ice [Mulholland, 2012], and a companion study concerning the assimilation of water vapour and ice opacity has been conducted in the Open University [Steele, 2014].

2.3. Surface processes

The balance between incoming fluxes and thermal conduction in the soil contributes to changes of surface temperature. Together with the surface thermal inertia field derived from TES data and Viking observations [Forget et al., 1999], the accurate measurements of detailed topography of Mars from the Mars Orbiter Laser Altimeter (MOLA) onboard Mars Global Surveyor [Smith D. E. et al., 2001] are used to calculate the surface processes.

According to the early estimate of Martian surface roughness length at Viking Lander sites by Sutton et al. [1978], for many years the roughness length z_0 was typically assumed globally homogeneous in most Martian modeling studies within the range 0.1-1 cm. Recently, however, an observationally based global z_0 map covering the full Martian surface has been compiled through the collaboration among workers at LMD, the Laboratoire Atmosphères, Milieux, Observations Spatiales (LATMOS), and the Laboratoire Interuniversitaire des Systèmes Atmosphériques (LISA) [Hébrard et al., 2012]. The details of the implementation of the variable z_0 map into the UK-LMD MGCM were described in the D.Phil work of Mulholland [2012]. Since the diagnosis of past assimilations is also part of the content of my thesis, both of these two treatments of z_0 are involved in different parts of my thesis. The work presented in Chapter 3 was conducted based on the datasets of the Mars Analysis Correction

Data Assimilation (MACDA) [Montabone et al., 2011b] in which z_0 is chosen as 1cm, while the variable z_0 map was applied in the work presented in Chapters 4, 5, 6 and 7.

2.4. Subgrid dynamics

The turbulent mixing in the vertical of any state variable a is generally computed as

$$\frac{\partial a}{\partial t} = \frac{1}{\rho}\frac{\partial}{\partial z}\left(K\rho\frac{\partial a}{\partial z}\right), \tag{2.6}$$

where K takes different values for velocity (u, v), potential temperature θ and dust tracers. The turbulent surface flux into the bottom atmospheric layer is represented by $\rho C_d U_1(a_1 - a_0)$, where a_1 and a_0 are respectively the variable values in the first model layer and at the surface, U_1 is the wind velocity in the first layer, and C_d is the drag coefficient. In the model, we simply use $C_d = \left(\kappa \Big/ \ln\left(\frac{z}{z_0}\right)\right)^2$. Here, κ represents the Von Karman constant, which is assumed to take the value 0.4 and z_0 is the roughness length, which is chosen to be 1 cm everywhere on Mars suggested by Sutton et al. [1978] for the Viking Lander sites, or in an updated model version with global variation ranging from $\sim$0.001 cm to 2 cm as in the highest resolution z_0 map [Mulholland, 2012].

The mixing coefficients are computed based on an equation for the evolution of the turbulent kinetic energy (TKE) [Mellor and Yamada, 1982]. The evolution of TKE (denoted as E) can be obtained from

$$\frac{\partial E}{\partial t} = \frac{q^3}{l}\left(S_u G_u + S_\theta G_\theta - \frac{1}{b_1}\right) + \frac{\partial}{\partial z}K_E\frac{\partial E}{\partial z} \tag{2.7}$$

where,

$q = \sqrt{2E}$,

$G_u = \frac{l^2}{q^2} M^2$,

$M = \sqrt{\left(\frac{\partial u}{\partial z}\right)^2 + \left(\frac{\partial v}{\partial z}\right)^2}$,

$G_\theta = -\frac{l^2}{q^2} \frac{g}{\theta_0} \frac{\partial \theta}{\partial z}$,

$S_u = \frac{\alpha_1 + \alpha_2 G_\theta}{(1 + \alpha_3 G_\theta)(1 + \alpha_4 G_\theta)}$,

$S_\theta = \frac{\alpha_5}{1 + \alpha_3 G_\theta}$,

$S_E = \alpha_6$.

The coefficients α_1, α_2, α_3, α_4, α_5, α_6, b_1 are assigned respectively the constant values, 0.393, -3.09, -34.7, -6.13, 0.494, 0.38, 16.6 [Forget et al., 1999].

2.5. Dust transport scheme

On Mars, dust particles can be injected into the atmosphere by various dust lifting mechanisms, and can go into suspension. Once they are lifted from the surface, the background wind and turbulent effects may be large enough to keep them aloft. Thus, they will possibly become part of the full atmospheric circulation.

To represent the above dust processes physically, the dust transport scheme includes a dust lifting scheme, tracer advection, gravitational sedimentation and deposition. Since the direct measurements of dust multi-size distribution are absent on Mars, for simplicity, I choose the size of 1.5 μm to be the single representative particle size in

the dust transport scheme. The choice of this particle size is based on the retrieval of airborne dust effective radius using various Landers' data [e.g. Pollack et al., 1995; Lemmon et al., 2004]. The detail of the latest rovers' data for the retrieval of dust effective radius can also be found in section 1.2.4 of this thesis. The two most important distinct mechanisms responsible for the injection of dust into atmosphere are thought to be dust lifting by near-surface wind stress and dust lifting by the activity of dust devils [Newman et al., 2002a], and they have also been parameterized in various dust numerical studies [Newman et al., 2002b; Basu et al., 2004; Basu et al., 2006; Kahre et al., 2006; Kahre et al., 2008; Mulholland, 2012; Mulholland et al., 2013].

The UK assimilation scheme did not include the representation of dust transport until the new update of the data assimilation system described in the Chapter 4 of this thesis. The work presented in Chapter 3 analyzes the existing assimilated results that were produced in the work of Montabone et al. [2005] and later published online as MACDA reanalysis [Montabone et al., 2011b]. Dynamical dust transport is therefore not involved in Chapter 3.

2.5.1. Dust lifting by near-surface wind stress

The near-surface wind stress lifting process has been generally noted to be threshold-dependent [Bagnold, 1954]. The actual drag velocity u_* is approximately related to the atmospheric wind velocity near the ground by the logarithmic relationship,

$$u(z) \simeq \frac{u_*}{\kappa} \ln\left(\frac{z}{z_0}\right) \tag{2.8}$$

where $u(z)$ is the wind velocity at different height, z is the height above the surface, κ is von Karman's constant, taken to be 0.4, and z_0 is roughness length. In the transport scheme, either a typical value of 1 cm is taken everywhere on Mars, or a roughness map derived from rock abundance map from TES thermal inertia data [Nowicki and Christensen, 2007; Hébrard et al., 2012] is applied at the corresponding grid-resolution.

Therefore, the actual drag velocity u_* can be obtained as,

$$u_* = \frac{\kappa u(z)}{\ln\left(\frac{z}{z_0}\right)} \tag{2.9}$$

The threshold drag velocity u_*^t was determined by a semi-empirical equation for conditions appropriate to both the Earth and other planets [Bagnold, 1954; Greeley and Iversen, 1985; Newman et al., 2002a]. It can be expressed in the form

$$u_*^t = A\sqrt{gD_p\frac{\rho_d - \rho}{\rho}} \tag{2.10}$$

where ρ_d represents the density of Martian dust (about 2500 $kg \cdot m^{-3}$), and D_p represents the diameter of the dust particle in the units of meter. Here, A is a factor dependent on the density of Martian dust ρ_d, the acceleration due to gravity, g, the diameter of the dust particle D_p, the friction Reynolds number R_{*t} at the fluid threshold determined by $u_*^t D_p / \nu$ (ν is the kinematic viscosity), and the interparticle cohesion parameter I_p. The equations for calculating A varies with the range of R_{*t}, and must be solved iteratively [Greeley and Iversen, 1985]. An additional scaling factor 0.7 is inherited from the work of Mulholland [2012] based on the same parameterization of near-surface wind stress dust lifting at T31 resolution. This value

was found to be appropriate to account for the subgrid scale gustiness and the effect of a low impact threshold for Mars.

Following the work of Newman et al. [2002a], we assume that the vertical flux V_N of particles lifted into suspension in atmosphere was roughly proportional to the vertically integrated horizontal sand flux H. Newman et al. [2002a] used a suggested form for H by White [1979] as,

$$H_{white} = \max\left[0, 2.61\frac{\rho}{g}(u_*)^3\left(1-\frac{u_*^t}{u_*}\right)\left(1+\frac{u_*^t}{u_*}\right)^2\right].$$

Another form of H (Eq. 2.11) from a more recent numerical model study was found by Kok and Renno [2008]. Mulholland [2012] implemented this new horizontal flux H into the UK-LMD MGCM and that is the version used in the work described in this thesis.

$$H = \max\left[0, 0.25\frac{\rho}{g}(u_*)^3\left(1-\left(\frac{u_*^t}{u_*}\right)^2\right)\left(7+50\left(\frac{u_*^t}{u_*}\right)^2\right)\right]. \quad (2.11)$$

Therefore, the vertical flux V_N can be expressed as Eq. 2.12.

$$V_N = \alpha_N H\,, \quad (2.12)$$

where α_N is the near-surface wind stress lifting efficiency. In practice, α_N is tuned to produce interannual variability and distinct storm events in a full model simulation [e.g. Newman et al., 2002a; Newman et al., 2002b; Basu et al., 2004; Basu et al., 2006; Kahre et al., 2006; Mulholland, 2012; Mulholland et al., 2013].

2.5.2. Dust lifting by the activity of dust devils

The second dust lifting mechanism is that by the activity of dust devils. A dust devil is an atmospheric convective vortex with low-pressure center and strong updrafts.

Thus, a dust devil is capable of sucking the dust from the surface and raising it to high altitude up to 8 km within the convective plume, and its horizontal scale can range from a few centimeters to the order of 100 meters [Fisher et al., 2005]. The occurrences of Martian dust devils have been confirmed by many observations, e.g. Balme et al. [2003], Fisher et al. [2005], Greeley et al. [2006].

The parameterization of dust devil lifting used in our studies concerning data assimilation is based on the modeling work of Rennó et al. [1998] in which results were shown to be consistent with the dust devil events recorded by Mars Pathfinder lander instruments, as well as with the observed wind and the pressure fluctuations [Rennó et al. 2000].

Heat engines are devices that convert heat into mechanical energy, so the natural convective phenomenon resembles a heat engine [Rennó et al., 1998]. Assuming the dust devil is in quasi-steady state, the work done by the heat engine should be balanced by mechanical friction. In the parameterization scheme, an example of dust devils is modeled as a heat engine. In this dust devil heat engine, the heat input is assumed to be the surface sensible heat flux F_s. The flux of mechanical energy made available by the convective heat engine drives the dust devil. According to Rennó et al. [1998], the vertical dust flux V_D generated by dust devil activity is therefore set equal to an empirical dust devil lifting efficiency α_D times the thermodynamic efficiency η of the dust devil convective heat engine and the surface sensible heat flux F_s, i.e.,

$$V_D = \alpha_D \eta F_s . \tag{2.13}$$

Rennó et al. [1998] showed that η may be obtained approximately by,

$$\eta = 1 - \frac{\left(p_s^{\chi+1} - p_{top}^{\chi+1}\right)}{\left(p_s - p_{top}\right)(\chi+1)\, p_s^{\chi}} \tag{2.14}$$

where p_s represents the ambient surface pressure, p_{top} represents the ambient pressure at the top of the boundary layer and $\chi = R / C_p$. Because the dust devil lifting is normally expected to be the major contributor to the airborne dust during the "quiet" season ($L_s = 0° - 180°$), α_D is normally tuned to reproduce the amount of dust during the "quiet" season [e.g. Newman et al., 2002b; Mulholland, 2012; Mulholland et al., 2013].

2.6. Initial data assimilation work

With spacecraft, including Mars Global Surveyor (MGS), Mars Odyssey and Mars Reconnaissance Orbiter (MRO), in orbit about Mars in sequence since 1997, there are now measurements of atmospheric temperature and dust extending over nearly 8 Martian years with unprecedented spatial coverage. Although those observations have greatly developed our understanding of the evolution, structure and climate of the Red Planet, the intermittent nature of the measurements still limits our ability to study the full details of the circulation, especially relating to dust activity. A numerical model, on the other hand, can provide continuous simulated data with high temporal and spatial resolutions, but typically fails to produce some significant features of dust storms, as well as their interannual variability. In this context, a data assimilation scheme combined with UK-LMD MGCM is able to provide a complete, balanced, four-dimensional solution consistent with observations [Lewis and Read, 1995; Montabone et al., 2005; Lewis and Barker, 2005; Montabone et al., 2006a; Montabone et al., 2006b; Lewis et al., 2007; Montabone et al., 2011b].

Previous attempts at data assimilation for Mars climate, they have been conducted without explicitly advecting a dust tracer field, mainly because the Mars Global

Surveyor/Thermal Emission Spectrometer (MGS/TES) did not provide more information on the dust vertical distribution. Thus, only the retrievals of temperature profiles and column dust opacity were assimilated into this early-version data assimilation system. Nevertheless, this data assimilation system has been applied in several previous studies to give us a better understanding of phenomena in the Martian atmosphere given incomplete and/or noisy measurements [Montabone et al., 2005; Lewis and Barker, 2005; Montabone et al., 2006a; Montabone et al., 2006b; Lewis et al., 2007; Wilson et al., 2008a; Rogberg et al. 2010; Mulholland, 2012].

The data assimilation scheme implemented in the UK-LMD MGCM is based on the analysis correction sequential estimation (AC) scheme [Lorenc et al., 1991], but with modifications specific to Mars [Lewis et al., 2007]. Compared to the UK-LMD MGCM itself, the data assimilation scheme is computationally inexpensive. The analysis iteration, which is based on the cost function, is performed at each dynamical time step of the model (currently 480 times per sol at the chosen resolution), and attempts to make the model predictions fit to the observations in terms of their relative errors. Observational increments to the model are determined in time and space in terms of empirical covariance functions (Eq. 2.15). In this AC scheme, the covariance functions are only determined empirically and they will not change during the analysis. This is the deficiency of the AC scheme compared to those more complicated Kalman Filters based data assimilation schemes in which the background error covariance evolves with the atmospheric flow [e.g. Greybush et al. 2012]. After the analysis correction of the temperature fields in the AC scheme, the temperature increments are balanced by non-divergent, thermal wind increments. Thus, the wind fields are adjusted by adding the wind increments in geostrophic thermal wind

balance. This balancing procedure is designed for retaining the newly introduced information to fast inertia-gravity waves [e.g., Daley, 1991].

The analysis correction of temperature profiles is typically performed first in the vertical direction followed by the horizontal and temporal analysis. The temperatures are interpreted as mean temperatures in layers between a standard set of pressure values, which can be considered to represent the resolution of the vertical temperature retrievals. The corresponding model layer thickness is calculated between each pressure value in terms consistent with the temperature retrievals. The philosophy behind this method is that the vertical scale of temperature increments should reflect the observational resolution instead of the model vertical resolution. This method also has the advantage of maintaining the physics of the model itself, even if this can not be resolved explicitly by the remotely-sensed data.

In the horizontal space, the increments to the model variables on each model grid location Δx_k are spread by the following function [Lorenc et al., 1991],

$$\Delta x_k = \lambda \sum_i \mu_{ki} \overline{Q_i} R_i^2 (\delta t_i) C_i \tag{2.15}$$

where,

k	refers to a model grid point,
i	refers to an observation,
λ	relaxation coefficient,
μ_{ki}	a function used to determine how the observational increments are spread in distance between model location and observation location,
$\overline{Q_i}$	normalization factor, i.e. a function of the ratio of observational error to first guess error and of the local observation density around each observation location,
R_i^2	a function used to determine how the observational increments are spread in time (refer to Figure 2.1),
δt_i	the time difference between model time and observation time,
C_i	the increments at the observation location.

Table 2.2 Notations in the Eq. 2.15.

According to Lewis et al. [2007], the relaxation coefficient λ can be related to the nudging relation with nudging coefficient G [Davies and Turner, 1977] by

$$G = \lambda / (1 - \lambda) \Delta t . \tag{2.16}$$

Here, Δt is the model dynamical time step. To achieve the best results, Lewis et al. [2007] set G to $5 \times 10^{-4} s^{-1}$ with a linear reduction, between 30 and 20 latitude in both hemispheres to $4 \times 10^{-4} s^{-1}$ at equator.

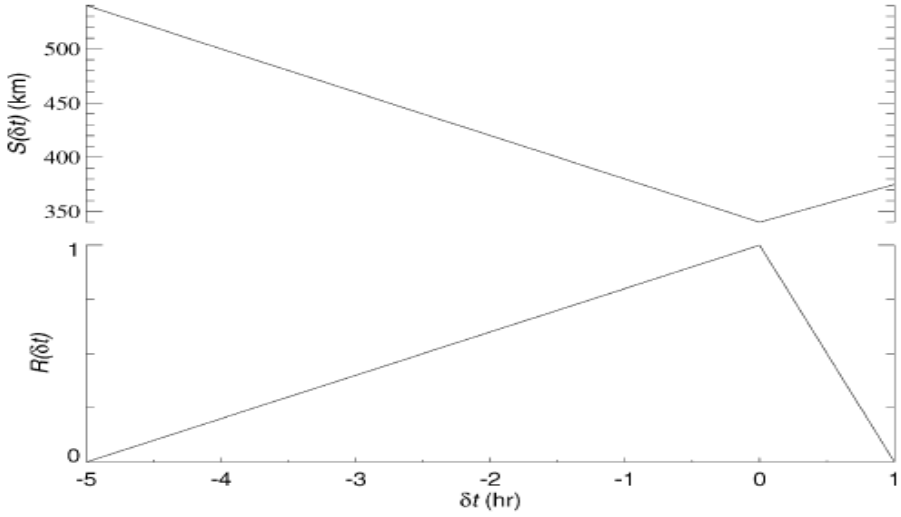

Figure 2.1, Horizontal correlation scale, S, and time factor, R, as a function of the model-observation time difference, δt (from the work of Lewis et al. [2007]).

The observational increments are spread by a second-order auto-regressive function of the distance, r_{ki}, between the location of observation i and each model grid point k,

$$\mu_{ki} = \left(1 + r_{ki} / S(\delta t_i)\right) \exp\left(-r_{ki} / S(\delta t_i)\right), \tag{2.17}$$

where $S(\delta t_i)$ is the correlation scale function, taken to be large at $\delta t = -5h$, and a minimum at $\delta t = 0h$. Overall, the increment reduces by a factor of half over nearly 570 km distance, but the maximum radius of influence is chosen at 3.5 $S(\delta t)$ (the spread is illustrated in Figure 2.1). In practice, therefore, the model will read in an

observation data 5 hours before it is valid and finally discards it 1 hour after its measured time.

However, in this initial data assimilation work, assimilation of column dust opacity was only conducted without advecting the dust tracer, mainly for simplicity. The vertical distribution of the dust opacity was instantly determined by an empirical relation following Conrath [1975]. At the given location and time, the dust opacity tau at pressure p is determined by,

$$tau = tauref \cdot \exp\left\{a\left[1-\left(p_0 / p\right)^{\left(b/z_{\max}\right)}\right]\right\}. \tag{2.18}$$

For pressure $p \le p_0$, where p_0 is taken to be $p_0 = 700Pa$, and with $tauref = tau$. For $p > p_0$, $tauref$ is the column dust opacity rescaled at reference level (here, $700Pa$). a and b are constant with values $a = 0.007$, $b = 70km$. $z_{\max}$ is the 'top' of the dust layer, varying with solar longitude L_s and latitude ϕ, and it is determined by

$$z_{\max} = 60 + 18\sin\left(L_s - 160°\right) - \sin^4\phi\left[32 + 18\sin\left(L_s - 160°\right) - 8\sin\left(L_s - 160°\right)\sin\phi\right].$$

In this thesis, Chapter 4 will document the extended dust-transporting data assimilation scheme developed during my DPhil project. This updated data assimilation scheme has been extended to assimilate both the column dust opacity and dust vertical profiles, together with the activated dust lifting and transport scheme. Subsequently, a new version of reanalysis based on this sophisticated data assimilation system has been obtained that is able to represent a more realistic dust distribution in the spatial and vertical dimension corresponding to the available observations.

Chapter 3 Investigating Interannual and Intraseasonal Variability of Martian Climate using Data Assimilation: The Semiannual Oscillation

3.1. Introduction

In the upper stratosphere and mesosphere of Earth, the semiannual oscillation (SAO) of the mean zonal wind in the tropical stratosphere and mesosphere was found as a clear feature [Reed, 1966; Garcia et al., 1997]. Reed [1966] used observational data to determine that the strongest westerly winds occurred shortly after the equinoxes in the lower mesosphere and then later extended to the lower levels. The pronounced SAO occurs at intermediate and upper levels of the stratosphere and mesosphere, and reaches a peak in amplitude at about the height of the stratopause.

Similar SAO-like features in the Martian tropics (between 10°-10°N) have been studied in the work of Kuroda et al. [2008], mainly based on a free-running Martian Global Climate Model (MGCM). Baldwin et al. [2001] described the important effects the SAO anomalies have on the distributions of trace species on Earth.

Suspended dust particles are widespread in the Martian atmosphere, and they strongly affect the dynamical and thermal structure of the Martian atmosphere. Studying and characterizing the SAO phenomenon on Mars may be essential to understand the dust cycle on Mars, as well as the Martian weather and climate.

So far, no comprehensive measurements of wind fields are available for the Martian atmosphere. At middle and high latitudes, horizontal winds may be approximately computed using the thermal wind relation, via temperature fields with incomplete coverage observed by the instruments onboard various satellites (e.g., Mars Global Surveyor (MGS), Mars Odyssey (MO), Mars Climate Sounder (MCS)). However, the thermal wind relation becomes invalid at low latitudes.

On the other hand, from variations in the structure and amplitude of solar thermal tides it may be possible to determine indirectly the corresponding variations of zonal-mean zonal wind. Lindzen and Hong [1974] discovered that the zonal wind could affect the propagation of solar tides. Wilson and Hamilton [1996] also showed evidence of the effect of the solstitial mean zonal wind on the tide propagation on Mars. Therefore, the seasonally varying wind should also affect the pattern of solar tides. In the work of Kuroda et al. [2008], the SAO signal was evident by analyzing the solar tides, derived from the observed temperature fields (from the Thermal Emission Spectrometer onboard MGS (MGS-TES)) and taking the difference between the daytime and the nighttime. The solar tides showed a clear SAO variation between 50 and 5 Pa in their study.

To conduct a detailed study of the SAO, Kuroda et al. [2008] made use of the simulation from a free-running MGCM. A clear SAO phenomenon between 10°S-10°N, similar to the stratospheric SAO in the Earth in terms of its appearance, was described in their results from a free-running MGCM (Figure 2 in Kuroda et al.

[2008]). To investigate the driving mechanism of the Martian SAO within tropics, Kuroda et al. [2008] went on to calculate the different contributions to the tendency of the mean zonal wind, $\partial\overline{u}/\partial t$ on intraseasonal timescales. Their conclusion was that at solstices, the horizontal cross-equatorial transport provided the westward forcing to the tropical zonal-mean zonal wind and the vertical advection mostly provided eastward momentum. The solar tides supplied eastward forcing at equinoxes. Somewhat surprisingly, at all seasons, Kelvin waves provided a westward forcing at all heights. Unlike on Earth, the effects of transient planetary waves and the eastward Kelvin waves on the Martian SAO were both quite weak.

Since the SAO may have further implications for the transport of tracers on Mars, as it has in the Earth's stratosphere, with the aim of understanding the Martian dust cycle more completely, it may be important to investigate the phenomenon of the Martian SAO in detail. The incomplete coverage of the available satellite measurements requires an interpolation in terms of time and space to acquire a complete observational coverage for the diagnosis of the Martian SAO. On the other hand, numerical models are able to overcome this difficulty to provide consistent data in time and three dimensional space. A MGCM is therefore a perfect tool for analyzing the Martian SAO. The modeling study of Kuroda et al. [2008] seemed to provide a reasonably plausible representation of the Martian SAO in the tropics. But is a free-running MGCM, with an unrealistically uniform dust distribution, sufficient to represent the real Mars atmospheric environment? Various numerical modeling studies have proved capable of reproducing the full seasonal variability of the Martian climate, but Martian Global Climate Models (MGCMs) still struggle to fully present the realistic interannual variability of the Martian climate system [Newman et al., 2002 a & b; Basu et al., 2004 & 2006; Mulholland et al., 2012 & 2013]. In this

context, data assimilation is another alternative approach towards obtaining a four-dimensional representation of atmospheric behavior that is consistent with both Martian observation-modeled physical constraints [Lewis and Read, 1995; Montabone et al., 2006a & 2011b; Lewis et al., 2007].

The goal of this chapter is to diagnose the observed Martian SAO based on the results from a Martian data assimilation system that can provide a more realistic climatology than free-running MGCMs. The phenomenology and driving forces of Martian SAO will be revealed and investigated in this study. We wish to confirm if we observe a similar phenomenon in the tropics of the assimilated Martian climate measurements as found in the work of Kuroda et al. [2008], and if the processes identified as driving the observed SAO are consistent with their analysis. A further question that can be answered by this observationally-based approach is that if components of an SAO can be observed outside of the tropics.

3.2. Data and methodology

The dataset used in this study for diagnosing the Martian SAO is the assimilated results from Mars Analysis Correction Data Assimilation (MACDA) dataset [Montabone et al., 2011b]. MACDA is based on the UK-LMD MGCM that was described in Chapter 2. A successive analysis correction scheme [Lorenc et al., 1991] was adapted and developed to assimilate the temperature profile-column-integrated dust opacity into UK-LMD MGCM [Lewis et al., 2007]. The modeled wind in this data assimilation system is adjusted to be consistent with the geostrophic thermal wind balance. Further technical details of this climate database can be found in the work of Montabone et al. [2011b] and the section 2.6 of Chapter 2 in this thesis.

This reanalysis dataset (MACDA) covers nearly three complete Mars years (MYs) corresponding to the MGS-TES observational periods, from 141° solar longitude (L_s) in MY 24 through $L_s = 82°$ in MY 27. Montabone et al. [2005] and Lewis et al. [2007] have already validated this dataset against available observations (other MGS-TES-radio occultation data), and this dataset has been proven to be reasonably consistent with those observations.

MACDA is provided at a standard resolution equivalent to spectral truncation T31, corresponding to a $3.75° \times 3.75°$ nonaliasing dynamical grid (see Chapter 2). For this analysis, the Martian atmosphere is divided into 7 latitude bands (60°- 90°N, 40°- 60°N, 10°- 40°N, 10°N- 10°S, 10°- 40°S, 40°- 60°S, 60°- 90°S) for investigating the Martian SAO both within and outside of the tropics. In section 3.3, the actual zonal wind from MACDA is shown to demonstrate the presence of a Martian SAO. Singular Spectrum Analysis (SSA) [Pike et al., 1984] is further used in each latitude band to reveal and decompose the phenomenology of Martian SAO. In section 3.4, the Transformed Eulerian Mean equation (TEM) [Andrews and McIntyre, 1978] are applied to study the different contributions to the tendency of the zonally-averaged zonal wind in the tropical middle atmosphere. The pressure and pseudo-height values used in the following figures were simply calculated from the model terrain-following vertical sigma coordinate using a reference pressure of 610 Pa and a uniform assumed scale height of 10 km. It is noted that because TES data only extends to 10 Pa, the reanalysis above that level might be only influenced by the adjustments being made below. Also, as the TES nadir data is only provided at the local time ~ 0200 and ~ 1400, this might not fully resolve the tides. Therefore, the reader should be cautioned that the tides in the reanalysis might mainly reply on the UK-LMD MGCM itself rather than the data assimilated.

3.3. Revealing the phenomenology of the observed SAO

3.3.1. Zonal wind

Figure 3.1 presents the zonal mean of the daily-averaged zonal wind from actual data (nearly 3 MYs in total) derived from MACDA Martian climate database in the different latitude bands defined above (60°- 90°N, 40°- 60°N, 10°- 40°N, 10°S- 10°N, 10°- 40°S, 40°- 60°S, 60°- 90°S).

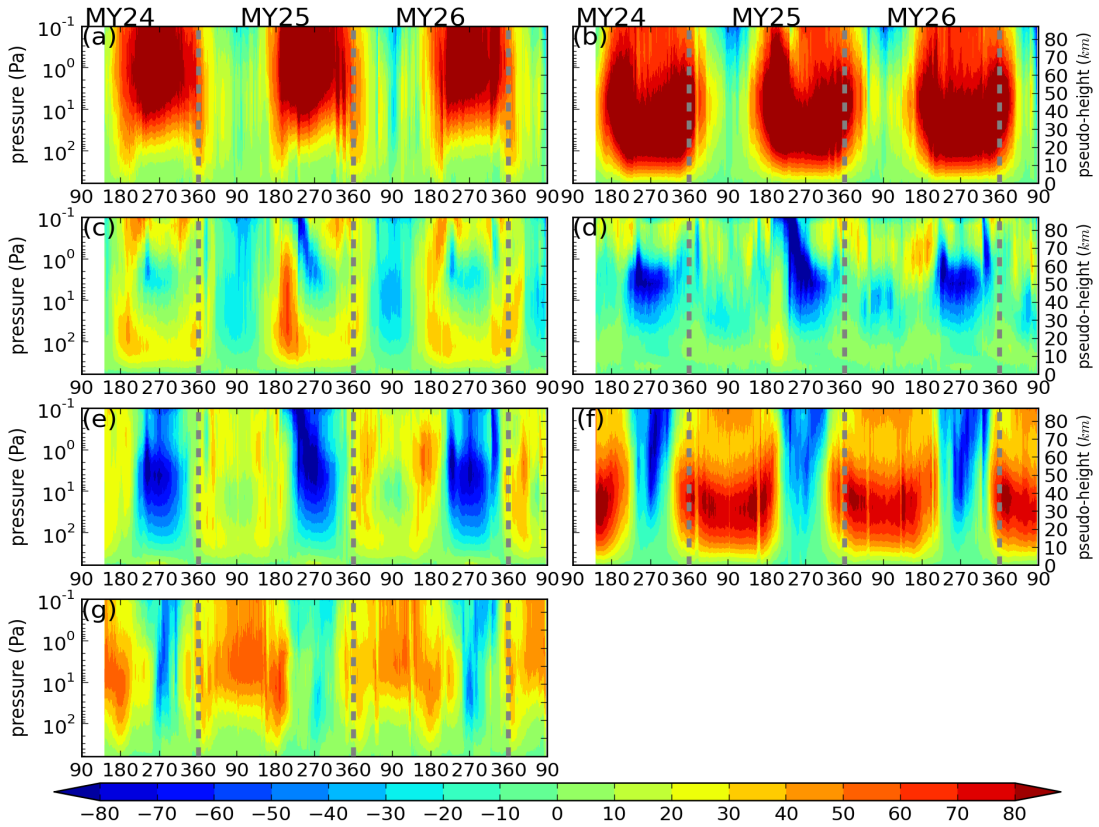

Figure 3.1 The raw zonal-mean of daily-averaged MACDA zonal winds ($m \cdot s^{-1}$) in different latitude bands, (a) 60°- 90°N, (b) 40°- 60°N, (c) 10°- 40°N, (d) 10°N- 10°S, (e) 10°- 40°S, (f) 40°- 60°S, (g) 60°- 90°S.

In the Martian tropics (between 10°N and 10°S), the eastward-westward alternating pattern associated with the SAO was mainly seen at altitudes between 100 Pa and 30 Pa. The zonal wind began with an eastward wind at the start of each MY, changing to

a westward wind some time afterwards. This oscillation evidently repeated twice a year, as in the experiments of Kuroda et al. [2008]. A similar SAO cycle could also be seen in the magnitude of zonal wind above 30 Pa until ~ 1 Pa, but the winds there only decelerated their westward component instead of completely reversing their direction from westward to eastward as at lower altitudes. In contrast to the cycles found by Kuroda et al. [2008], however, during each MY one of the two semi-annual cycles appeared to be stronger than the other. Clearly intensified eastward winds were also noticeable between L_s ~ 190° and ~ 230° during the MY 25 global dust storm (GDS). Normally, the eastward wind dominated below 20 Pa, but it was strongly reinforced and extended to higher altitudes (~ 1 Pa) during this strong dust event.

Apart from the tropics, the zonal wind within other latitude bands across the whole planet was also examined in the current study. It was clear from these that the SAO feature was also evident in latitude bands other than the tropics, though it was less pronounced towards the poles. The SAO pattern was also quite noticeable in the middle atmosphere (100 Pa – 1 Pa) of the sub-tropics (10°- 40°N and 10°- 40°S). The zonal-mean zonal wind direction oscillated from eastward to westward within a half-year cycle. Similarly to the tropics themselves, the two cycles in each year were of unequal magnitude, such that only one of the two cycles could be seen to extend throughout the whole atmosphere above 200 Pa. When the westward wind of the first SAO cycle dominated in the northern atmosphere, this corresponded to the westward wind of the second SAO cycle in the southern hemisphere extending vertically to the whole atmosphere above ~ 200 Pa. This phenomenon was coincident with the annual cycle of the motion of the sub-solar point in latitude – this is located in the Northern Hemisphere in the first half-year, moving to the Southern Hemisphere in the second half-year. The sub-tropical SAO cycle in each hemisphere tended to be stronger when

the sunlight directly imposed on that hemisphere. The SAO could also be seen in the middle and high latitude bands (60°- 90°N, 40°- 60°N, 40°- 60°S, 60°- 90°S) but much less strongly. They did not lead to a full reversal of the wind direction as in the tropical atmosphere at altitudes higher than 30 Pa, but tended to slow down the prevailing eastward wind during the weaker cycle of the two in a given year.

3.3.2. Singular spectrum analysis

To further study the Martian SAO, I performed a Singular Spectrum Analysis (SSA) on the daily-averaged zonal-mean zonal wind, in order to adaptively isolate the semiannual variations in each latitude band. SSA is a statistical technique applied in the time domain that is widely used in signal processing [Pike et al., 1984] and is similar to the Empirical Orthogonal Function (EOF) analysis which is usually applied in the spatial domain [e.g., Barnston and Livezey, 1987; Ghil et al., 1990]. Compared to other types of spectral analysis, the filters derived in SSA are not prescribed *a priori*, but are determined, optimally with respect to variance, from the data themselves [Collins et al., 1996]. Further, much more information could be obtained by studying its principal components. SSA was employed here to demonstrate thoroughly the relative importance of SAO signal compared to other oscillations especially in those latitudes and altitudes where SAO signal was embedded in other harmonies.

In order to smooth the day-to-day fluctuations of zonal wind fields, a 5-sol running-mean was applied to the diurnally-sampled zonal-mean zonal wind. Afterwards, the data was resampled by choosing every fifth data point for SSA analysis. The analysis time window here was chosen to be 335 sols (67 data points being resampled by choosing every fifth data point) which is approximately half a Martian year. It was

tested over at least a 30-sol range to ensure that the results were not sensitive to the choice of this time window in relation to the period of the semiannual oscillation. The eigenvectors of such a SSA represent recurrent patterns within the time window of the dataset with a variance fraction that is proportional to the corresponding eigenvalue.

3.3.2.1. Principal Components

Because the first 6 eigenvalues already capture a large contribution (increasing from a minimum of 63.8% % in the tropics to 92.7% in the middle and high latitudes, and the details can be found in Table 3.1) to the variance of the final solution of zonal wind, their frequencies (and other characteristics) are discussed here in detail (and are shown in Figure 3.2). In the middle (40°- 60°N Figure 3.2b, 40°- 60°S Figure 3.2f) and high (60°- 90°N Figure 3.2a, 60°- 90°S Figure 3.2g) latitude bands, the first two leading Principal Components (PCs) normally presented an annual oscillation, while in the sub-tropical bands (10°- 40°N Figure 3.2c, 10°- 40°S Figure 3.2e) and in the tropics (10°N - 10°S Figure 3.2d), the influence of SAO perturbations was noticeable in the first two PCs, though the main features of the annual oscillation still dominated. This suggests that the annual oscillation component still contributed most to the zonal-mean zonal wind variations at these latitudes.

latitude band	PC 1	PC 2	PC 3	PC 4	PC 5	PC 6	total contribution
60°-90°N	42.6%	40.2%	3.5%	1.9%	1.7%	1.0%	90.9%
40°-60°N	40.5%	40.3%	5.9%	3.6%	1.3%	1.0%	92.6%
10°-40°N	22.6%	22.4%	14.5%	7.8%	4.3%	3.2%	74.8%
10°S-10°N	19.6%	16.9%	11.1%	6.6%	4.9%	4.7%	63.8%
10°-40°S	39.8%	30.7%	11.7%	4.5%	1.4%	1.0%	89.1%
40°-60°S	41.2%	34.5%	11.1%	4.0%	1.0%	0.9%	92.7%
60°-90°S	36.6%	28.1%	10.3%	6.0%	3.5%	1.7%	86.2%

Table 3.1 The contribution of the first 6 eigenvalues to the variance of the final solution of zonal wind.

In all the latitude bands, the third and fourth PCs captured most of the SAO signal (all the middle rows of Figure 3.2). Within each latitude band, five relatively clear cycles could be seen within the whole analysis period. In the Southern Hemisphere including 10°- 40°S, 40°- 60°S, 60°- 90°S, SAO signals were more obvious in both

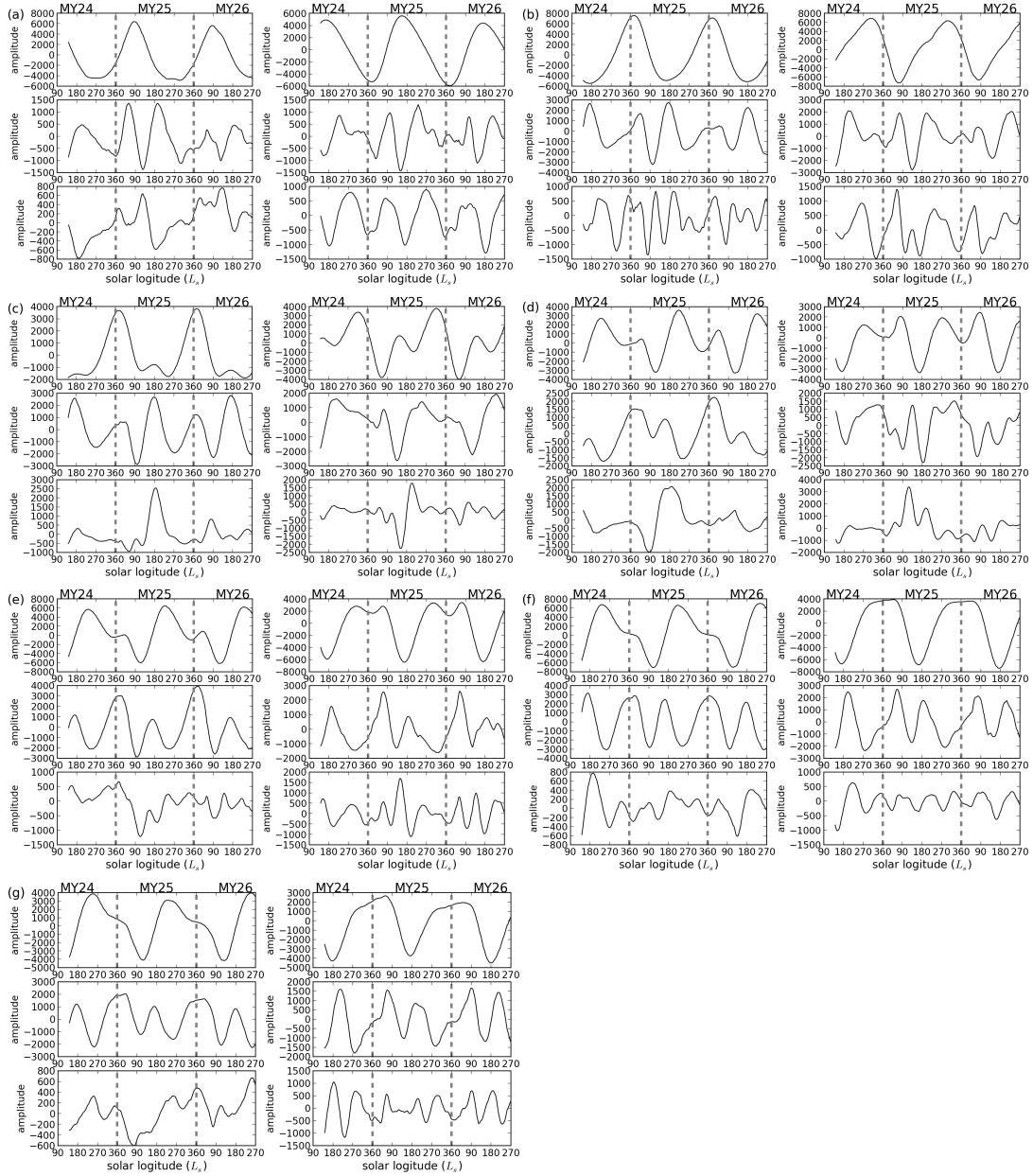

Figure 3.2 The PCs of the first 6 eigenvalues in different latitude bands. In each figure the upper two frames represent the first pair of PCs, the middle two represent the second pair and the lower two the third pair of PCs, (a) for 60°- 90°N, (b) for 40°- 60°N, (c) for 10°- 40°N, (d) for 10°S - 10°N, (e) for 10°- 40°S, (f) for 40°- 60°S, and (g) for 60°- 90°S.

the third and fourth PCs than those in the Northern Hemisphere, and the amplitudes of the signals were more consistent. In the Northern Hemisphere, one of the two PCs in each latitude band had relatively clear signal of half-year oscillation, while the other had some small oscillations superimposed on top of the semiannual cycles which could be due to the impact of higher frequency waves.

Except in the high latitudes of the Northern Hemisphere (60°- 90°N), the fifth and sixth PCs mainly represent the high-frequency transient patterns, especially in the Southern Hemisphere. The fifth and sixth PCs in the high latitudes of the Northern Hemisphere exhibited signals with similar cycles to the SAO as in the third and fourth PCs. It is interesting to mention that these two PCs in the tropics (10°S -10°N) and sub-tropics of both hemispheres (10°- 40°N, 10°- 40°S) showed abrupt changes of amplitude during the MY25 GDS (corresponding to mid-2001 on Earth). The further relationship between these two components, corresponding to an increase of actual zonal wind and perhaps connected to the triggering/response and evolution of the MY25 GDS, could be an interesting topic to investigate further in future.

3.3.2.2. Eigenvectors

Within the chosen analysis time window (335 days, approximately half a MY) for SSA analysis, height-time plots present the distribution of patterns of recurrent SAO activity (i.e. corresponding to the third and fourth eigenvectors) in height and time (see Figure 3.3). It is obvious that in each latitude band, a slight phase difference exists between the third and fourth eigenvector, i.e. the signals represented by the third eigenvector almost started from their highest positive value, then changed to the lowest negative value, and back to positive values again. In contrast, the signals represented by the fourth eigenvector except at the tropics started from positive values

but changed quickly to low values, and went through a full half-cycle to negative values again. It indicates that the phase of the fourth eigenvector is roughly a quarter of a cycle ahead of the phase of the third eigenvector.

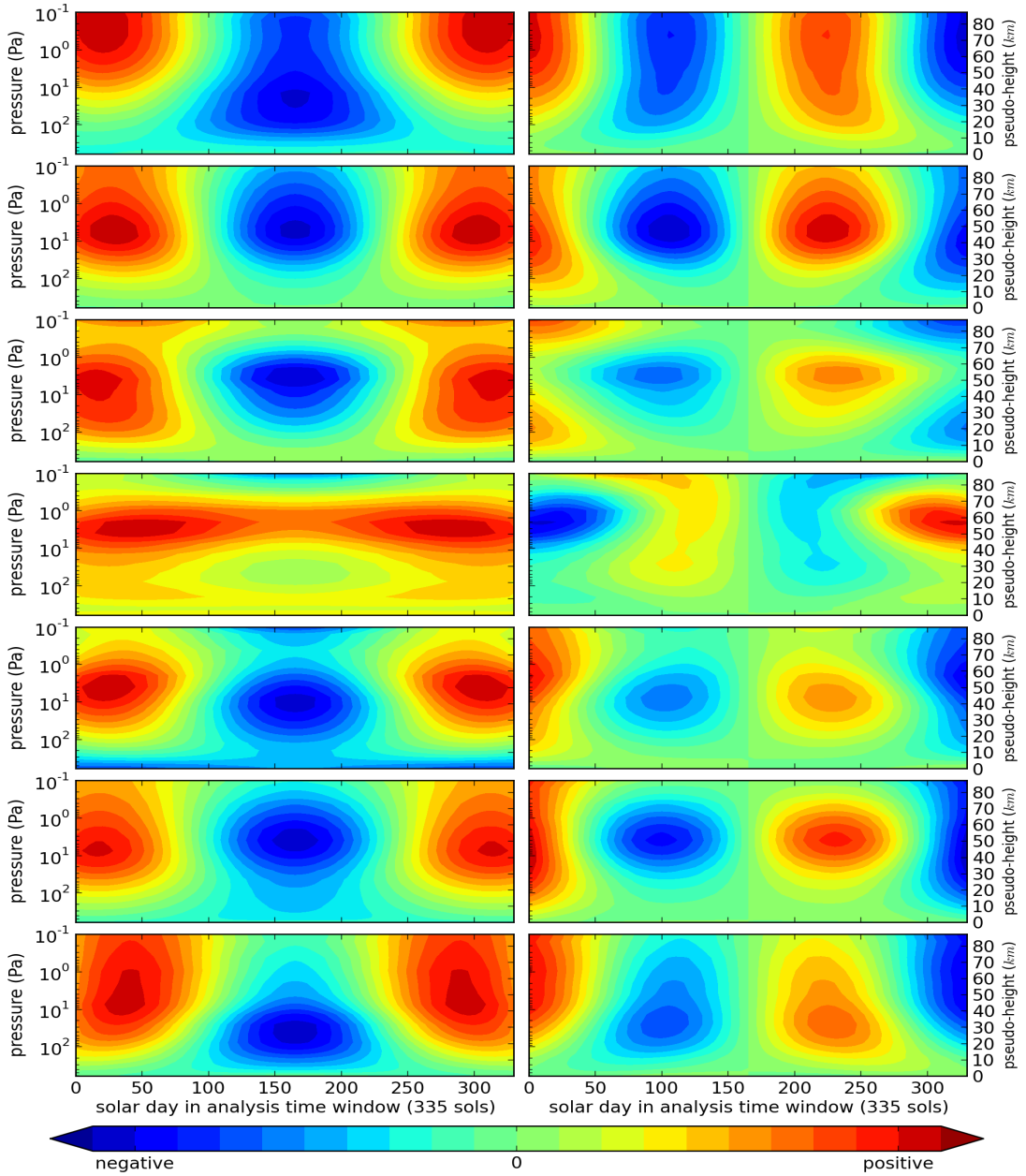

Figure 3.3 the third eigenvector height-time contour (left column) and the fourth eigenvector height-time contour (right column). From the topmost row to the lowest row, the results are presented for each latitude band in the order 60°- 90°N, 40°-60°N, 10°-40°N, 10°S-10°N, 10°-40°S, 40°-60°S, 60°-90°S.

In the vertical direction, signals with an SAO period could be seen clearly aligned with height. The SAO signals were normally strongest between 100 Pa and 1 Pa. The

phases of the third eigenvectors remained nearly uniform with height in each latitude band with no phase tilt. In the tropics (10°S -10°N) between 10 Pa and 1 Pa, the cycle of the third eigenvector did not reverse to exhibit negative values; instead, it only decreased towards smaller values but remained always positive. Except in the tropics, the cycle of the fourth eigenvector remained at the same phase all the way to high altitudes. In the tropics, there was a change of signal frequency above 0.5 Pa for the fourth eigenvector. Between 100 Pa and 0.5 Pa, a full cycle could be observed within this half-MY window. The cycle started from its largest negative value gradually increased towards the positive values, becoming negative again in the third quarter of the cycle. Thereafter, the cycle reached its largest positive values. Above 0.5 Pa, the eigenvector starts from the largest positive value-decreases all the way to its largest negative values, and this should be the signal of annual pattern.

3.3.2.3. Reconstruction of SAO components

In order to better demonstrate and isolate the SAO signal embedded in the daily-averaged zonal-mean zonal wind, the SAO-dominated components were reconstructed using only the third and fourth PCs in the SSA analysis in each latitude band (see Figure 3.4). As discussed in section 3.3.2.1, the SAO signal in some latitude bands (10°-40°N, 10°S-10°N, 10°-40°S) could also be seen in the first and second PCs. As a result, the zonal-mean zonal wind reconstructed only from third and fourth PCs might lose some of this information. It is entirely possible that the SAO signals were even more pronounced in the raw zonal-mean zonal wind in some latitude bands. This, however, should not disguise the presence of SAO signals at each latitude band.

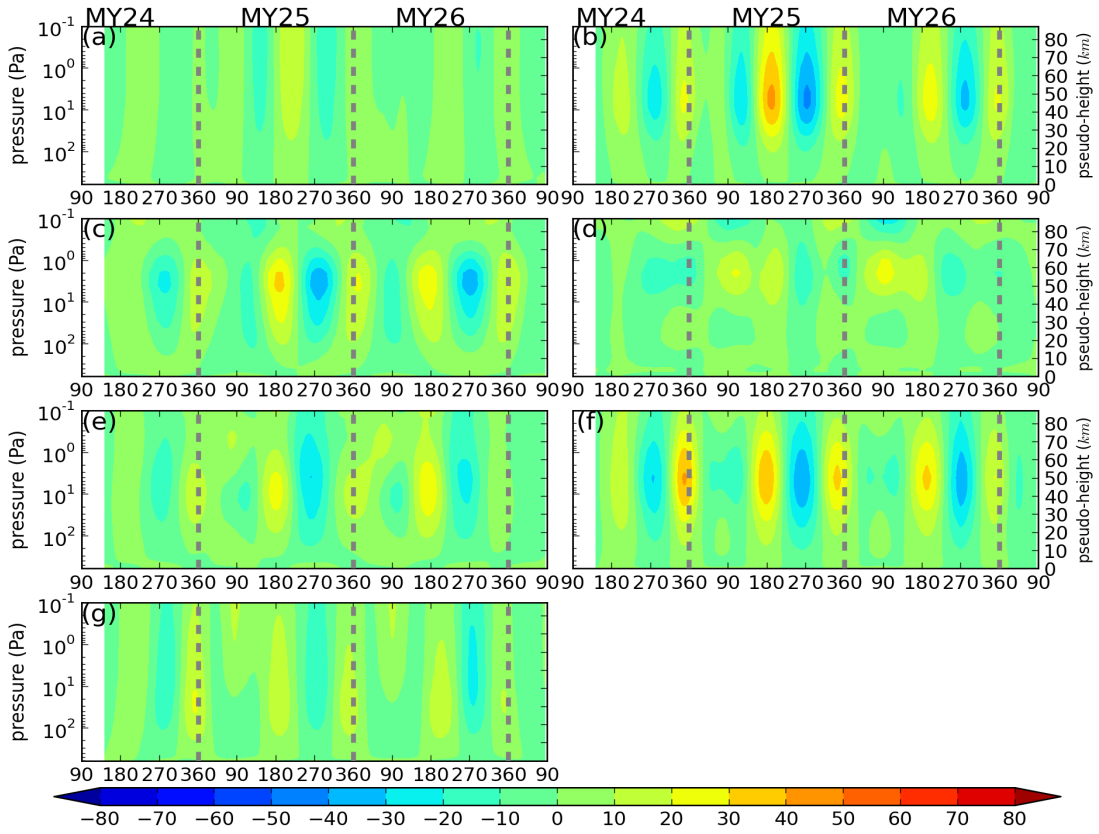

Figure 3.4 The reconstruction of the wind structure ($m \cdot s^{-1}$) due to the third and fourth PCs in the SSA analysis, which approximately correspond to the SAO component, (a) for 60°-90°N, (b) for 40°-60°N, (c) for 10°-40°N, (d) for 10°S-10°N, (e) for 10°-40°S, (f) for 40°-60°S and (g) for 60°-90°S. The color scales are chosen to be the same as Figure 3.1.

In the tropics (between 10°S - 10°N), the pattern represented by these two PCs in the reconstruction was relatively complicated, perhaps because dynamical conditions close to the equator could be strongly affected by a number of different factors. The SAO could be observed quite clearly in the middle atmosphere (100 Pa ~ 20 Pa), and between 10 Pa and 0.4 Pa, the frequency of the oscillation mainly displayed as annual cycle. Above 0.4 Pa, the oscillation of the zonal wind corresponding to these two PCs varied from year to year. The zonal-mean zonal wind in MY 25 showed a clear SAO pattern, for example, while the zonal-mean zonal wind in MY 26 favored an annual oscillation more strongly. In the sub-tropical bands (10°- 40°N, 10°- 40°S), the SAO signals were noticeable between 100 Pa and 1 Pa. Between two cycles in each MY, one of them had a westward component that nearly dominated the whole atmosphere

(called “westward-dominated” cycle in this study, the other one we call the “part-westward” cycle). The “westward-dominated” and “part-westward” cycles alternated each year, but they happened in the reverse phase in different hemispheres. The “westward-dominated” cycle started first in the Northern Hemisphere, while the “part-westward” cycle started first in the Southern Hemisphere. However, the stronger westward components happened at the same time of year for both hemispheres. The westward component was stronger in the “part-westward” cycle in the Northern Hemisphere, while it was stronger in the “westward-dominated” cycle of the Southern Hemisphere. Extending to the polar regions, the SAO component became more significant and usually dominated most of the atmosphere in the reconstructed component of zonal-mean zonal wind. The overall amplitude reached its maximum in the middle latitude bands (40°-60°N, 40°-60°S) in both hemispheres. However, unlike in the tropical low latitudes, one of the two SAO cycles in the middle latitude bands (40°-60°N, 40°-60°S) and in the high latitude bands (60°-90°N, 60°-90°S) were not so obvious in the corresponding raw zonal-mean time-height maps of daily-averaged zonal wind (see Figure 3.1). This was because the annual cycle was stronger than the SAO outside the tropics. In the southern polar region (60°-90°S), an eastward wind component seemed to invade the lower part of the atmosphere at $L_s \approx 90°$, and limited the SAO component to below 10 Pa. Furthermore, it is interesting to point out that within Northern Hemisphere, a maximum of SAO components seemed to appear during the MY 25 GDS, but it did not stand out in the Southern Hemisphere.

3.4. A TEM momentum budget for the SAO in the tropics

In order to identify the dominant processes generating the Martian SAO, the pressure-coordinate TEM equation, from the work of Andrews and McIntyre [1978], was applied to decompose the terms of this wave-mean-flow problem. If all the contribution terms to the zonal-mean zonal wind tendency were moved to the right-hand side of the equation, the formulation would be as follow,

$$\overline{u}_t = \left(f - \frac{(\overline{u}\cos\varphi)_\varphi}{r_0 \cos^2\varphi} \right) \overline{v}^* - \overline{u}_p \overline{\omega}^* - \left(\frac{1}{r_0 \cos^2\varphi} \left(S_{(\lambda\varphi)} \cos^2\varphi \right)_\varphi + \left(S_{(\lambda p)} \right)_p \right) - \overline{X}, \qquad (3.1)$$

where $\overline{u}$ is the zonal-mean zonal wind, f the Coriolis parameter, φ is latitude, r_0 is the radius of the earth, the meridional circulation $\left(0, \overline{v}^*, \overline{\omega}^*\right)$ is defined by

$$\overline{v}^* = \overline{v} - \left(\frac{\overline{v'\theta'}}{\overline{\theta}_p} \right)_p, \qquad \overline{\omega}^* = \overline{\omega} + \left(r_0 \cos\varphi \right)^{-1} \left(\frac{\overline{v'\theta'}}{\overline{\theta}_p} \cos\varphi \right)_\varphi,$$

and

$$S_{(\lambda\varphi)} = \overline{v'u'} - \overline{u}_p \frac{\overline{v'\theta'}}{\overline{\theta}_p}, \qquad S_{(\lambda p)} = \overline{\omega'u'} + \left(\left(r_0 \cos\varphi \right)^{-1} \left(\overline{u} \cos\varphi \right)_\varphi - f \right) \frac{\overline{v'\theta'}}{\overline{\theta}_p}.$$

The $\overline{X}$ in Eq. 3.1 represents unspecified zonal components of parameterized forcing or dissipation processes, such as friction or other nonconservative mechanical forcings.

The terms containing the $\overline{v}^*$ represent the acceleration of the mean zonal wind by meridional advection of momentum, while the second part (containing $\overline{\omega}^*$) represents the forcing due to vertical momentum advection. The third group of terms results from the non-zonal eddies, and is proportional to the divergence of the Eliassen-Palm flux (hereafter called the total wave forcing). These three parts were computed respectively from the assimilated meteorological fields from MACDA and averaged in the tropics (between latitudes 10°S and10°N).

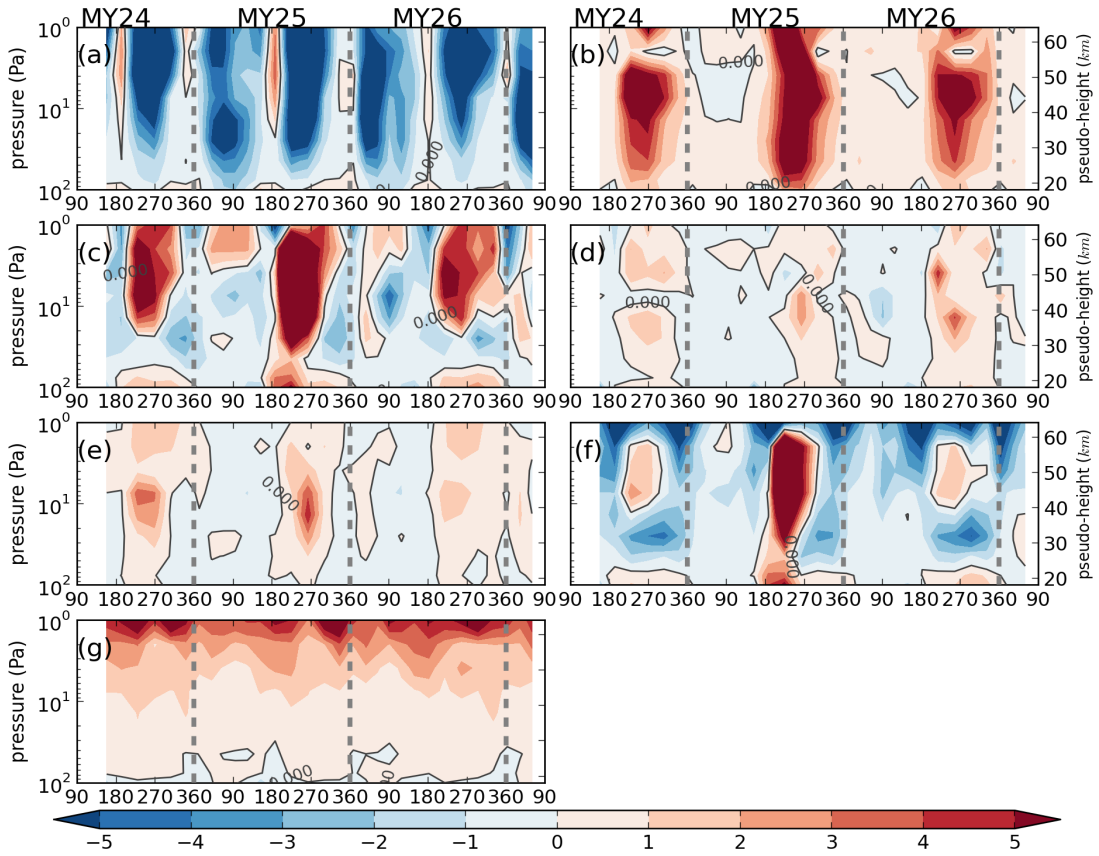

Figure 3.5 The forcing terms on the zonal-mean zonal wind, decomposed from the TEM zonal momentum equation and averaged between latitudes 10°N and 10°S within every 60-sol time window, due to (a) meridional advection, (b) vertical advection, (c) total forcing from different non-zonal waves, (d) quasi-stationary waves only, (e) transient waves only, (f) westward thermal tides only, and (g) eastward Kelvin waves. The forcings are presented in units of $m \cdot s^{-1} sol^{-1}$, and the contour lines only present the zero value to distinguish the eastward (red) and westward (blue) accelerations.

To further investigate the roles of different wave spectral components on the zonal-mean zonal wind, a 2D (i.e. temporal and zonal dimensions, respectively) Fast Fourier Transform (FFT) was applied to the MACDA 2-hourly outputs to decompose the meteorological variables into various spatial and temporal harmonics. The contributions from different wave spectral components could be calculated, therefore, through the formulation of the EP flux terms using the decomposed meteorological variables. The different wave components decomposed in the present work consisted of 1) quasi-stationary waves with periods longer than 30 sols, 2) transient waves with

periods between 2 and 30 sols, 3) westward thermal tides with periods shorter than 2 sols, 4) eastward Kelvin waves with period shorter than 2 sols.

As the SAO phenomenon mainly happened above 100 Pa and up to altitudes of 1 Pa, the diagnosis of the forces driving it only focused on this part of the Martian atmosphere. Figure 3.5 shows the decomposed contributions to the torque acting on the zonal-mean zonal wind, $\overline{u}_t$. In this 3-year dataset, the meridional advection (Figure 3.5a) provided most of the westward (retrograde) forcing to the zonal-mean zonal wind, especially at the solstices. In the MY with a GDS (MY 25), the westward forcing due to meridional advection was much weaker during northern spring and summer, while the contours with westward forcing ≥ 5 $m \cdot s^{-1} sol^{-1}$ penetrated lower down (to 30 Pa) in northern fall and winter than in other MYs. The maximum of westward forcing was ~ 15 $m \cdot s^{-1} sol^{-1}$ for the average of 60-sol time windows. However, it was surprising to see that the meridional advection forcing had no substantial difference of magnitude for both solstices in a year without global dust storm. The meridional advection also supplied most of the eastward (prograde) forcing at the equinoxes, but may not be strong enough to completely reverse the direction of the zonal-mean zonal wind from westward to eastward. This eastward forcing indeed contributed to the eastward zonal-mean zonal wind between 100 Pa and 70 Pa at the equinoxes. Overall, the meridional advection displays a clear SAO cycle correlated with the variation of zonal-mean zonal wind.

In contrast, the vertical advection (Figure 3.5b) mainly supplies eastward forcing to the zonal-mean zonal wind, but this forcing was significantly stronger during the northern fall and winter seasons (maximum ~ 11 $m \cdot s^{-1} sol^{-1}$ in 60-sol average). Mild westward forcing could mainly be seen between 15 Pa and 3 Pa during northern spring and summer with a magnitude not larger than 1 $m \cdot s^{-1} sol^{-1}$. The total forcing

from different non-zonal waves (Figure 3.5c) exhibited more variation than the other two terms in Eq. 3.1. In MY 25 with a GDS, it only provided westward forcing below 4 Pa in the first half of the year, while in MY 26 without a GDS, it also provided eastward forcing in $L_s \approx 30° \sim 70°$ below 4 Pa. In the second half of the year, this total wave forcing supplied strong eastward accelerations above 20 Pa or below 50 Pa except for during the GDS year itself (MY 25), but this eastward forcing clearly reached its minimum at ~ 40 Pa in MY 25. The total wave forcing exhibited a half-year cycle above ~ 40 Pa. The phase of this oscillation was almost opposite to the forcing due to meridional advection above ~ 3 Pa. Below 3 Pa altitude, the total wave forcing also partly contributed some westward forcing to the SAO of zonal-mean zonal wind. The eastward forcing below 3 Pa started at $L_S \sim 180°$, but it expanded in most part of the second SAO. As a result, the eastward forcing due to total wave forcing may support the eastward component of the SAO, but also weakens the westward forcing to some degree. Compared to the study by Kuroda et al. [2008], in this analysis the eastward forcings in the second half of the year were obviously stronger in all three terms (meridional advection, vertical advection and total wave forcing). This is likely because of the increased thermal forcings due to a more dusty season in the second half of the year (perihelion). As a result, the thermal forcing increases. This effect was mentioned by Kuroda et al. [2008] as well, when they discussed the forcings due to meridional advection. Also, the eastward forcings in the vertical advection and total wave forcing terms reached their maximum around $L_S \sim 220°$ in current study instead of ~ 180° in the study by Kuroda et al. [2008]. This might be because the dustiest period in general may not happen at equinox, and this can not be represented by a seasonally uniform dust distribution in a free-running simulation as in the study by Kuroda et al. [2008].

Among different wave forcings, quasi-stationary waves (Figure 3.5d) mainly supplied weak westward momentum to the zonal-mean zonal wind in the first half of the year, and then supplied eastward momentum in the second half of the year. Unlike in the study of Kuroda et al. [2008], the transient waves were claimed to have little contribution to the tendency of zonal-mean zonal wind. In current study, the transient waves (Figure 3.5e) exhibited a similar effect to that of quasi-stationary waves. The westward thermal tides (Figure 3.5f) displayed an SAO cycle above 10 Pa but with opposite forcing to counteract the momentum supplied by the meridional circulation. In the first half of the year, the thermal tides imposed a westward forcing on the zonal-mean zonal wind, but in the second half of the year, its effect varied with pressure. Between 50 Pa and 10 Pa of a typical MY without a GDS (MY 24 and MY 26 in MACDA), the thermal tides provided westward forcing that could contribute to the westward component seen in the second SAO cycle of the zonal-mean zonal wind. Between 10 Pa and 2 Pa or below 50 Pa, the thermal tides provided eastward forcing. They have been found to lead to superrotation within the height range of tide forcing in Martian atmosphere [Fels and Lindzen, 1974; Lewis and Read, 2003]. The eastward Kelvin waves (Figure 3.5g) consistently provided eastward momentum to u above 30 Pa. This is consistent with the study conducted by Moudden and Forbes [2008], in which the eastward propagating Kelvin waves were found to lead to strong eastward acceleration in the upper atmosphere associated with their dissipation. On the contrary, the westward forcing yielded by the eastward Kelvin waves in the study by Kuroda et al. [2008], is contradictory to the findings in this study and other studies [e.g. Moudden and Forbes, 2008], and is likely wrong. The possible reason might be that the Kelvin waves in their model are forced nonphysically, rather than generated spontaneously by the model physics. Below 30 Pa, the oscillation of the forcing due

to eastward Kelvin waves had an SAO signature but with the opposite effect compared to the forcing due to meridional advection.

It is also worth mentioning the changes of these wave forcings during the GDS year, i.e. MY 25, although only one GDS event was included in the period of this analysis. In general, the thermal tides dominated in the total wave forcing. During the GDS, the significant increase of total wave forcing was mainly the result of increasing forcing due to thermal tides. Although the forcing due to quasi-stationary waves and transient waves exhibited some similarity in the annual pattern, they showed different responses to the GDS. The forcing due to transient waves supplied stronger eastward forcing during the GDS event, while the forcing due to quasi-stationary waves only led to a mild increase in the eastward forcing. However, in the year following the MY 25 GDS, the eastward forcing due to quasi-stationary waves was obviously stronger. In contrast, the GDS event had almost no impact on the eastward Kelvin waves.

3.5. Concluding discussions

In current study, the phenomenology of the SAO in the zonal-mean zonal wind was reviewed. Unlike the preceding study of a Martian SAO by Kuroda et al. [2008], the present study used a climatological dataset produced from a data assimilation system [Montabone et al. 2006a & 2011b; Lewis et al., 2007]. In the analysis, the SAO phenomenon appeared to happen not only in the tropics, but it also extended to higher latitudes. This oscillation appeared not to manifest itself in completely reversing the direction of the zonal-mean zonal wind, but at some latitudes or pressure levels, it was found to appear as the deceleration of a prevailing unidirectional zonal-mean zonal wind.

A Singular Systems Analysis of *u(t,p)* suggested that the second pair of principal components (PC) was mainly dominated by this SAO cycle, though the SAO signal was also strong enough to appear in the first pair of eigenvectors and corresponding PCs. The reconstruction of the second pair of PCs showed that the magnitude of the SAO could easily reach 20 $m \cdot s^{-1}$ or even greater amplitudes.

Due to the limited time of my DPhil project, the pressure-coordinate TEM analysis was only applied in the tropics to further investigate the nature of the forcing processes driving the tendency of the zonal-mean zonal wind. The meridional advection term exhibited a clear SAO cycle strongly correlating with the observed oscillation of zonal-mean zonal wind, and supplied the majority of westward (retrograde) forcing in the SAO cycle. The vertical advection term mainly supplied eastward forcing to the zonal-mean zonal wind with a strong annual cycle. The decomposition into different wave contributions suggested that the quasi-stationary waves and transient waves partly supplied the eastward and westward forcings to the first cycle of SAO, but they tended to weaken the strength of the westward component in the second SAO of the year. The thermal tides dominated in the pattern of total wave forcing. They mainly supplied the westward forcing in the first half of the year, and also supplied the westward forcing for the second cycle of the year between 50 Pa and 10 Pa. In the total wave forcing, the mild eastward forcing above 3 Pa in the first half of year was mainly a result of eastward Kelvin waves.

The diagnostic results here based on MACDA were different from the work of Kuroda et al. [2008] that was based on a free-running model simulation with uniform dust distribution. The processes driving the tendency of zonal-mean zonal wind were mainly different in the following ways, (1) the forcing due to the meridional advection was less asymmetric between the two SAO cycles of a year, (2) the total

wave forcing and decomposed thermal tides did not consistently display the oscillation as an SAO of zonal-mean zonal wind in any pressure level, (3) the strength of the forcing due to transient waves was comparable to that of the quasi-stationary waves, and (4) similar to the Earth, eastward Kelvin waves mainly supplied eastward momentum to the zonal-mean zonal wind, consistent with their dissipation of wave action.

As the period of this dataset also included the period of the MY 25 GDS, the diagnosis also brought some distinctive features of the forces driving the circulation in this GDS year to our attention. The meridional advection supplied weaker westward momentum before the onset of MY 25 GDS, and the eastward momentum and westward momentum evident during the GDS were obviously stronger than those in other MYs. Along with the onset of the MY 25 GDS, the vertical advection and total wave forcing were also stronger. Among different wave components, the thermal tides were significantly intensified, most probably due to the enhanced solar heating effect due to increased dust during the GDS. Although the forcings due to quasi-stationary waves and transient waves in general displayed a similar pattern, the eastward forcing due to quasi-stationary waves appeared to be stronger in the year after the MY 25 GDS instead of during the MY 25 GDS itself.

In future work, the TEM analysis should be extended to the latitude bands outside of tropics, and it is possible to discover the differences of different processes across different latitudes. To establish any further link between the features of different forcings and the trigger/response of a GDS, at least one other GDS event should be studied accordingly. This will require the extension of the climatological dataset to completely include a MY with another GDS, such as MY 28.

Chapter 4 Development of an Updated Martian Dust Data Assimilation Scheme with Activated Dust Transport

A new dust data assimilation scheme is developed in this thesis for the UK version of the LMD Martian General Circulation Model (UK-LMD MGCM). Together with the activated dust lifting and dust transport, the Analysis Correction scheme (adapted from the Meteorological Office) is applied to analyze simultaneously the temperature, column-integrated dust opacity (CIDO) rescaled to a reference level (hereafter, called *tauref*) and layer-integrated dust opacity (LIDO), respectively. This upgrade of the assimilation of dust consists of two tasks, 1) to activate the dust transport scheme while correcting *tauref* during the simulation, 2) to assimilate the retrievals of dust profiles with dust lifting and transport scheme activated. I address the methodology and implementation of these two major updates in this chapter, respectively. In both tasks, the results have been proven to converge to the assimilated observations. However, through examining the assimilations and the characteristics of each observation dataset, simply assimilating either of the observation separated may not produce the results that fit the available data optimally. This demonstrates that the

dust data assimilation system needs to assimilate both CIDO and LIDO together in order to benefit greatly from the advantages of different types of dataset. We state that the final reanalysis, produced by this extended data assimilation system, is able to converge to those in-sample assimilated CIDO and LIDO, and capture some of the details of dust vertical distribution, especially the elevated dust layer. The full validation of this reanalysis against those independent observations will be discussed in the Chapter 5.

4.1. Introduction

Mars, the nearby planet to the Earth, intrigues scientists to understand the climate of this red planet, as well as investigate the possibility of extant life. The dust cycle is a key component of the Martian climate, and a full understanding of the dust cycle may be extremely useful to study the evolution of the Martian atmosphere, further the environment of the planet. Once dust particles are injected into the atmosphere by dust lifting mechanisms, and then captured by the atmospheric circulation, they greatly affect the dynamic and thermal state of the Martian atmosphere.

Intensive measurements of atmospheric temperature and dust extending over nearly 8 Mars years (MY) are now available with unprecedented spatial coverage, thanks to the various spacecraft in orbit around Mars since 1997. These include Mars Global Surveyor (MGS), Mars Odyssey (MO) and Mars Reconnaissance Orbiter (MRO). Those observations have already helped scientists to improve our understanding of the weather and climate on Mars. However, the incomplete coverage of the measurements still restrains our ability to study the full details of the circulation, especially for those aspects related to dust opacity. For instance, the Thermal Emission Imaging System

(THEMIS) carried by the MO spacecraft can provide some measurements of CIDO, but the coverage of the data in space and time is quite limited.

On the other hand, a numerical model can provide four-dimensional simulated data with high temporal and spatial resolution, but often fails to produce the realistic variability of the dust cycle. Newman et al. [2002b] conducted a series of numerical experiments with different combinations of parameters, and the results showed that the global circulation model (GCM) could capture the onset and growth of regional dust events, but missed the observed amount of the interannual variability. Specifically, Newman et al. [2002b] could not reproduce the relatively 'quiet' year for dust activity right after the global dust storm (GDS) year.

In this context, data assimilation has become one of the optimal approaches to provide a four-dimensional solution that is consistent with both observations and modeled physical constraints. The model-predicted variables are corrected towards to the observations in a data assimilation system so that the resulting solution is able to represent the full observed variability of the climate. This approach has been widely used as an effective tool in operational weather forecasting systems or climate models for analyzing the meteorological variables for the Earth [e.g. Lorenc et al., 1991]. Until recently, this approach has been already extended to the tracer/chemical numerical simulation for the earth studies. [e.g. Collins et al., 2001; Wang et al., 2004; Schutgens et al., 2010]. For the region of Indian Ocean, for example, Collins et al. [2001] used an optimal interpolation approach in an off-line chemical transport model (CTM) to assimilate satellite retrievals of total column aerosol opacity depth (AOD), and their assimilation system was shown to reproduce the daily variations of AOD at a single model grid point. Wang et al. [2004] introduced a simple Newtonian nudging scheme into a nonhydrostatic atmospheric model for assimilating the AOD,

and their assimilation was able to capture the observed evolution of a chosen major dust event near the Puerto Rico. More recently, Schutgens et al. [2010] applied the Local Ensemble Transform Kalman filter (LETKF) to the assimilation of the AOD from a global surface observation network (AERONET). Generally speaking, their results showed that the assimilation of AOD was able to help the numerical model to capture the evolution of the measurement, and also greatly reduced the uncertainties in the model estimates of the evolving aerosol distribution.

Similar to the evolution of application of data assimilation for the earth, the data assimilation approach has also now been introduced into Martian modeling for analyzing meteorological fields. One of the pioneering works was conducted by Lewis and Read [1995], based on the analysis correction scheme [Lorenc et al., 1991]. Lewis and Read [1995] implemented the analysis correction (AC) scheme into a simple version of Martian General Circulation Model (MGCM) for assimilating the temperature profiles that was being assimilated at that time from the Pressure Modulator Infrared Radiometer (PMIRR) on-board the Mars Observer spacecraft. Their results successfully demonstrated that the assimilation of the spacecraft observations was feasible and was expected to improve the degree of agreement between model and observation [Lewis and Read, 1995]. Following the work of Lewis and Read [1995], Lewis et al. [2007] extended this data assimilation approach to also include dust tracer assimilation, combined with a full MGCM for assimilating the thermal profiles and *tauref* derived from the CIDO retrievals of the Thermal Emission Spectrometer (TES) on-board MGS [Smith, 2003]. The overall performance of this data assimilation system was validated against independent radio occultation measurements in the work of Montabone et al. [2006a]. This comparison showed that the combined temperature and *tauref* data assimilation approach was able to reduce

the discrepancies between the model and radio occultation data below 20 *km*, although some large discrepancies were found to inherit from the known inconsistency between the TES temperature profiles and radio occultation data [Montabone et al., 2006a]. More recently, an ensemble Kalman filter data assimilation was initially developed, for assimilating the TES temperature retrievals only, and discussed in the work of Hoffman et al. [2010]. Generally speaking, the results of this approach showed improved agreement with TES temperature observations. In their following study [Greybush et al., 2012], the assimilation of TES temperature with forced 2-D dust field by TES data was shown to further improve the agreement of model forecasts with TES temperatures. However, at the time of writing, the published work exploring dust tracer assimilation on Mars is still limited to the work of Lewis et al. [2007] and subsequent studies associated with the University of Oxford and the Open University. As a first step in Martian dust assimilation, they conducted the data assimilation of the retrievals of TES temperature profiles and *tauref* without explicitly advecting the dust tracer field, and an empirical relation [Conrath, 1975] was used to prescribe the vertical distribution of dust (see Section 2.6 of this thesis for details). This data assimilation system has been applied in several studies to better understand the Martian weather and climate [Montabone et al., 2005; Lewis et al., 2005; Montabone et al., 2006b; Lewis et al., 2007; Wilson et al., 2008a; Rogberg et al. 2010; Mulholland, 2012]. More recently, a reanalysis from this data assimilation system has been published online as a climate database for further analysis by the whole Mars community [Montabone et al., 2011b]. I am also aware that with only assimilating MCS temperature profiles, Navarro et al. [2014] modified dust vertical distribution using its correlation with temperature that was drawn from the ensemble of simulations. However, it is essentially different from the work presented in this chapter in

which the dust observations are directly assimilated, and the objective validation of their method is difficult to be very accurate.

The data assimilation system developed in my project is based on the same AC scheme as in the work of Lewis et al [2007]. TES nadir retrievals did not provide information on the dust distribution in the vertical direction. The newly-available measured dataset from Mars Climate Sounder (MCS; carried by MRO [Kleinbohl et al., 2009]), however, provides vertically resolved, global measurements of the atmospheric dust distribution. With this new information on the dust vertical distribution, it is timely to update the existing data assimilation system to better represent the Martian dust cycle, and thereby allow us to study in unprecedented detail the formation and life cycles of regional and larger scale dust storms and other processes.

The full details of this upgrade will be addressed in two steps in this chapter. The previous Martian dust assimilation analyzes the modeled temperature and *tauref* without transporting the dust physically [Lewis et al., 2007]. Section 4.3 will describe the task of extending the assimilation of CIDO (in practice, *tauref* is the variable analyzed in the data assimilation) with activated dust lifting and transport. Section 4.4 will describe the new methodology of assimilating LIDO data into the assimilation system. Section 4.5 will discuss how we make use of these data to achieve a representation of the Martian atmosphere that best fits to the available observations. Along with the assimilation experiments in this chapter, the initial conditions for the fields of meteorology and dust tracer are typically taken from a free-running spin-up run, which is self-initialized for two years until the start of these experiments. In this and the following chapters, the assimilation of temperature will be always included without being explicitly specified in the assimilation experiments. A free-running

simulation without any data assimilation (temperature or dust) is run as a control simulation with identically the same dynamics and physical parameters as those used in the assimilation. The different experiments and related input data are summarized in Table 4.1.

Experiment	Data assimilated	
	THEMIS CIDO	MCS LIDO
free-running simulation		
assimilation of CIDO	✔	
assimilation of LIDO		✔
joint assimilation of CIDO & LIDO	✔	✔

Table 4.1 Summary of experiments conducted in this chapter.

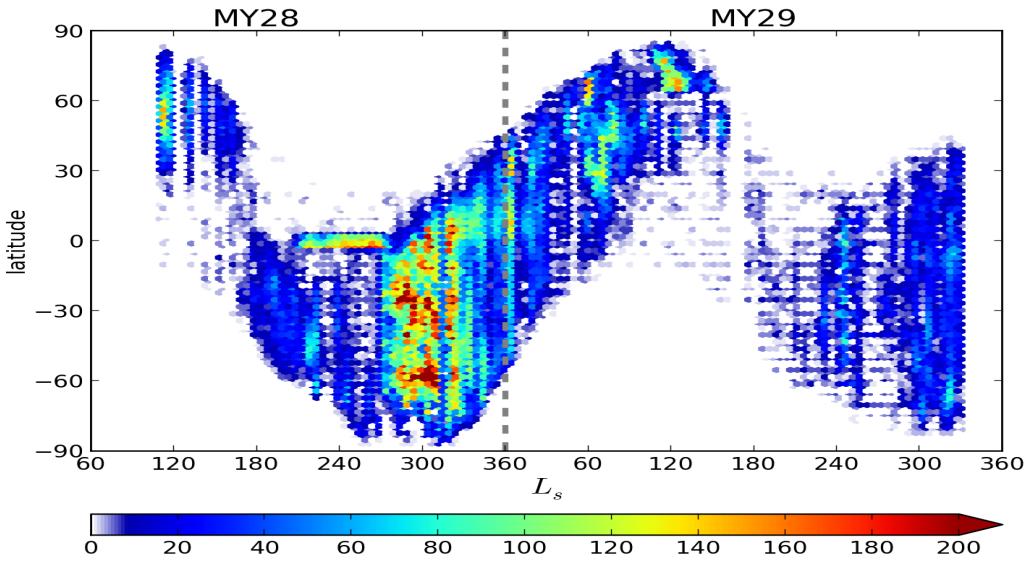

Figure 4.1 The distribution in L_s and latitude of the THEMIS retrievals of CIDO. The color scale shows the number of measurements per 5° in L_s and every 3° in latitude.

4.2. Input observations of Martian dust

A key aim of my thesis project is to study the Martian climate and dust cycle with a unique and advanced assimilation system that enables a complete, four-dimensional,

multivariate reconstruction of the state of the atmosphere by combing observational data with predictions from a global numerical model of the Martian atmospheric circulation and dust transport cycle. Data availability is essential to the application of a data assimilation system. Thanks to various spacecraft in orbit around Mars since 1997, the measurements of atmospheric temperature and dust covering over nearly 8 MYs provide unprecedented spatial and vertical coverage of the Martian atmosphere. These include MGS, MO and MRO. The instruments for measuring temperature and dust on-board these spacecraft are TES [Smith, 2004], THEMIS [Smith, 2009] and MCS [Kleinbohl et al., 2009] respectively. Different spacecraft have different operational periods in the satellite orbits, therefore, the retrievals from various instruments have different temporal and spatial coverage. The THEMIS dataset is the only one that has overlapping observational periods with other two datasets. One important step, therefore, is to devise a means of assimilating the LIDO into the dust assimilation system. However, the retrievals of TES and THEMIS both only contain information as CIDO, while MCS dataset is the most up-to-date satellite observation (MCS Version 3 is used in the work of this thesis) that first provides vertically resolved, simultaneous global measurements of atmospheric temperature, dust and water, with information on the day-to-day variability of Martian weather from the near surface to the top of Martian middle atmosphere about 80 km altitude [Kleinbohl et al., 2009].

For a better preliminary intercomparison among the assimilation of different dust properties, I therefore use part of the MCS mapping period as the time window (i.e. from solar longitude (L_s) $L_s = 110°$ of MY 28 to $L_s = 330°$ of MY 29) to demonstrate the updated data assimilation system and test its performance. During this period, the CIDO data from THEMIS and the LIDO data from MCS are both

available. In general, however the spatial coverage of THEMIS retrievals varies significantly with L_s. The spatial coverage of MCS retrievals is more consistent and uniform except during the global dust storm season (roughly from $L_s = 270°$ to $L_s = 305°$ in MY 28). Within the study period I choose here, their distribution in L_s and latitude are shown in Figures 4.1 and 4.2, respectively. Because the dust is generally assumed to be well mixed in the dust opacity retrieval algorithm, in order to remove the effects of the variable topography on Mars, the CIDO data from THEMIS is commonly reported as rescaled to a reference pressure 610 Pa (i.e. *tauref*) [Smith, 2009]. However, this assumption may introduce uncertainty when the dust is not well mixed. For instance, if an intense elevated dust layer exists, the rescaling under the well-mixed assumption could lead to overestimate of the *tauref* .

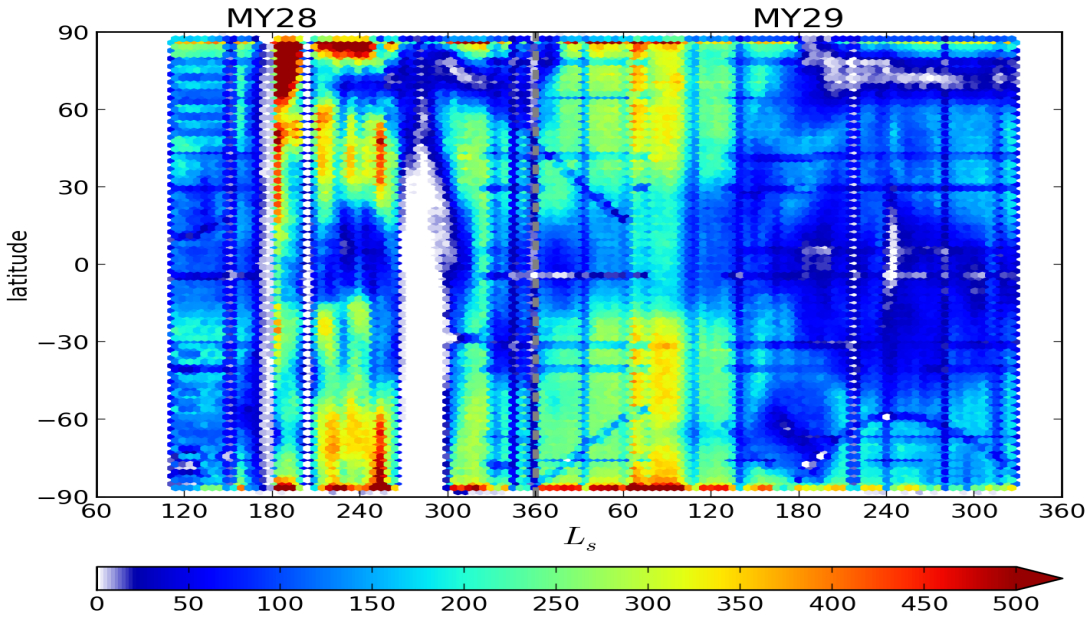

Figure 4.2 Same as Figure 4.1, but for MCS dust retrievals. The color scale shows the number of retrieved profiles per 5° in L_s and every 3° in latitude.

It is also important to point out that the THEMIS dust observation is provided as an absorption optical depth measured at infrared wavelengths, while the modeled *tauref* is defined as the extinction optical depth at visible wavelengths. Smith [2009]

determined the ratio of converting the absorption optical depth to extinction optical depth (γ) to be ~1.3 by numerical experiments. Clancy et al. [2003] used a scaling factor of 2 (ε) to convert from infrared to visible optical depths for dust particles of size 1.5-2.0 μm dust particles. Lemmon et al. [2004] compared visible optical depths with those at 9 μm as measured by the Mars Exploration Rovers, and showed that they are also in accordance with the study of the Clancy et al. [2003]. As mentioned earlier in Chapter 2, the dust particle size is chosen here to be approximated by a single size (1.5 μm) in this numerical study for simplicity. The selection of this prescribed dust particle size is reasonably consistent with various observational studies [e.g., Pollack et al., 1995; Clancy et al., 2003; Lemmon et al., 2004]. Thus, through multiplication of γ (1.3) and ε (2), a factor of 2.6 is obtained here for converting the THEMIS infrared absorption optical depth to the model-compatible extinction optical depth at visible wavelength, and the CIDO and *tauref* mentioned in this study is generally referred to as the visible extinction optical depth unless otherwise specified. Further details of the THEMIS dataset including the retrieval algorithm can be found in the work of Smith et al. [2000], Smith et al. [2003] and Smith [2009]. The ratio of observational error to first guess error ($\overline{Q_i}$ in Eq. 2.15) is chosen to be 1 for temperature observations as previously used by Lewis et al. [2007] for the assimilation of TES temperature, which implies that both the model and observation errors are of comparable magnitude. For the dust observations, an error ratio of $\overline{Q_i}$ =1 is used for each retrieval, and this follows the companion study done by Steele [2014] for the assimilation of ice opacity. With this procedure, the assimilation scheme is essentially used here to build a four-dimensional time-space map of dust distribution that is consistent with other atmospheric variables. Following this study, it is also possible to extend the dust assimilation beyond the current study period.

4.3. Assimilation of CIDO-only with activated dust transport

4.3.1. Approach

Previous studies based on the UK-LMD MGCM, performing data assimilation excluded active dust transport while simply correcting the temperature profiles and *tauref* . In those studies, the dust remained static when observation was absent and were vertically distributed by prescribed relation. A schematic diagram of illustrating this sequence of data assimilation system is shown in Figure 4.3. The full details are briefly described in the section 2.6 of this thesis.

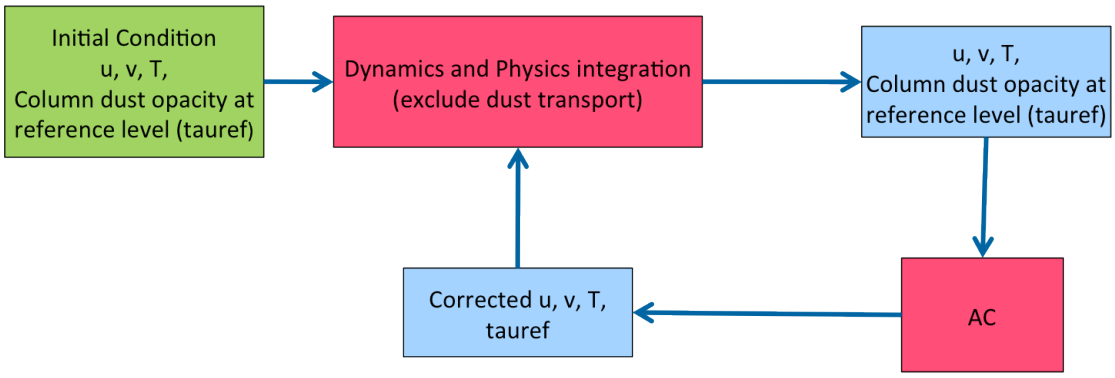

Figure 4.3 Illustration of the main calculation of atmospheric properties in the work of initial data assimilation, green box means the values from initial condition, blue box means data generated by MGCM integration and red box means the MGCM modules. (only the variables related to data assimilation scheme (AC) are included).

In this sequence, the model predicts the meteorological variables (e.g, u , v , T) through the dynamical and physics schemes for the next timestep. The dust vertical distribution is then determined by Eq. 2.18 in Chapter 2 in the physics integration, and the radiative transfer can take into account the modified dust opacity. In the AC scheme, the modeled T is adjusted according to the measured thermal profiles. Following the temperature correction step, the u , v are adjusted using the thermal

wind balance to be consistent with the temperature increment. Finally, *tauref* is corrected by the available dust observations. Thus, these corrected variables become the input for next integration timestep.

Although the modeled *tauref* at each timestep has been corrected by the available observations, in order to represent the dust cycle in the simulation more physically, it is desirable to activate the dust transport. In the new scheme presented here, the data assimilation system is now updated to include full dust transport, lifting and sedimentation while correcting *tauref* . This update is the first step to ultimately implementing the assimilation of dust profiles with a full dust cycle in the model.

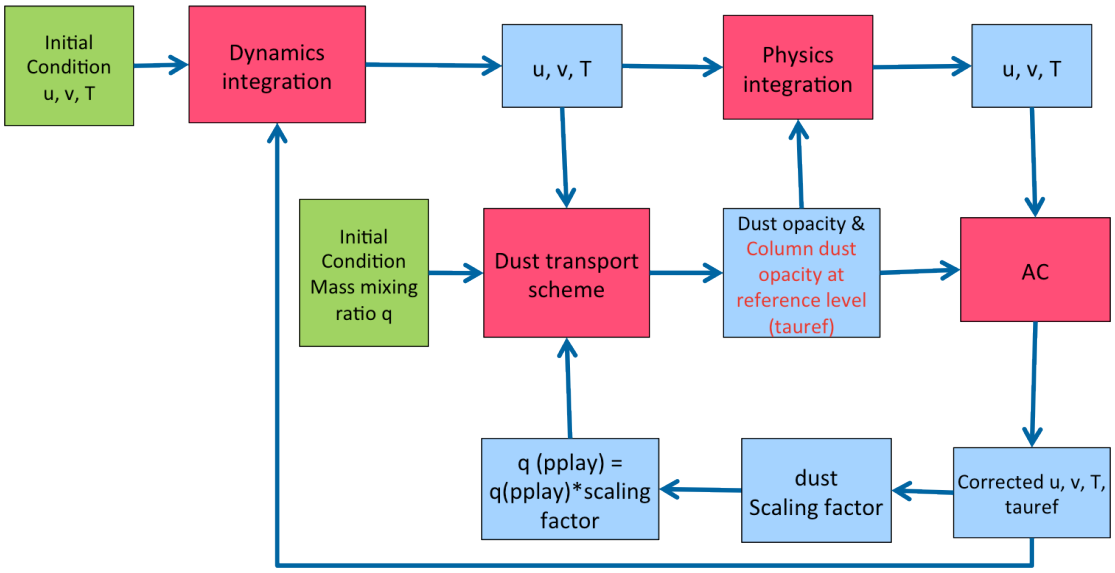

Figure 4.4 Illustration of the main calculation of atmospheric properties in the newly developed data assimilation. Green boxes are the values from initial condition, blue boxes are data generated by MGCM integration and red boxes are the MGCM modules. (only the variables related to data assimilation scheme (i.e. AC) are included, text in red color emphasizes the analyzed dust variable in AC)

The flow of integration in the newly updated data assimilation system is shown in Figure 4.4. In this updated data assimilation system, the meteorological variables are used in the dynamics and physics integration that now include the dust transport. The dust transport and lifting scheme is briefly described in section 2.5 of this thesis, and more details can be found in the work of Newman et al. [2002a] and Mulholland

[2012]. Because the dust is transported based on the dust mass mixing ratio instead of dust opacity, the field of mass mixing ratio is also included in the initial condition. The three dimensional (3D) distribution of dust mass mixing ratio is predicted in the dust transport scheme and the predicted CIDO (τ_{CIDO}) is obtained by linearly summing up the total dust opacity in each model layer, i.e. LIDO. The LIDO in the model (use symbol τ_{LIDO} in the equation) can be calculated by,

$$\tau_{LIDO}(L) = \int_{p_{L+1}}^{p_L} q(L) qext \frac{dp}{g} \tag{4.1}$$

where the notations of the variables are in Table 4.1.

$qext$	$\frac{3}{4}\frac{Q_{ext}}{\rho \cdot r}$
L	index of model level
p	pressure at particular model level
$q(L)$	dust mass mixing ratio at model level L
g	gravitational acceleration on Mars (3.72 $m \cdot s^{-2}$ is used in this thesis)
Q_{ext}	extinction coefficient
ρ	density of dust particle (2500 $kg \cdot m^{-3}$ is used in this thesis)
r	the radius of dust particle (for simplicity, choose 1.5 μm in this thesis)

Table 4.1 Notations in the Eq. 4.1.

$tauref$ can be calculated in the observations by,

$$tauref = \tau_{CIDO} \frac{700}{p_s}, \tag{4.2}$$

and is determined from modeled variables by,

$$tauref = \left(\sum_L \tau_{LIDO}(L) \right) \frac{700}{p_s}, \tag{4.3}$$

here, p_s is the surface pressure. The reference pressure level is arbitrarily chosen to be 700 Pa. However, to compare the results with observations, the CIDO are rescaled to 610 Pa to reflect an updated estimate of the mean Mars surface pressure. The choice

of this reference pressure level should not affect the model result, though, as the observations are processed in the same way as modeled variable in both cases.

After calculating *tauref* in the model, the new value of *tauref* together with those of u, v, T, are updated in the AC scheme. Because the dust tracer is transported in 3D in the dust transport scheme in terms of the dust mass mixing ratio, it is required to adjust the dust mass mixing ratio at each model layer. Since *tauref* is a column-integrated quantity, an assumption has to be made in order to propagate the adjusted dust information into the vertical direction. *tauref* is proportional to the linear sum of $\tau_{LIDO}(L)$ (see Eq. 4.1), and a scale factor λ is defined for each model layer to ensure that the shape of each dust profile remains the same before and after the assimilation,

$$\lambda = \frac{\tau_{LIDO}(L)'}{\tau_{LIDO}(L)} = \frac{tauref'}{tauref}$$

Here, the variables with primes are the corrected variables after assimilation, and those without primes are the predicted variables before assimilation. Meanwhile, the equation to calculate the LIDO ($\tau_{LIDO}(L)$, see Eq. 4.1) suggests that the dust mass mixing ratio $q(L)$ is proportional to the $\tau_{LIDO}(L)$ given that the extinction coefficient and layer thickness remain the same within a particular integral time step. Thus, if $q(L)$ at each model layer is multiplied by λ, it can keep the shape of dust profiles before and after the assimilation but also use the information for the corrected *tauref* to reduce the uncertainty of the dust transport scheme. A similar assumption was also used in the works of assimilation of AOD on Earth [Collins et al., 2001; Wang et al., 2004].

4.3.2. Results compare with assimilated MCS temperature profiles

Before comparing the assimilated dust distribution with the observations, it is worth to first exampling the agreement between the assimilated temperatures and observed temperature profiles in this chapter. The assimilation of temperature had previously been validated against the independent radio occultation measurements for the TES period [Montabone et al. 2006]. In their results, regardless of a possible systematic bias between the independent dataset (radio occultation data) and the assimilated dataset (TES retrievals), the comparison exhibited reasonable agreement of the assimilated results and the independent radio occultation temperature data, as well as with the assimilated TES temperature retrievals.

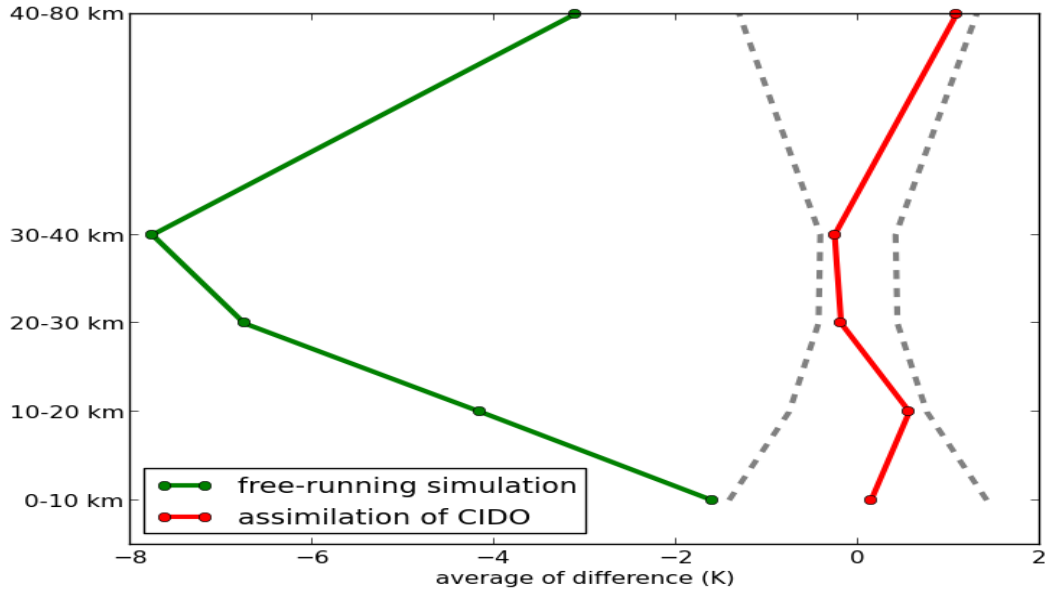

Figure 4.5 The average difference of temperature (in the unit of K) between model and assimilated MCS data in the chosen study period (from $L_s = 110°$ of MY 28 to $L_s = 330°$ of MY 29). Grey dashed lines are the average errors of MCS observations.

In this thesis, I will not place much emphasis on the temperature assimilation. since the assimilation of temperature based on the UK-LMD MGCM had been demonstrated to provide a set of reanalysis with increasing consistency with the observed datasets [Montabone et al., 2006; Lewis et al., 2007; Montabone et al., 2011b]. Hence, only the average of the temperature difference in different height

ranges (i.e. 0-10 *km*, 10-20 *km*, 20-30 *km*, 30-40 *km* and 40-80 *km*) is shown here, in order to demonstrate the reasonable improvement of the assimilated temperature results (Figure 4.5). The temperatures from the model are interpolated onto the pressure levels of the retrievals first, followed by the calculation of the average of the mean temperature with respect to the observations in different height ranges. The free-running simulation has a difference of about -1.7 K in the 0-10 *km*. The difference increases up to about -7.8 K in the middle atmosphere, afterwhile the difference reduces to ~ -3.2 K in the upper atmosphere. The temperature in the assimilated results clearly has a smaller error than the temperatures in the free-running simulation, and the differences remain within the observation errors in all height ranges. In the 0-10 *km* height range, the error in the assimilation is about 0.1 K, and the difference remains warm bias in 10-20 *km*. The differences change to cold bias in 20-30 *km* and 30-40 *km* (~ -0.2 K). In the upper atmosphere (40-80 *km*), the assimilation suggests a warm bias ~ 1 K. Overall, the assimilation of temperature appears to converge towards the MCS temperature observation.

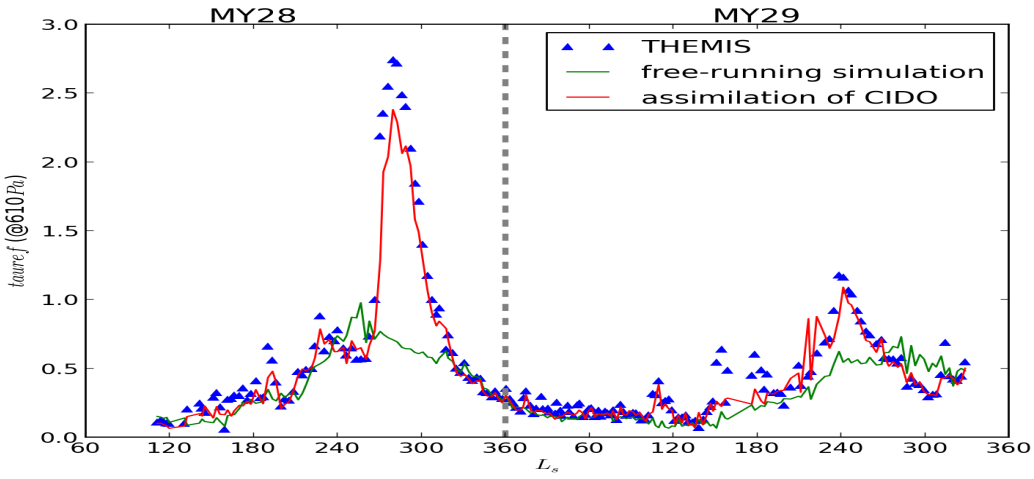

Figure 4.6 5-sol global average of *tauref* (rescaled to 610 Pa) for the study period.

4.3.3. Results compare with in-sample assimilated THEMIS dust observations

The model-predicted and assimilated *tauref* (CIDO rescaled to 610 Pa) were interpolated to the location of THEMIS measurement for further comparison. The time series plot of 5-sol global average *tauref* in the assimilation converges to the assimilated THEMIS data (Figure 4.6). The dust devil lifting is normally expected to be the dominant contributor to the total amount of airborne dust. Under the assumption of single dust particle (1.5 μm), the dust devil lifting efficiency α_D in the free-running model is tuned to roughly produce the observed amounts of dust loading during the "quiet" season ($L_s \approx 0° \sim 180°$). Due to the difficulty of correctly producing the nonlinear process of positive feedback of wind stress lifting in the model [Newman et al., 2002a], the tuning of the dust lifting efficiency α_N of wind stress lifting mainly focuses on producing the variability of dust loadings during the dusty season ($L_s \approx 180° \sim 360°$), though the free-running simulation in general underestimates the *tauref* during this season. Therefore, in spite of the failure of generating MY 28 GDS, the free-running simulation is able to exhibit weak interannual variability of the dust season. For the consistency of the comparison with free-running simulation, the dust lifting efficiencies in the assimilation runs hereafter are chosen to the same as in the free-running simulation for dust devil lifting (α_D=2×10^{-9} kgJ^{-1}) and wind stress lifting (α_N=1×10^{-5} m^{-1}), respectively. The assimilation of CIDO helps the model to converge to the assimilated THEMIS dataset, and the results show similar evolution as the assimilated data during the initialization and the dissipation of GDS, except around the maximum *tauref* of the GDS. More importantly, the assimilated results display a more realistic interannual

variability of *tauref* globally. However, in some periods (e.g. $L_s \approx 110° \sim 180°$ in MY28 and $L_s \approx 150° \sim 180°$ in MY29), the assimilated results still appear to underestimate *tauref* .

The scatter plots between THEMIS and model prediction (Figure 4.7) show that the free-running simulation generally produces a reasonable *tauref* , when the *tauref* ≤ 0.5 . The free-running simulation can significantly underestimate *tauref* when the *tauref* ≥ 1 . This high-dust condition normally associates with the dusty season on Mars. The assimilation of CIDO is able to reproduce those high *tauref* . The assimilated results exhibit good converge to the assimilated THEMIS data, especially when the value of *tauref* is lower than 2. Overall, the coefficient of determination between THEMIS data and the assimilation of CIDO is 0.82, while it is 0.34 between THEMIS data and the free-running simulation.

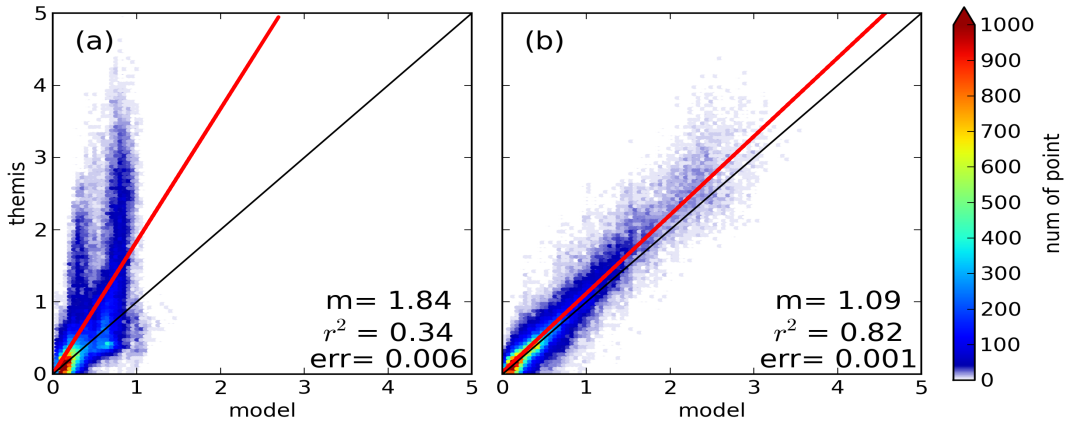

Figure 4.7 Scatter plots of THEMIS-model *tauref* during the whole study period. The color indicates the data density per 0.05 *tauref* . The red lines are the linear least square fit between THEMIS and model. m is the coefficient of the fittings, i.e. the slope of the red lines, r^2 is the coefficient of determination, and err is the standard error of the slope. The black lines represent the lines with coefficient 1. (a) the correlations between THEMIS and the free-running simulation, (b) the correlations between THEMIS and the assimilation of CIDO.

4.3.4. Discussion

The results clearly show the benefit in activating the dust transport scheme in the assimilation of CIDO. The assimilation is then able to reproduce realistic *taurefs* in the global average. More importantly, this data assimilation system is then able to ensure the model to display an improved level of interannual variability in the dust evolution.

It is also worth comparing the assimilated results with the time-average zonal dust distribution. A set of dust distribution data (hereafter, MCS-binned observations) was produced by L. Montabone (personal communication) by sampling the MCS dust profiles in a $5°$ horizontal grids in terms of daytime (defined as period between local time 6:00 and 18:00) and nighttime (defined as period between local time 18:00 and 6:00) after binned in $5°$ L_s interval. To compare the zonal mean dust distribution, the model results were interpolated to the same horizontal grids and vertical levels and were averaged within the same L_s time windows to obtain the corresponding daytime and nighttime 3D dust distributions. The modeled mean dust distributions were further filtered by the availability of MCS-binned observations along latitude before taking the zonal mean.

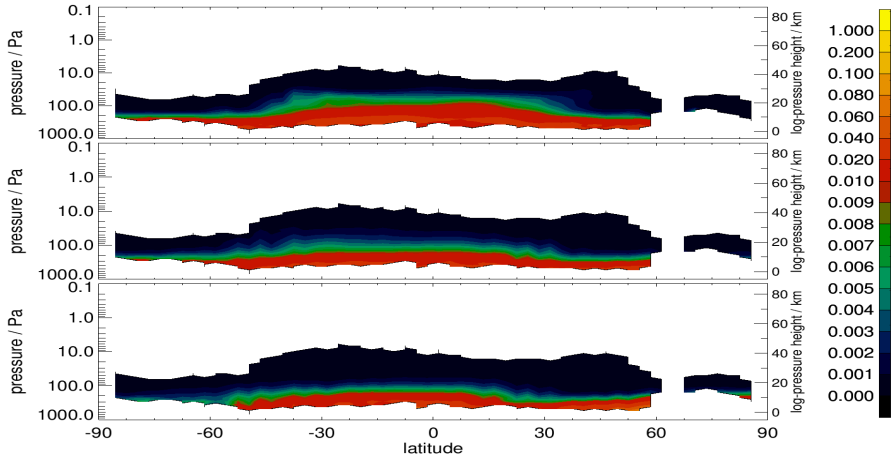

Figure 4.8 The comparisons of nighttime zonal mean dust opacity (km^{-1}) as a function of latitude and pressure (and log-pressure height) among observations (top panel), free-run simulation (middle panel) and assimilation of CIDO (bottom panel). They are all binned in $5°$ L_s centered at $L_s = 352.5°$ of MY28.

Generally, compared to the free-running model, the results of the assimilation of CIDO show similar representations of the top of dust layer as a function of position, but slightly lower tops than a free-running model (e.g. Figure 4.8). However, some observed features of the dust vertical distribution cannot be matched in the simulations. Elevated dust layers as observed in the MCS nighttime retrievals were discussed by Heavens et al. [2011a] (called high-altitude tropical dust maxima in their work). These elevated dust layers were also confirmed in other studies using the observational datasets measured by different instruments [e.g., Smith et al., 2013; Guzewich et al., 2013]. Both model runs fail to simulate this elevated dust layer however. The dust is lifted to a lower height than that of elevated dust layer and the dust is well mixed all the way to the ground in both experiments, without the feature of elevation (e.g. Figure 4.9).

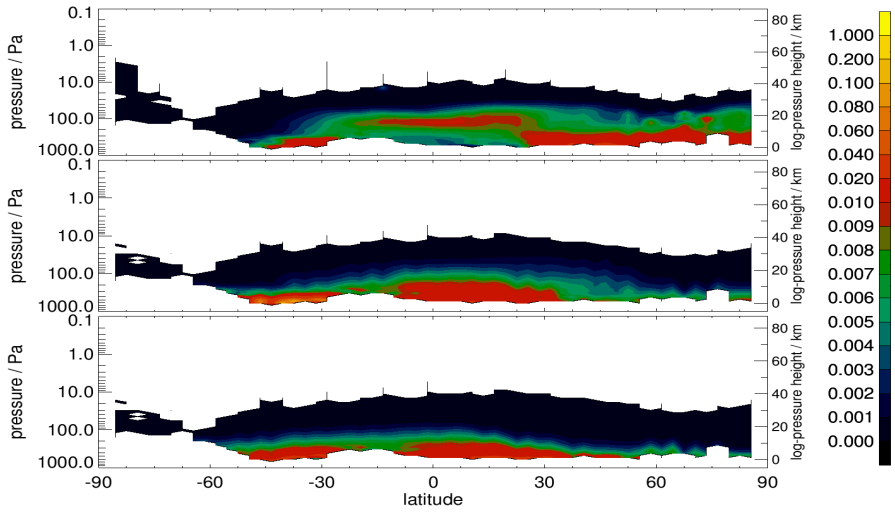

Figure 4.9 Same as Figure 4.8 but for $L_s = 122.5°$ of MY28.

Possible causes of these elevated dust layers were discussed in the work of Heavens et al. [2011a] and Rafkin [2012], respectively. Heavens et al. [2011a] also discussed the difficulties of verifying their proposed drivers of this phenomenon, while Rafkin

[2012] pointed out the challenges of reproducing this observed elevated dust layer in the available MGCMs. It therefore seems necessary to assimilate the vertically resolved dust measurements to be able to simulate elevated dust layers in the UK-LMD MGCM. Some assimilated results are possible to provide an insight into the evolution of this feature in a continuous temporal and spatial scale. Upon this, the following section 4.4 will describe the introduction of the assimilation of LIDO.

4.4. Assimilation of LIDO-only with activated dust transport

4.4.1. Approach

The dust transport and dust lifting have been successfully activated to work within the data assimilation system. The results obtained from the assimilation of CIDO-only have shown to converge to the assimilated observations, and are able to reproduce features of the observed dust interannual variability. The MCS dataset is also now available with unprecedented spatial coverage and almost continuous measured dust profiles [McCleese et al., 2010]. A more advanced data assimilation system is required however to make proper use of this unique dataset. In this section, only the retrievals of dust profiles from MCS are assimilated into the new data assimilation system (i.e., without assimilating CIDO). The schematic diagram is very similar to the assimilation of CIDO-only. Instead, however, the modeled LIDO (τ_{LIDO}) is analyzed directly (Figure 4.10).

On Earth, a number of dust assimilation studies only focus on the assimilation of the dust horizontal distribution, i.e. AOD, and the assimilation of the dust vertical distributions is not yet widely used ever in earth aerosol modeling. Limited

publications to date include that by Yumimoto et al. [2008], they assimilated vertical profiles of the dust extinction coefficients in a regional dust transport model. In their study, the data from a ground-based lidar network were interpolated to the vertical model levels for analyzing the model prognostic dust variables. More recently, Sekiyama et al. [2010] directly assimilated the total attenuated backscattering coefficient from the Cloud-Aerosol Lidar and Infrared Pathfinder Satellite Observations (CALIPSO) mission into a global chemistry-transport model. The measurements were averaged approximately to the model horizontal and vertical resolution before the assimilation.

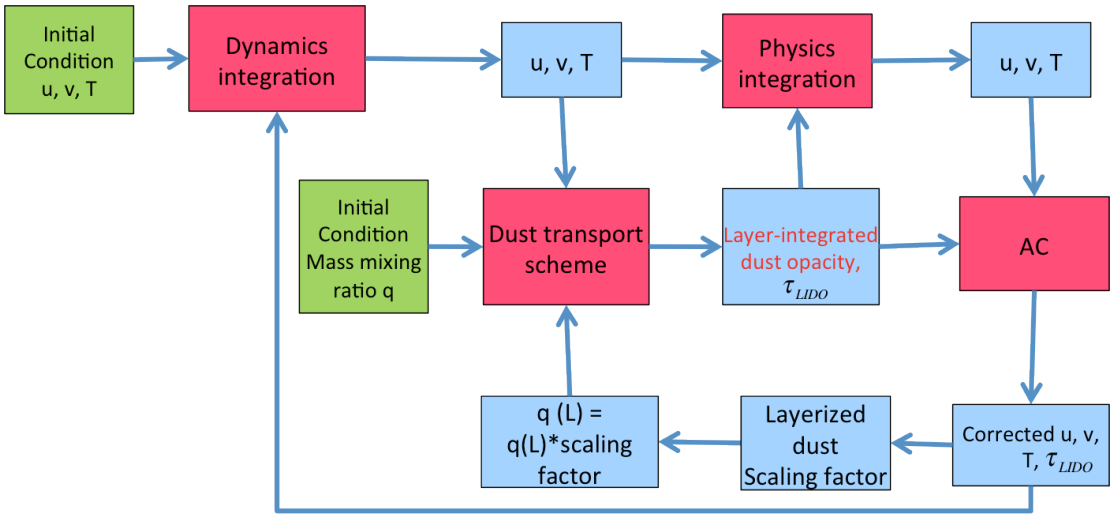

Figure 4.10 The schematic diagram for the assimilation of LIDO.

Regardless of the different advantages of various dust measurements, the retrievals of dust opacity are the only available, vertically resolved dust observations on Mars. In a similar way to the Earth, most other studies of dust assimilation broadly focus on the assimilation of the columnized dust property. It is noteworthy that this study is probably the first attempt to assimilate the dust vertical distribution in a Martian atmospheric model, more specifically, to assimilate the retrievals of dust profiles from

MCS. Since the satellite measurements are not in general taken at the same levels as those used in the model, the assimilation of the Martian dust vertical distribution also requires the processing of observations that helps analyze the modeled dust variable. A different approach from that in the work of Yumimoto et al. [2008] and in the work of Sekiyama et al. [2010] is then proposed in this thesis.

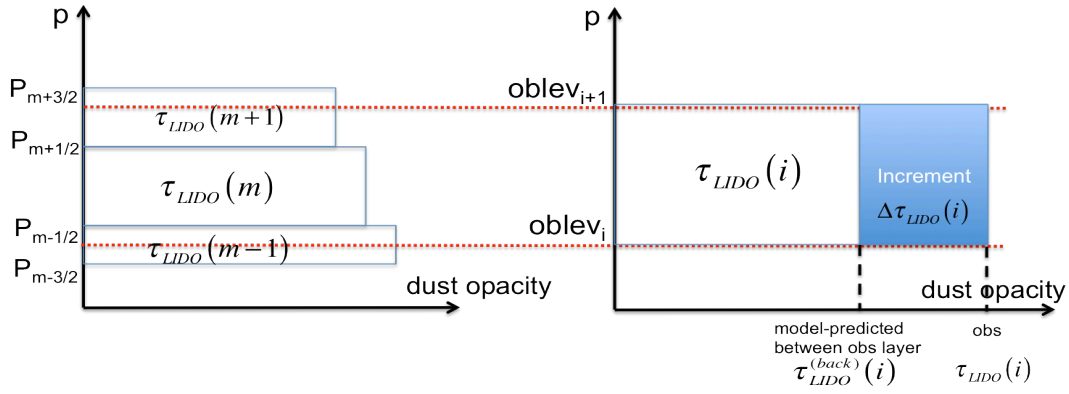

Figure 4.11 Illustration of calculating the increment of dust opacity in observation layer. $\tau_{LIDO}(m)$ is the LIDO in the model layer between $P_{m-1/2}$ and $P_{m+1/2}$. $\tau_{LIDO}(i)$ is the LIDO in the observation layer between $oblev_i$ and $oblev_{i+1}$.

The dust retrievals from MCS are reported at pressure levels that typically have a distance of between 1 and 1.5 *km* to the adjacent level, but the actual MCS measurements typically have an intrinsic vertical resolution of 5 *km* [Kleinbohl et al., 2009]. Thus, the dust retrievals oversample the information in the actual MCS measurements. In the current study, the MCS dust retrievals are integrated vertically with a 5 *km* spacing to achieve the LIDO derived from observations. This process ensures the assimilated data has the same resolution as the actual measurements, avoiding the oversampling. Thus, to assimilate this variable enables us to preserve the dust vertical structure that is simulated in the model but may be too subtle to observe given the resolution of MCS's actual measurement.

To obtain the increments of modeled LIDO from the observations at each observation layer, this newly-invented data assimilation system takes into account the

layer thickness. The approach used here resembles the assimilation of the thermal profiles in the UK-LMD MGCM [Lewis et al., 2007] that was adapted from the work of Lorenc et al. [1991]. The predicted LIDO ($\tau_{LIDO}^{(back)}$ in Eq 4.4 & Eq 4.5) is first calculated in the corresponding observation layer for the vertical analysis. An example with 3 model layers overlapping 1 observation layer demonstrates the calculation of $\tau_{LIDO}^{(back)}$ (see Figure 4.11). In this example, the $\tau_{LIDO}^{(back)}$ corresponding to the observation layer between $oblev_i$ and $oblev_{i+1}$ is calculated by,

$$\tau_{LIDO}^{(back)}(i) = \tau_{LIDO}(m-1)\frac{\ln(oblev_i)-\ln(p_{m-1/2})}{\ln(p_{m-3/2})-\ln(p_{m-1/2})} + \tau_{LIDO}(m) + \tau_{LIDO}(m+1)\frac{\ln(p_{m+1/2})-\ln(oblev_{i+1})}{\ln(p_{m+1/2})-\ln(p_{m+3/2})} \quad (4.4)$$

The increment of LIDO within this observation layer $\Delta\tau_{LIDO}(i)$ is acquired by,

$$\Delta\tau_{LIDO}(i) = \tau_{LIDO}(i) - \tau_{LIDO}^{(back)}(i). \quad (4.5)$$

Afterwards, the increment of LIDO at each model layer is obtained by,

$$\Delta\tau_{LIDO}(m-1) = \frac{\ln(oblev_i)-\ln(p_{m-1/2})}{\ln(oblev_i)-\ln(oblev_{i+1})}\Delta\tau_{LIDO}(i), \quad (4.6)$$

$$\Delta\tau_{LIDO}(m) = \frac{\ln(p_{m-1/2})-\ln(p_{m+1/2})}{\ln(oblev_i)-\ln(oblev_{i+1})}\Delta\tau_{LIDO}(i), \quad (4.7)$$

$$\Delta\tau_{LIDO}(m+1) = \frac{\ln(p_{m+1/2})-\ln(oblev_{i+1})}{\ln(oblev_i)-\ln(oblev_{i+1})}\Delta\tau_{LIDO}(i). \quad (4.8)$$

Following the vertical analysis, the horizontal analysis is performed as for *tauref* (details are presented in Section 2.6). Since the dust is transported in terms of dust mass mixing ratio, the dust mass mixing ratio needs to be corrected in order to update the information for the dust transport scheme. As the dust mass mixing ratio is proportional to the LIDO, the dust mixing ratio is multiplied by a factor

$\eta = \frac{\tau_{LIDO}(m)'}{\tau_{LIDO}(m)}$ in order to introduce the assimilated information at each layer respectively. Here, $\tau_{LIDO}(L)$ with prime is the corrected LIDO after assimilation, and $\tau_{LIDO}(L)$ without prime is the predicted LIDO before assimilation.

In some circumstances, the model layer may have a smaller vertical spacing than the actual MCS measurements ($\sim 5km$), especially in the lower and middle atmosphere, and this approach avoids the direct interpolation of observational data to the model levels. To assimilate the LIDO without interpolation is likely to keep the fine vertical features modeled by the physics of UK-LMD MGCM.

4.4.2. Results compared with in-sample assimilated MCS dust observations

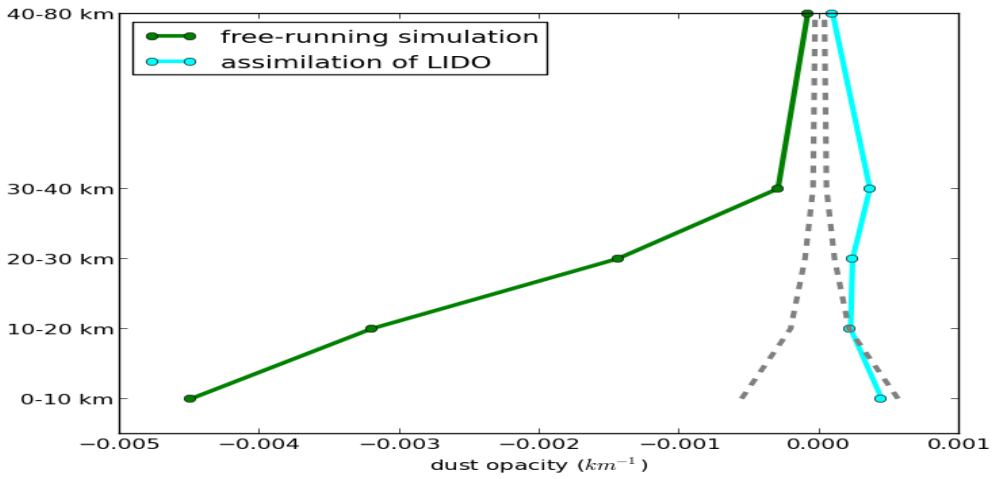

Figure 4.12 The average difference of dust opacity (km^{-1}) between model and assimilated MCS data in chosen study period. Grey dashed lines are the average errors of MCS observations.

To compare with the assimilated MCS dust data, the modeled results are interpolated into the pressure level as in the MCS dust retrievals, and the average of the dust opacity is taken over different pseudo-height ranges, i.e. 0-10 km, 10-20 km, 20-30

km, 30-40 km and 40-80 km. The difference of the average of dust opacity is calculated between the model results and the assimilated MCS dust retrievals in each pseudo-height range (Figure 4.12). In the current setting, the free-running MGCM in general tends to underestimate the dust opacity at all heights, and this absolute difference decreases with height. The assimilation of LIDO shows better convergence to the assimilated data. For instance, in the lower atmosphere (0-10 km), the difference reduces from about -0.0045 km^{-1} in the free-run simulation to about 0.0004 km^{-1} with the assimilation of LIDO. In Figure 4.6, the free-running simulation appeared to have general good agreement with the THEMIS data. Compared with Figure 4.12 here, this suggest that the dusts accumulate heavier near the ground in the very low level of atmosphere in the free-running simulation than those in the assimilation of LIDO, which is generally below the bottom of the retrieved profiles (5-10 km according to Kleinbohl et al. [2009]). This further suggests that the physics embedded in the free-running model is incapable of transporting the dusts in the vertical direction efficiently.

The example of modeled zonal mean dust opacity (at $L_s = 122.5°$) presented in Figure 4.13 shows that the assimilation of LIDO now makes it possible to capture the elevated dust layers over the tropics (see Figure 4.13). In this example, the MCS observations, however, suggested the elevated dust layers had larger magnitudes and gradients from the boundary to the center, and extended further north. Unlike the free-running simulation (middle panel in Figure 4.13), the height of the dust layer top in the assimilation of LIDO remained near 10 km in the northern middle latitudes (middle panel in Figure 4.13) as in the MCS observation (top panel in Figure 4.13) and had a slight variation between $70° \sim 80°$ latitude. The low-dust latitude band could be seen over the $-25° \sim -15°$ latitude band in the assimilation of LIDO, and this

was corresponded to the MCS observation. Further south, the dust only accumulated in the area below 10 *km* . Overall, the heights of the dust layer top now have exhibited similar latitudinal variation as in the MCS zonal mean dust opacity.

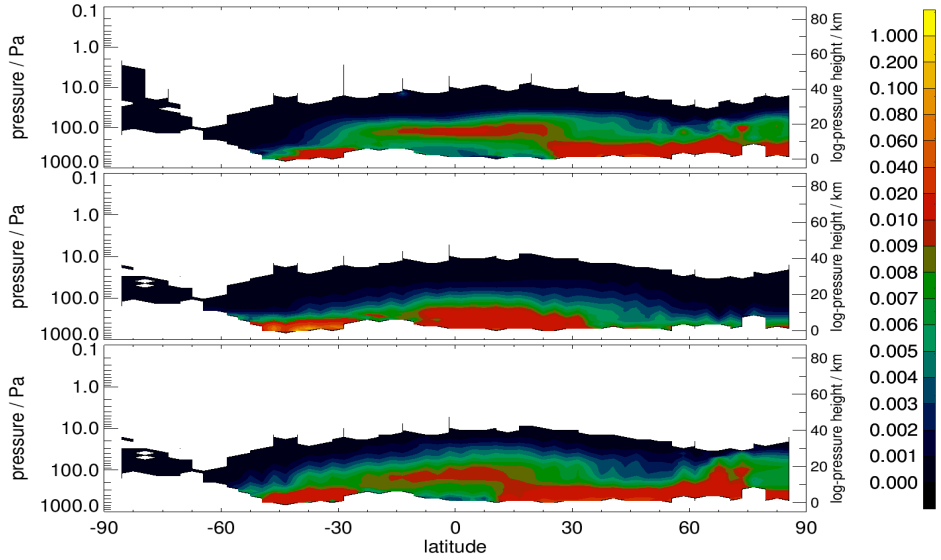

Figure 4.13 Same as Figure 4.9, but the bottom panel is for the assimilation of LIDO.

4.4.3. Discussion

The assimilation of vertical dust profiles is still not widely implemented in the Earth modeling, and it just starts to intrigue the Martian modeling scientists. A good coverage of vertically resolved Martian dust retrievals has become available recently, which make it possible to assist the MGCM to reproduce the observed interannual variability of dust cycle.

Considering the assimilation of the dust profiles still remains at an early stage of its full implementation in the MGCM, a unique and yet reasonable method of assimilating the retrievals of dust profiles, different from that used for Earth dust assimilation, is described in this thesis. The results suggest that the assimilation of LIDO is able to significantly reduce the model system errors in the simulation of the vertical dust distribution. Compared to the assimilation of CIDO, in particular, the

assimilation of LIDO also helps the model to better resolve and represent the elevated dust layers.

The THEMIS-model scatter plot shows that the assimilation of LIDO helps to partly reduce the underestimates of free-running model (see Figure 4.7a), regarding of the whole study period (Figure 4.14a). On the contrary, the results of assimilation of LIDO displayed overestimates when *tauref* < 0.3 or *tauref* > 1.2 . If the data measured in MY 28 are removed from this comparison, however, the assimilated results exhibit significantly better correlation with THEMIS data (Figure 4.14b). The coefficient of linear regression fitting between the THEMIS data and model for MY 29 is 1.02 versus 0.39 if data in MY 28 are also included.

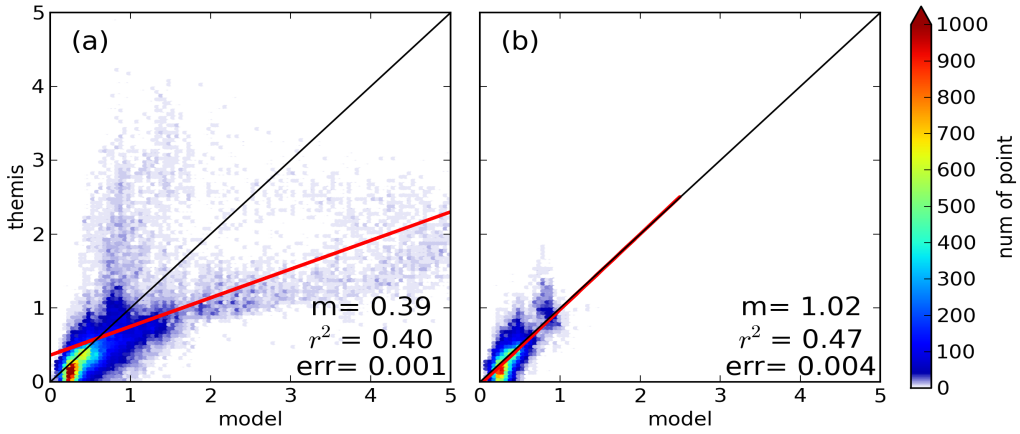

Figure 4.14 Same as Figure 4.7 but only for the assimilation of LIDO. (a) for the whole study period including MY 28 and 29, (b) only for the period in MY 29.

In general, the assimilation of CIDO described in section 4.3 produces more realistic *tauref* overall, especially during MY 28 GDS. This is mainly because the THEMIS data was directly assimilated into the model. In this section, compared the results from the assimilation of LIDO with THEMIS data, it demonstrates that only assimilating the LIDO data may not be sufficient to produce a reanalysis dataset that best fits all available observations. The coefficient of determination is only 0.4 for the whole period, which is much smaller than that of the comparison between the

THEMIS data and the assimilation of CIDO, i.e. 0.82. This is likely to be because the limb-viewing MCS instrument could not provide consistent measurements extending into the lower Martian atmosphere where the dust normally has a higher concentration than higher up in the atmosphere. The *tauref* in the assimilation was less representative in MY 28. One important reason was that MCS observations provided very limited coverage during MY 28 GDS. Another possible reason could be that the model would have larger error during GDS; as a result, the assimilation might have comparably large error. We may anticipate that assimilating both CIDO and LIDO can be more important for extracting the information from two different datasets.

4.5. Joint assimilation of CIDO and LIDO

In the above experiments, compared to the free-running simulation, the assimilation of CIDO is able to improve the simulation of the dust horizontal spatial distribution and the assimilation of LIDO can have a better representation of the dust vertical distribution. To make use of the advantages of these two datasets, it is possible to assimilate both CIDO and LIDO together in the data assimilation system. In theory, it is possible to use the measured dust profiles to correct the corresponding amount of dust in each model layer, then use the CIDO data to correct the dust in the rest part of that particular atmospheric column. This may avoid adjusting the dust vertical distribution by the CIDO data unnecessarily when part of the vertical dust distribution has already been corrected by the LIDO data. However, the THEMIS measurements and MCS measurements normally are not measured at the same time and at the same location. It is difficult to use these two datasets simultaneously to assess the dust distribution at one location. Therefore, I ignore the possibility of these two datasets

happening to measure the same place at the same time. The strategy I am using here is instead simply to assimilate two datasets independently. A simple experiment was done to suggest that assimilating CIDO data ahead of the LIDO data in the assimilation loop was leading towards slightly better results, although there was no substantial difference about which dataset the data assimilation system should assimilate ahead of the other. Therefore, after the temperature assimilation, the CIDO was assimilated first in this experiment followed by the assimilation of LIDO data.

4.5.1. Results compared with in-sample assimilated THEMIS dust observations

The assimilation of both CIDO and LIDO is able to benefit from both datasets, and it can thus produce for example the interannual variability of global average *tauref* as in the THEMIS observation (Figure 4.15). The joint assimilation of both CIDO and LIDO captures the evolution of the global average *tauref* during the MY 28 GDS as in the assimilation of CIDO-only. In spite of the limited coverage of MCS data during MY 28 GDS (see Figure 4.2), the assimilation of LIDO-only still produces a period with global dust storm feature. Before the onset of the MY 28 GDS and at the very early stage of the storm, the MCS data had reasonable coverage, and it was also available in the northern high latitudes (to the north of 45°N) during the whole storm period. These data make the assimilation (only with MCS LIDO) able to constraint the initial condition and boundary condition of this GDS. However, this high dust opacity period happens later in the assimilation of LIDO-only ($L_s = 295°$) than the observation suggests for the MY 28 GDS ($L_s = 281°$), and it is also with a much higher global average *tauref* than the actual observation (4 versus 2.7). The main reason for this later start in the assimilation of LIDO-only is likely because the onset

of MY 28 GDS happened in the Southern Hemisphere, thus, the MCS measurement to the north of 45°N captured this GDS feature in a later time. This delayed the happening of the GDS in the assimilation of LIDO-only. Until the MCS data became gradually available in the Southern Hemisphere during the "cleanup" of the storm, the excessive dusts in the assimilation of LIDO-only started to be removed efficiently in the Southern Hemisphere by the assimilation but in a time later than it was observed in the THEMIS data. This suggests the modeled sedimentation solely is not efficient enough to remove the dusts transported from the northern boundary of this GDS, and it leads to the overestimate of the global average *tauref* during the peak of GDS in the assimilation of LIDO-only. For the "quiet" season (northern spring and summer), the assimilation of CIDO and LIDO also exhibits reasonable agreement of dust loadings compared to the THEMIS observations, for instance, reproducing *tauref* during the "quiet" season in MY 28. Compared to the assimilation of LIDO-only, the overestimates in MY 29 "quiet" season were reduced in the assimilation of both CIDO and LIDO. The results show almost the same THEMIS-model correlations (Figure 4.16) as for the assimilation of CIDO-only (Figure 4.7). It suggests *tauref* from the joint assimilation of CIDO and LIDO is slightly overestimated in the low-value areas (< 0.3) and underestimated in the relatively high-value areas (> 2). Since most of measured dust loadings are below 1, generally speaking, the *tauref* from the joint assimilation of CIDO and LIDO converges reasonably well to the THEMIS data as in the CIDO-only case, only with slightly smaller coefficient of fitting (1.06 versus 1.08 for the assimilation of CIDO-only) and slightly smaller coefficient of determination.

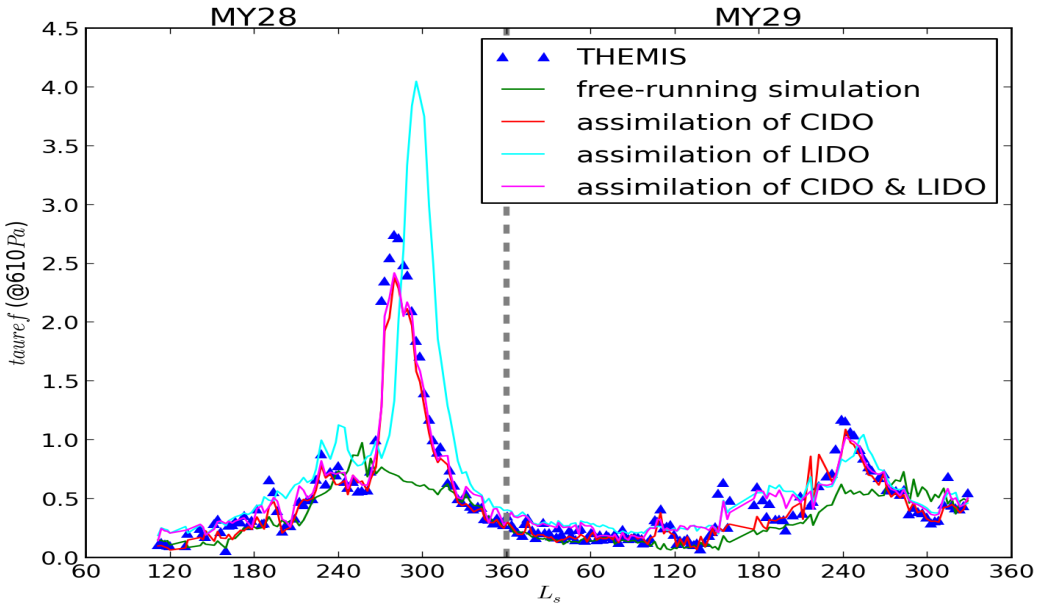

Figure 4.15 Same as Figure 4.6 but for free-run simulation, the assimilation of CIDO, the assimilation of LIDO and the assimilation of both.

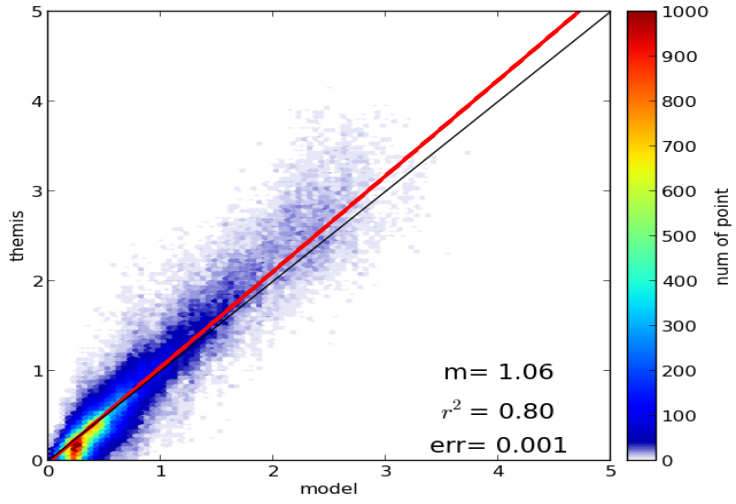

Figure 4.16 Same as Figure 4.7 but only for the joint assimilation of CIDO and LIDO.

4.5.2. Results compared with in-sample assimilated MCS dust observations

The average difference of mean dust opacity suggests the joint assimilation of CIDO and LIDO can also greatly reduce the model errors in the vertical dust distribution among these model results (Figure 4.17). It is worth pointing out that, although the

assimilation of CIDO-only assimilates the observed information of the dust spatial distribution, the assimilated results still improve the simulation of dust vertical distribution in terms of a smaller difference with respect to the observations. The assimilation of the dust profiles (i.e. the assimilation of LIDO-only, or the joint assimilation of CIDO & LIDO) assists significantly improving the agreement of the model results to the MCS dust retrievals. Although the assimilation of LIDO-only and the joint assimilation of CIDO and LIDO both assimilate the same MCS retrievals of dust profiles, the joint assimilation of CIDO and LIDO exhibits better agreement with the assimilated MCS data in the entire atmosphere, and the differences below 30 km are well within the observational errors. It is evident that assimilating the dust spatial distribution (THEMIS) can further help the modeled dust vertical distribution to match the observed dust profiles statistically.

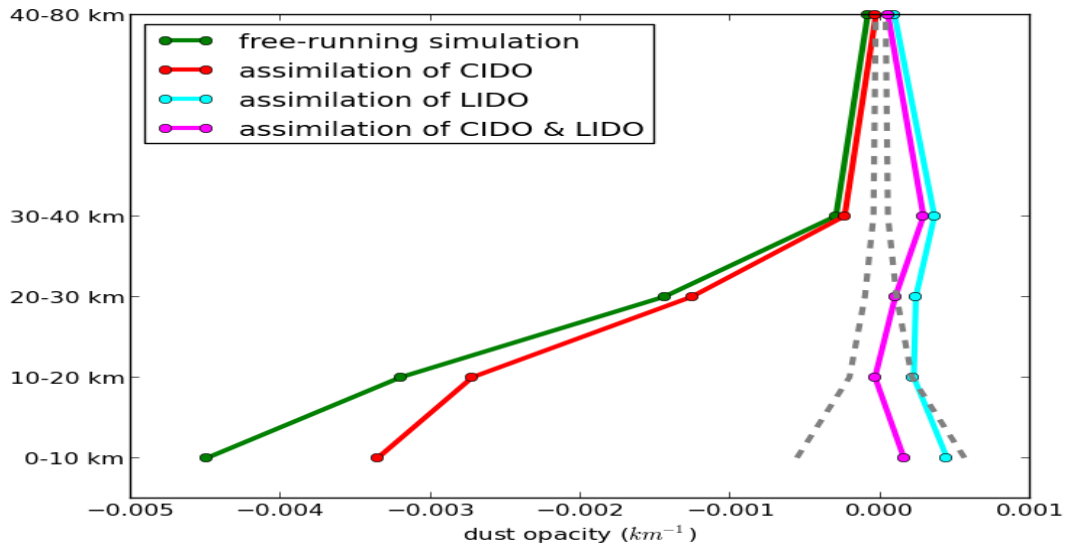

Figure 4.17 Same as Figure 4.12, but for all the model results.

Compared to the zonal mean dust opacity of MCS binned observations centered at $L_s = 122.5°$, the joint assimilation of CIDO and LIDO (bottom panel in Figure 4.18) produces very similar results to the assimilation of LIDO-only (bottom panel in

Figure 4.13). In the joint assimilation of CIDO and LIDO, a clear elevated dust layer can be seen over the tropics, and the tops of the dust layer over the rest of the latitudes remain below $10\,km$. These features correspond better to the MCS observations (top panel in Figure 4.18) than those in free-running simulation.

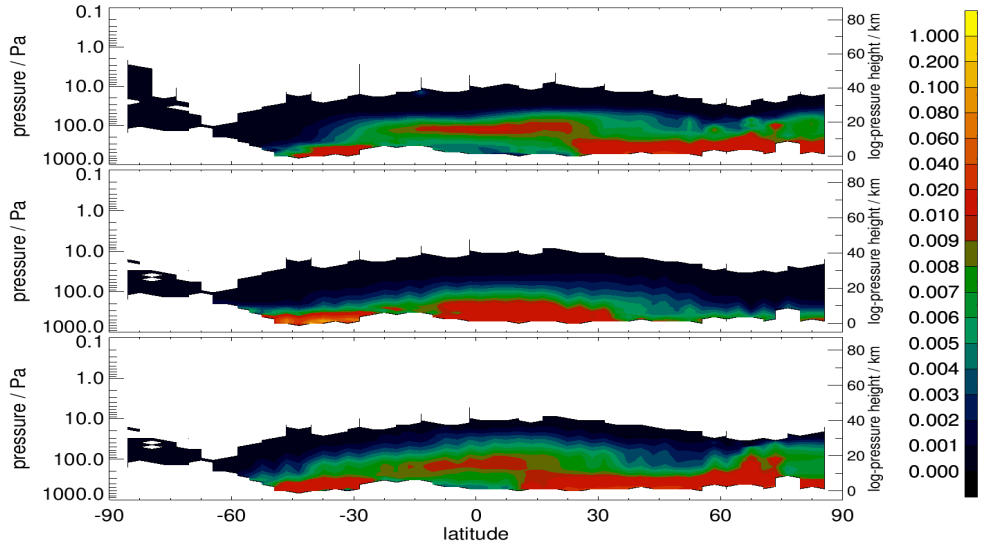

Figure 4.18 Same as Figure 4.9, but the bottom panel is for the joint assimilation of CIDO and LIDO.

4.6. Conclusions and discussions

A new data assimilation system has been described in this thesis. Unlike the previous attempt [Lewis et al., 2007] in which dust tracers were only distributed vertically by an empirical function, the new data assimilation system consists of the assimilation of temperature profiles, and either the assimilation of column-integrated dust opacity (CIDO; rescaled to a reference pressure as *tauref* to be analyzed against model variable), the assimilation of layer-integrated dust opacity (LIDO), or both simultaneously together with activated dust transport, lifting and deposition. It is evident that the assimilation of temperature is able to assist the modeled results to converge to the assimilated MCS temperature profiles, and the results of each

assimilation experiment converges to the dust observations that are assimilated into the UK-LMD MGCM.

The assimilation of CIDO-only with activated dust transport is thus able to demonstrate the convergence to the interannual variability of the dust spatial distribution with the almost simultaneous generation and dissipation of the MY28 GDS, as in the assimilated THEMIS observations. Without assimilating the MCS LIDO data, the assimilated results still miss the feature of elevated dust layers in the northern spring and summer. These elevated dust layers have been discussed in the context of the MCS observation [Heavens et al., 2011a] and model simulations [Rafkin, 2012; Spiga et al., 2013]. These remain a challenge for all MGCMs. Overall, the average differences to the MCS observations suggest that even by only assimilating the dust spatial distribution (i.e. *tauref* derived from THEMIS retrievals), the assimilation of CIDO-only helps reduce systematic errors in the model estimate of the dust vertical distribution. This result is particularly intriguing to the period that only has the observation of dust spatial distribution such as TES periods (from $L_s \approx 104°$ of MY 24 to $L_s \approx 82°$ of MY 27), as the assimilation of CIDO-only is also able to provide more realistic dust vertical distributions in general.

The assimilation of LIDO-only with activated dust transport can help reproduce some of the features of elevated dust layers with a reasonable interannual variability in a global average standard. The average difference with respect to the MCS observations is reduced greatly by converging to the assimilated MCS retrievals of dust vertical distribution. However, the limb-viewing MCS may not observe the lower part of atmosphere all the time where the dust concentration is normally higher than in the upper part of each atmospheric column. As a result, the assimilation of LIDO-

only does not provide an evolution of the global average *tauref* that is as good as the direct assimilation of CIDO-only, for instance, overestimates during MY28 GDS.

The joint assimilation of CIDO and LIDO can benefits from the advantages of both THEMIS and MCS datasets. It displays the evolution of the MY28 GDS, as in the assimilation of CIDO-only, and the magnitude of dust loadings between 150° and 180° of MY29, as in the assimilation of LIDO-only. Besides, the assimilated results partially recover the feature of elevated dust layers. Therefore, we conclude that this updated data assimilation system with the joint assimilation of CIDO and LIDO is a powerful tool that can help us to reconstruct the climate of the Martian atmosphere as well as individual dust events. It is important, however, to validate the reanalysis from this data assimilation system as well as against independent data. This will be discussed in the following chapter.

It is also worth mentioning that, apart from the experiments I describe in detail, an assimilation experiment with only the assimilation of temperature was conducted during this project. The dust lifting and dust transport were also activated in that experiment. It is evident in the work of Montabone et al. [2006] and in the work of this chapter that the assimilation of temperature does reduce the error of simulated temperature, thus leading towards better meteorological fields. However, since the dust transport and dust lifting scheme itself, together with the prescribed parameters, are commonly not a perfect representation of the "true" dust cycle on Mars, better meteorological fields do not necessary predict a better dust distribution. In the experiment with only temperature being assimilated, the simulated dust distribution, sometimes, appeared to have a slightly larger bias than the dust distribution in a free-running simulation. Some possible causes for this may include the use of an "over-naïve" size distribution, inappropriate choice of the dust lifting parameters, an

imperfect understanding of the dust source and sink processes, the dust transport scheme itself and so forth. Occasionally, the assimilation of temperature-only might lead to an unrealistically large dust opacity in the dust simulation which made the model crash. Even if I intentionally increased the physical time step to resolve more dusts in the dust transport scheme, the dust levels couldn't reduce back to reasonable values. Thus, a different set of parameters for dust transport and liftings is likely to be determined for the assimilation of temperature-only. In the end, I chose to compare the assimilation experiments with a completely free-running simulation instead of an assimilation of temperature-only, mainly because I wanted to compare with the "best" dust distribution without any assimilation of atmospheric properties and too much parameter tuning. But it remains a future task beyond this thesis to conduct experiments to produce an appropriate set of parameters for different combinations of the assimilation strategy.

Chapter 5 Validation of the Reanalysis from the New Data Assimilation System

5.1. Introduction

A newly-developed data assimilation system, based on the UK version of the LMD Martian General Circulation Model (UK-LMD MGCM), has been described in Chapter 4 of this thesis. The data assimilation system was successfully applied to analyze the column-integrated dust opacity (using retrievals from THEMIS, i.e. the Thermal Emission Imaging System on board Mars Odyssey) and layer-integrated dust opacity (using retrievals from MCS, i.e. the Mars Climate Sounder on board the Mars Reconnaissance Orbiter), and the assimilated results were shown to converge to those data. In this chapter, the reanalysis from this new data assimilation system is validated against non-assimilated data, including the independent datasets from the upward-looking measurements from the Mars Exploration Rovers (MER) "Spirit" and "Opportunity". In order to have a more comprehensive validation, about 10% of the THEMIS and MCS data were kept from the assimilation, and they are also used as an out-of-sample validation. Those withheld data were selected from 1 in every 10 of the data (for THEMIS) and of the profiles (for MCS). It is not surprising to see that these selected spacecraft-based data for validation may have correlation with the data

assimilated into the model, and this, to some degree, weakens their application to validate the model. However, at the current status of Mars exploration, these datasets are the best available data for the assimilation and related validation which favors the dataset with better global coverage. In another aspect, the completely independent datasets from MER mission provide a complementary way of validation. Hereafter, the reanalysis/assimilation refers to the joint assimilation of CIDO and LIDO as described in section 4.5 of the previous chapter.

5.2. Overview of the dust opacity in the reanalysis

In chapter 4, the assimilated results have been showed to converge to the observational data used in the assimilation. Since the measured dust vertical profiles usually do not provide much information in the lower part of the atmosphere, assimilating the layer-integrated dust opacity (LIDO), together with the column-integrated dust opacity (CIDO; converted to *tauref* to remove the effects of topography) is found to be important in order to recover the full variability of dust cycle. In this chapter, the reanalysis from the joint assimilation of CIDO and LIDO will be presented and compared against the non-assimilated datasets, including out of sample THEMIS and MCS dust observations and independent upward-looking measured dust opacity depth from the MER mission.

Figure 5.1 compares the results of the zonally averaged dust opacity in both a free-running simulation and the reanalysis. Because the dust is generally assumed to be well mixed in the lower atmosphere, the CIDO is rescaled to 610 Pa pressure surface to remove the effect of topography (i.e. *tauref*). Within a Martian year (MY), the seasonal variability of the dust opacity in both free-running simulation and the

reanalysis are generally consistent with the available observations observed by various spacecraft [Smith, 2008]. The dust opacity is higher on a global scale during the second half of the year (solar longitude $L_s = 180° - 360°$), while it is relatively "quiet" in terms of dust activity during the first half of the year ($L_s = 0° - 180°$). In the free-running simulation (Figure 5.1a), the dust-active period in each MY lasts longer than the observations presented in the work of Smith [2009]. The dust opacity in the reanalysis (Figure 5.1b) shows more realistically intermittent seasonal variability within each dusty season. The dust peak during the dusty season in the reanalysis is less broad in terms of L_s than the dust peak in the free-running simulation, and it tends to shut down prior to the decline in solar forcing which occurs toward the end of northern winter.

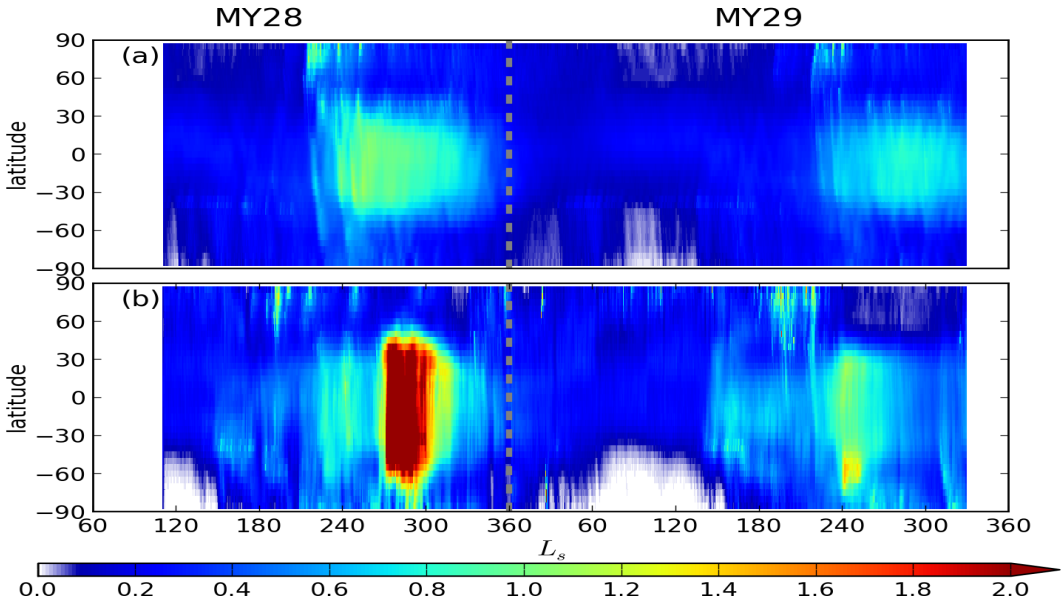

Figure 5.1 Seasonal and latitudinal evolution of the zonal averaged *tauref* , (a) for the free-running simulation, (b) for the reanalysis.

The interannual variability exhibited in the reanalysis (Figure 5.1b) is found to be essentially the same as the pattern found in the observations (Figure 8a in Smith [2008] and upper panel of Figure 6 in Smith [2009]). Planet-encircling or global dust

storms (GDS) do not happen every MY, but the reanalysis successfully reproduces the most-recent observed GDS that occurred around $L_s \approx 265° - 310°$ in MY 28. The initiation and duration of the GDS in the reanalysis are also both consistent with the THEMIS retrievals (upper panel of Figure 6 in Smith [2009]). A mild dusty season in MY 29 following the MY28 GDS year also suggests a more realistic interannual variability. In contrast, the free-running simulation displays a certain degree of variability in these two MYs, with slightly stronger dusty season in MY 28 than that in MY 29 (Figure 5.1a). However, the maximum magnitude of *tauref* and its related timing during GDS do not completely match the observation (upper panel of Figure 6 in Smith [2009]).

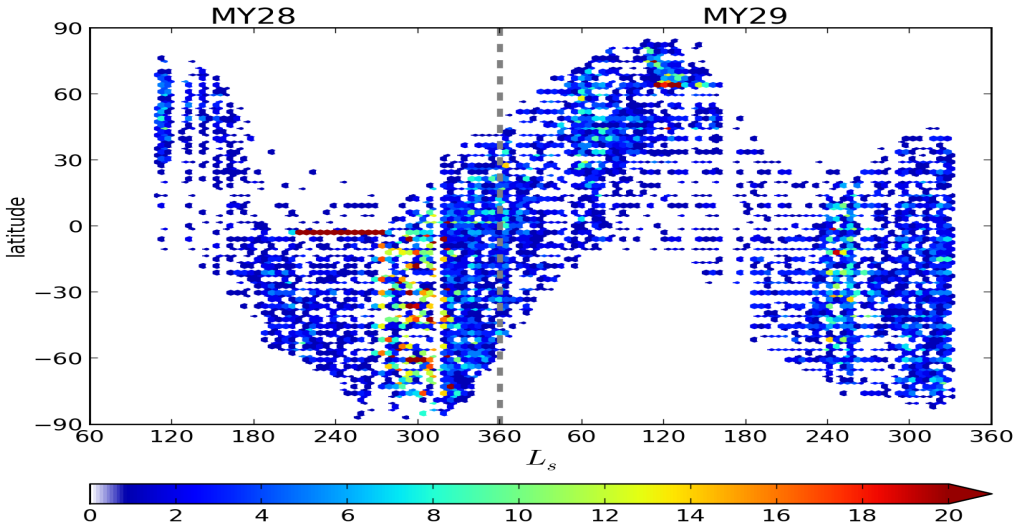

Figure 5.2 The distribution in L_s and latitude of the non-assimilated THEMIS retrievals of CIDO. The color scale shows the number of measurements per 5° in L_s and every 3° in latitude.

5.3. Correlation with non-assimilated THEMIS dust observations

The distribution of non-assimilated THEMIS dust observations that are roughly contemporaneous with those that are assimilated is shown in Figure 5.2. This

distribution maintains the same spatial coverage in L_s as in the full THEMIS dataset (Figure 4.1), but with fewer data points. Withholding this dataset should not, therefore, greatly affect the assimilated results, and its distribution in latitude and L_s can still represent the character of the latitudinal availability of the THEMIS dataset. Therefore, the correlation between non-assimilated THEMIS dust observations and reanalysis should reasonably represent the agreement of the reanalysis to observations across different latitudes.

To compare with the non-assimilated THEMIS data, both the observations and model results are rescaled to the 610 Pa pressure level as representing *tauref* , and the model results are first interpolated to the same location and time as the non-assimilated data. The global averaged values of *tauref* shows better agreement between the non-assimilated THEMIS data and the reanalysis (Figure 5.3). The *tauref* in the free-running simulation shows increase similar to THEMIS data in $L_s = 180° - 240°$ of MY 28, but it continues to increase to ~ 1 at ~ 260° without the decrease as in the THEMIS data. The dust activity ceases before successfully growing into a GDS. The free-running model predicts relatively mild dusty season in MY 29 compared to MY 28. The *tauref* in the free-running simulation increases and decreases at similar time to the THEMIS data. For both dusty seasons, the free-running model does not produce the observed amount of dust. Compared to the free-running simulation, the reanalysis shows evidence for precursor initiation events and captures the decay of the MY 28 GDS, as well as the increasing interannual variability in MY 29's dusty season. The magnitudes of the dust loadings in the reanalysis are also more consistent with the observations. Although the estimates of dust loadings during the MY 28 GDS have been improved significantly in the reanalysis, the maximum of *tauref* (~ 2.2) is still lower than the peak of global

average of non-assimilated THEMIS observations (~ 2.7). However, this difference may not necessarily mean that the reanalysis fails to reproduce the dust loadings during the peak, as the measurement uncertainties of THEMIS data is not well evaluated, and can be 20% of the measurements or even higher [Smith 2004]. In the "quiet" season, the free-running model seems to agree with the THEMIS data well, especially for MY 29. The reanalysis provides higher *tauref* than the free-running model. For both results, their differences from THEMIS data are still smaller than the minimum of observational uncertainty (0.104 for visible extinction opacity) according to Smith [2009].

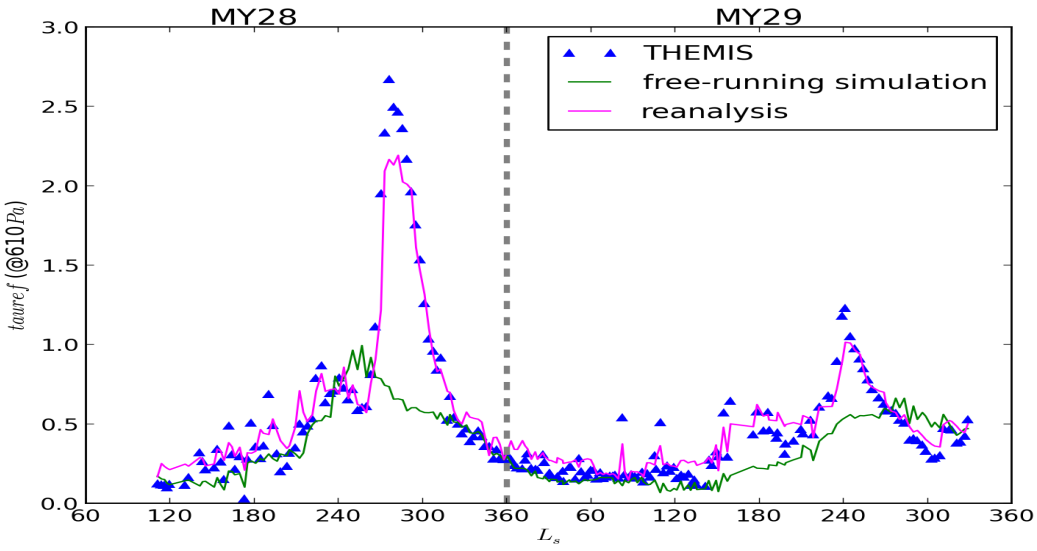

Figure 5.3 5-sol global average of *tauref* for the study period. The THEMIS values plotted are taken from outside of the assimilated THEMIS dataset.

The correlations of *tauref* between non-assimilated THEMIS data and free-running simulation, non-assimilated THEMIS data and the reanalysis for MY28-29 are shown in Figure 5.4. In the current setting, the free-running simulation generally tends to underestimate the dust loadings (Figure 5.4a) mainly in the dusty season (Figure 5.3). It is evident that significantly better correlations with the non-assimilated THEMIS data are found in the reanalysis (Figure 5.4b). The *tauref* in the reanalysis is only

slightly overestimated when the dust loadings are below 0.5, although it turns to be underestimated when the dust loadings are above 2.

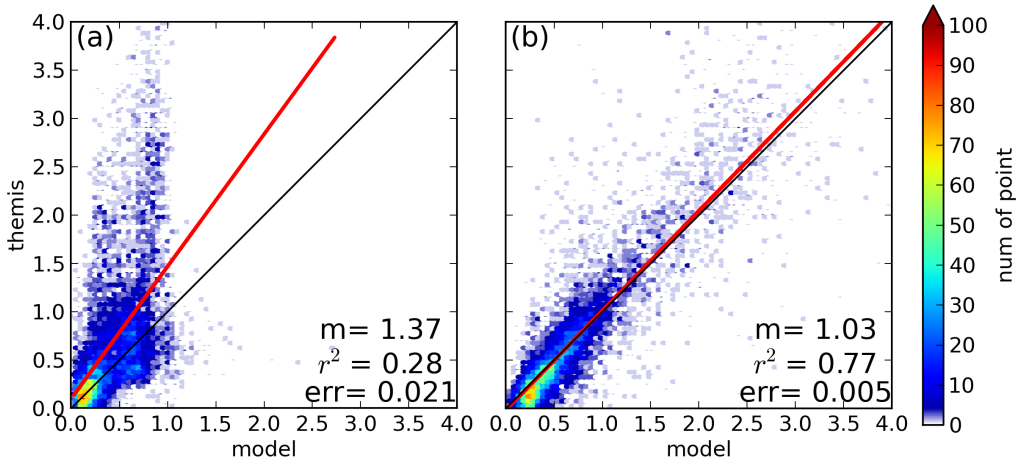

Figure 5.4 Scatter plots of THEMIS-model *tauref* during the whole study period. The color shows the data density per 0.05 *tauref* . The red lines are the linear least square fit between THEMIS and model. m is the coefficient of the fittings, i.e. the slope of the red lines, and r^2 is the coefficient of determination, and err is the standard error of the slope. The black lines represent the lines with coefficient 1. (a) Scatter plot of non-assimilated THEMIS observations against data from the free-running simulation, (b) corresponding plot of non-assimilated THEMIS against data from the reanalysis.

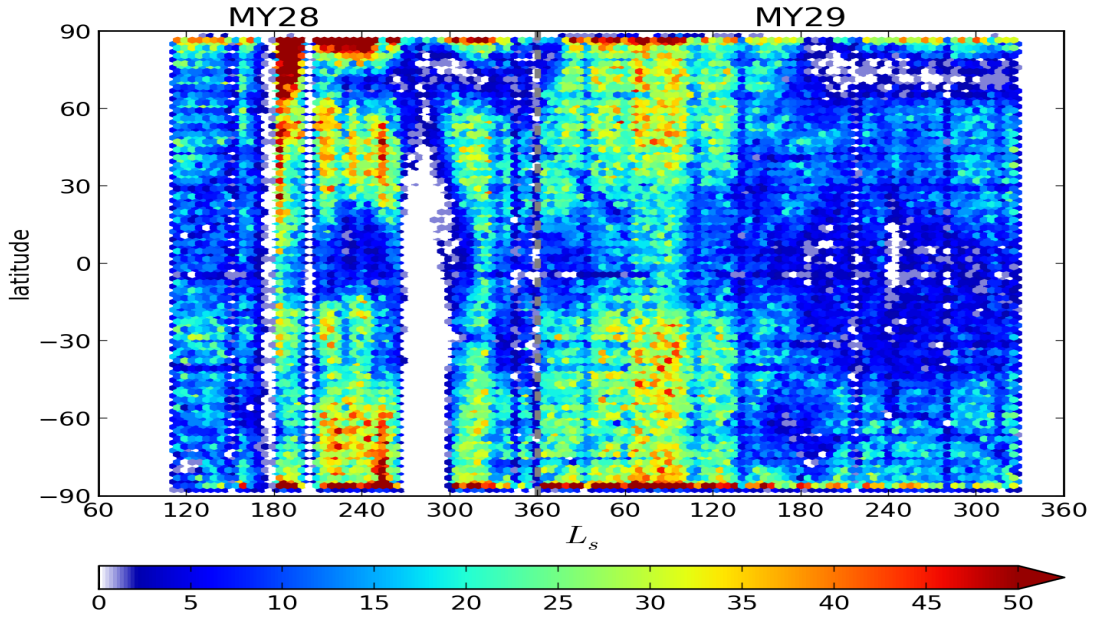

Figure 5.5 Same as Figure 5.2, but for non-assimilated MCS dust retrievals, and the color scale shows the number of retrieved profiles per 5° in L_s and every 3° in latitude.

5.4. Correlation with non-assimilated MCS dust observation

Figure 5.5 shows the distribution of the non-assimilated MCS dust profiles in L_s and latitude. A similar distribution pattern to the full MCS dust dataset can be seen, with less data available in the tropics and very limited data during the MY 28 GDS.

In order to achieve broader and more general views of the model performances, the model results are grouped into different pseudo height ranges (0-10 km, 10-20 km, 20-30 km, 30-40 km and 40-80 km). The pseudo-heights are calculated in terms of the scale height 10 km and reference surface pressure 610 Pa. As the MCS retrievals are reported at pressure levels with approximately 1-1.5 km distance [Kleinbohl et al., 2009], another advantage of this grouping is to smooth the oversampling of MCS retrievals and compare the models against observations at a distance larger than the true instrumental resolution (5 km). The model results are first interpolated to the pressure levels as in the MCS dust retrievals in the unit of km^{-1}, and in each pseudo-height range, the average difference of dust opacity between non-assimilated data and the reanalysis (positive means overestimate, and vice versa) are shown in terms of different latitude bands (-90 ~ -50°, -50° ~ -15°, -15° ~ 15°, 15° ~ 50° and 50° ~ 90°).

Figure 5.6 shows the average differences of dust opacity between non-assimilated MCS data and free-running simulation and between non-assimilated MCS data and the reanalysis in "quiet" season ($L_s = 0° - 180°$). During the "quiet" season, the uncertainties of MCS data are obviously larger in northern high latitudes (50° ~ 90°) than other latitude bands. The free-running model exhibits reasonably good agreement with the MCS dust profiles, and the average differences are well within the observational uncertainties. The differences between the non-assimilated MCS data and the reanalysis are also within the observational uncertainties above 10 km, but the difference is slightly larger than the observational uncertainty below 10 km. In

southern high latitudes (-90° ~ -50°), the free-running model significantly underestimates the dust opacity below 30 km with maximum -0.008 km^{-1} at the bottom of the dust profiles, and the reanalysis appears to reproduce the dust vertical distribution with reasonable deviation from the MCS observations.

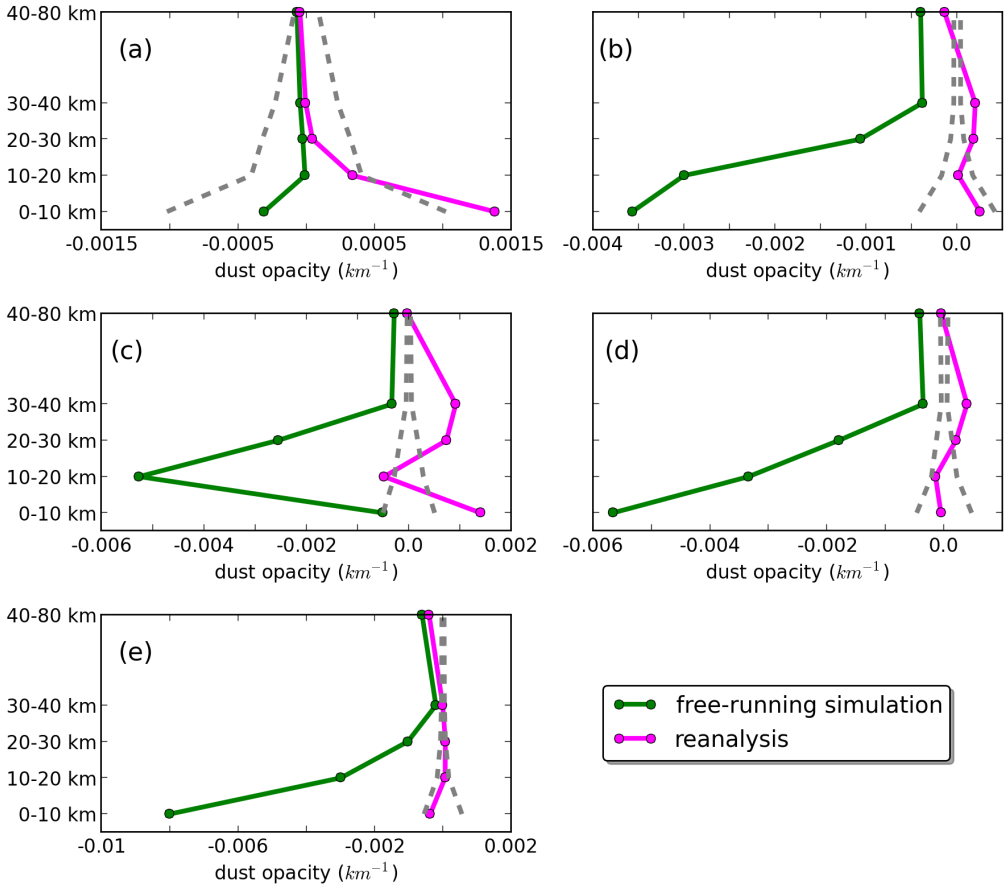

Figure 5.6 The average difference of dust opacity (in the unit of km^{-1}) between non-assimilated MCS data and the reanalysis in "quiet" season ($L_s = 0° - 180°$) of chosen study period in MY 28-29. Grey dashed lines are the average uncertainties of MCS observations. For different latitude bands, (a) 50° ~ 90°, (b) 15° ~ 50°, (c) -15° ~ 15°, (d) -50° ~ -15°, (e) -90° ~ -50°.

In the middle latitudes of both hemispheres (15° ~ 50° and -50° ~ -15°), the free-running simulation exhibits similar underestimates. The underestimates reduce with pseudo-heights, and range from -0.0037 km^{-1} to -0.0005 km^{-1} in Northern Hemisphere or from -0.0057 km^{-1} to -0.0002 km^{-1} in Southern Hemisphere. In these middle latitudes, the average differences between non-assimilated MCS data and the

reanalysis are within or close to the observational uncertainties with both largest differences in 30-40 km.

In the tropics (-15° ~ 15°), the free-running simulation generally underestimates the dust opacity. The difference increases from -0.0005 km^{-1} at the bottom of profiles to the maximum 0.0053 km^{-1} at 10-20 km height range, and then it starts to reduce with height. The differences are in general larger than the MCS observational uncertainties except in the height range 0-10 km. The distribution of the difference between non-assimilated data and the reanalysis displayed similar shape to that for the free-running simulation but at different values. The average of difference between non-assimilated data and the reanalysis shows improvement of the results in the height ranges 10-20 km, 20-30 km and 40-80 km, but it also shows that the reanalysis overestimates the dust opacity in the 0-10 km and 30-40 km height range with absolute differences larger than those of the free-running simulation.

Figure 5.7 shows the average differences of dust opacity between non-assimilated MCS data and free-running simulation, and between non-assimilated MCS data and the reanalysis in dusty season ($L_s = 180° - 360°$). In general, the reanalysis exhibits better agreement with MCS data than the free-running simulation during dusty season. The maximum of average difference of free-running simulation reduces from north to south, ranging from 0.0085 km^{-1} to 0.0008 km^{-1}, and this may result from the difficulty of realistically predicting frontal dust storms in the northern high latitudes during dusty season. The maximum of average difference of the reanalysis is smaller than that of free-running simulation, ranging from 0.0018 km^{-1} to 0.0003 km^{-1}. In northern high latitudes (50° ~ 90°), the average differences for the reanalysis are either within or very close to the MCS observational uncertainties, while the average differences for the reanalysis reduce with height, and the maximum is ~ 0.0085 km^{-1}

in 0-10 km height range. In the northern middle latitudes (15° ~ 50°), the underestimates of free-running simulation become smaller, but the differences are still larger than the observational uncertainties. The reanalysis underestimates the dust opacity below 30 km, but the differences are still smaller than the free-running simulation. Above 30 km, the reanalysis overestimates the dust opacity with differences even larger than those of free-running simulation.

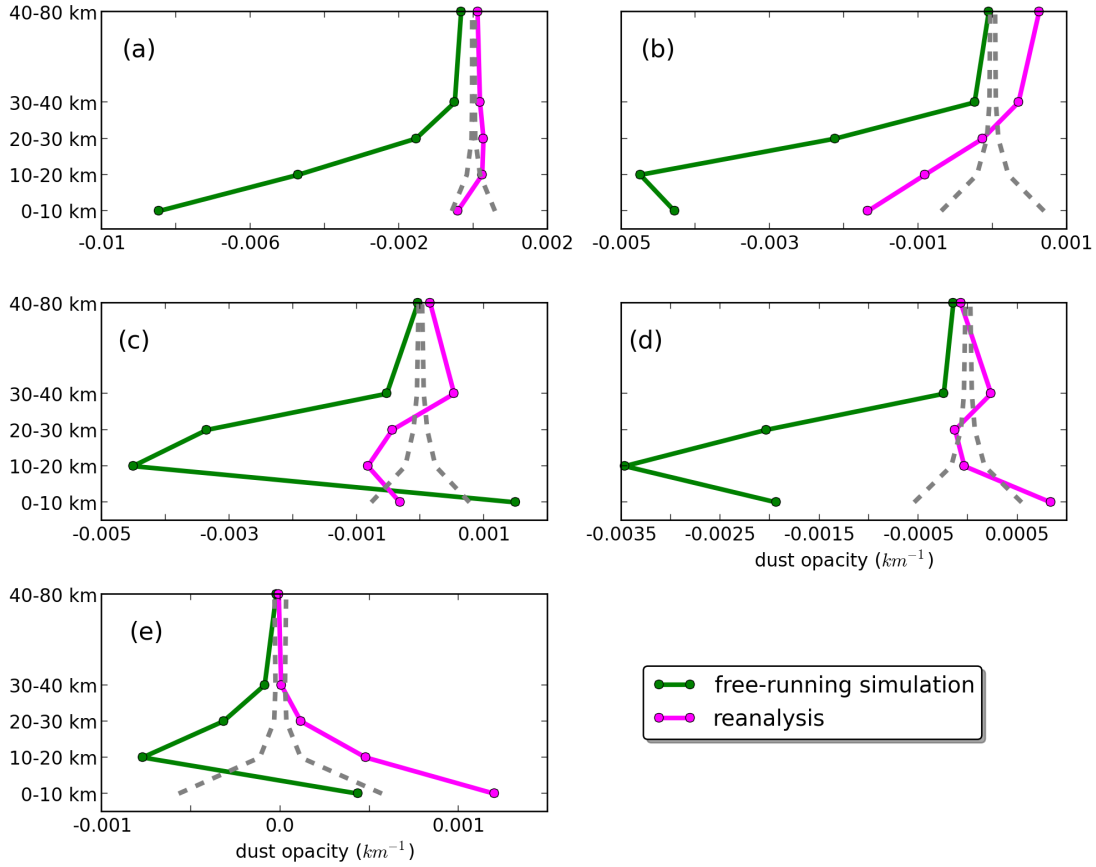

Figure 5.7 Same as Figure 5.6, but for the dusty season ($L_s = 180° - 360°$).

In the tropics (-15° ~ 15°), the maximum underestimate of free-running simulation is similar to that of northern middle latitudes ~ 0.0045 km^{-1} at 10-20 km height range, and the free-running simulation slightly overestimates the dust below 10 km. The average difference of the reanalysis from MCS data is within the observational error

in 0-10 km height range (~ 0.0003 km^{-1}). The reanalysis tends to underestimate the dust opacity between 10 and 30 km, and overestimate the dust opacity above 30 km.

In the southern middle latitudes (-50° ~ -15°), the reanalysis has smaller differences than it does in the tropics and northern middle latitudes, and the differences in the height range 10-20 km, 20-30 km and 40-80 km are within or close to the observational uncertainties. In the southern high latitudes (-90° ~ -50°), the free-running simulation tends to underestimate the dust opacity above 10 km. The reanalysis tends to overestimate the dust opacity below 30 km. The differences between the non-assimilated MCS data and the reanalysis are within the observational uncertainties above 30 km. However, in the height range close to the ground (0-10 km), the free-running simulation appears to produce a better result than the reanalysis. It should be noted that the estimate of the uncertainty of MCS data in the area with relatively high dust opacity (e.g. 0-10 km height range) might be less accurate due to the various uncertainty sources (briefly discussed in section 1.2.3 of this thesis).

5.5. Comparisons against independent Mars Exploration Rovers' data

Apart from the satellite measurements, upward-looking surface observations represent another important dataset against which to validate the reanalysis. Among the limited number of upward-looking observations, the measurements from the MER mission, i.e. "Spirit" and "Opportunity" rovers, provide almost continuous data coverage during MY 28 and MY 29 that are concurrent with the chosen study period in this thesis. The brief description of these two datasets can be found in the section 1.2.4.

The solar filters, at wavelengths of 440 *nm* and 880 *nm*, were designed for the Pancam camera to image the Sun. However, according to the MER team, the 440 *nm* filter is significantly affected by a red leak [Lemmon et al., 2014]. As there should not be a significant difference between the CIDO at 880 *nm* (wavelength chosen for one of the Pancam filter) and the CIDO at 700 *nm* (used as the model visible wavelength), in this validation, I rescale the measurements at the wavelength of 880 *nm* to the reference pressure 610 *Pa* (i.e. *tauref*), and make the comparison directly with the modeled sol-averaged *tauref* (also rescaled to the 610 Pa).

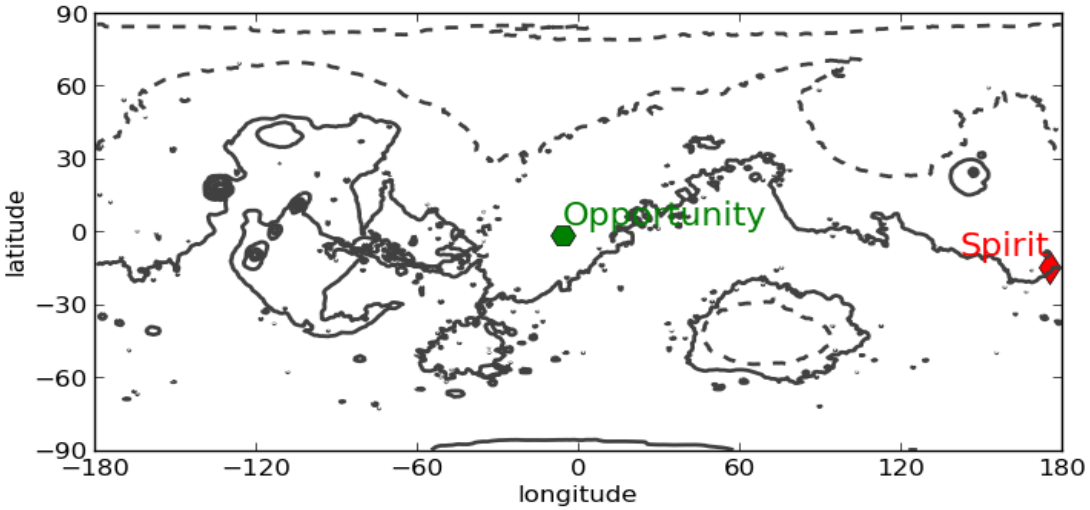

Figure 5.8 The locations of the landing sites for the "Spirit" and "Opportunity" MERs. The black line is the indication of topography with respect to areoid (referred to Figure 1.1).

5.5.1. Comparison against the "Spirit" Pancam

The comparison with corresponding modeled values in the reanalysis and free-running simulation is shown in Figure 5.9. During the relatively "quiet" season for dust activity ($L_s = 0° - 180°$), the "Spirit" Pancam observations show that *tauref* is normally below 0.3. Although the free-running simulation exhibited good agreement with the THEMIS observations globally in "quiet" season (see Figure 5.3), at Spirit landing site, the free-running simulation generally underestimates the dust loadings

during this season. The *tauref* only reaches ~ 0.1 in the "quiet" season at this location. During the dusty season ($L_s = 180° - 360°$), the free-running simulation suggests increase of *tauref* in "Spirit" landing site, but the intensity of increase can not match the intensity of increase in the observation.

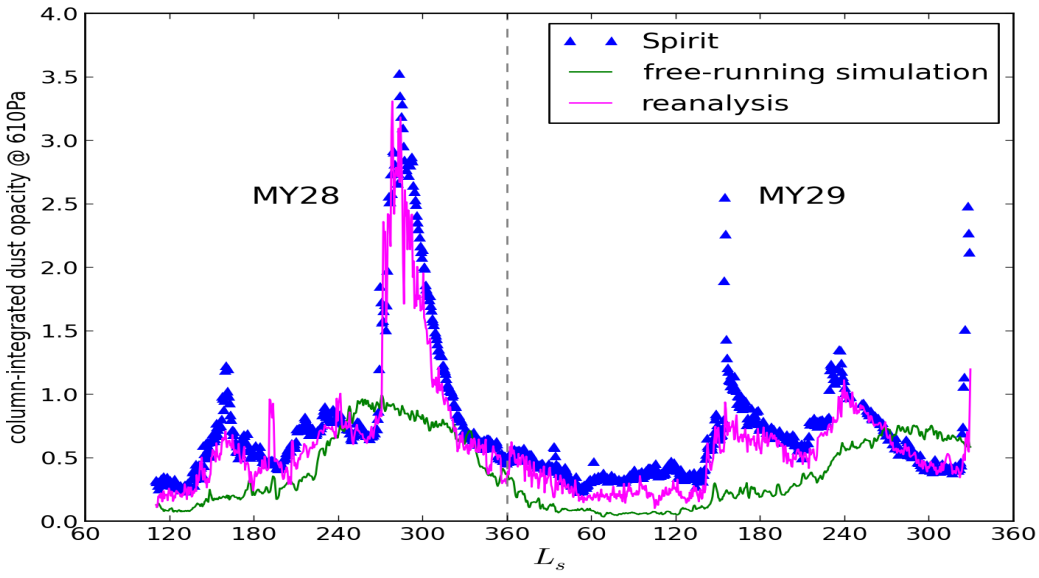

Figure 5.9 The comparison of modeled sol-averaged *tauref* against the observations of the "Spirit" Pancam.

On the other hand, the reanalysis displayed better agreement with the "Spirit" Pancam data than the free-running simulation. It well captures the annual and interannual variability as in the "Spirit" Pancam data. In the "quiet" season, the reanalysis is able to simulate the variation and the magnitude of *tauref* at the "Spirit" landing site, Gusev Crater. Underestimates are mostly seen in $L_s = 60° - 120°$ of MY 29. Afterwards, the reanalysis can capture the increase of dust loadings in $L_s = 140° - 160°$, but not the peak value of *tauref* . The dust events are more active during dusty season, and a GDS is observed in MY 28 when *tauref* reaches 3.5 at the "Spirit" landing site. The reanalysis is thus able to reproduce the simultaneous

initiating events and decays of the episodes of high dust loadings during the MY 28 GDS, and it also reproduces the variability of dust loadings in MY 29. In the reanalysis, the modeled high dust loading has a better agreement with the observations, and appears to capture the variability of *tauref* seen by "Spirit" at Gusev Crater in both "quiet" and dusty seasons. But in the reanalysis, the modeled dust loadings during the first peak of the MY29 ($L_s \approx 160°$) still do not reach the maximum observed by "Spirit". It is worth to noting that although the free-running simulation fails to produce the observed amount of dust in both dusty seasons, it does exhibit a certain degree of interannual variability between these two dusty seasons.

5.5.2. Comparison against the "Opportunity" Pancam

Figure 5.10 shows the *tauref* comparison of "Opportunity" observations (located at Meridiani Planum) and both free-running and reanalysis model data. The observed dust loading at Meridiani Planum has a similar evolution to that seen at Gusev Crater, but with slightly higher values in general with a maximum ~ 4.1 during the MY 28 GDS. Both the free-running simulation and the reanalysis underestimate the peak of MY 28 GDS, though the *tauref* in the reanalysis is obviously closer to the measurements. The reanalysis is also able to better reproduce the observed variability of dust loading in both dusty seasons at Meridiani Planum. The free-running simulation and the reanalysis are both found to underestimate the dust loading at Meridiani Planum in the "quiet" season. However, this mismatch is not raised first in my thesis when making the comparison between the "Opportunity" observations and other datasets at Meridiani Planum.

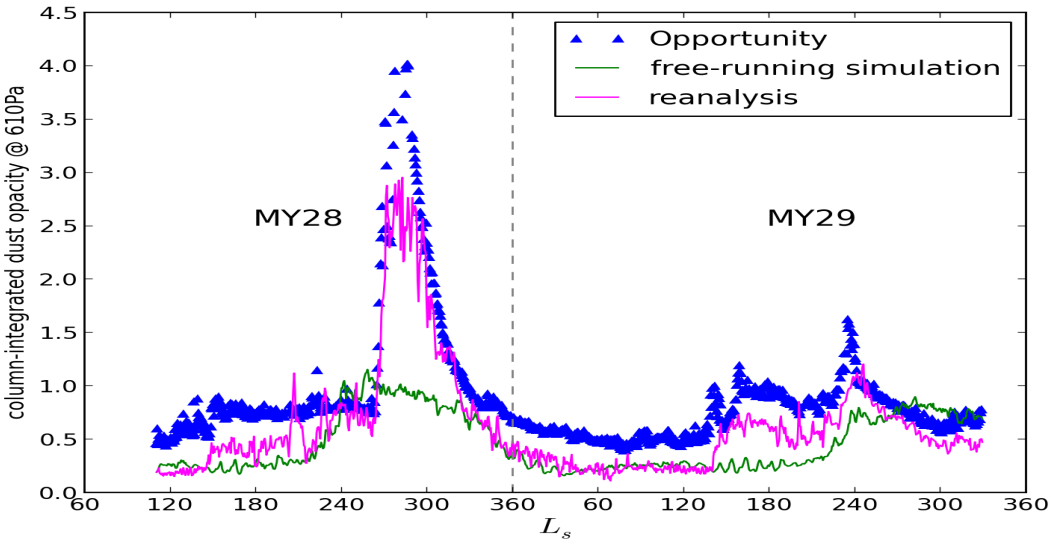

Figure 5.10 The comparison of modeled sol-averaged *tauref* against the observations of "Opportunity" Pancam.

A similar discrepancy was also noticed in earlier studies when making an intercomparison of datasets from different instruments. Montabone et al. [2011a] pointed out that a systematic underestimate of dust opacity over Meridiani Planum in both TES and THEMIS datasets could be found starting from the spring equinox, and this systematic disagreement could reach a factor ~2 during northern summer. They also struggled to explain this difference among their different datasets. Since the THEMIS data assimilated in this study also falls within the period they discussed, it is not surprising to observe the corresponding discrepancy in our reanalysis dataset compared to the "Opportunity" Pancam data. In the latest study [Lemmon et al., 2014], the MERs team also raises problems with Opportunity data ($880\,nm$) at Meridiani Planum around $L_s = 30° - 130°$. This issue remains under discussion at the time of writing until a clear conclusion can be drawn from the intercomparison of different observations.

5.6. Conclusions

In this chapter, an overview of the zonal average of dust opacity within the chosen period ($L_s = 110°$ of MY 28 to $L_s = 330°$ of MY 29) is presented first, and thereafter, the reanalysis of dust from the updated data assimilation system is validated separately against different dust observational datasets that are separate and independent from the assimilated observations. These include the column integrated dust opacity (CIDO) from THEMIS, MCS dust profiles and independent upward-looking surface measurements of CIDO from the MERs mission. The details of the updated data assimilation were described in the Chapter 4. In the rest of this thesis, we only assimilate the dust observations excluding the validating observations discussed in this chapter ($\sim 90\%$ of the total spatial coverage for both THEMIS and MCS dust observations). Those observations includes the THEMIS CIDO data, MCS dust profiles (in the form of layer-integrated dust opacity) and MCS thermal profiles.

The free-running simulation, without any interactive observational constraint, can be tuned (in terms of choosing the dust lifting efficiencies; refer to section 4.3.3) to exhibit a reasonable seasonal variability within a given MY within which the first half of the MY ($L_s = 0° - 180°$) is relatively "quiet", while the second half of the MY ($L_s = 180° - 360°$) is much more dusty. However, the free-running simulation in the form used here fails to reproduce adequately the observed interannual variability of the dust cycle. Instead, the annual pattern of the dust cycle is very similar from year to year.

The reanalysis from the joint assimilation of CIDO and LIDO is also able to recover a realistic variability of dust cycle within a given MY which has a "quiet" season in the first half of the MY and a relatively dusty season in the second half. Moreover, the reanalysis can evidently present a simultaneous initialization and decay of the MY 28 GDS with a promising global average dust opacity magnitude. Since it is difficult to

retrieve directly the complete vertical dust distribution from MCS measurements during the MY 28 GDS, the assimilation approach provides an unprecedented possibility of mapping the four-dimensional dust distribution during the MY 28 GDS through this numerical product. The reanalysis also appears to reproduce a more realistic interannual variability of the dust cycle that exhibited an obviously mild dusty season in the MY following the one with a southern summer GDS.

The full validation of this dust assimilation has been further conducted by comparing the reanalysis against non-assimilated THEMIS and MCS measurements. The correlations show a significant improvement of the dust distribution in the reanalysis compared with the free-running simulation. Generally speaking, the free-running model tends to underestimate *tauref* in current setting mainly during the dusty season. A tendency to underestimate *tauref* can be significant particularly during major dust storm events. The assimilation of dust observations thus serves to greatly reduce the model uncertainty of the dust estimates. Although the free-running simulation appears to reproduce the observed amount of *tauref* during "quiet" season, it still exhibits underestimates in the vertical dust distribution except in the latitude band 50° ~ 90°. This suggests that most of the dusts in the free-running simulation are strongly confined near the ground where it is mostly beyond the bottom of MCS profiles.

In a further demanding test of the dust assimilation approach, fully independent upward-looking surface observations from the MER surface rover missions are also compared with the reanalysis. At the Gusev Crater ("Spirit" landing site) the reanalysis is in better agreement with the observations, and can evidently capture the variability of dust opacity at that location in both "quiet" and dusty seasons. Comparing with the observations at Meridiani Planum (using "Opportunity" Pancam data), the dust loadings in the reanalysis during the dusty season match with the

observations reasonably well. At that location, however, a large discrepancy between surface observations and the reanalysis is encountered mainly during the northern spring and summer. Since the THEMIS data is assimilated into this data assimilation system, this discrepancy is likely associated with a systematic disagreement between the THEMIS and "Opportunity" data, as reported by Montabone et al. [2012]. Thus, it may be the reanalysis produced in the work of this thesis is the best that can be done unless the similar disagreement at Meridiani Planum among different observational datasets can be explained and resolved in future investigations.

Overall, taking the advantage of the observational constraints, the dust reanalysis shows a large degree of improvement in estimating the dust spatial and vertical distributions. This reanalysis is thus able to provide a solution that is consistent to the available dust observations on Mars, and shows considerable potential as a powerful tool to continuously map the three-dimensional distribution of dust in order to study the dust cycle and individual dust raising events.

Chapter 6 Study of a Southward Moving Dust Storm

6.1. Overview

Dust activity is a key component of the Martian atmosphere, and it can greatly change the thermal and dynamical state of the atmosphere during significant dust events. Dust, therefore, is one of the major contributors to the observed climatic variability on Mars, and the distribution of dust also reflects the meteorological conditions and the characteristics of the Martian climatology. Unsurprisingly, studies of dust storms and dust distributions are one of the most important areas of Mars-oriented climate research.

After successfully retrieving Martian atmospheric temperatures from TES observations, Conrath et al. [2000] studied the thermal structure associated with a regional dust storm in Noachis Planum. Smith et al. [2000] and Smith et al. [2001] documented two large regional dust storms and three other less extensive dust storms using TES-observed dust opacities. The initiation, evolution and decay of those dust storms were briefly discussed in their work. Wang et al. [2003] illustrated two southward moving dust storms using MGS observations. The images from the Mars Orbiter Camera (MOC) on-board MGS displayed the moving path of these two

southward moving dust storms that led to the largest dust storm in the first MGS mapping year (MY24, $L_s = 220° - 226°$). They further studied the possible tracks and triggering mechanisms of southward moving dust storms using an off-line Lagrangian particle transport model [Eluszkiewicz et al., 1995] driven by a version of the free-running GFDL Mars Global Climate Model (GFDL MGCM) [Richardson and Wilson, 2002]. Three channels favourable to the development of southward moving storms were identified in their work, namely, Acidalia-Chryse, Arcadia and Utopia Planitias. Hinson et al. [2012] used MOC images to identify a frontal dust storm that would flush southward. They also made a survey of the origins of frontal, flushing and cross-equatorial dust storms during the winter of MY 25 and found that more dust events originated in Acidalia than in Utopia or Arcadia during that period. Based on the Mars Daily Global Map archive, Wang and Richardson [2013] visually identified large dust storms during Mars year (MY) 24-30 including two global dust storms (which happened in the dusty seasons of MY 25 and MY 28). They also discussed the origin, evolution and trajectory of those large dust storms regardless of the thermal and dynamical details of individual events.

In addition to documenting and studying large dust storms, dust vertical distributions on Mars gradually became one of the focal areas in Mars studies when the limb-viewing dust measurements [Kleinbohl et al., 2009] became available to scientists. McCleese et al. [2010] first noticed persistent elevated dust layers from the vertically resolving MCS dust observations [see also Heavens et al. 2011a]. These persistent elevated dust layers were found at least in the night side retrievals of the MCS datasets, and they remained aloft at heights of 15-25 km during northern spring and summer with significant longitudinal variability.

A newly developed data assimilation system for dust observations was introduced in Chapter 4 of this thesis, and was validated against independent observations in Chapter 5. The reanalysis produced from this data assimilation system was then shown to achieve reasonable agreement with the available observations and, moreover, is consistent with the physics represented and parameterized in the UK-LMD MGCM. In this chapter and the following chapter, therefore, I use this reanalysis to provide insights into selected dust events, with the main objective to document the evolution of those dust events in terms of the strength of the dust storm and its thermal structure. Such studies of individual dust cases can also verify the capability of the reanalysis to reproduce the dust events.

In this chapter, a southward moving dust storm is described in detail from its initiation to its dissipation. Apart from validating the reanalysis against THEMIS and MCS data, the dust spatial distribution, the track followed by the dust storm, sources of dust and the associated thermal structure are studied. Other studies have referred to this type of dust storm as a *cross-equator dust storm* [Wang et al., 2003]. In this study, however, we prefer to call it a *southward moving dust storm*, as this study suggests that the initial dust originated from the middle latitude in Northern Hemisphere, but the storm was formed as an isolated system near the equator. Important reasons to study this event include, (a) the dust cloud associated with this storm appeared to travel through one of the important channels connecting the Northern and Southern hemisphere, Utopia-Isidis; (b) the duration of this storm was relatively long, facilitating a detailed study; (c) the THEMIS and MCS datasets provided excellent coverage for the area affected by this moving dust storm; finally, (d) this dust storm was identified simultaneously by visual images [Malin et al.,

2009a; Malin et al., 2009b; Malin et al., 2009c, Malin et al., 2009d] and were thoroughly documented in the study by Wang and Richardson [2013].

6.2. Background to this southward-moving dust storm

This chosen moving dust storm was reported in weekly MRO (Mars Reconnaissance Orbiter) MARCI (Mars Color Imager) Weather Reports (MMWR) [Malin et al., 2009a; Malin et al., 2009b; Malin et al., 2009c], and was noted in three consecutive MMWRs for more than 20 sols. In the MMWR, a detailed commentary was provided on the evolution and trajectory of this moving dust storm. It first formed over Utopia and western Elysium on about 18 July 2009 ($L_s \approx 305.2°$ of MY 29), after which it moved southward along the Utopia storm track down through Isidis and into Hellas (the location of each topographic feature can be found with reference to Figure 6.1). It increased in intensity with additional dust lifting between Hellas and Noachis, and continued to move westward through Noachis. This dust storm then halted in Noachis, but dust was still being continually spread from the storm over Noachis, Hellas, Promethei and part of Cimmeria before the storm started to decay towards 2 August 2009 ($L_s \approx 313.9°$ of MY 29). Even afterwards, however, dust falling out from this dust storm still affected the area until at least 7 sols later [Malin et al., 2009d].

The main tracks followed by dust storms from the Northern to the Southern hemisphere are classified into three main routes; Acidalia, Utopia and Arcadia [Wang et al., 2003; Wang and Richardson, 2013]. Wang and Richardson [2013] also briefly mentioned this moving dust storm in their discussion of the travel routes of dust storms originating in the Northern hemisphere, noting that the path followed by this

dust storm was categorized as passing through Utopia en route from the Northern to the Southern hemisphere.

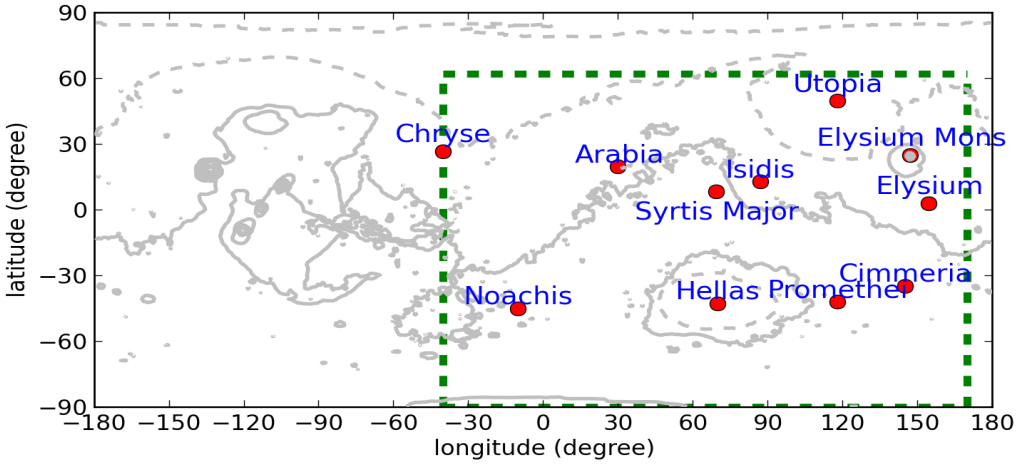

Figure 6.1 The locations of topographic features mentioned in this study. The grey line is the indication of topography with respect to the standard areoid (referred to Figure 1.1, and the topography in following figures should be referred to the same). The green dashed line is the focal area in this reanalysis study.

Both the above studies are based on the visual images taken by the camera onboard the MRO spacecraft, which is insufficient to determine the thermal and dynamical structure of a moving dust storm that travel through one of these major Northern-to-Southern-hemisphere channels. Since it is a long-lasting cross-equatorial dust storm (lasting ~ 26 sols), based on the observational evidence, the long time window makes it possible to examine its structure and evolution in detail throughout its lifetime and moving path. The new reanalysis of dust climatology, introduced in this thesis, is able to provide continuous and high-resolution data records for this aim.

6.3. Study area and availability of dust observations

According to the MMWR, this moving dust storm originated in the Northern hemisphere near Utopia, then found its way to the Hellas and Noachis regions with increasing strength. When it finally came to rest in Noachis before dissipating, the

dust clouds diffused further east. The study area for this moving dust storm, therefore, was chosen to reasonably cover the affected area, including Utopia, Elysium, Isidis, Hellas, Noachis, Promethei and Cimmeria (see Figure 6.1 for the focal area of this study).

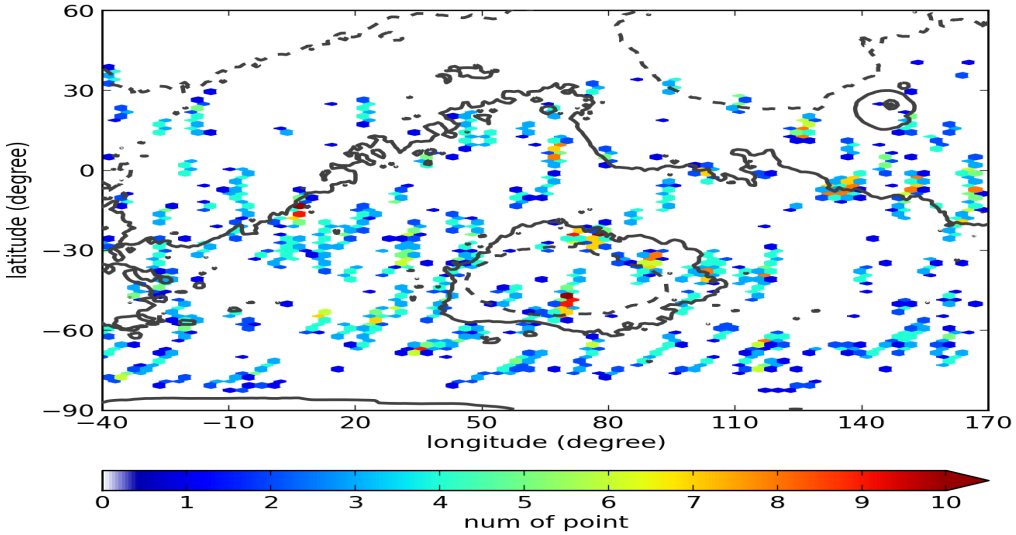

Figure 6.2 The distribution of assimilated THEMIS retrievals of CIDO in longitude and latitude between $L_s \approx 304.9°$ and $L_s \approx 320.9°$. The color shading shows the number of measurements per 3° in both longitude and latitude. The black line is the indication of topography.

The major benefit that makes the reanalysis different from the results of a free-running model is that the reanalysis takes the observations fully into account. Those observations reduce the systematic errors of free-running model along the length of the simulation period. As a result, the performance of the reanalysis strongly depends upon the input data presented to the data assimilation system. The availability of the observations during the lifetime of this dust storm is therefore shown here before I describe the results from the reanalysis.

Figure 6.2 shows the horizontal spatial distribution of assimilated THEMIS nadir-view column-integrated dust opacity (CIDO) in the area affected by the dust storm between $L_s \approx 304.9°$ and $L_s \approx 320.9°$. During this period, the THEMIS data provides reasonable coverage over Hellas and the west of Noachis. This area

corresponds to the track followed by this dust storm in the Southern hemisphere. Between the north of Hellas and Utopia, the THEMIS CIDO data is limited in its spatial coverage. Figure 6.3 shows the horizontal spatial distribution of assimilated MCS limb-viewing dust profiles (for deriving the layer-integrated dust opacity (LIDO) in Chapter 4). The MCS dataset appears to have a more even coverage than that of the THEMIS dataset. It also provides high-density spatial coverage in the study area except for some less intensive measurements between latitude -30° and 0°.

In the data assimilation, the THEMIS CIDO dataset is used to correct the total dust optical depth fields. It is possible that the reanalysis may have relatively large errors in the areas where the THEMIS dataset has poor coverage, such as in Utopia and western Elysium, close to the likely origin of the dust storm as indicated in the MMWR Report [Malin et al., 2009a]. The MCS dataset, in general, only provides information on the dust vertical distribution above at least several kilometers above ground. The more even horizontal spatial coverage of the MCS dataset (Figure 6.3), however, helps to minimize the systematic errors over Utopia and western Elysium resulting from the limited availability of THEMIS data.

The storm's intensity was weak when and where it first formed. Accordingly, its vertical scale was probably quite limited and confined below 10 km. This is likely to have been beyond the lowermost extension (at altitudes of ~ 5-10 km) of the MCS dataset [Kleinbohl et al, 2009]. The spatial constraints of the data mentioned above are therefore likely to limit the ability of the reanalysis to fully represent the real state of the dust storm at its point of origin, but the recovery of its evolution and trajectory across the planet should be more reliable as it grew in intensity and travelled south into places with more observations.

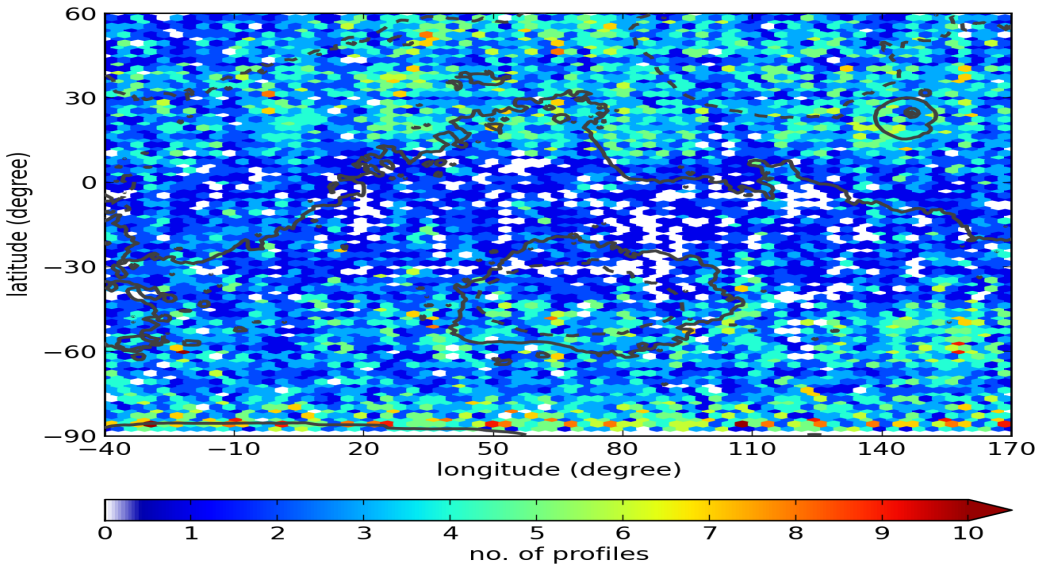

Figure 6.3 Same as Figure 6.2, but for assimilated MCS dust retrievals. The color shading shows the number of retrieved profiles per 3° in both longitude and latitude. The black line is the indication of topography.

6.4. Comparison of the reanalysis with observations

Comparing the model with the raw observations during this dust storm is important to establish if the reanalysis is able to reproduce the general pattern of the dust distribution for this particular event to a precision that lies within the intrinsic uncertainty of the measurements. Since this moving dust storm did not directly affect two operational rovers in the Mars Exploration Rover Mission (MER) at the time, i.e. "Spirit" and "Opportunity", I can only compare the reanalysis with THEMIS and MCS observations. The data fields in the reanalysis were interpolated in time and space to the locations of the observations that fell inside the study domain, the area of which was indicated as the green dashed line in Figure 6.1. Before making a direct comparison, the THEMIS dataset and MCS dataset were multiplied by different factors in order for their optical depths to be equivalent to the visible extinction dust opacity used in the model (as explained in Chapter 4). In order to correct for the leading order effects of the topography, CIDO in both THEMIS data and reanalysis

were rescaled to an equivalent surface pressure of 610 Pa to represent comparable estimates of *tauref* .

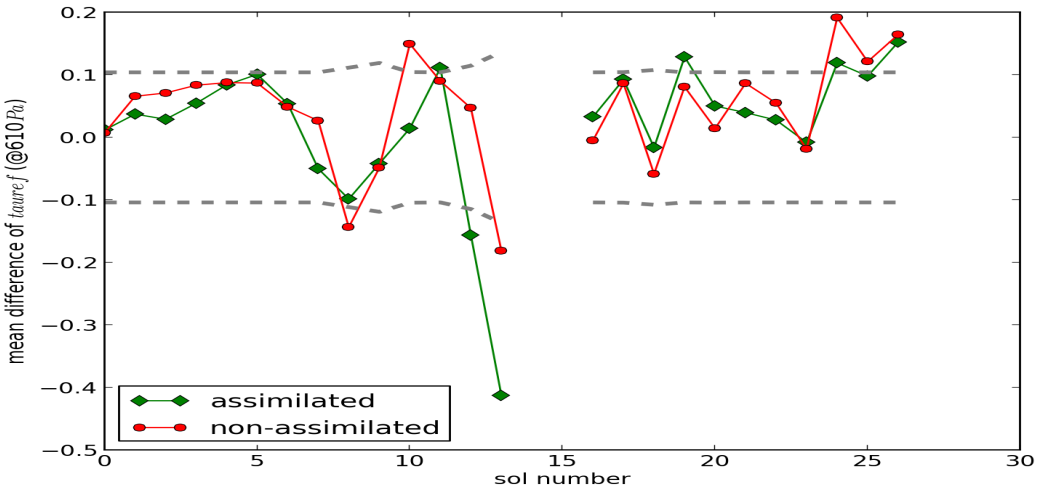

Figure 6.4 Mean differences between reanalysis and THEMIS data inside the study domain, starting from sol 0 ($L_s \approx 305.2°$) at the start of the dust storm to its end at sol 26 ($L_s \approx 320.64°$) according to the MMWR. The green line represents the mean difference between reanalysis and assimilated THEMIS data, the red line is the mean difference between reanalysis and non-assimilated THEMIS data, and the grey dashed lines are the uncertainties of THEMIS dataset. No THEMIS data was available in sol 14 and sol 15.

6.4.1. Validating against THEMIS data

Figure 6.4 shows the mean difference between reanalysis and THEMIS data (both in- and out-of-sample) within the study domain during this dust storm. Sol 0 is chosen to be the first sol ($L_s \approx 305.2°$) mentioned in the MMWR report. Based on our experience with the TES retrievals, the uncertainty of the THEMIS dataset was determined in the work of Smith [2009] as the larger value of 0.04 or 10% of each measurement for the infrared absorption optical depth. In order to correct the uncertainty for comparison with the visible extinction optical depth, this value is multiplied by a factor of 2.6 (explained in section 4.2 of this thesis). An uncertainty value of 0.104 for visible extinction opacity depth is implied, therefore, if the uncertainty is 0.04 for the infrared absorption optical depth. For assimilated THEMIS *tauref* observations (green line), the mean differences between the reanalysis and the

in-sample THEMIS dataset normally remain within or are close to the estimated intrinsic THEMIS uncertainties except during sols 12, 13 and 26. The mean difference decreases to ~ -0.41 in sol 13. Upon comparison with THEMIS data that was excluded from the assimilation, the reanalysis exhibits promising results but the mean differences from these non-assimilated data show slightly larger variations before the decay of the dust storm. Overall, the comparisons suggest that the reanalysis presents a reasonable agreement with both in- and out-of-sample THEMIS data when the dust storm is intensifying in strength. Before sol 7, the reanalysis tends to infer a higher *tauref* , while a larger discrepancy can be seen after sol 7. However, Smith [2004] pointed out that measurement uncertainties could be higher (perhaps 20% of the measurements or even higher) during intense dust storms. So the larger variation of discrepancy does not necessarily mean that the reanalysis produces less representative results when the dust diffuses from the storm to affect a larger area.

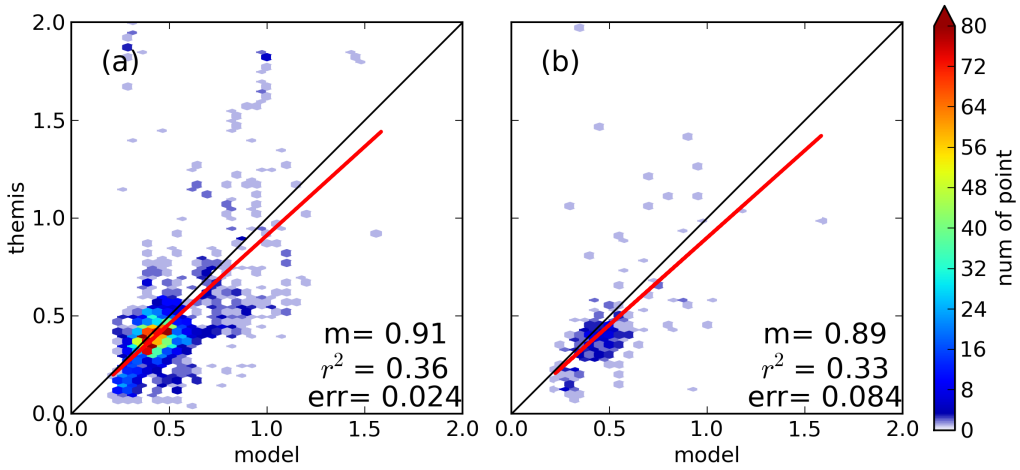

Figure 6.5 Scatter plots of THEMIS-model *tauref* between sol 0 and sol 26 inside the study domain. The color indicates the data density per 0.05 *tauref* . The red lines are the linear least square fit between THEMIS and model. m is the coefficient of the fittings, i.e. the slope of the red lines, r^2 is the coefficient of determination, and err is the standard error of the slope. The black lines represent the lines with coefficient 1. (a) scatter plots between reanalysis and assimilated THEMIS data, (b) scatter plots between reanalysis and the non-assimilated THEMIS data.

The scatter plots between the reanalysis and the THEMIS datasets (in- and out-of-sample) are shown in Figure 6.5. Most of the data assimilated in the reanalysis took values between 0.3 and 0.5 (see Figure 6.5a). Comparison with assimilated THEMIS data shows better agreement than the comparison with non-assimilated THEMIS data. In general, however, both comparisons display a good correlation with either THEMIS dataset during this dust storm.

6.4.2. Validating against MCS data

To compare with the MCS dust data, the results in the reanalysis are interpolated into pressure levels as in the MCS dust retrievals, and the average of the dust opacity is taken for each profile over different pseudo-height ranges, i.e. 0-10 km, 10-20 km, 20-30 km, 30-40 km and 40-80 km. The difference of the average of dust opacity is calculated between the reanalysis and the MCS dust retrievals in each pseudo-height range for each profile.

Figure 6.6 shows the average difference between the reanalysis and corresponding raw MCS data. In general, the MCS dataset has its largest absolute observational errors in the lower atmosphere, with uncertainties decreasing with height. Both the comparison with in-sample (assimilated) observational data (Figure 6.6a) and with non-assimilated (out of sample) data (Figure 6.6b) suggest a reasonable recovery of the dust vertical distribution in the reanalysis, with the (signed) differences falling within or very close to the intrinsic observational errors. The reanalysis even seems to exhibit a slightly smaller difference in the comparison with the non-assimilated (out of sample) data. In both comparisons, the model shows a tendency to underestimate dust opacity at each height except near 30-40 km. The largest underestimate is ~

0.0005 km^{-1} in the 0-10 km height range, while the smallest underestimate is below 0.0001 km^{-1}. The overestimate in the 30-40 km band is ~ 0.0002 km^{-1}.

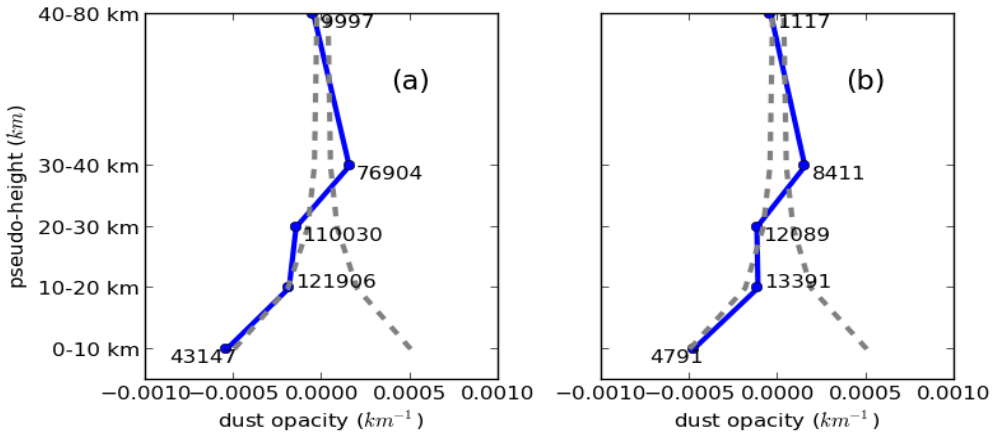

Figure 6.6 Average difference between reanalysis and in-sample or out-of-sample MCS data within the study domain. The blue line shows the average difference, grey dashed lines represent the intrinsic observational errors, and the numbers are the numbers of data points available in each height range. (a) for assimilated MCS data, (b) for non-assimilated MCS data.

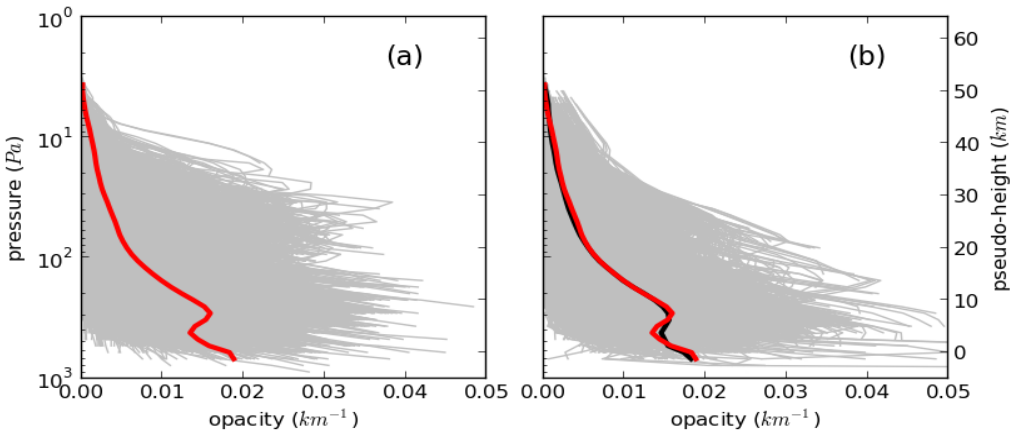

Figure 6.7 Ensemble of profiles corresponding to the assimilated MCS profiles inside the study domain between sol 0 and sol 14. (a) the raw MCS profiles that were assimilated (grey lines) and the average profile (red line), (b) the profiles from reanalysis corresponding to the MCS profiles in (a). The red line is simply the average of the MCS profiles as in (a) and the black line is the average of the grey lines in (b). An average of the profiles is only taken when the number of profiles is larger than 30.

Ensembles of the raw MCS profiles within the study domain are also compared to the reanalysis here. The comparisons are based on two periods, namely, the development phase of the dust storm (between sol 0 and sol 14), and the decay phase (between sol 15 and sol 26). During the development phase there were 11146 profiles

assimilated into the reanalysis (Figure 6.7) while 1238 raw profiles (Figure 6.8) were withheld from the assimilation. For the average of the assimilated profiles (red lines in Figure 6.7a & b), the maxima of the dust opacity distributions are found in the lowest part of atmosphere, such that the dust opacity decreases until ~ 400 Pa. The typical profile reaches a second maximum near 250 Pa. The ensemble of profiles from the reanalysis (indicated by the black line in Figure 6.7b) suggests the reanalysis provides a good representation of the MCS profiles and reproduces the shape of the average of the MCS profiles, though slightly underestimates *tauref* within the two

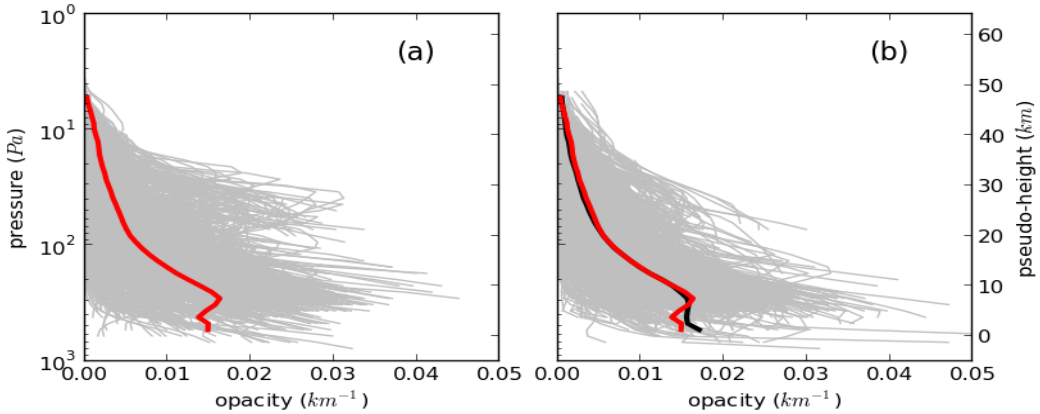

Figure 6.8 Same as Figure 6.7 but for the non-assimilated raw MCS profiles.

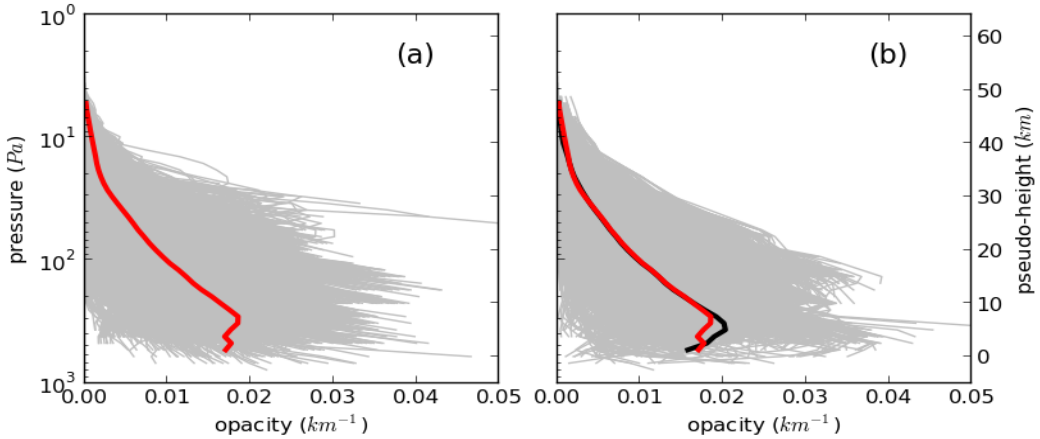

Figure 6.9 Same as Figure 6.7 but for the period between sol 14 and sol 26.

peaks below 100 Pa. For the average of the non-assimilated (out of sample) MCS profiles (shown as red lines in Figure 6.8a & b), the profile also displays a second

peak above the ground. The ensemble of the profiles from reanalysis (black line in Figure 6.8b) shows a reasonable shape compared to the raw MCS observations (red line in Figure 6.8). Below the 300 Pa level, the reanalysis tends to overestimate dust opacity. However, it does not exhibit a clear second peak above the ground, unlike the raw MCS observations (red line). Instead, a well-mixed feature can be seen between 300 Pa and 500 Pa before the profile decreases again.

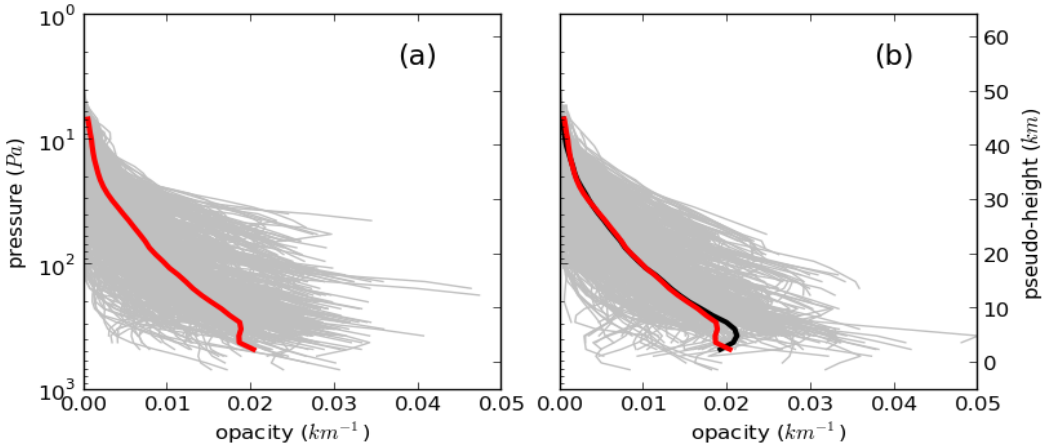

Figure 6.10 Same as Figure 6.8 but for the period between sol 14 and sol 26.

During the decay phase, the observations were taken with a lower data density, with just 6042 profiles assimilated into the reanalysis (Figure 6.9a) and 665 profiles withheld from the reanalysis (Figure 6.10a). The average assimilated profiles (red lines in Figure 6.9 a & b) showed a peak at ~ 300 Pa, which resembled an "inversion" as the dust normally reduces with height. The reanalysis was successfully able to capture this "inversion". Above ~ 300 Pa, the ensemble profile in the reanalysis (black line in Figure 6.9b) well represented the features of the assimilated raw profiles. The peak, however, appeared to be placed lower at ~ 400 Pa with a higher opacity. In comparison with the non-assimilated raw profiles (Figure 6.10), the ensemble profile in the reanalysis also reached its maximum at ~ 400 Pa where the

average of non-assimilated observations showed a well-mixed signature extending from 450 Pa up to 300 Pa.

6.5. Temporal evolution of the horizontal dust distribution

Figure 6.11 shows daily average maps of the distribution of *tauref* obtained in the reanalysis during the lifetime of this moving dust storm. As before, sol 0 here refers to the time ($L_s \approx 305.2°$) when this dust storm was first mentioned in the MMWR. The lifetime of this dust storm was ~ 26 sols, during which it changed its intensity dramatically three times along its moving track, i.e. in sol 2, sol 5 and sol 8 before it finally reached its peak.

In sol 0, dust accumulated in western Elysium and to the south of Elysium Mons and *tauref* reached values of about 0.5. A clear path of dust transport was noticeable to the southwest of this high dust opacity spot. By sol 1, the intensity of the highest dust opacity spot in the previous sol had already reduced, as dust was continuously transported southwest. The majority of the dust then started crossing Isidis and arrived to the north of Hellas, while another stream of dust moved southward towards Cimmeria but with less intensity. In sol 2, the high dust opacity to the north of Hellas intensified. A noticeable concentration of dust then emerged from the surrounding area, and *tauref* associated with this dust storm went on to reach values above 0.6. In sol 3, the intensity of dust storm appeared to weaken slightly, and the peak *tauref* reduced below 0.5 so that dust became more diffuse in the region to the north of Hellas. The dust in Elysium, close to the possible origin of this dust storm, seemed to

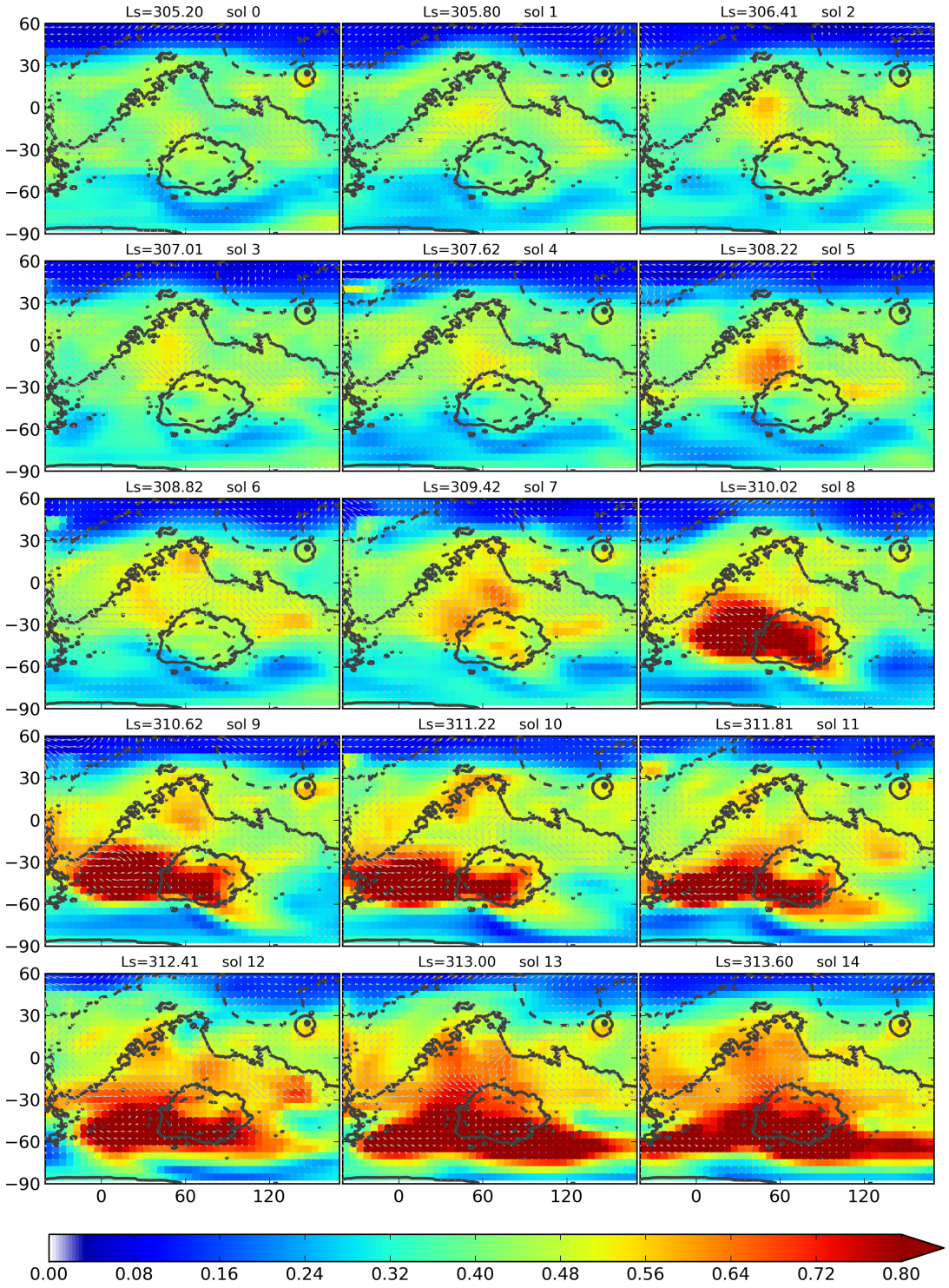

Figure 6.11 Spatial maps of the daily-averaged vertically-integrated *tauref* within the study area. Sol 0 corresponds to the sol ($L_s \approx 305.2°$) when this dust storm was first reported in the MMWR. The arrows in each map indicate the wind velocity at the lowest model level (at altitude ~ 4 m). The black line is the indication of topography with 4 km interval (referred to Figure 1.1).

clear compared to the previous sol. The center of the dust storm moved southward towards the northern border of Hellas in sol 4, as the winds from the northeast and northwest tended to form a converging zone over northern Hellas. The affected area of this dust storm was smaller but it remained at a similar intensity to that of sol 3. However, the peak *tauref* increased again in sol 5, and the size of the dust storm grew. The dust storm seemed to regain its strength in this sol. However, in the following sol (sol 6), the main dust center split into two. One moved further north close to Isidis while the other one shifted slightly to the northwest of Hellas acquiring a stripe shape. The dust layer also extended to cover part of the Hellas. One sol later (sol 7), the winds favored pushing the two centers towards the border of Hellas, and the wider associated dust veil accumulated more over Hellas with *tauref* > 0.5. In the next sol (sol 8), several dust centers appeared to join together and intensify significantly. The dust storm had now grown to cover an area with a size of 90° zonally and 45° meridionally. Meanwhile, the peak *tauref* reached above 0.8. The wind fields to the western border of Hellas formed a cyclonic pattern (NB now in the southern hemisphere), with stronger winds coming from northwest and weaker winds from the south and east. The dust storm continued to move southwest, eventually arriving at Noachis in sol 9. The affected area of the dust storm had now expanded to become larger than 100° in the longitudinal direction with additional dust emerging from the Chryse region, and the cyclonic wind patterns can now be seen more clearly. Additional dust clouds were also observed at this time near the southern border of Arabia and to the east of Elysium Mons. In the following two sols (10 and 11), the dust storm extended further in the east-west direction and its shape became narrower in the north-south direction. More dust crossed to the west of Noachis, and distributed itself to the southeast of Hellas. The southward wind also became more dominant in

the main storm center that was located between Noachis and Hellas. In sol 12, the storm moved southward beyond -60° latitude, and a dust veil spread out from the storm center while more dust was also carried from the north of Hellas by the prevailing wind. The main dust storm became more diffuse during sol 13 and sol 14, and the center of this moving dust storm proceeded to move eastward to settle near Hellas. By this point the dust storm stretched extensively in the east-west direction, and dust continued to be distributed away from the storm center to cover most of the area between the northern border of Hellas and polar region. Additional dust was also observed to gather between Arabia and Hellas.

The dust clouds in the east and west parts of the dust storm started to separate from the main storm in sols 15 and 16. The storm then began to lean in a northeast-southwest direction during sol 17 and extended south into the polar region. The storm continued to stretched into the polar region while slowly travelling east during sols 18 to 20, and additional dust was transported from the northwest, from outside of this study domain, into the north of Noachis during these sols. From sols 21 to 23, the dust storm appeared to move eastward faster than before, and began to dissipate so that it gradually affected a smaller area. The additional dust coming from the area outside of this study domain cleared away during this time, but new dust clouds could still be observed emerging in Arabia. By sol 24, the dust storm had already become very diffuse, although more dust continued to be advected from the Arabia region after going through the Chryse channel. In the following sols 25 and 26, large areas were dominated by dust concentrations travelling with the southwestward prevailing wind, especially from Isidis and Elysium. Dust clouds from previous travelling dust storm still contributed to the highest *tauref* in the region, but only within a narrowly confined band in the polar region.

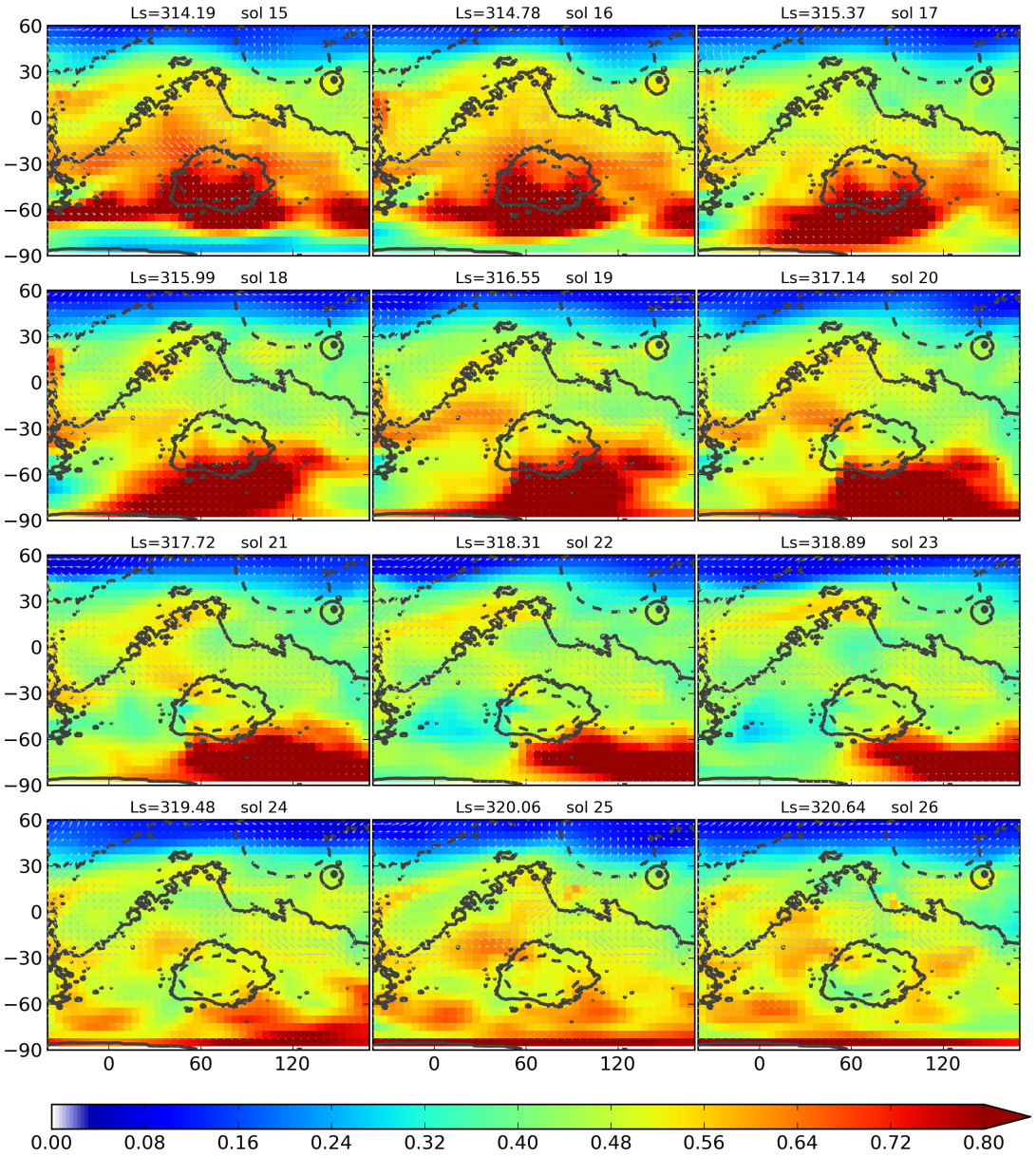

Figure 6.11 (continued).

6.6. Tracking the motion of the dust storm in the reanalysis

According to the comparison between reanalysis and observations (Section 6.4), the reanalysis appears to represent the evolving dust distribution reasonably well. The daily-averaged *tauref* maps, therefore, also represent a reasonable record of the evolution of this moving dust storm. One of the particular advantages of using reanalysis in this way is that it is possible to quantitatively track the travel route of a

migrating dust storm, such as the one presented in the previous section, which is what we now examine here.

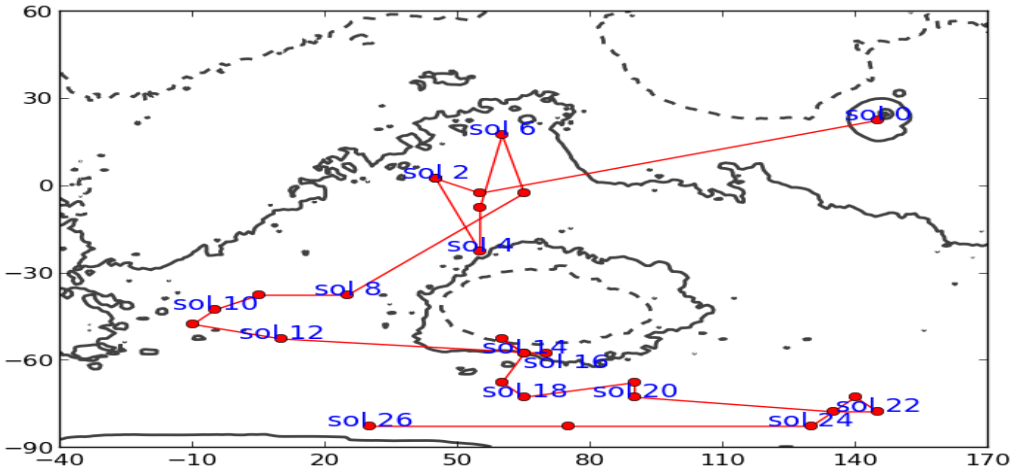

Figure 6.12 The route followed by the main center of the moving dust storm discussed in Section 6.5. The red dots represent the locations of the storm center in each sol. The sol number refers to the sol number used in Figure 6.4, labeled in 2 sol intervals. The storm center was at the same location in sols 2 & 3, so only one point is shown representing these two sols. The black line is the indication of topography with 4 km interval (referred to Figure 1.1).

To quantitatively record the location of the dust storm at each sol, the shape of the dust storm is schematically assumed to be of rectangular shape. When this dust storm first formed near Elysium, the storm size was significantly smaller compared to its size after crossing the equator. I, therefore, arbitrarily vary the size of the rectangle during these two periods to track the location of this moving dust storm. From sol 0 to sol 2 (here and hereafter, sols are numbered with reference to the sol number used in Section 6.4.1), the size of the rectangle is defined as 3×3 grid cells, equivalent to 11.25°×11.25° in latitude and longitude. Starting from sol 3, the size of the rectangle representing the dust storm extent is then increased to cover 9×9 grid cells, equivalent to 33.75°×33.75° in latitude and longitude. The rectangle with the highest average *tauref* is then taken as the location of the storm, and the grid cell with the highest *tauref* within that rectangle is referred to as the center of the dust storm. The dots

shown joined by the red line in Figure 6.12 thus correspond to the trajectory followed by the center of the dust storm as identified by the method above. Although the size of the rectangle is defined arbitrarily, changes of the assumed size (at least varied it from 1×1 to 15×15 grid cells) of this region would not affect the route plotted here dramatically, except for sol 0 when the area with the highest *tauref* was confined to a rather small region in the initial state. However, provided the size of the rectangle for sol 0 lies between 1×1 and 3×3 grid cells, this moving path still remains the more or less the same as shown in Figure 6.12.

Figure 6.12 shows the path followed by the moving center of this dust storm, as identified in the reanalysis. In sol 0, the dust storm center was located in Elysium Mons. Dust was then transported downwind towards the southwest (sol 0 in Figure 6.11). When the intensity of the dust source in Elysium Mons decreased in sol 1, the high values of *tauref* in the downwind area that was to the north of Hellas at this point immediately became the effective storm center. The location of this dust center was slightly to the south of the equator at ~ -2.5° latitude. From sol 2 to sol 3, the storm center moved back into the Northern Hemisphere (~ +2.5°) and stayed at more or less the same location for these two sols. By sol 4, however, the storm center proceeded to move across the equator again towards the northern border of Hellas (~ -22.5° latitude). As discussed above the dust storm then intensified in sol 5 and, when it split into two centers in sol 6, the stronger one was located near the border of Arabia in the Northern Hemisphere. This stronger center then crossed the equator in the following sol. When the two storm centers joined together in sol 8 (see Figure 6.11), the new storm center was then located further south, ~15° to the west of Hellas. From sol 8 to sol 11, the dust storm center continued to move progressively westward, arriving at the most westward point near Noachis in sol 11. After sol 11, the path of

the dust storm center was seen to reverse into an eastward direction with accelerating speed. After the storm started to dissipate in intensity, its center stayed near the southern border of Hellas between sols 14 and 20. The storm center then moved into Cimmeria in sol 21, and stayed in that region for 4 more sols until sol 24. In sols 25 and 26, the storm had already begun to decay as a narrow east-west band (see Figure 6.11), so that the points for these two sols only represent the centers of an area with highest average *tauref* within this narrow band.

We see, therefore, that the travelling path of this dust storm could be separated into four main phases, each accompanied by a significant change of speed. The storm center was originally located near Elysium in sol 0, and then relocated to the north of Hellas in sol 1. The storm center then stayed around Syrtis Major until sol 7. Another big move of the dust storm happened in sol 8 when the dust storm center moved towards the west of Hellas. After this, the dust storm center travelled slowly within this area until sol 12. In sol 13, the storm center had already moved eastward towards Hellas. The last big move happened in sol 21, and the storm center was then located in Cimmeria for 4 sols before the storm eventually dissipated as a narrow band in polar region. It is admitted that the way of tracking the storm traveling is very simple here. The dust storm may not be a coherent system along its path showed here. However, it is rather difficult to define an isolated dust storm analogous to the synoptic storm on Earth. It is possible that the changing location of the dust storm is the sequential initiation of discrete lifting events instead of the physical movement of the dust storm as a coherent system. This remains a major issue for understanding the Mars dust cycle and the evolution of individual dust events.

6.7. Evolution of peak storm opacity

As for the trajectory of the motion of this dust storm, the evolution of the peak opacity at the storm center could also be grouped into four stages. In the first stage (from sol 0 to sol 5), dust was transported from its possible origin in Elysium and the center remained between Arabia and Hellas until the dust cloud formed a clear shape in sol 5. *tauref* at the dust storm center also reached its maximum during these 6 sols at this early stage (see Figure 6.13). In the second stage (from sol 6 to sol 7), the well-defined storm split into two (see Figure 6.11), and the stronger dust center weakened during these two sols (see Figure 6.13, which shows the peak value of *tauref* at the storm center on each sol). In the third stage (from sol 8 to sol 11), the two separate storm centers combined and moved westward (see Figure 6.11), and the dust storm went on to reach its maximum opacity (with *tauref* ~ 2) in sol 10 (see Figure 6.13), one sol before it arrived at the farthest westward point of its path. From sol 11, when it actually arrived at its farthest westward point, the strength of the dust storm center then started slowly to decay, though still had a peak value of around *tauref* = *0.7* by the end of sol 26.

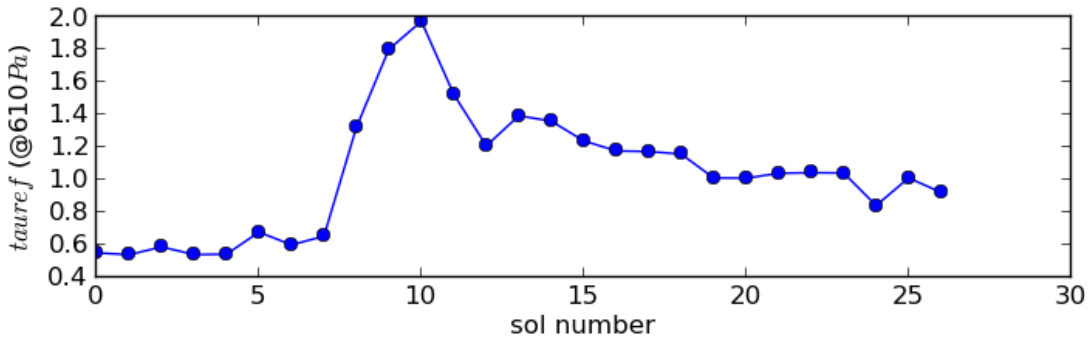

Figure 6.13 Peak value of *tauref* at the dust storm center, as identified by the method described in Section 6.6.

6.8. Evolution of the thickness of dust layers

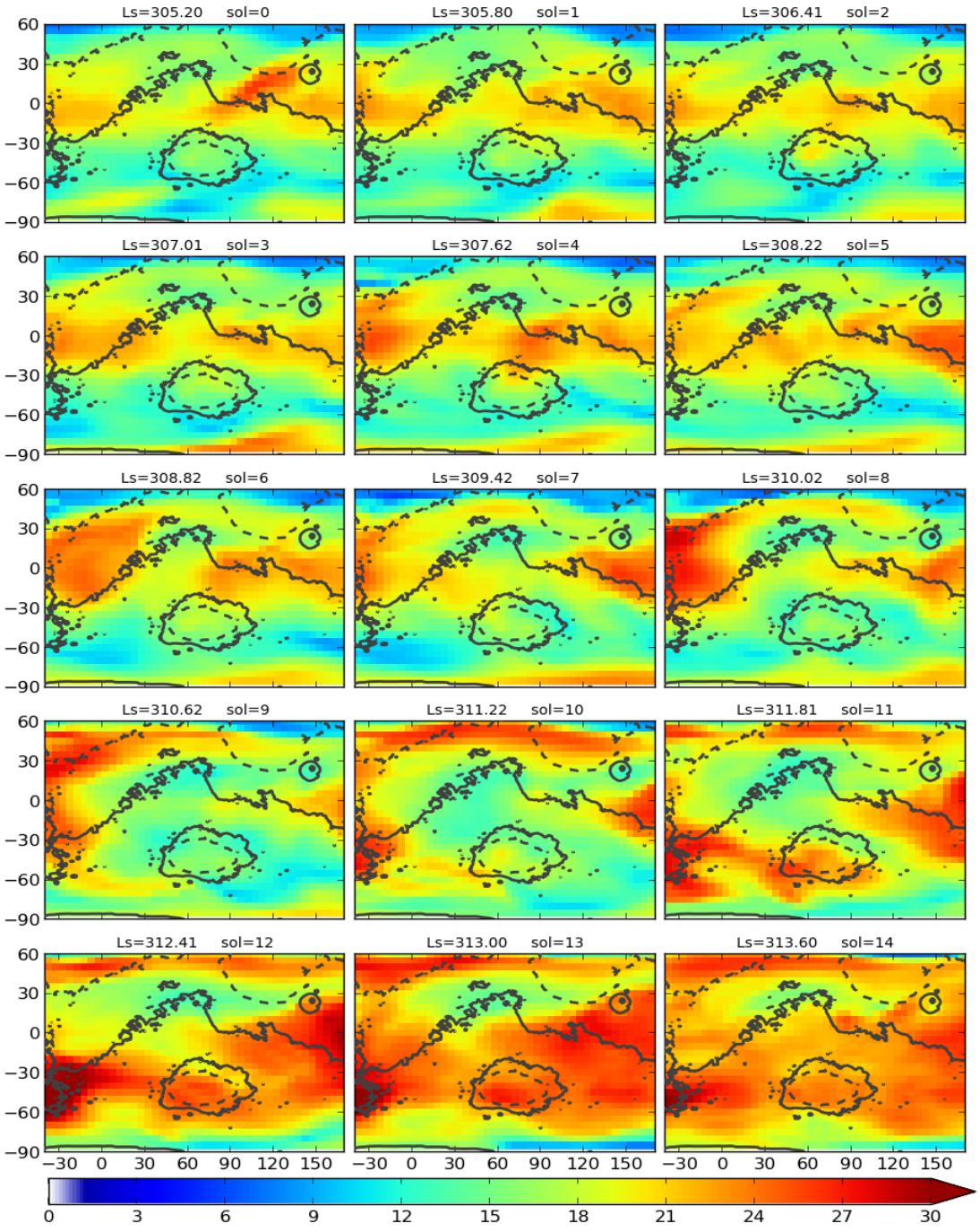

Figure 6.14 The maps of the daily-average h_d (km) of the dust layer top from the ground.

The profile information from MCS observations allows us to recover not only the varying total column dust opacity in our reanalysis but also the vertical distribution of the dust during the course of the storm. Figure 6.14 shows the maps of the daily averaged height (h_d) of the dust layer top from the ground in the study domain. The

dust layer top h_d is determined as the height from the ground below which it contains 90% of the total column mass of dust particles. Along the storm path, the h_d during the present storm in question reached ~ 30 km when the storm originated in Elysium in sol 0. Those high dust tops, however, became lower (~ 22 km) in the following 3 sols (to sol 3). It was possible that dust was transported upwards without accumulating too much in the lower atmosphere in the sol 0. The lower h_d suggested

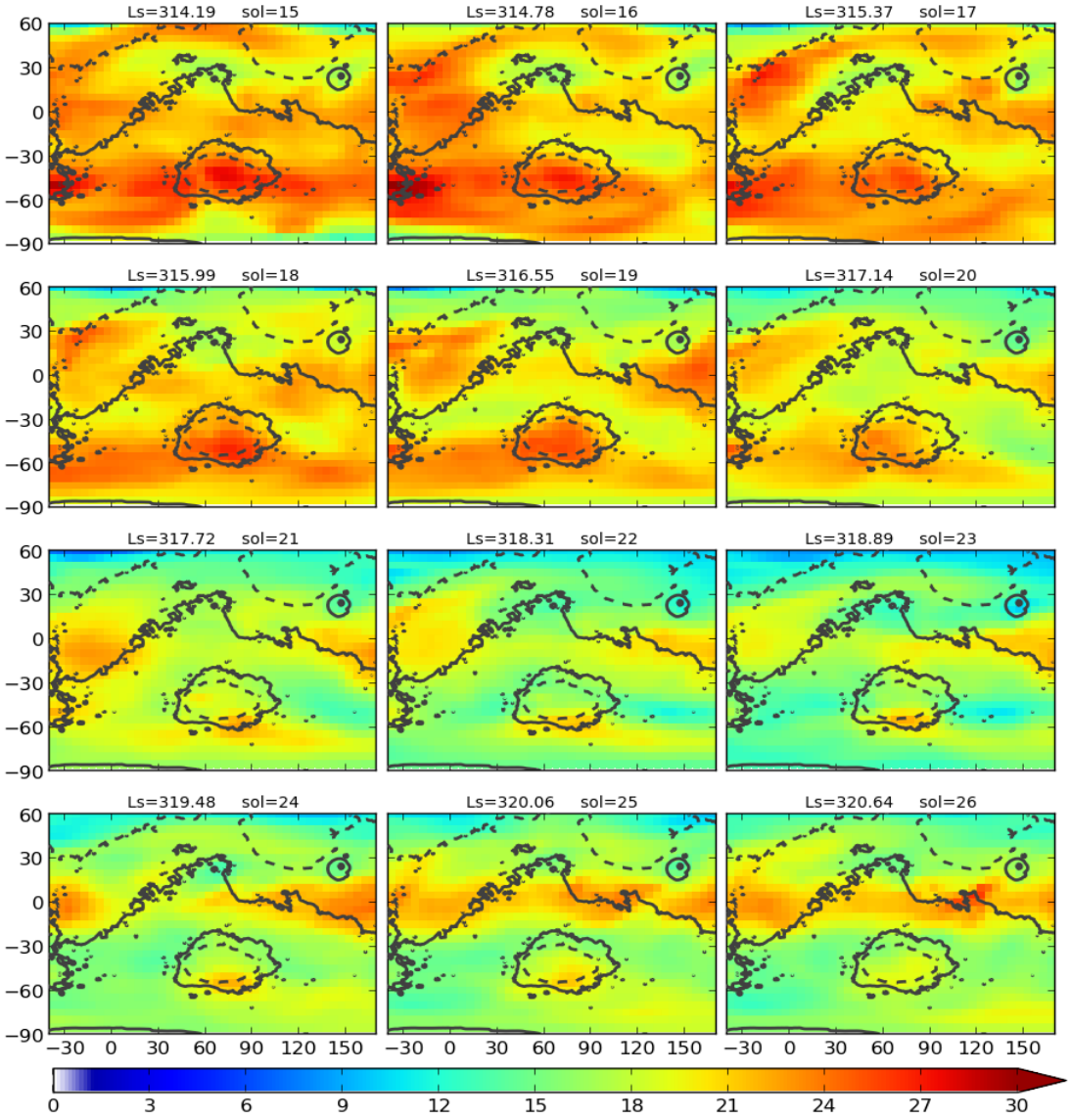

Figure 6.14 (continued).

that the dust became more condensed in the lower part of the atmosphere, when the storm appeared to be a more confined system. In sol 4 and 5, the h_d increased again to ~ 27 km. After that, the dust storm center split into two with a h_d at 20 km in sol 6. When these two centers came closer in sol 7, the h_d increased slightly.

When the dust storm intensified and became well confined in sol 8 (see Figure 6.11), h_d only increased from ~ 9 km to ~ 14 km in the south of the storm, but decreased from 21 km to 13 km near the storm center shown in Figure 6.12, west of Hellas. This suggests that the increased amount of dust accumulated mostly below 13 km so that the mass was more condensed close to the ground, leading to a smaller h_d. Meanwhile, h_d in the polar region decreased from ~ 22 km to ~ 18 km, which also corresponded to a decrease in *tauref* in this region (see Figure 6.11). The gradual increase in h_d from sol 9 to sol 11 also indicated the influence of additional dust being advected in from Chryse. The dust layer top height then increased in the direction from west to east of Noachis, eventually reaching ~ 29 km in this area. From sol 11, h_d increased over the whole study domain. In sol 13, the dust tops over Noachis and Elysium were slightly lower, but the area between 15° and -45° latitude were all covered by dust with h_d ~ 23 km. From sol 9 to 14, a narrow band with relatively large h_d (~ 27 km) could be noticeable to the north of 50°, and this was likely to be a feature of elevated dust layer associated with the additional dust near the winter polar vortex. This was also evident in the zonal anomaly of dust opacity shown later in this chapter (Figure 6.19 in section 6.10.) Until sol 15, the h_d reduced with the strength of the dust storm, but the h_d in the polar region increased from ~ 16 km up to ~ 22 km, with the incursion of the moving dust storm. After sol 17, the h_d in polar region slowly descended following the dust layer top altitudes near Hellas. When the dust storm eventually dissipated near Cimmeria at sol 26, h_d in the polar region still

remained at ~ 19 km. It is worth noting that in sol 24-26 when the dust storm had already been quite diffuse, a narrow band with h_d > 22 km was consistently available near the equator. This also corresponded to the elevated dust that could be seen in the Figure 6.20 of section 6.10.

6.9. Sources of dust in the study domain

In this reanalysis, there are only three different ways that are represented to inject dust into the model simulation. These include the parameterized physical pathways, namely, wind stress lifting and dust devil lifting, and (arguably non-physical) reanalysis increments, which artificially inject or remove dust to correct the model dust fields towards observational data by the assimilation of observed dust properties.

Dust lifting is an important process for producing various dust-transporting events, although wind stress lifting or dust devil lifting, which are relatively crudely parameterized in the numerical model, may exhibit large variations compared to the real environment. Unfortunately, this information is difficult to quantify in the current method of making and analyzing observations. The model here, with the analysis of temperature and dust, however, may provide some insights into the likely location and intensity of dust lifting associated with a moving dust storm, such as the one under investigation here. The reader should be cautioned that the wind stress lifting and dust devil lifting in the model were tuned to produce reasonable interannual variability of global average dust loading in a free-running UK-LMD MGCM (see section 4.3.3 of this thesis), though not intentionally for this moving dust storm event. It may require more efforts and complication in future to assess the relative strength of this tuning in the reanalysis.

Figure 6.15 shows a set of daily maps of the wind stress lifting rate (in units of $kg \cdot m^{-2} \cdot s^{-1}$) indicated at each model gridpoint. In sol 0, active wind stress lifting could only be seen to the northwest of Utopia. This would suggest that wind stress lifting local to this region might not be directly linked to the origin of this moving dust storm. However, between sol 9 and sol 12, additional dust arriving from the Chryse region does appear to have a strong connection to local wind stress lifting, as active lifting could be seen to the north of Chryse just prior to this period. Active local wind stress lifting was also apparently responsible for the additional dust seen in Arabia between sol 15 and sol 18. A patch of dust injected by wind stress lifting could also be observed over Isidis, which was clearly responsible for the small amount of dust seen to travel over Isidis in sols 25 and 26.

Dust devil lifting was more active in the reanalysis during this dust event (see Figure 6.16). Dust devil lifting is normally associated with an area subject to intense solar heating, usually between latitudes -45° and 45°. In this season of Southern Hemisphere summer, the strongest heating occurs between latitudes -30° and 0°. As a result, a band with consistently stronger dust devil lifting is observed during the daytime at latitudes close to ~ -30°. Dust devil lifting was very active near Isidis and to the west of Elysium between sol 0 and sol 2. It seems possible then, that the moving dust storm studied here was at least partly associated with dust devil lifting during its initiation. It is also evident that dust devil lifting played an important role in increasing the intensity of this moving dust storm. When the dust storm was located around the area to the north of Hellas, *tauref* associated with this storm was seen to increase gradually. This area also corresponded to the band of active dust devil lifting in the reanalysis at this time. It is possible, therefore, that dust devil lifting might have partially contributed to the significant growth of the atmospheric dust loading from

sol 7 to sol 8, when the dust storm happened to travel through the band with the strongest dust devil lifting in the study domain (between -20° ~ -30°).

However, the major reason to reproduce this sudden increase in dust loading in the reanalysis was an injection from increments within the data assimilation scheme itself (explained below). This suggests that the physics modeled by UK-LMD MGCM failed to reproduce this sudden increase in dust loading. The dust devil lifting was certainly not the main reason for this increase, and it is likely that the model failed to simulate some strong wind stress lifting events and/or dust transport which could be responsible for this strong increase. Obvious dust devil lifting could also be seen to the north of Chryse during this event, and this also suggests that dust devil lifting also contributed to the source of additional dust from the Chryse region. In sol 25, more dust was apparently lifted by dust devils over Isidis compared to the previous sol. Although the intensity of lifting was smaller than that due to wind stress lifting (see Figure 6.15), the dust lifted also probably contributed to the additional dust loading in the area (see Figure 6.11).

It is interesting to note the negative feedback associated with parameterized dust devil lifting. Newman et al. [2002a] noted that the reduced thermal contrast between surface and air due to increased dust levels in the atmosphere would lead to the shutting down of the dust devil lifting. This negative feedback started to be evident when the dust storm became stronger in sol 5. A zone of inhibited dust devil lifting (ZIDL) appeared ~ -10° latitude to the north west of Hellas, corresponding to the location of the dust storm in sol 5. The ZIDL became less clear during the following two sols, as the dust storm split into two weaker storms. Between sol 8 and sol 12, a narrow stripe of ZIDL could be seen associated with the dust storm within the area between Hellas and Noachis. When the dust storm spread out zonally to cross the

study domain in sol 13, a ZIDL appeared to the south of ~ -40° latitude which corresponded to the area of the storm. The main areas of dust devil lifting were activated again across ~ -45° latitude in sol 18 until the dust storm shrank into a confined shape.

In this reanalysis, the third means of injecting dust into the numerical model simulation is through the data assimilation procedure itself, where dust observations deviate strongly from the dust field predicted by the model. For the dust assimilation, two observational datasets, the THEMIS CIDO and MCS LIDO data, provided information to activate the possible dust injections in this reanalysis. These two datasets are fundamentally different, and so they influence the model simulation in different ways. At each analysis time step, the increments $\Delta\tau_{col}$ to the dust column at each model gridpoint (for THEMIS CIDO data) or at each model gridpoint and model level $\Delta\tau_p$ (for MCS LIDO data) are produced. For the THEMIS CIDO data, the increments correspond to the CIDO, rescaled to a surface pressure of 700 Pa. For the MCS LIDO data, the $\Delta\tau_p$ increments correspond to the LIDO between each two adjacent model levels. In order to produce the total dust injection/removal at each model gridpoint comparable to the spatial maps of dust distribution, these two different increments need to be converted to a quantity that is possible to compare with *tauref* . The increments $\Delta\tau_{col}$ due to THEMIS CIDO data can be simply rescaled to 610 Pa to be comparable to *tauref* (refer to Eq. 4.2). For the increments $\Delta\tau_p$ due to MCS LIDO data, the increments in different layers are first summed up vertically. The sum, which is the vertical-integrated increment, $\Delta\tau_{col}$, is then rescaled to 610 Pa according to the local simulated surface pressure ($\Delta\tau_{ref,}$ similar to Eq. 4.3). The resulting quantities are thus both comparable to *tauref* . Afterwards, both increments,

one due to THEMIS CIDO data and one due to MCS LIDO data, can be summed up to give the total increment to be applied to *tauref* (denoted as $\Delta\tau_{ref}$ here).

Maps of the daily total positive and negative analysis increments to *tauref* are shown in Figure 6.17 and Figure 6.18, respectively. From sol 0 to sol 7, the background *taurefs* were in general above 0.4 (see Figure 6.11), and the increments were relatively small ($|\Delta\tau_{ref}| \leq |0.04|$) and well scattered across the study domain. In sol 0, no substantial dust injection through assimilation increments was evident near Elysium where the dust accumulated to form the growing dust storm. Mild dust injection increments could be seen at this time in Isidis, the downwind area of Elysium. This would seem to imply that the initiation of the moving dust storm was likely to have been generated spontaneously by the UK-LMD MGCM without needing the direct intervention from data assimilation increments. In sols 1 & 2, no consistent dust injections or removals were found near the area surrounding Hellas, but positive increments were seen corresponding to the high dust spots. From sol 4, dust increments started to become significant especially in the South Polar Region. Compared to the prevailing background dust level ($tauref \geq 0.5$), however, the dust amounts injected by assimilation were not substantial in the moving path of the storm. Mild dust increment injections near Hellas continued until sol 7. In sol 8, dust was heavily injected by the data assimilation scheme to the west of Hellas, and the strength of opacity induced by this injection was up to ~ 0.2. During the same sol, the dust storm was observed in the reanalysis to increase its intensity significantly (see Figure 6.11). Thus, dust injection by the data assimilation scheme appeared to be mainly responsible for this sudden growth. In sol 9, the data assimilation scheme continued adding a considerable amount of dust into the dust storm, though the affected area was much smaller than in the previous sol. The injection/removal

became smaller again in sol 10, when the dust storm started to stretch zonally. In sol 11, when the model attempted to transport dust further west towards the west of Noachis, the data assimilation scheme tended to remove some of that dust.

From sol 12, the path followed by this dust storm reversed from southwestward-moving to eastward-moving (see Figure 6.12). The data assimilation increments seem to have played a key role in this reversal of direction. It continued to remove dust during sol 11 in Noachis, while increasing the dust opacity in the eastward-moving direction. The data assimilation scheme continued to inject dust into the direction of travel of the dust storm in sol 13, and excess dust was removed in the South Polar Region. During the early decay phase of this moving dust storm (from sol 15 to sol 19), the dust injections and removals became relatively small ($|\Delta\tau_{ref}| \leq |0.06|$) again. The data assimilation scheme seems to have mainly worked on gently adjusting or "nudging" the dust distributions towards the observations within the dust storm. The scattered increments in sol 20-22 were simply the result of limited MCS data. When those limited data was available near the location of the dust storm in these sols, the simulated dust loadings still appeared to be reasonably consistent with the observations. From sol 24 to 26, the assimilation struggled to modify the dust in the polar region close to Argyre and Noachis. These large increments (positive and negative) were more associated with the dust coming from the north near the boundary of this study domain. Only in sol 24 of these 3 sols, slightly large negative increments ($\Delta\tau_{ref} \sim -0.07$) could be found near the location of the storm, the south border of Hellas (see Figure 6.11), showing that the assimilation assisted the model to remove the dust. After sol 24, the negative increments became mainly limited to the polar region close to Argyre and Noachis. The general mild increments (from sol 15 to 26) suggest that the UK-LMD MGCM was actually spontaneously producing a

reasonable representation of the true dust distribution during the decay phase of this moving dust storm, when the dust evolution was largely dominated by simple advection and sedimentation.

6.10. Vertical cross sections of the dust storm

In addition to the fields already presented above, the reanalysis is also able to provide continuous vertical cross sections to study the evolving vertical structure of the dust storm. Since the dust storm might only appear in part of the study domain at any one time, different longitudes were chosen at different times to produce the vertical cross sections. Figure 6.19 presents the zonal anomaly between longitudes -30° and +90° during sols 0 to 14, while Figure 6.20 shows the same for longitudes between +30° and +170° during sols 15 to 26. From sol 0 to sol 1, the positive zonal anomaly of dust opacity was mainly below the 100 Pa level between latitudes -60° through 45°, though the values were all relatively small (~ 0.003 km^{-1}). The dust storm did not intrude into the Hellas region until sol 7, so that a negative zonal anomaly of dust opacity could always be seen below 700 Pa between -35° and -55° latitude. In sol 3, the positive zonal anomaly between latitudes 15° and 45° seemed to become negative close to the ground, this corresponded to the southward travel of the dust storm. Below ~ 50 Pa, the temperature anomaly also closely corresponded to the dust anomaly, such that temperatures appeared to be warmer than the zonal average when increased dust loading existed. By sol 3, the strength of the zonal anomaly of dust opacity had reduced to below 0.002 km^{-1}, but the dust distribution was more diffuse compared to the previous sol. This can also be noticed in Figure 6.11. *tauref* over the dust storm also became more diffuse in sol 3 than in sol 2. The temperature

anomaly close to the ground became more homogeneous along with the diffusing dust. In sol 5, the area with a positive anomaly of dust opacity grew larger, when the dust storm intensified near the northern edge of Hellas (see Figure 6.11 for *tauref* in sol 5). In sol 8, when a well-defined dust storm formed by combining two separated storm centers together to the north of Hellas, a 2 K warm anomaly could be found at the same latitude, expanding up to ~ 50 Pa in the vertical direction.

In the following sols, the positive zonal anomaly of dust opacity extended to above 10 Pa until sol 14. The associated warm anomaly of temperature always reached its maximum higher up in the atmosphere (above ~ 100 Pa) instead of near the ground, where the anomaly of dust opacity was usually the highest. Below this warm anomaly, at the bottom of the dust storm, a slight cooling could be seen with an anomaly of ~ -2 K. This amplitude is consistent with the cooling effect associated with the MY 25 global dust storm discussed by Cantor [2007]. In the latitudinal direction, this positive anomaly of dust opacity moved southward towards the South Polar Region associated with the southward movement of the dust storm. The warm anomaly associated with the dust storm center increased to 4 K in sol 10 and continued to last for at least a further 5 sols. As the dust storm moved southward, the area associated with a cold anomaly over the South Polar Region was squeezed continuously by the heating with increasing dust concentration. A region with a cold anomaly was always seen above the positive zonal anomaly of dust opacity after sol 8. It is interesting to note that dust appeared to be depleted over tropics (with a negative anomaly of dust opacity between 100 Pa and 10 Pa) when the dust storm intensified at levels below this depletion (from sol 6 to sol 10). This negative anomaly (with color shades between 100 Pa and 10 Pa) above appeared to become smaller when the dust storm weakened (from sol 11).

However, further investigation is required to understand fully the relationship between positive zonal anomalies of dust opacity and the corresponding negative anomalies lying above. Along with the southward movement of the dust storm during its dissipation, the zonal anomalies of dust opacity and temperature associated with the storm also moved towards the South Polar Region from sol 15 to sol 16. The zonal anomaly of dust opacity appeared to have two peaks above the dust storm (see Figure 6.20). One of the centers slightly detached from the bottom one, and could be seen after sol 16. This suggests that the dust storm vertical structure became looser and less coherent as some dust spread out from the bottom of the storm. Nevertheless, this higher altitude dust positive anomaly could still lead to a ~ 2 K temperature anomaly in the layers between 100 Pa and 10 Pa until the storm finally decayed in sol 26.

6.11. Summary and discussion

In this chapter, the reanalysis obtained using the methods developed in this thesis was applied to study the evolution of a southward moving dust storm that began around 18 July 2009 ($L_s \approx 305.2°$ of MY 29). The long duration of this mobile dust storm provided an excellent opportunity to explore the capability of the reanalysis to study individual regional-scale dust events.

The reanalysis was first validated against THEMIS and MCS observations during this dust event. With ~ 90% of THEMIS data being assimilated into the reanalysis, the mean differences between the reanalysis and THEMIS data (assimilated and non-assimilated data) were usually found to remain within the observational errors of THEMIS. As anticipated for any successful scheme, the reanalysis displayed a strong correlation with the observed amounts of dust. The comparison between reanalysis

and MCS observation also indicated good agreement between these two datasets. The mean differences were in general smaller than or very close to the MCS observational errors and uncertainties. During the development phase (sol 0 to sol 14) of this dust storm, the reanalysis appeared to well represent the ensemble of assimilated MCS profiles in the study domain. However, the reanalysis missed a second peak in the vertical as found in the non-assimilated observations. During the decay phase (sol 15 to sol 26), the reanalysis was then more successful in reproducing this "inversion", as evident in the ensemble of assimilated MCS profiles, but it missed the well-mixed layer in the ensemble of non-assimilated MCS profiles. This implies that the reanalysis might still reproduce an imperfect vertical distribution of dust regard of current setting. The reanalysis in general displayed similar features of observed ensemble of assimilated MCS profiles, especially when more observed dust profiles were available in the development phase than in the decay phase. However, the recover of the vertical ensemble of non-assimilated dust profiles suggested that the model physics was struggling to simulate the observed structure. This mismatch might partly result from the simple sedimentation due to the one-size assumption in the dust transport scheme (discussed in the section 2.5 of Chapter 2).

Although the daily MMWR gave a rough description of this southward moving dust storm, based on sequences of visual images, the reanalysis provided unprecedented insights into how this cross-equator storm developed along its evolving path. Its route across the planet was able to be determined quantitatively through analyzing the spatial maps of daily-averaged *tauref* . Along its travelling path, the *tauref* at the storm center was found to reach ~2.0. Four-dimensional reanalysis could also depict how high the dust cloud penetrated during the evolution of this storm. Before this dust storm, the dust layer tops were normally seen to reach to heights of ~12 km from the

ground, whereas this storm was seen to transport dust up to altitudes as high as ~ 30 km before it finally dissipated.

The maximum of the zonal warm anomaly associated with this particular dust storm normally occurred near the top of the storm. Along with the growth of this dust storm, a cooling effect was observed near the ground that increased to ~ 2 K which was of a similar magnitude to what was found during the MY 25 global dust storm. Dust depletion was found above the tropics when the storm grew to a certain intensity, and this depletion increased its strength as the storm grew.

The three sources of dust injection in this reanalysis were also explored to investigate how this storm was generated. In this analysis, the initial disturbance surprisingly appeared to be at least partly provided by dust devil lifting. Dust devil lifting was evidently rather active near the origin of this storm and downwind from the area where the storm initiated. A weak signature of the ceasing of dust devil lifting could be found as the dust storm passed through. Wind stress lifting appeared to play a less important role during this event. It mainly seemed to provide some additional dust from outside of the study domain and contributed to the dust left after the storm dissipated.

In this particular event, the UK-LMD MGCM was found to simulate a reasonable evolution of this dust storm from sol 0 to sol 7, since the data assimilation scheme only needed to apply relatively mild increments in this period. However, significant increments were found in the reanalysis when the separated storm centers joined together and grew intensively in sol 8. The UK-LMD MGCM also required the "help" from data assimilation scheme in sol 12 when the dust storm reversed its route to move towards the east. After that, mild increments were mainly found necessary in the South Polar Region to gently adjust the dust distribution within the dust storm.

This suggested that UK-LMD MGCM alone seemed capable of reproducing a reasonably realistic decay for this mobile dust storm. Despite this apparent success, the UK-LMD MGCM still needed some significant corrections to be applied by the data assimilation scheme at several critical points in the storm evolution, for instance, in sol 12, at the reversion of the track of the moving dust storm. Nevertheless, the gentle amplitude of the increments applied in most of the sols during this period provides evidence that the UK-LMD MGCM was able to project a reasonable development of this dust storm and realistically capture most phases of its life cycle apart from a few points when large errors were found.

To our knowledge, this is the first application of a reanalysis to study a real dust event on Mars. This application not only provides confidence in utilizing this dataset to study real dust events with continuous coverage in time and space, but also documents in some detail the four-dimensional multivariate development of this particular dust storm, revealing some fine structure associated with such a southward moving dust storm. Of course, this reanalysis might still contain errors that exceed the observational uncertainties, since it clearly missed the "inversion" in the ensemble of raw dust profiles. Beyond this thesis, therefore, some further tuning of the data assimilation scheme and improvements to the physical parameterization schemes may be required to fix those issues here.

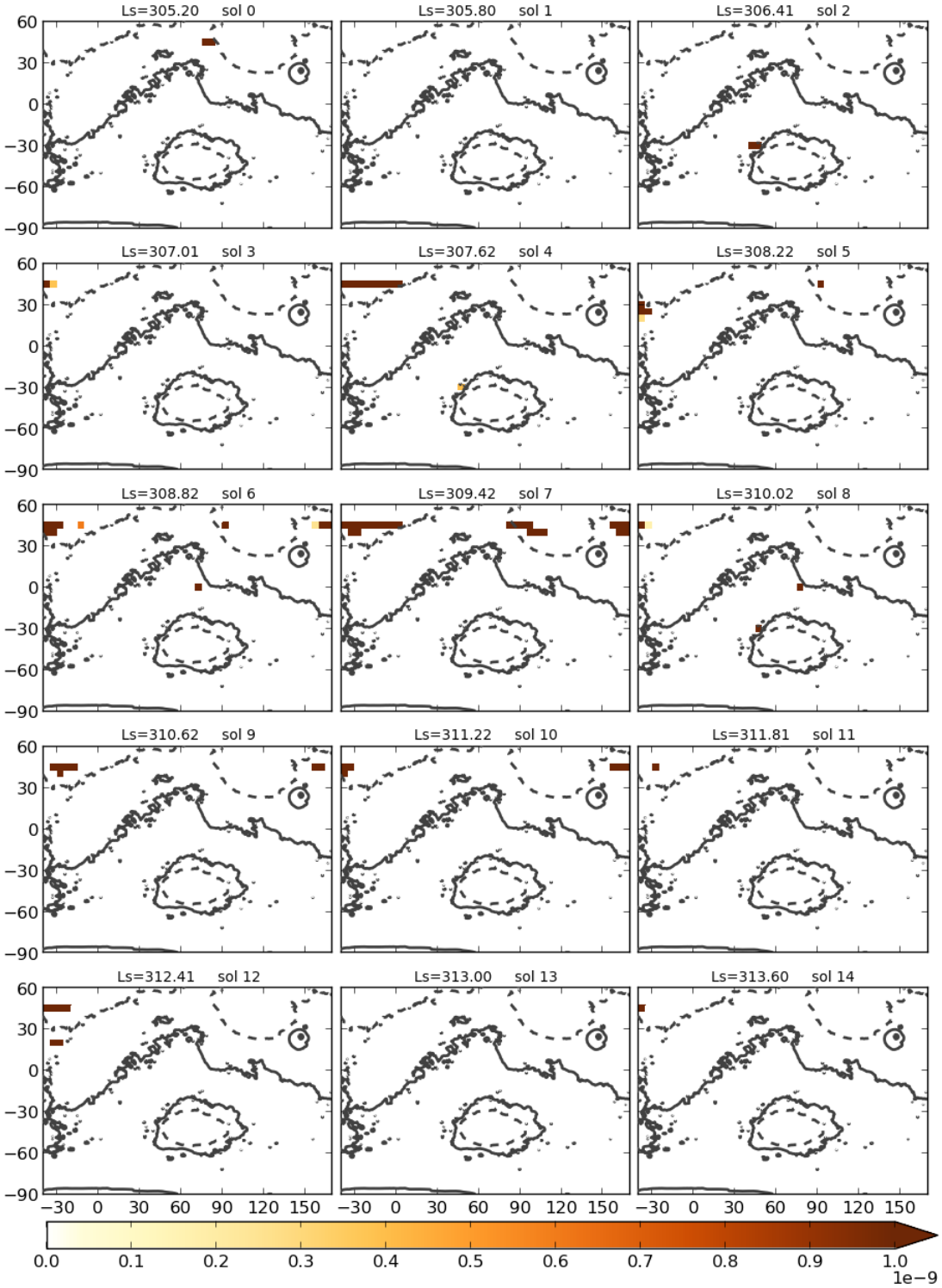

Figure 6.15 Maps of the daily average wind stress dust lifting rate (in units of $kg \cdot m^{-2} \cdot s^{-1}$) derived from the reanalysis of THEMIS and MCS data.

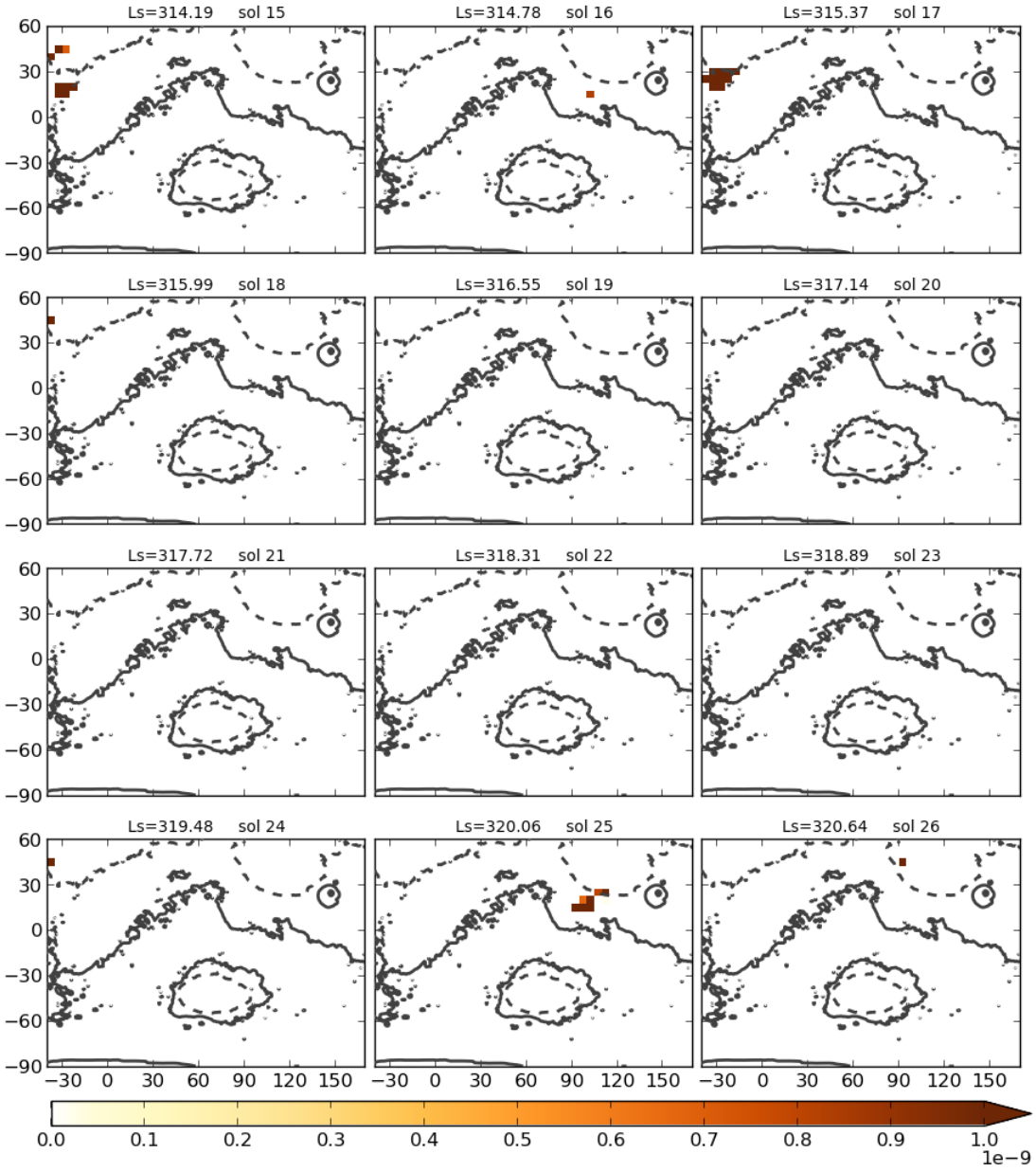

Figure 6.15 (continued)

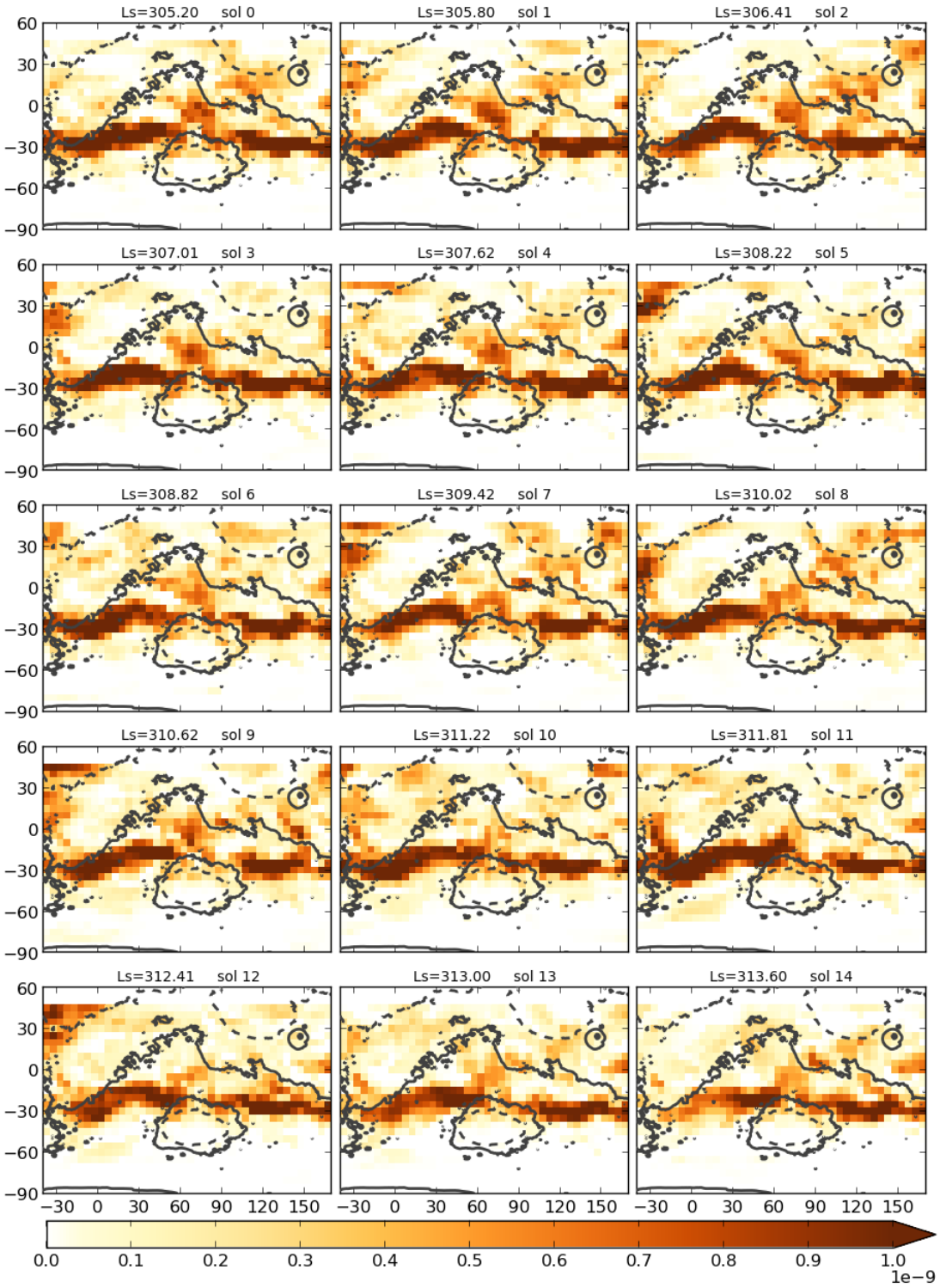

Figure 6.16 Maps of the daily average dust devil lifting rate (in units of $kg \cdot m^{-2} \cdot s^{-1}$) in the reanalysis of THEMIS and MCS data.

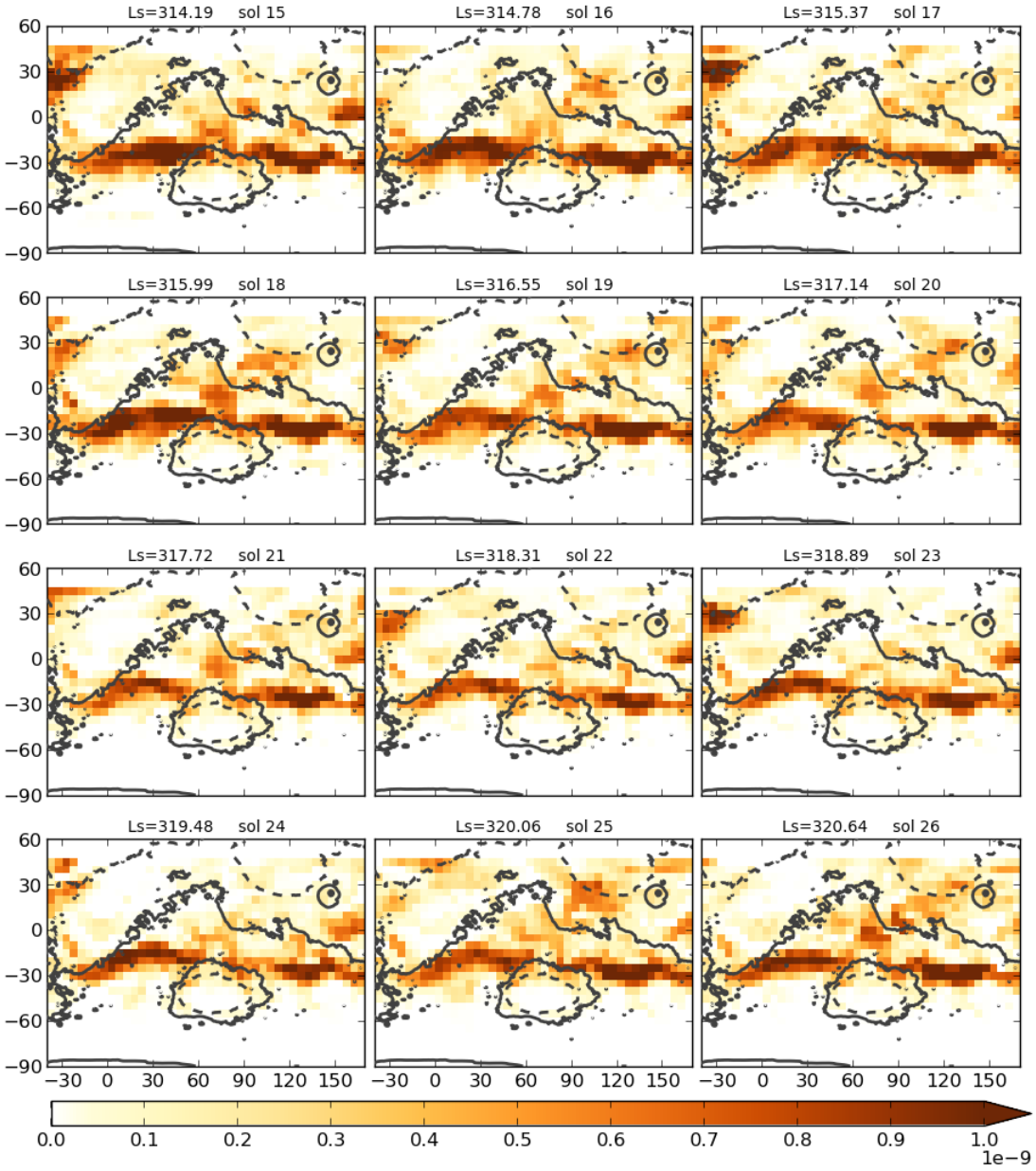

Figure 6.16 (continued)

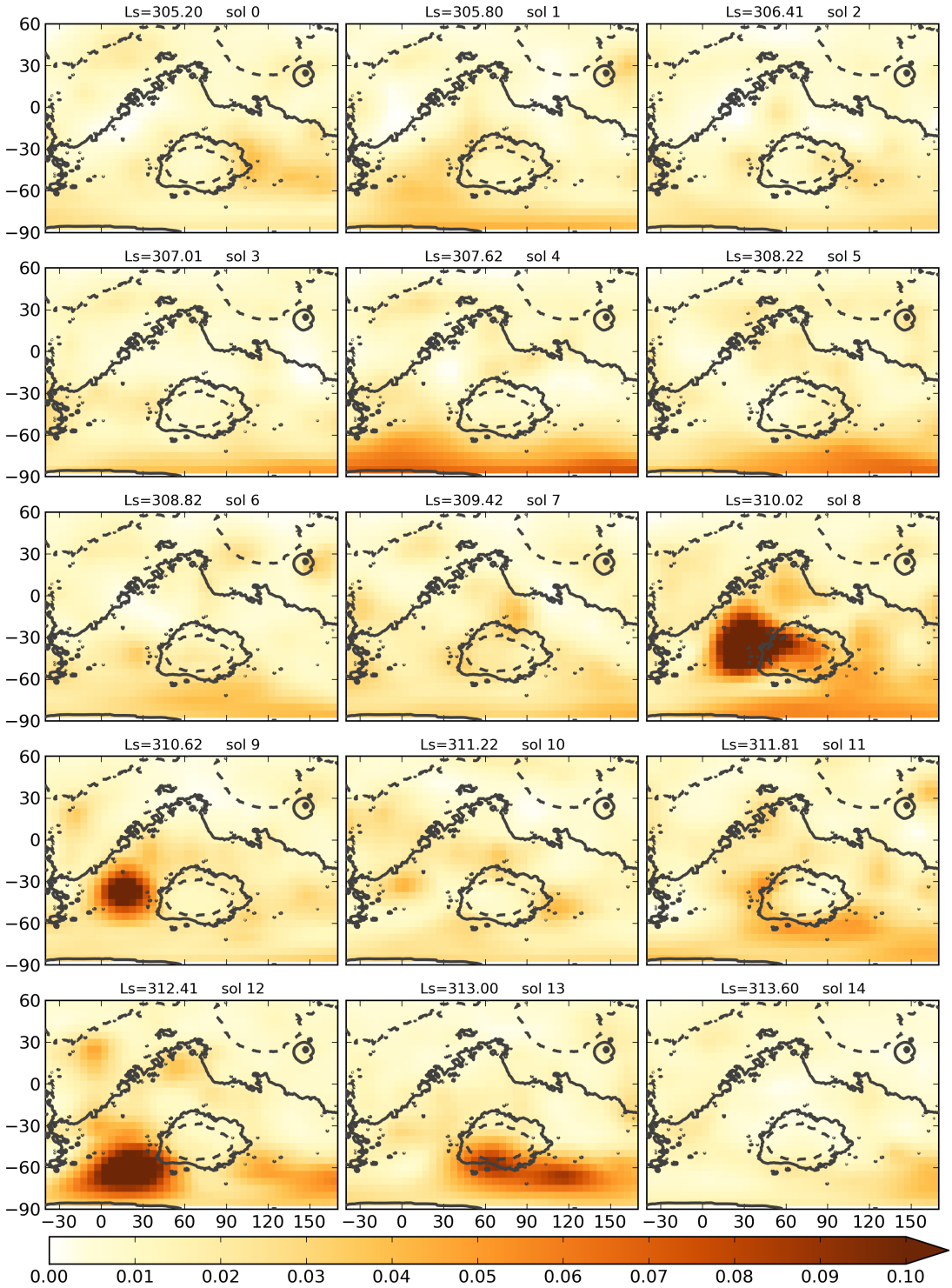

Figure 6.17 Daily total positive analysis increments to *tauref* during the course of the reanalysis of THEMIS and MCS data.

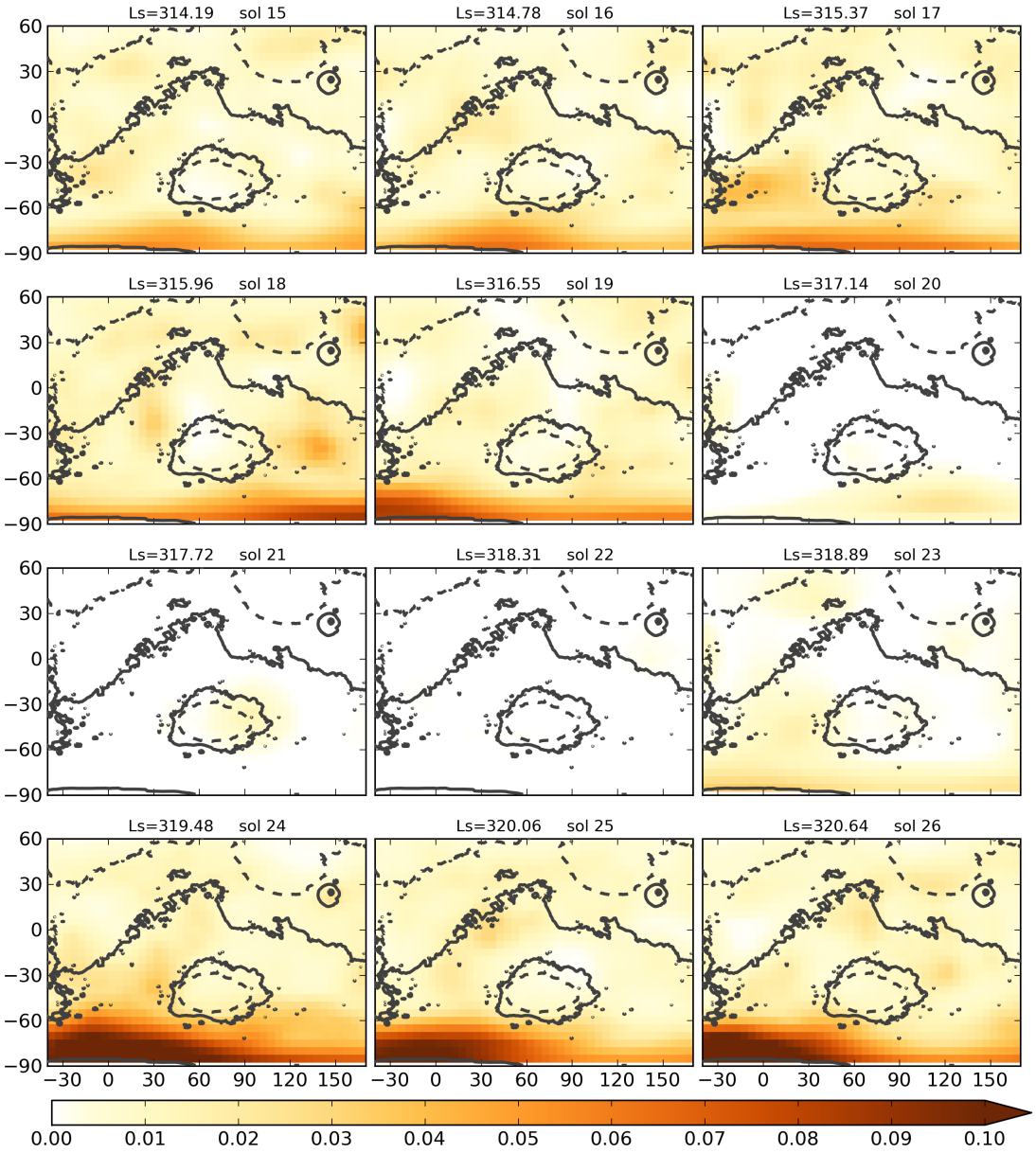

Figure 6.17 (continued)

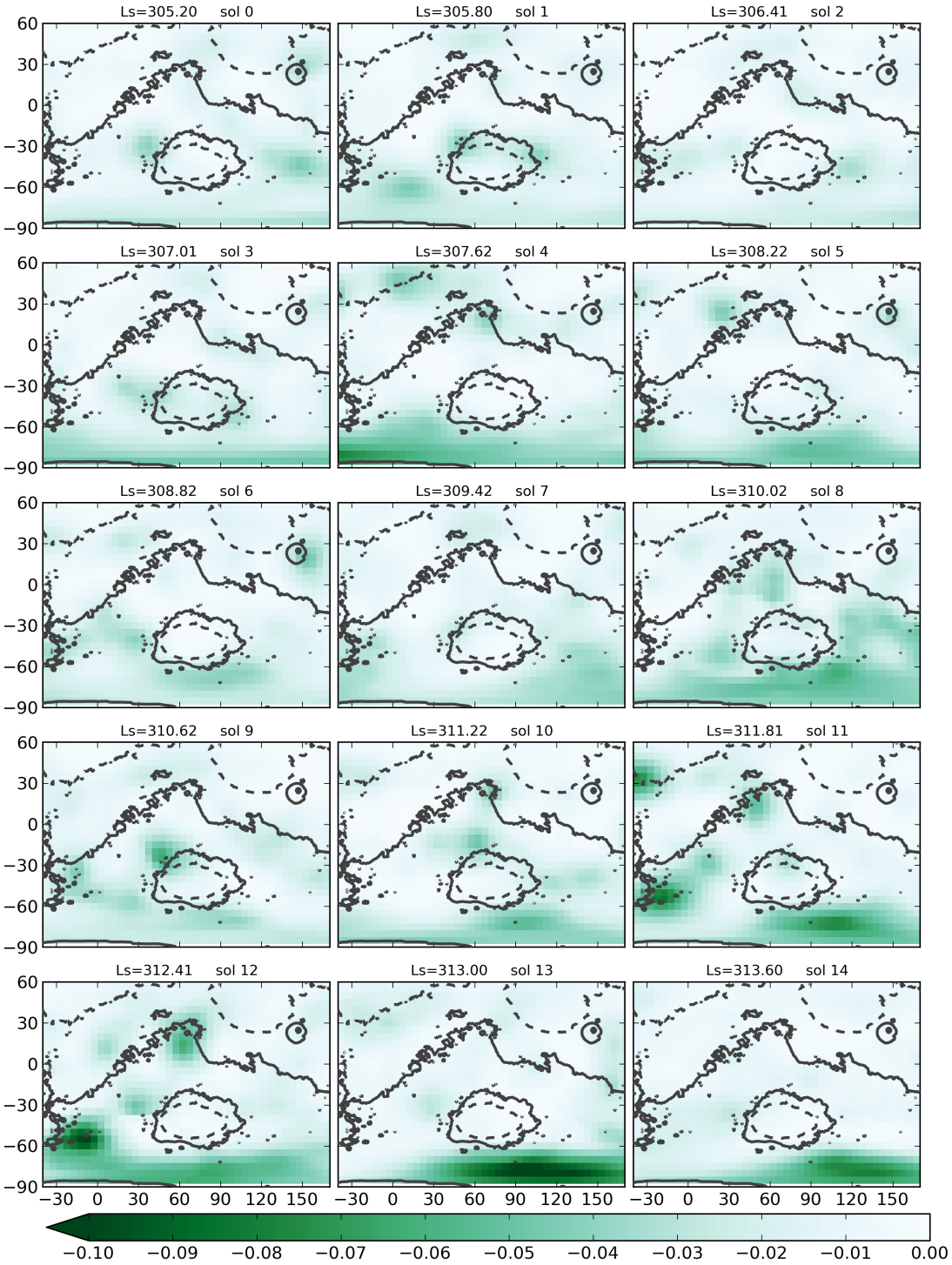

Figure 6.18 Daily total negative analysis increments to *tauref* during the course of the reanalysis of THEMIS and MCS data.

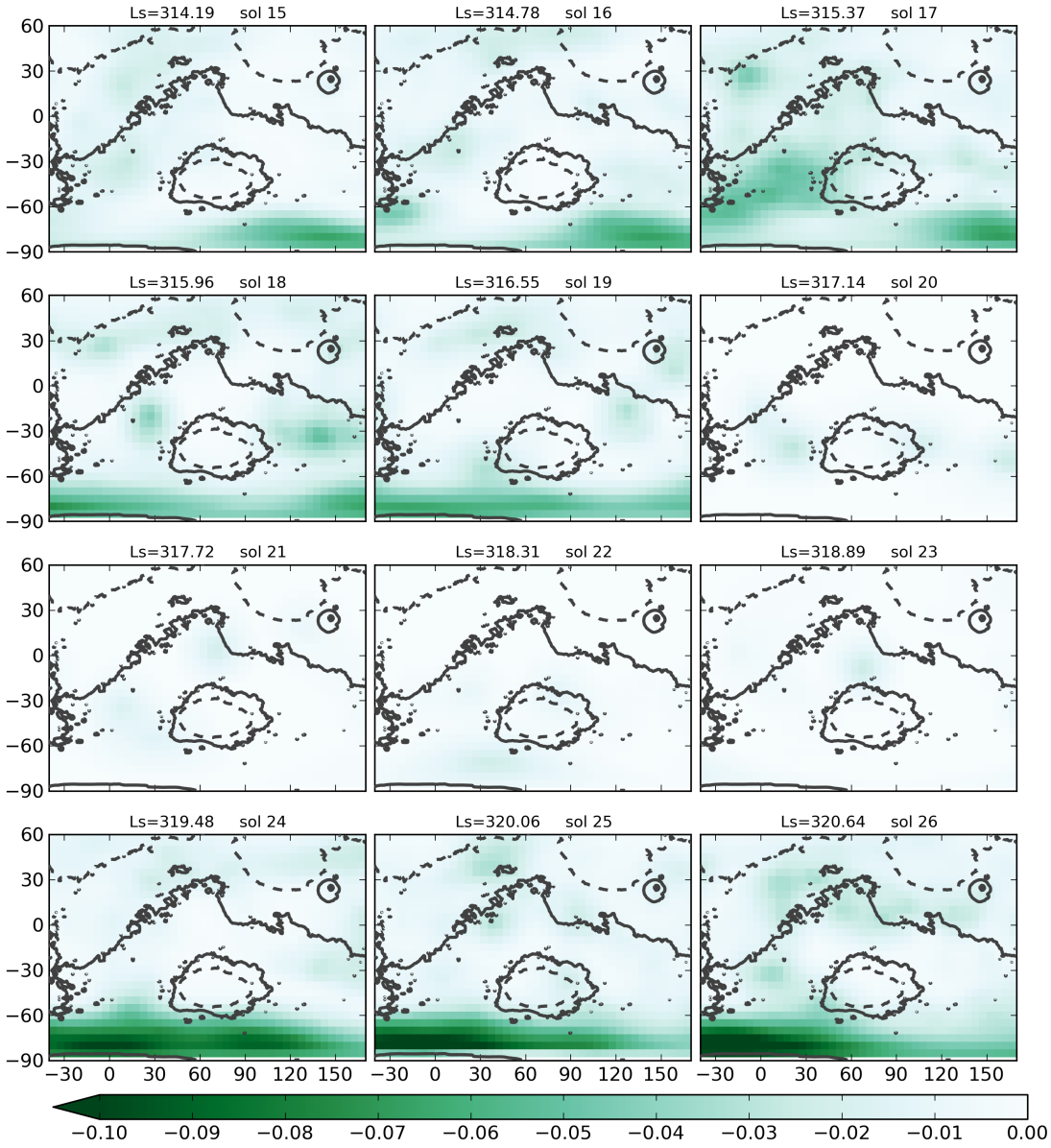

Figure 6.18 (continued)

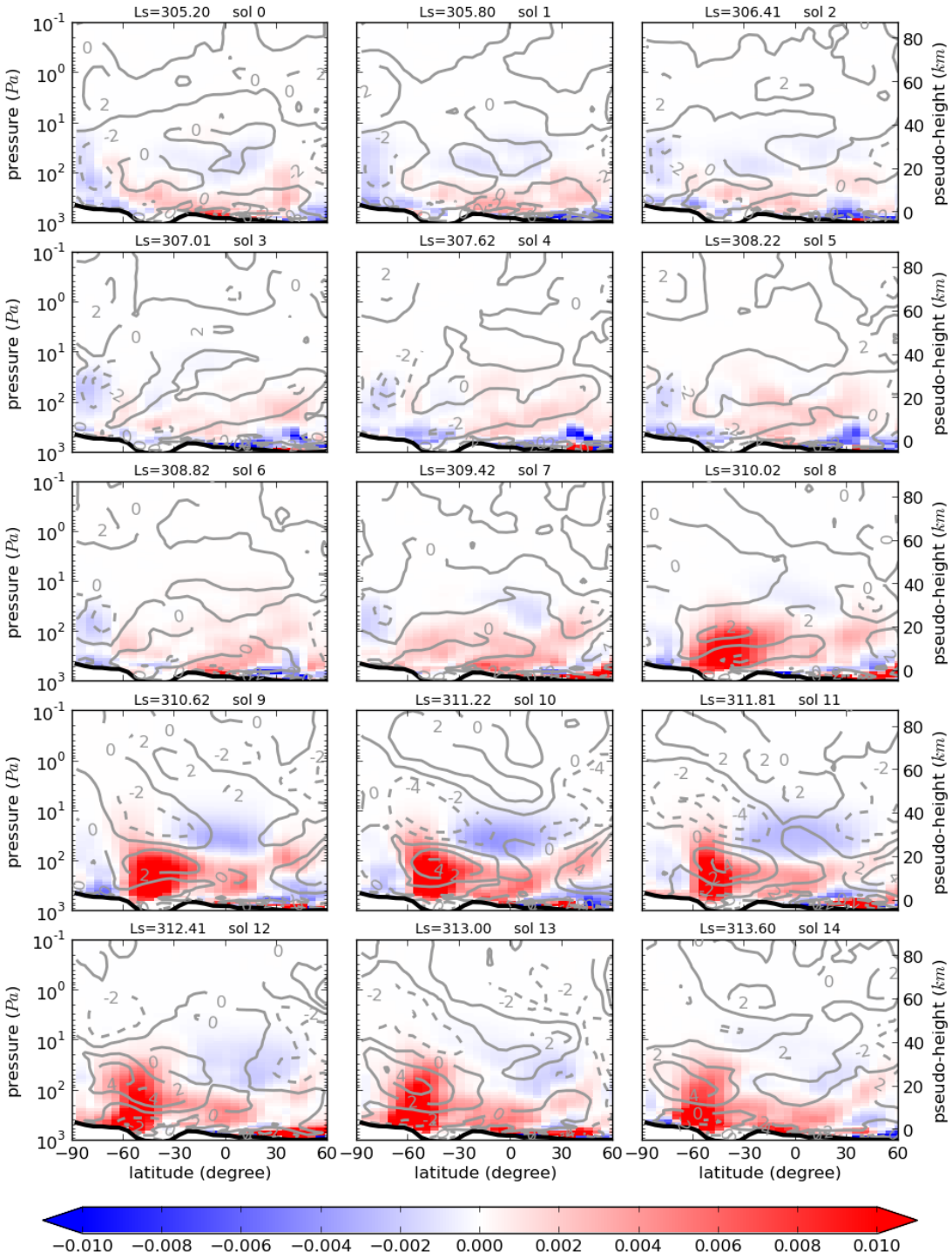

Figure 6.19 Daily maps in the latitude-height plane of zonal anomalies of dust opacity and temperature between longitudes -30° and +90° for sols 0 to 14. Color shading denotes the zonal anomaly for dust opacity in units of km^{-1}, and the contour lines represent the zonal anomaly of temperature with a 2 K interval. The black line indicates the approximate zonal mean topography over the same range of longitude.

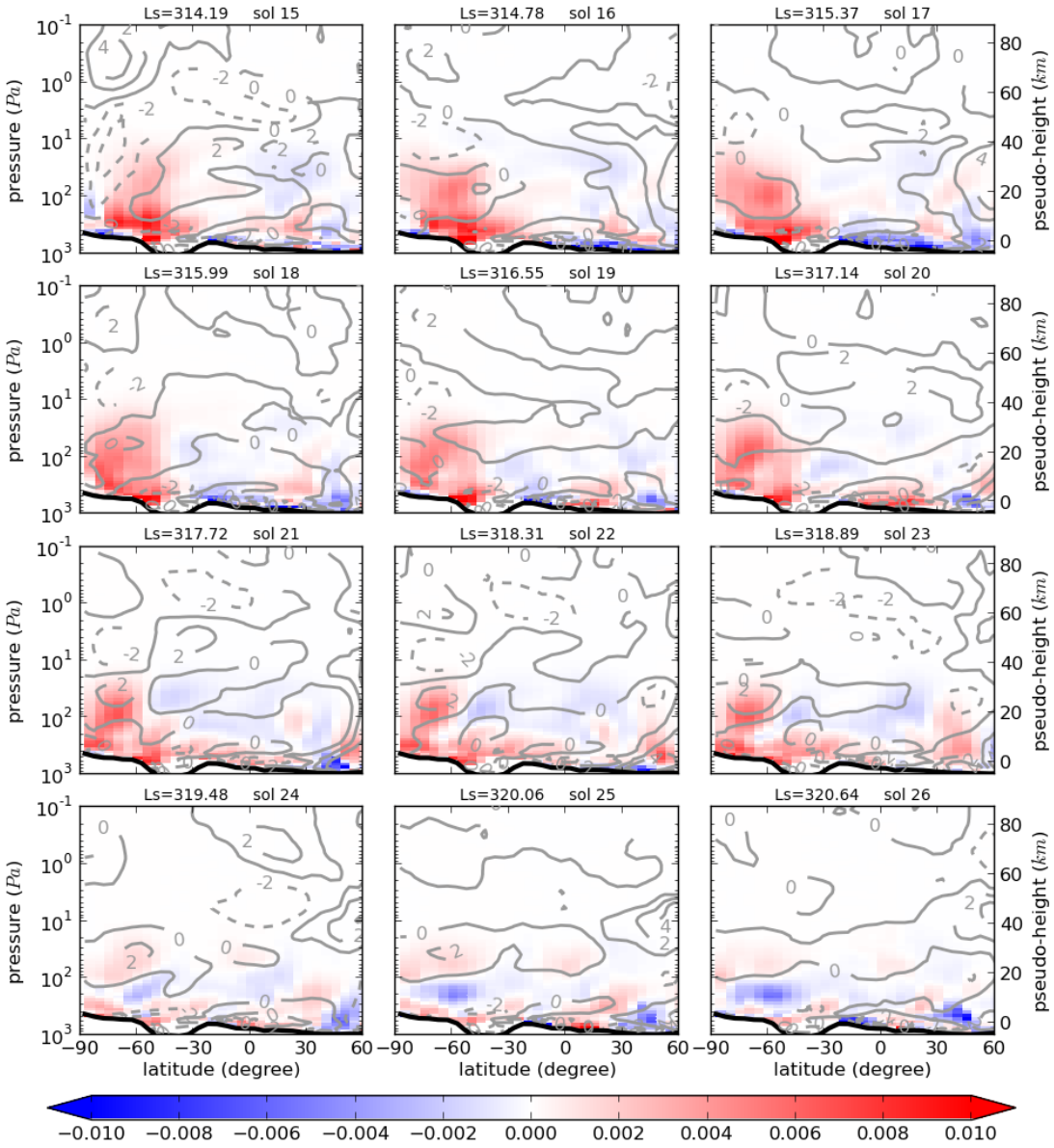

Figure 6.20 Daily maps in the latitude-height plane of zonal anomalies of dust opacity and temperature between longitude +30° and +170° for sols 15 to 26. Color shading denotes the zonal anomaly for dust opacity in units of km^{-1}, while contour lines represent the zonal anomaly of temperature with 2 K interval. The black line indicates the approximate zonal mean topography over the same range of longitude.

Chapter 7 The MY 28 global dust storm

Dust storms are clearly frequently occurring phenomena on Mars, but their size varies widely. They broadly fall into three categories that were first defined in the work of Martin and Zurek [1993], and then refined by Cantor et al. [2001]. These categories are commonly denoted as *"Planet-encircling" dust storms*, *"Regional" dust storm*s and *"Local" dust storms* in terms of their areal coverage and duration. The global dust storm (GDS) discussed in this section is referred to as an example of the "planet-encircling" dust storm, as in some other published studies [e.g. Cantor, 2007; Smith, 2009]. Among the various kinds of dust storm, the "planet-encircling" form is the most intriguing scenario to many scientists.

7.1. Background to the MY28 Global Dust Storm

There have so far been only two GDSs that have occurred since the time when comprehensive satellite measurements (i.e. from various instruments on-board Mars Global Surveyor (MGS), Mars Odyssey (MO) and Mars Reconnaissance Orbiter (MRO)) became available from Mars orbit, i.e. since 1999. One of these was the MY 25 GDS (also called the *2001 Mars planet-encircling dust storm,* as it happened in the Earth year 2001), while the other was the MY 28 GDS (similarly, also often called the

2007 Mars planet-encircling dust storm). The former one (MY25 GDS) coincided with the mapping period of the MGS. The origin and evolution of this GDS had been studied using various observations, including MOC (Mars Orbiter Camera) observations [e.g. Strausberg et al., 2005; Cantor, 2007] and retrievals of CIDO and temperature profiles from TES [e.g. Strausberg et al., 2005]. Montabone et al. [2005] used an assimilation of TES CIDOs and temperature profiles to study the dust distribution and impact on the thermal structure of the atmosphere of the MY 25 GDS. In contrast, the MY 28 GDS has so far not been as well studied because of the limitations on the availability of adequate data.

The TES instrument provided CIDO observations only until late 2004. The following mission, MRO, which was intended to extend the scientific mapping of Mars in the MGS mission, started in September 2006 ($L_s \approx 111°$ in MY 28) before the MY 28 GDS. However, for various technical reasons, CIDO is not one of the regularly available measurements in MCS datasets obtained from the MRO mission. Instead, the vertical profile of limb optical depth is the major dust property measured by the instrument. MCS datasets could not, therefore, provide the variables necessary to quantitatively depict the nadir-view spatial dust distribution. Moreover, the limb-view data in the MCS datasets could only retrieve limited information where the dust opacities were too high, especially during the MY 28 GDS [Kass et al., 2014]. Since the THEMIS instrument on-board MO was also able to measure nadir-view CIDOs, however, Smith [2009] briefly mentioned about the duration of this MY 28 GDS using THEMIS datasets. He pointed out that several dust storms were observed to begin around $L_s = 265°$, that were later followed by a GDS event. The infrared absorption dust optical depth (different from *tauref* in this thesis by a multiplicative factor of 2.6; see section 4.2 in Chapter 4) stayed above 0.5 at least until $L_s = 310°$.

However, the data coverage of the THEMIS datasets was still not enough to present the full dust storm life cycle.

The details of MY 28 GDS evolution were not well described until the work of Wang and Richardson [2013]. Wang and Richardson [2013] used MARCI (Mars Color Imager) images to first visually discuss the initiation of MY 28 GDS. They also determined the location of the maximum heights of the zonal mean dust top with MCS cross sections, derived from a limited number of MCS dust profiles. The names of the topographic features mentioned in their study and in this chapter can be referred to the topography map presented in Chapter 1 (Figure 1.1). In their work, a possible precursory dust storm was observed to travel southwards from the Chryse region before they observed larger dust storms near Noachis. The mosaic of visual images used to characterize this event suggested that this moving dust storm originated from Chryse Planitia at $L_s \approx 261°$. During the first three sols of this dust storm, it traveled southward, passing to the east of Valles Marineris. After sol 5, dust clouds were observed near Noachis, where the dust storms grew significantly in scale and intensity, developing into planet-encircling scales soon afterwards. However, in Wang and Richardson's work, using only visual images and dust measurements that covered only part of the atmosphere, it was impossible to establish unambiguously a clear relationship between the precursor dust storm from Chryse Planitia, dust events in Noachis, and what actually led to the initiation of the MY 28 GDS.

The gridded reanalysis datasets produced in this thesis was shown in Chapter 5 to reproduce reasonable representations of the evolution of *tauref* globally (see Figure 5.3) which were also consistent with surface-based measurements at different landing sites (see Figure 5.9 for the "Spirit" rover and Figure 5.10 for "Opportunity"). As a result, it may then provide an unprecedented opportunity to investigate the evolution

of the MY 28 GDS, especially to explore the possible link between the southward-moving Chryse storm precursor and perhaps to determine the trigger for the MY 28 GDS. It is also possible to study within this dataset the structure and influence of this GDS on the wider circulation more comprehensively. The precursor event of the MY 28 GDS is discussed below in section 7.3. The evolution, as well as the impacts of the MY 28 GDS on the dust distribution and zonal temperature structure, especially regarding the polar warming, is analyzed in section 7.4. Validations of this reanalysis specific to the period of MY 28 GDS are also carried out in sections 7.3 and 7.4 for the precursor event and GDS respectively.

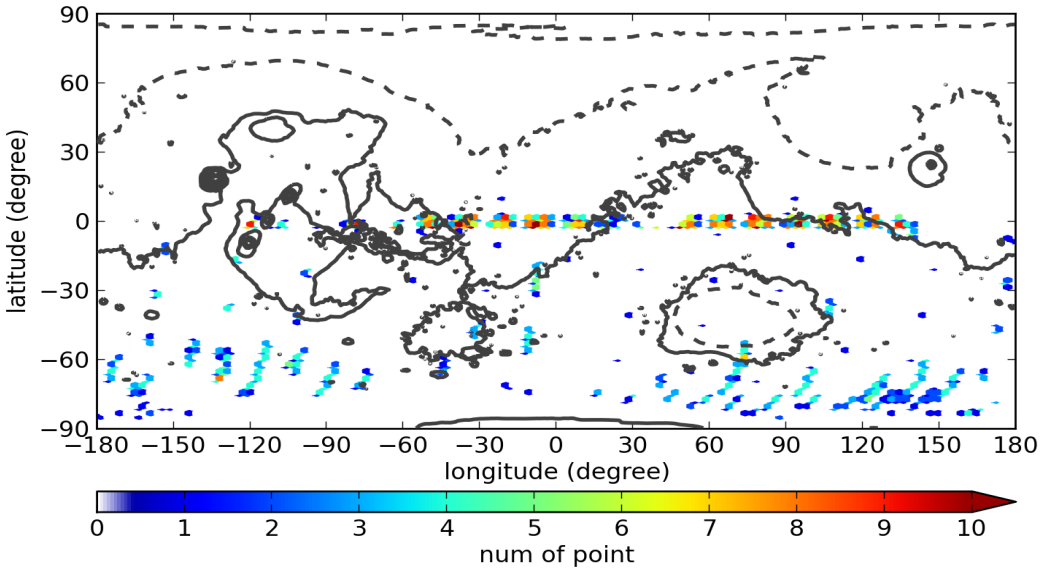

Figure 7.1 The distribution of assimilated THEMIS retrievals of CIDO in longitude and latitude between $L_s \approx 260.7°$ and $L_s \approx 269.1°$. The color shades show the number of measurements per 3° in both longitude and latitude. The solid grey line is the indication of topography above the standard areoid (i.e. equipotential surface whose average value at the equator is equal to the mean radius; also referred to Figure 1.1) and dashed grey line is the topography below the standard areoid. The contours are from -4 to 20 km with 4 km interval. The topography in other latitude-longitude figures follows the same definition.

7.2. Observations assimilated into the reanalysis

As the possible link between the southward-moving Chryse storm and the activation of MY 28 GDS is one of the main focuses in this chapter, it is also of interest to

examine the availability of useable observations during the period of this possible precursor to the main storm.

THEMIS retrievals of CIDO were in general quite sparse over the planet. During the period of the MY 28 GDS and its possible precursor event ($L_s \approx 260° \sim 310°$), the distribution of THEMIS data as a function of L_s and latitude showed that THEMIS data mainly covered the Southern Hemisphere (see Figure 4.1), but the measurements appeared to have a higher data density during the planet-encircling period of the MY 28 GDS. The MCS dataset contained more profiles outside of the Martian tropics in general (see Figure 4.2), but almost no data was available to the south of ~ 45° latitude within the time window ~ $L_s \approx 270° \sim 295°$ that corresponded to most of the period of the MY 28 GDS. However, this could be compensated by a relatively high data density from THEMIS in the Southern Hemisphere. The distributions of THEMIS CIDO data and MCS profiles during the precursor event ($L_s \approx 260.7° \sim 269.1°$) of the MY 28 GDS are shown in Figures 7.1 and 7.2. These datasets were both used as the dust observations assimilated into the reanalysis. For validation purposes, some data was held back from the reanalysis. This non-assimilated data had a similar distribution in space but comprised only ~ 10% of the total data density. During the precursor event, relatively intensive measurements were available near the equator and covered the moving pathway (within the Chryse region) followed by those individual dust events. Almost no data was available in Northern Hemisphere, while some sparse measurements were taken in Southern Hemisphere. Although the THEMIS dataset had limited coverage during the precursor event, the MCS dataset provided good global coverage. In contrast, the THEMIS dataset had much more intensive data coverage in the Southern Hemisphere during the MY 28 GDS itself (during $L_s \approx 269.1° \sim 309.5°$; see Figure 7.3). The MCS dataset

usually had a relatively even distribution globally. During the peak of the MY 28 GDS, however, limited data were only available to the north of ~ 45° latitude. Thus, higher data densities can be seen in the area to the north of ~ 45° latitude in Figure 7.4. As a result, these two datasets of dust observations were able partly to compensate for the absence of each other either during the precursor event or during the peak of the main MY 28 GDS.

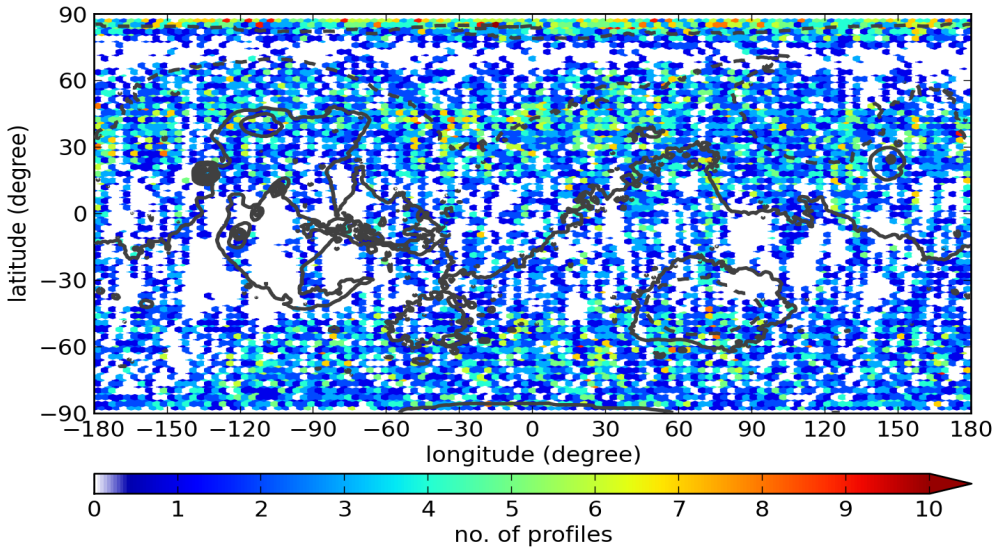

Figure 7.2 Same as Figure 7.1, but for assimilated MCS dust retrievals. The color shades show the number of retrieved profiles per 3° in both longitude and latitude. The grey lines indicate the topography.

7.3. The precursor event of the MY 28 GDS

7.3.1. Comparing the reanalysis with observations

In this section, the results in the reanalysis are directly compared with the observations during the precursor event of the MY 28 GDS. The sol numbers used hereafter are referred to sol 0 at $L_s \approx 260.7°$. This sol designation should be roughly the same as the sol numbers used in the study of Wang and Richardson [2013], but the global images of the dust distribution in section 7.3.2 may not correspond identically since their results were taken from mosaics comprising 13 separate snapshots.

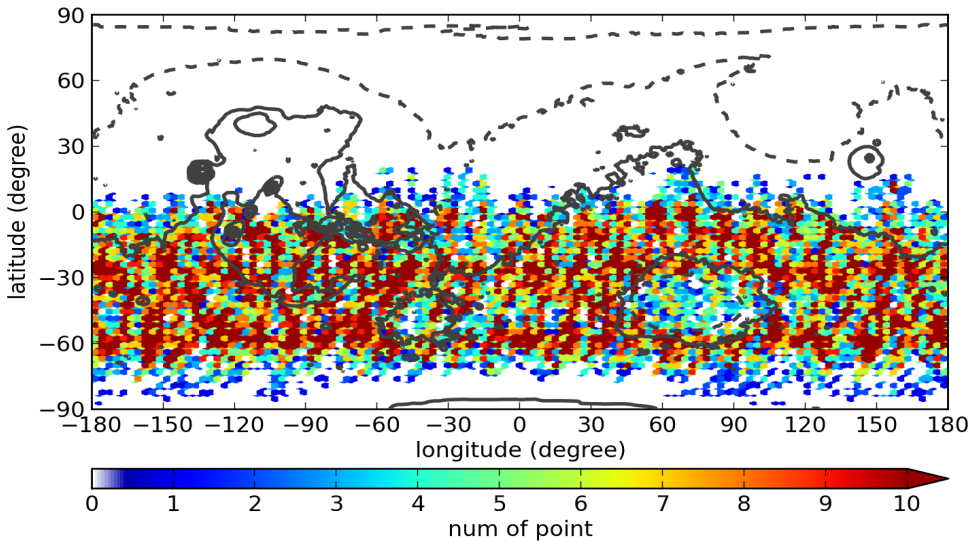

Figure 7.3 Same as Figure 7.1 but for the period between $L_s \approx 269.1°$ and $L_s \approx 309.5°$.

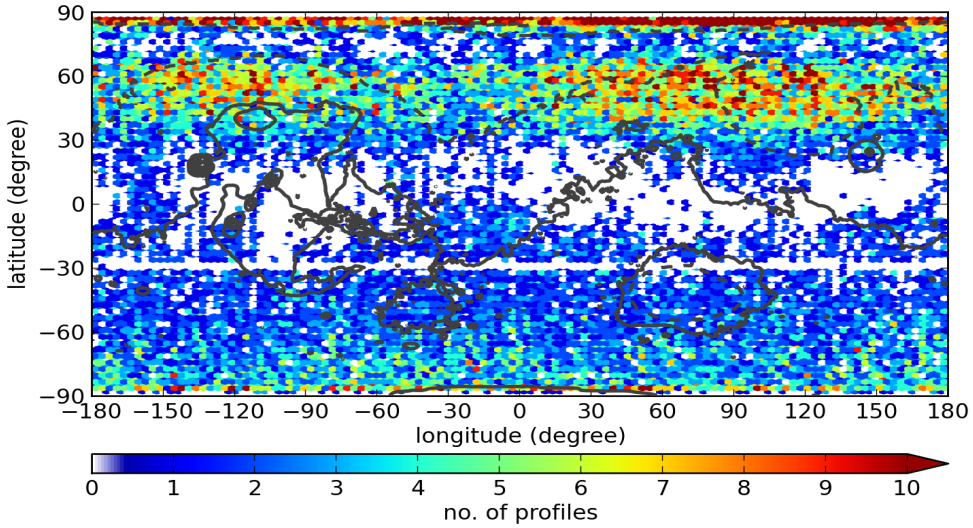

Figure 7.4 Same as Figure 7.2 but for the period between $L_s \approx 269.1°$ and $L_s \approx 309.5°$.

7.3.1.1. Validation against THEMIS dust data

Figure 7.5 shows the daily mean (signed) difference between reanalysis and the THEMIS data during the precursor event, as well as indicating the uncertainties of the THEMIS dataset. Smith [2004] pointed out that the uncertainties could be larger (perhaps 20% of the measurements or even higher) during the most intense dust storms. Since this precursor event eventually led to a very intense dust event (with

tauref ≥ 2) before the MY 28 GDS, the absolute uncertainties in terms of visible extinction opacity depth (shown as grey dashed lines in Figure 7.5) are chosen to be the larger of 0.104 (explained in section 6.4.1 of Chapter 6) or 20% of the observations. However, the actual uncertainties could be larger than those shown in Figure 7.5 [Smith, 2004]. During the precursor event (sol 0-13), the daily mean differences between the reanalysis and the assimilated THEMIS data were either within the observational uncertainties or reasonably close to the uncertainties. For the non-assimilated data sample, they were normally in poorer agreement with the reanalysis than the assimilated data, but the reanalysis in sol 7 compared to the non-assimilated data had a smaller discrepancy in this case than the formal difference from the assimilated data.

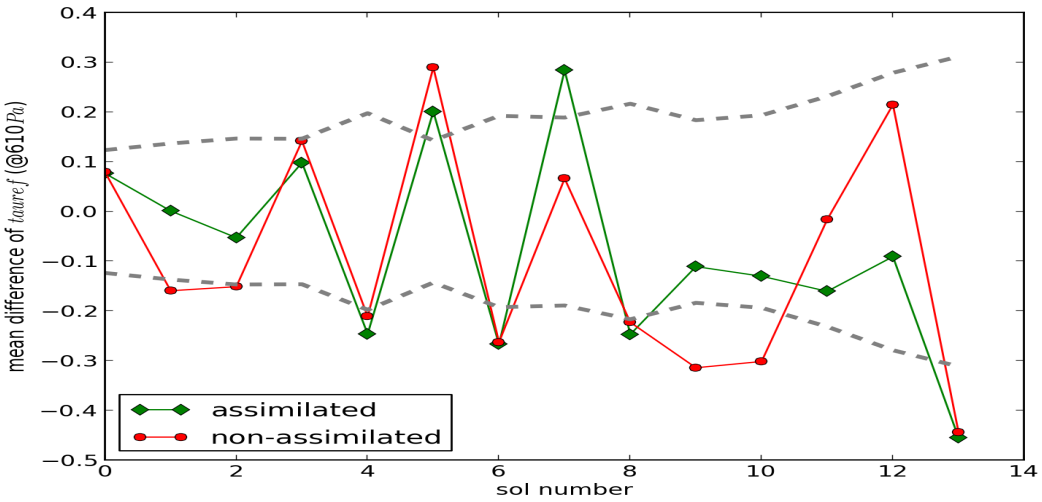

Figure 7.5 Mean difference of *tauref* between reanalysis and THEMIS data, starting from sol 0 ($L_s \approx 260.7°$) of the precursor event to sol 13 ($L_s \approx 269.1°$). Green line is the mean difference between reanalysis and the THEMIS data that was actually assimilated. The red line is the mean difference between the reanalysis and the set of non-assimilated THEMIS data; the grey dashed lines indicate the uncertainties of THEMIS dataset.

Figure 7.6 shows the scatter plots between THEMIS data and the reanalysis. During this precursor event, most of the *taurefs* assimilated into the reanalysis were between 0.3 and 1.5. The reanalysis was shown to successfully reproduce the *tauref* at the location of assimilated THEMIS observations (Figure 7.6a). The coefficient of the

least square fitting between assimilated THEMIS and the reanalysis was 0.82. Because the availability of the non-assimilated THEMIS data was extremely limited, the correlation between non-assimilated data and reanalysis (Figure 7.6b) might therefore be less representative. It is noticeable that the reanalysis exhibited a weaker correlation with those THEMIS data not used for assimilation than compared to assimilated THEMIS data, but the agreement was still reasonable (see Figure 7.6b, the coefficient of the fitting was 0.67).

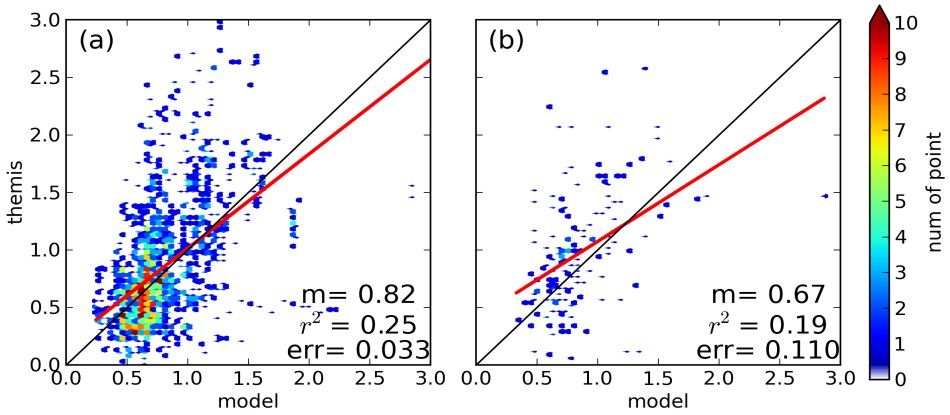

Figure 7.6 Scatter plots of THEMIS-model *tauref* between sol 0 and sol 13 inside the study domain. The color indicates the data density per 0.05 *tauref* . The red lines are the linear least square fit between THEMIS and the reanalysis. m is the coefficient of the fittings, i.e. the slope of the red lines, r^2 is the coefficient of determination, and err is the standard error of the slope. The black lines represent the lines with coefficient 1. (a) scatter plot between reanalysis and assimilated THEMIS data, (b) scatter plot between reanalysis and non-assimilated THEMIS data.

7.3.1.2. Validation against MCS dust data

Similar to Section 6.4.2, the reanalysis data were interpolated onto pressure levels, as in the MCS dust retrievals, so as to compare the difference of the average of dust opacity between the model results and MCS dust retrievals in different pseudo-height ranges (Figure 7.7). The average observational uncertainty ranged from 0.00003 km^{-1} to 0.00016 km^{-1}. The profiles of differences between the reanalysis and observations were found to be similar in the comparison with both assimilated MCS data (Figure

7.7a) and non-assimilated MCS data (Figure 7.7b). Dust in general accumulated in large quantities in the 0-10 km height range, so the free-running model struggled to predict the right amount of dust at the right location in that part of the atmosphere. The MCS data available within that height range (0-10 km) was limited, so as to place weaker constraints on the model simulation. As a result, the differences were found to be ~10 times larger than the average observational uncertainty at the bottom (0-10 km) with an overestimate of ~0.0034 km^{-1}. However, the observational uncertainty can be larger for dust due to the systematic errors which are not included in the presented uncertainty (dashed lines in Figure 7.7), e.g. due to the uncertainty of dust size distribution, the uncertainty of spectroscopic parameters. These uncertainties are very difficult to quantify. Therefore, the actual uncertainty of the data could be larger than the uncertainty given here. In contrast, the differences in other parts of atmosphere were more consistent with expectations. The differences found in the ranges 10-20 km and 30-40 km fell within the estimated uncertainties of the observations. The reanalysis seemed to underestimate opacities within 20-30 km range, and slightly overestimate them above 40 km.

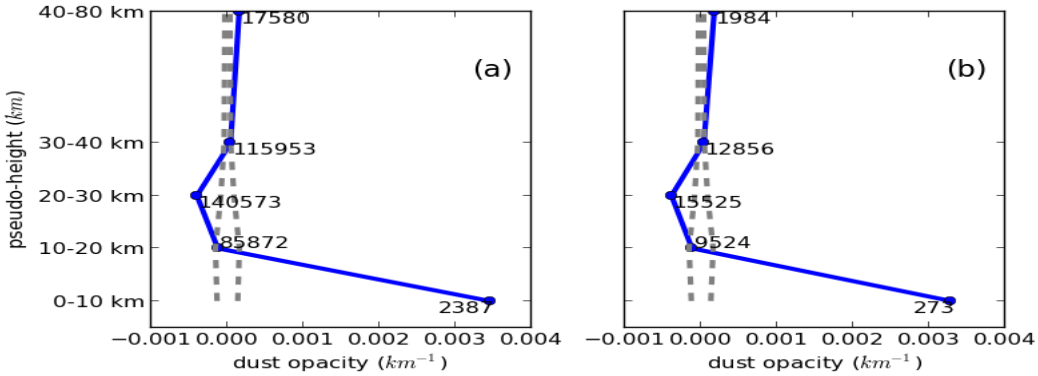

Figure 7.7 Average differences between reanalysis and MCS data in sols 0-13. Blue line shows the average difference, grey dashed lines indicate the observational errors, and the numbers denote the numbers of data available in each height range. (a) for assimilated MCS data, (b) for non-assimilated MCS data.

7.3.2. Spatial maps of dust distribution during the precursor event

The precursor event documented by Wang and Richardson [2013] from a survey of the visual images available during this time can also be seen in the reanalysis but with higher temporal and spatial resolution.

Figure 7.8 shows spatial maps of the daily-averaged *tauref* . In sol 0, a patch of suspended dust could be seen in an area in Chryse Planitia subject to high winds, with $tauref \geq 0.9$. In sol 1, this patch of dust moved downwind to approach Xanthe Terra with similar size and intensity. Some additional dust was also seen to be lifted over Alba Patera as well. The dust storms originally from Chryse Planitia travelled over Xanthe Terra in sol 2, and the dust lifted over Alba Patera in the previous sol was carried from their origin towards Chryse Planitia. The winds near Chryse seemed to drop in intensity after the dust storm moved southward, while more dust was seen to be lifted over other regions, including the area between Arabia Terra and Hellas and the area to the south of Elysium Planitia. In sol 3, however, a strong southward wind dominated in Chryse Planitia again, transporting more dust into the Chryse-Xanthe channel. The dust storm that was over Xanthe Terra in the previous sol continued to intensify and proceeded to enter Noachis Terra with the prevailing wind. Additional dust could be seen near Elysium Planitia and along the border of Arabia Terra. The dust near Elysium Planitia appeared to disperse compared to the previous sol, but some of the dust was seen also to spread southward while another small patch of dust travelled through Isidis Planitia.

In sol 4, the dust in Chryse Planitia travelled southward to strengthen the dust storm over Xanthe Terra and to the east of Valles Marineris (increasing in intensity to $tauref \geq 1.2$). The strong eastward wind consistently transported dust into Noachis Terra, forming a narrow convergent zone along the southern flanks of the strong wind

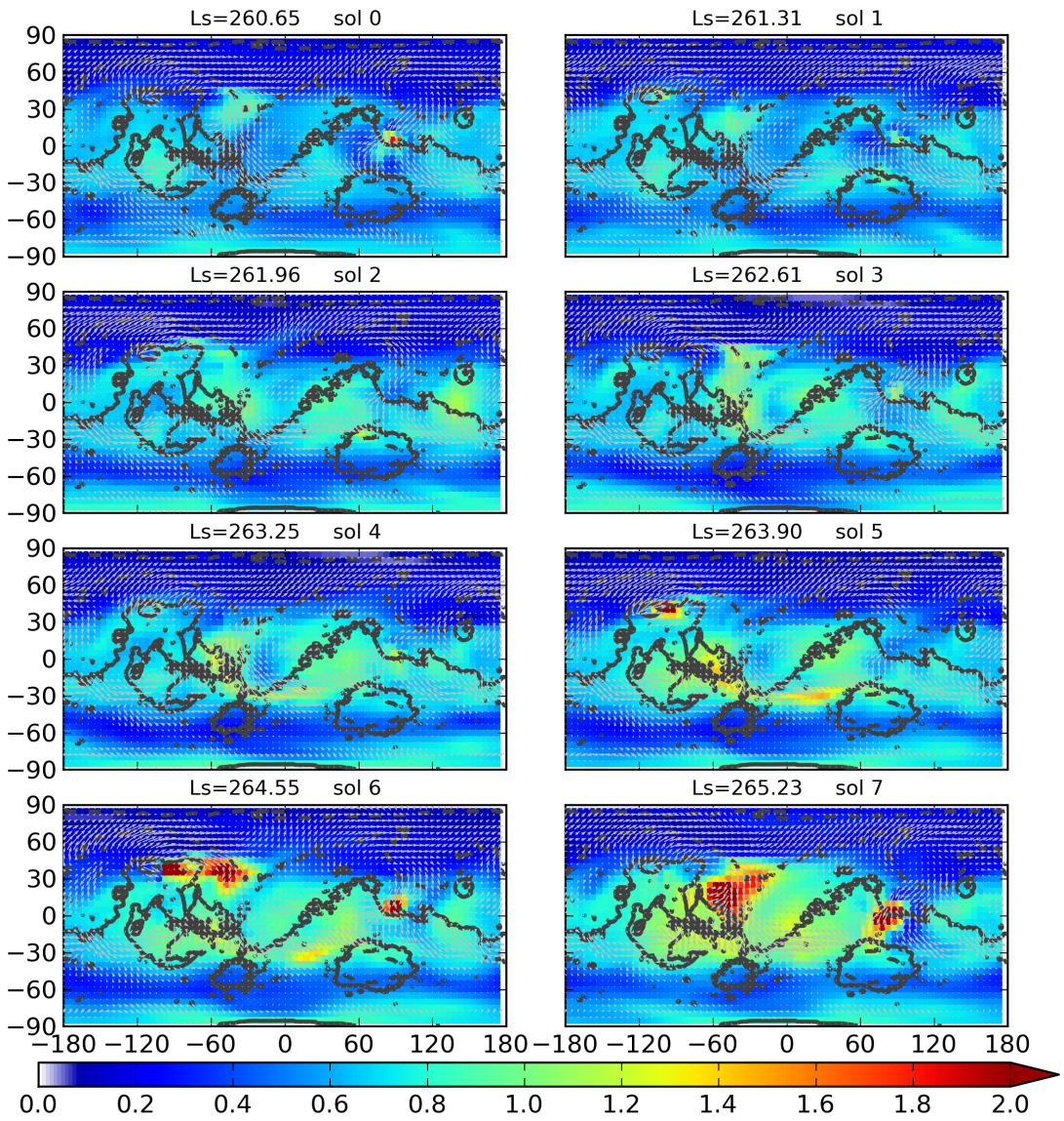

Figure 7.8 Spatial maps of daily-averaged *tauref* during the lead up to the MY28 GDS. Sol 0 is the first sol ($L_s \approx 260.7°$) when this dust storm was first reported in the MMWR. The arrows in each map indicate the wind velocity at the first model level (at altitude ~ 4 m). The grey lines indicate the surface topography.

belt. Small patch of dust travelled through Isidis Planitia into Tyrrhena Terra. In addition, some dust was also directly lifted in Alba Patera. In sol 5, the dust storm located to the east of Valles Marineris and Noachis Terra had two centers, each with *tauref* ≥ 1.4 . The center to the east of Valles Marineris proceeded to move slightly southwest, while the wind in Chryse Planitia weakened again when the storm moved out of the area. The dust lifted over Alba Patera in sol 4 moved slightly eastward in

sol 5 with significantly growing strength ($tauref \geq 2$). In sol 6, two intense dust centers, one over Noachis Terra and the other to the east of Valles Marineris, started to disconnect from each other and weaken, but *tauref* in both centers was still above 1.2. The dust storm originating over Alba Patera in sol 4 slowly moved eastward and gained more strength. Additional dust could be seen over Chryse Planitia just downwind of the Alba Patera storm.

Over Isidis, a small confined dust storm with $tauref \geq 2$ appeared in sol 7. The dust close to Alba Patera seemed to catch up with the dust over Chryse Planitia, coalescing to become a large southward-moving dust storm. The dust over Noachis Planitia then became very diffuse, but dust opacities remained with $tauref \geq 1$. Meanwhile, the dust storm that was over Isidis Planitia found its way to Tyrrhena Terra, and even reached the border of Hellas. The storm over Chryse Planitia travelled into Xanthe Terra in sol 8, and the storm at the border of Hellas proceeded to enter Hellas while decreasing in size. Dust storm center that was at Valles Marineris ($tauref \sim 1.3$) moved to near Solis Lacus in association with a cyclonic wind pattern in sol 8.

By sol 9, most of the area in Xanthe Terra was covered by dust. The wind patterns near the east end of Valles Marineris and over Noachis Terra combined to deliver patches of dust into Noachis Terra, forming an intense narrow band full of dust. The dust storm near Solis Lacus meanwhile intensified significantly within the convergent zone to values of up to $tauref \sim 1.8$, by which time the position of the storm was slightly to the west compared to that of sol 8. The small storm which travelled into Hellas in sol 8 had already dissipated by this sol. Wang and Richardson [2013] also pointed out that dust covered these three areas in day 9 of their study that corresponded to almost the same period as sol 9 in this study.

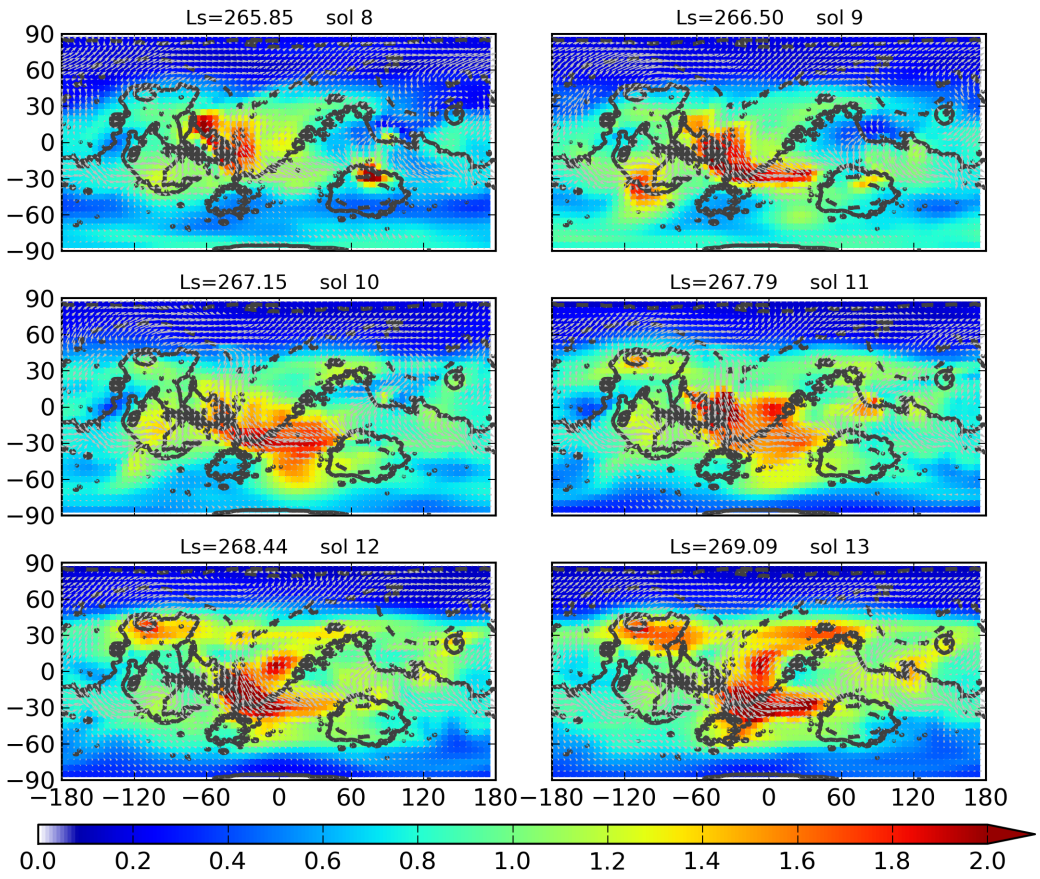

Figure 7.8 (continued)

The dust storm near Solis Lacus moved northward slightly in sol 10 and then began to disperse, becoming more diffuse. The dust storm over the east of Valles Marineris continued to spread dust into Noachis Terra, while the narrowly confined dust band proceeded to expand to cover a larger area within Noachis. This area then became the major active area of dust during this sol. In sol 11, dust kept spreading out from the storm near Noachis Terra, and even crossed over to reach Arabia Terra. A more intense dust storm ($tauref \geq 2$) was then initiated over the Chryse-Xanthe channel. Two additional dust centers were notable near Alba Patera and Isidis Planitia respectively.

By sol 12, an active dust band started to form around ~ 30° latitude in the Northern Hemisphere. Significant amounts of dust could then be seen near Alba Patera. The dust storm that was in the Chryse-Xanthe Channel in sol 11 started to move

southward with growing intensity, while another dust center formed in Arabia Terra. During sol 13, more dust centers were activated globally, especially near Alba Patera, Arabia Terra and Elysium Planitia. The Chryse-Xanthe dust storm then slowly travelled into Noachis Terra having entrained large amount of dust. These active dust centers eventually led to the formation of a planet-encircling dust storm (MY 28 GDS) shortly afterwards.

7.3.3. Sources of dust

In this reanalysis, three different ways of dust injection into atmosphere are present, either physical or not. They are respectively the wind stress dust lifting parameterization, the dust devil lifting parameterization, and injection due to relaxation of the model towards observational data through the data assimilation scheme (introduced in Chapter 4).

Figure 7.9 shows maps of the daily average wind-stress dust lifting rate ($kg \cdot m^{-2} \cdot s^{-1}$). In sol 0, the wind stress lifting mainly occurred in the Acidalia-Chryse and Elysium-Isidis regions. In sols 1 & 2, active wind stress dust lifting could be seen near and downwind of Alba Patera. These corresponded to regions where the dust concentration was relatively high during these sols (see Figure 7.8). In sol 3, additional wind stress dust lifting was evident in the Chryse-Xanthe channel, and dust was also observed to cross this channel in the reanalysis during the same sol. In sol 4 & 5, when dust could be seen in Noachis Terra that was downwind from the Chryse-Xanthe channel, wind stress dust lifting appeared in Noachis Terra. The wind stress lifting apparent near Alba Patera corresponded to the new dust storm seen in the spatial maps of dust opacity (Figure 7.8). In sol 6, a large area of wind stress dust

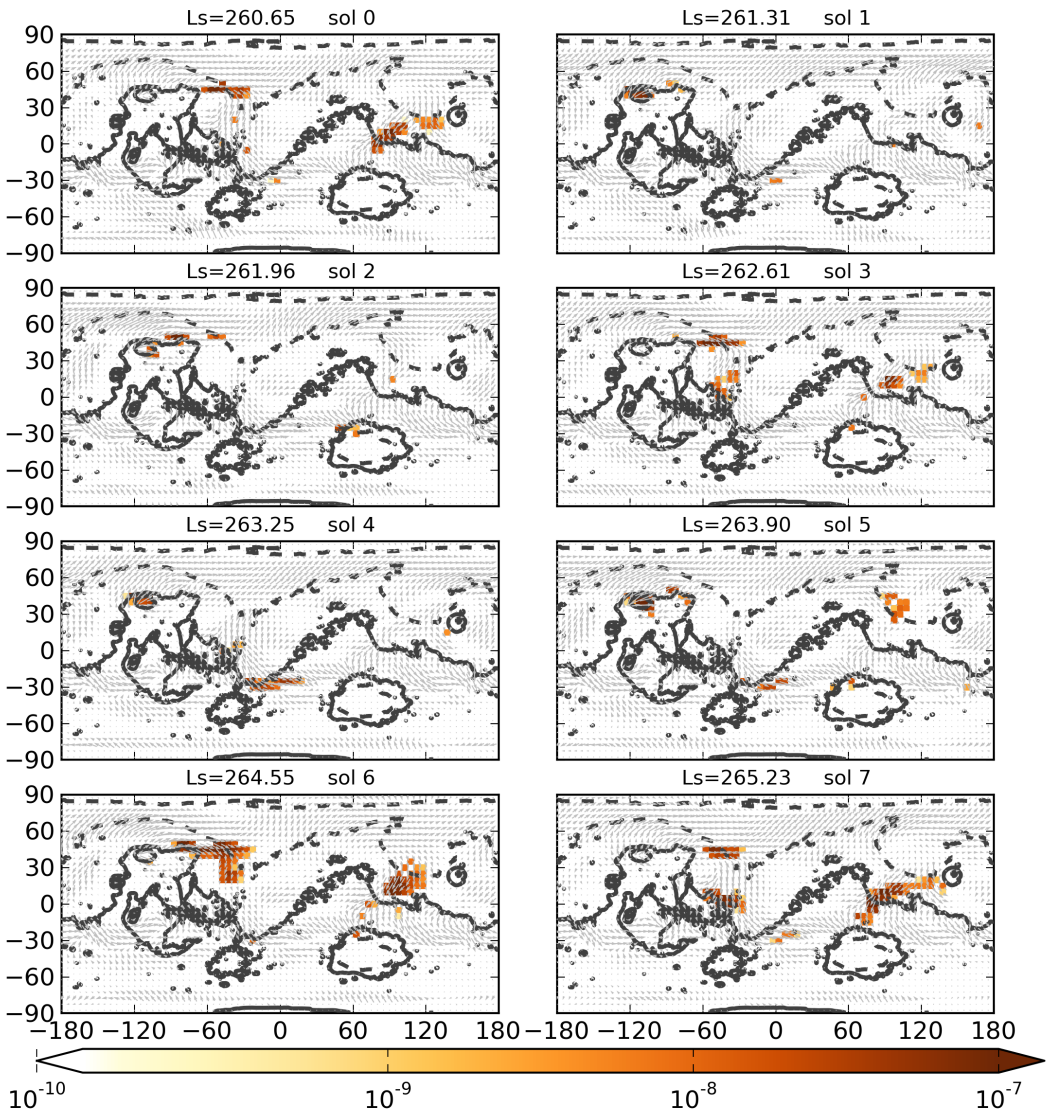

Figure 7.9 Daily average maps of the wind-stress dust lifting rate over the same period as in Figure 7.8. The color shades indicate the magnitude of the daily average wind stress dust lifting rate (in units of $kg \cdot m^{-2} \cdot s^{-1}$).

lifting appeared in Tempe Terra in the northern hemisphere, while also in this sol the dust storm from Alba Patera seemed to gain in strength in Chryse Planitia. Meanwhile, another dust storm was apparently generated by wind stress lifting in western Elysium Planitia and proceeded to move southward towards Tyrrhena Terra. Sol 8 & 9 were then relatively quiet for wind stress dust lifting. Wind stress dust lifting then began to appear over a large area of the Chryse-Xanthe channel in sol 10 & 11. During these two sols, the dust also started to spread from the Chryse-Xanthe

channel according to the maps of dust distribution (Figure 7.8). When multiple dust lifting regions were activated in sol 12 & 13, wind stress dust lifting was quite sparse and occurred mainly between 0° and -30° latitude.

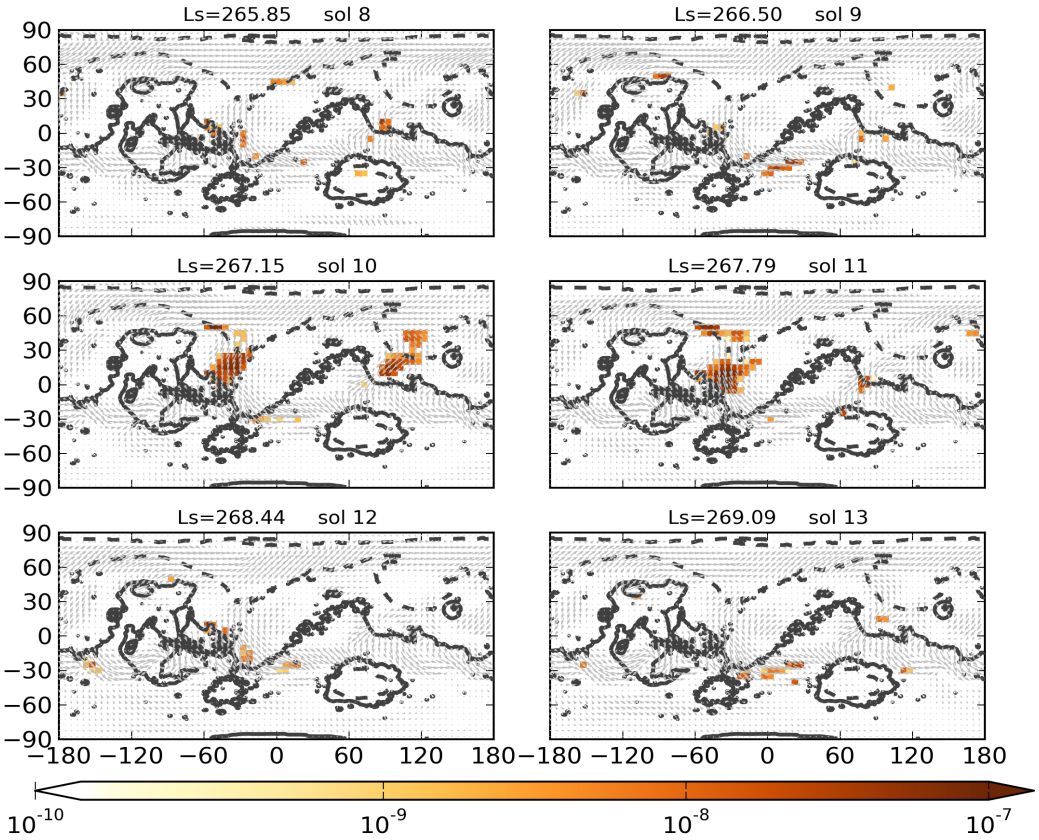

Figure 7.9 (continued).

Figure 7.10 shows the daily average dust devil lifting rate ($kg \cdot m^{-2} \cdot s^{-1}$). During the period of this precursor event, an active band of dust devil lifting could be seen between -20° and -40° latitude. The dust devil lifting also happened in other regions, although on a smaller scale to those inside the band. In sol 0, dust devil lifting appeared active in Chryse-Xanthe and Elysium. The dust lifting area of Chryse-Xanthe was now to the south of the area with high dust opacity. Dust devil lifting was therefore unlikely to have provided the initiation of this precursor event. When the dust patches travelled southward, the intense dust devil lifting centers were sometimes seen surrounding the most dusty area of the storm, while the dust devil lifting was

apparently suppressed to only a limited level within the area covered by the moving dust storm itself.

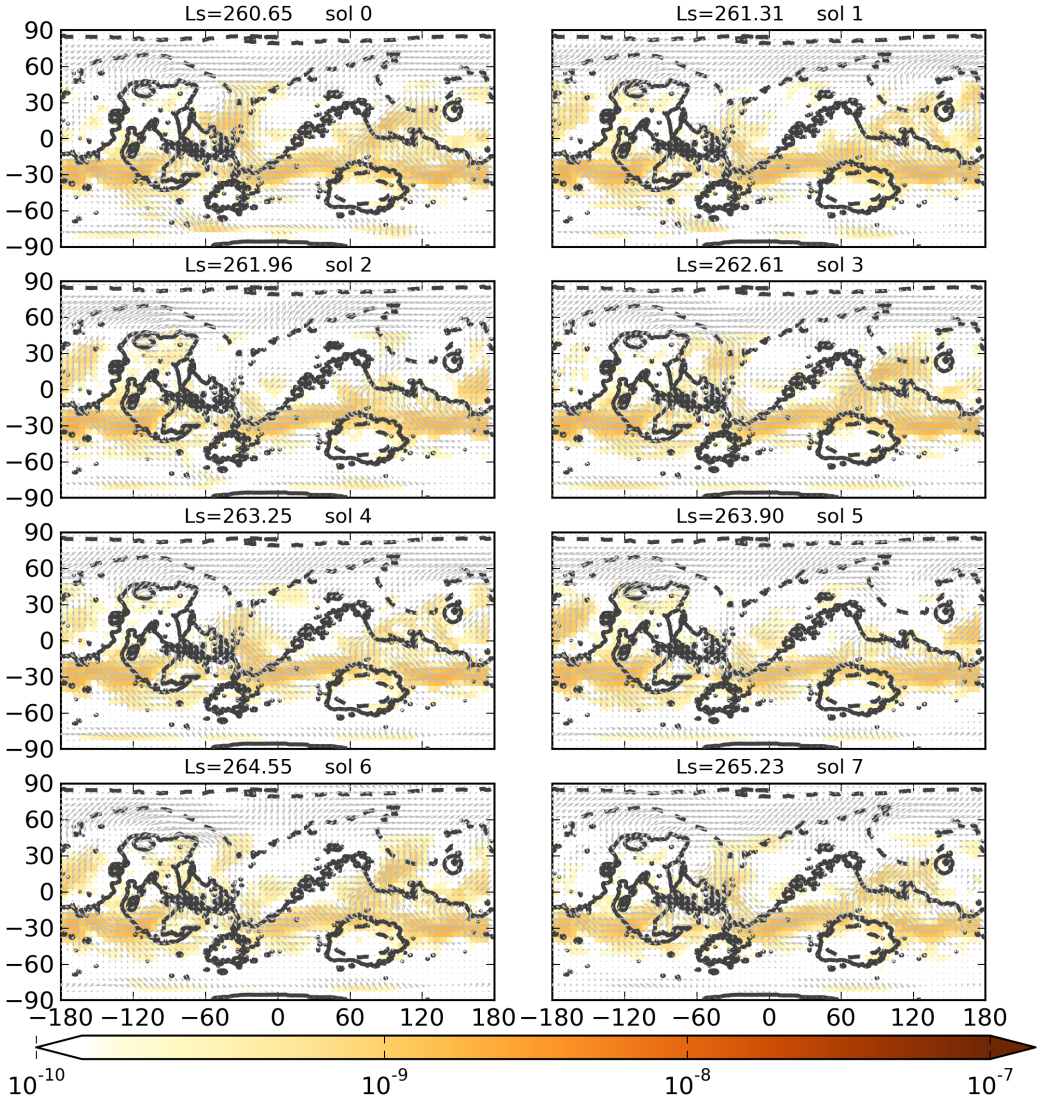

Figure 7.10 Same as Figure 7.9, but the color shades now show the daily average of the parameterized dust devil lifting rate (in the unit of $kg \cdot m^{-2} \cdot s^{-1}$).

In this reanalysis, assimilation of dust is the third way of changing the dust content of the atmosphere during the model simulation. This procedure relies on comparing the dust concentration predicted by the model with the available dust observations, rather than through a deterministic physical parameterization. For the dust assimilation, two observational datasets, THEMIS CIDO data and MCS LIDO data, provided the possible sources of dust injection/removal in this reanalysis. These two

datasets are fundamentally different in their character, in that one constrains the total column dust amount and the other the vertical distribution, so the analysis modified the model simulation in different aspects. In the same way as in Section 6.9, the model increments from these two observational datasets were processed and combined to result in an assimilated dust concentration that was comparable to the normalized column-integrated quantity, *tauref* .

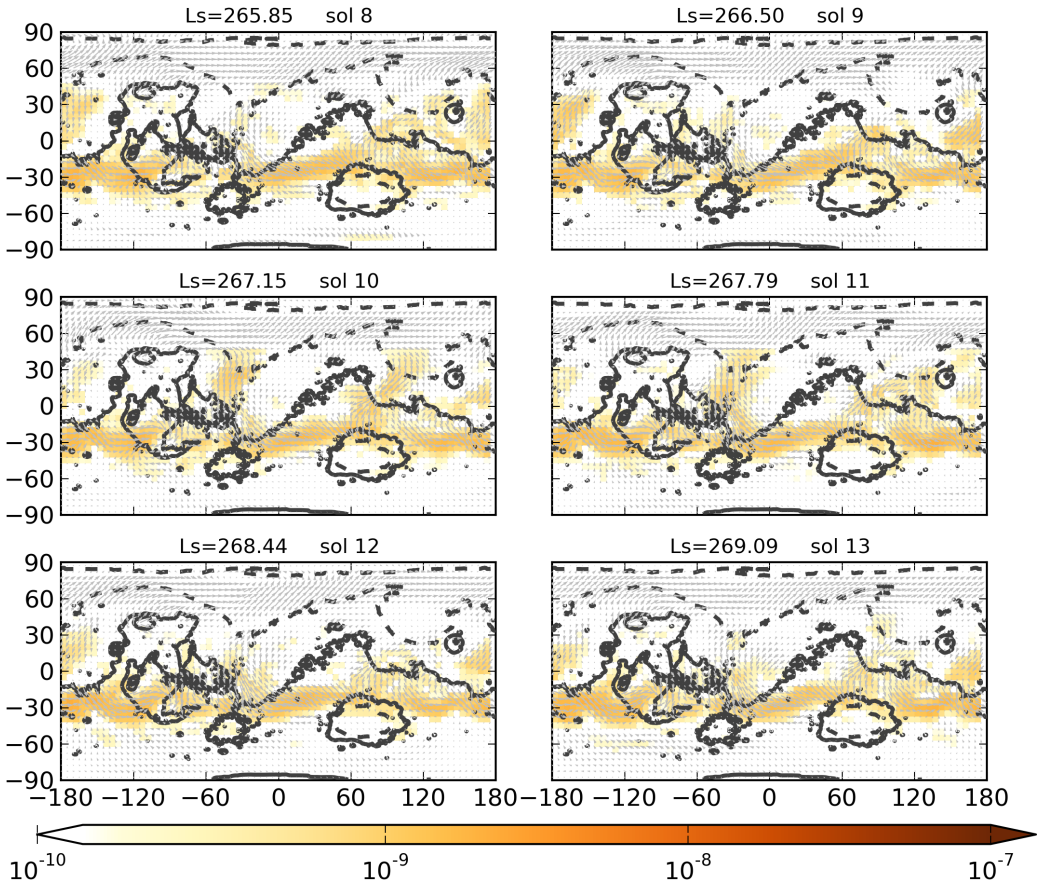

Figure 7.10 (continued).

Figure 7.11 shows the daily total observational increments applied to *tauref* . In sol 0, the positive increments were in general very small (~ 0.02). Since the increments were so small over Chryse Planitia, we may conclude that the initiation of the precursor dust events to GDS MY28 in our reanalysis was not solely the result of adding dust artificially into the model from the observational analysis. The largest

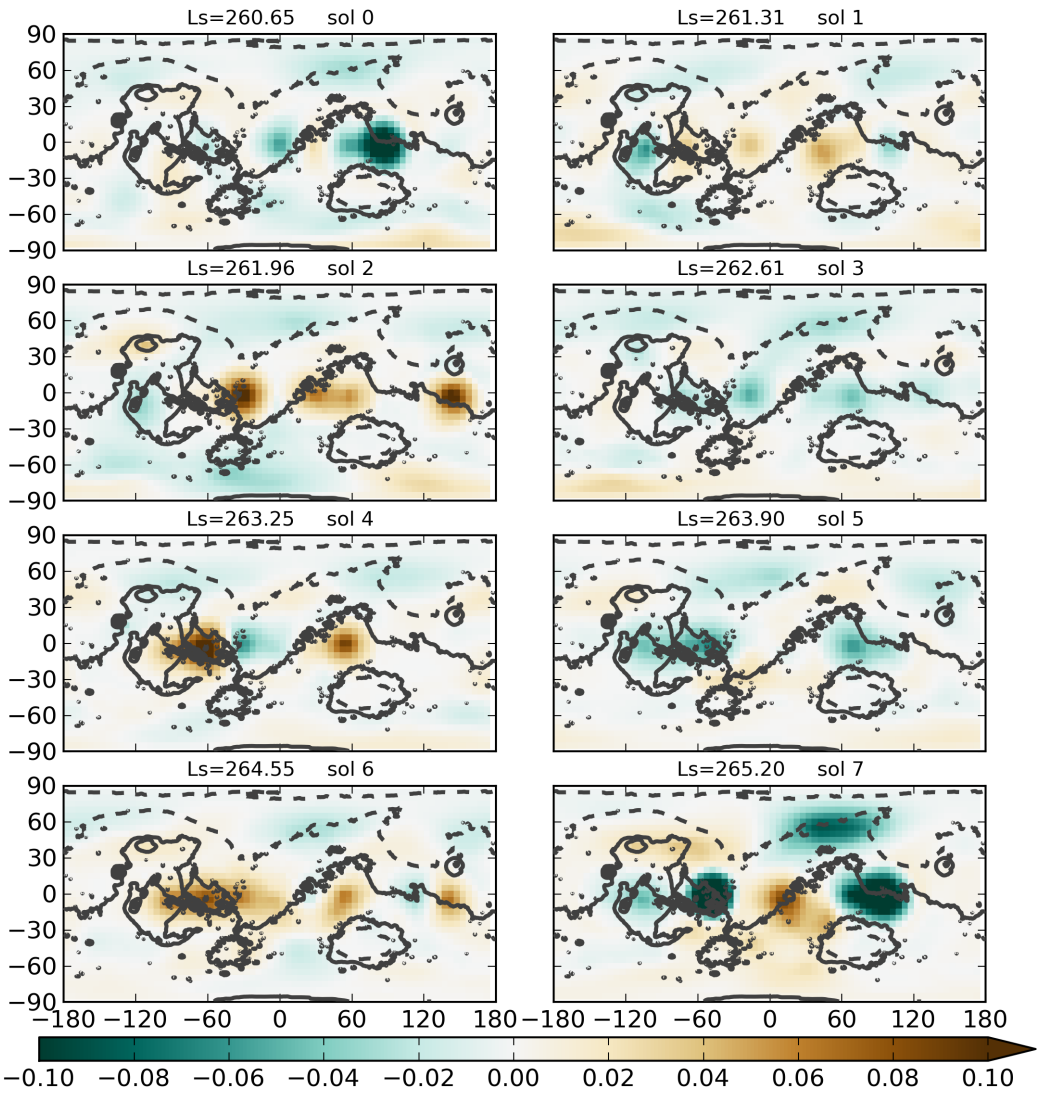

Figure 7.11 Similar to Figure 7.10, but the color shades now show the daily total observational increments applied to the *tauref* field.

negative increments (~ -0.1) were found near Tyrrhena Terra, and this was the same location where the wind stress dust lifting was active in the same sol (see Figure 7.9). This may suggest that the assimilation was trying to remove the excessive dust lifted by wind stress lifting. However, the wind stress dust lifting was designed to lift the dust into the lowest the model level, and the negative increments may only try to remove the dust from the higher levels within the column. In that case, the negative increments may possibly be the consequence of poor representation of dust transport. This question may intrigue future study for assessing the capability of dust lifting

parameterization. Apart from these large negative increments, some small negative increments could be found near Meridiani Planum and the North Polar region. In sol 1, the increments were all within ± 0.04. Some significant dust amounts were injected by the observational increments mainly in Xanthe Terra, Meridiani Planum and south of Elysium Planitia in sol 2. These also showed some correlation with the dusty areas, as in Figure 7.8. In sol 3, the increments were relatively small again. This suggests that the dust filling Chryse-Xanthe in sol 3 (see Figure 7.8) was actually mostly injected self-consistently by the physical dust lifting schemes and transported by the prevailing wind. With transport, some dust already invaded into Noachis during this sol. During sol 4 & 5, however, the data assimilation scheme struggled to correct the dust amounts in Xanthe Terra and Valles Marineris. In contrast, the high-dust concentration found near Alba Patera and the dusty band over Noachis (Figure 7.8) were spontaneously produced by the physics represented in UK-LMD MGCM. The wind stress lifting was responsible for the small dust event near Alba Patera in sol 4 & 5. The dust band over Noachis Terra probably resulted from the combined effect of wind stress lifting near Valles Marineris, the general dust devil lifting band (between -20° and -40° latitude) and, perhaps even more importantly, the transport of dust by the eastward prevailing wind in Noachis Terra itself. When the dust storm that originated from Alba Patera in sols 4 & 5 grew and moved into Acidalia-Chryse in sol 6, this evolution appeared to be consistent with the available observations since the observational increments over Acidalia-Chryse at this time were relatively small.

In sol 7, however, some negative increments (~ -0.1) could be seen. The area of such large negative increments near Xanthe Terra (~ -0.2) was by now at the front of the dust storm, so it probably implied that the dust intrusion simulated in the reanalysis evolved too rapidly compared with the observations or the wind stress dust lifting

tended to lift too much dust in this sol (see Figure 7.9). In sol 8, the data assimilation was injecting dust by this time (leading to a ~ 0.2 increase in *tauref*) in Solis Planum and Xanthe Terra. The dust injection in Solis Planum, together with the cyclonic wind pattern, formed a dust storm center in Solis Planum in sols 8 & 9. The positive inrements taking place in the Xanthe region in sol 8 was at similar location as the negative increments in the previous sol. This might suggest that the reanalysis was producing reasonable amounts of dust as it travelled through the Acidalia-Chryse channel. The whole dust storm, however, was moving too fast in the reanalysis compared with the observations. In this situation, the data assimilation scheme then tried to reduce the dust amount in the front part of the dust storm in sol 7, while in the following sol (sol 8), the assimilation scheme was adding dust into the region to compensate for the amount of dust removed from the previous sol. This probably resulted from an incomplete representation of the meteorological fields (wind velocity) and tracer transport in the UK-LMD MGCM.

In sol 9, positive observational dust increments (~ 0.15) could be found near Hellas. These increments helped produce relatively high values of *tauref* in the south of Noachis close to the South Polar Region. In sols 8 & 9, with the help of the data assimilation scheme, the reanalysis was able to successfully reproduce many of the observed features of the dust distribution in Xanthe Terra, Solis Planum and south of Noachis Terra. These features were not spontaneously simulated by the UK-LMD MGCM, and it was evident, therefore, that the internal representation of the physical dust lifting mechanisms and dust transport still require further study and improvement to achieve a more realistic representation of at least some aspects of the dust cycle. In sol 10, the dust continuously spreads out into Noachis. In sol 11, along with more active dust events, the dust increments became more variable globally. Dust was

added into the south and east of Valles Marineris, but the data assimilation scheme then seemed to remove dust from other surrounding areas. In sol 12, the dust increments were relatively smaller than those in the previous sol, and the increments near Xanthe moved slightly to east but changed sign. In sol 13, more dust centers were activated, and dust clouds started to expand to occupy a larger area. Subsequently, those dust clouds were entrained into the global transport cycle, and encircled the planet, which then became noted as the MY 28 GDS.

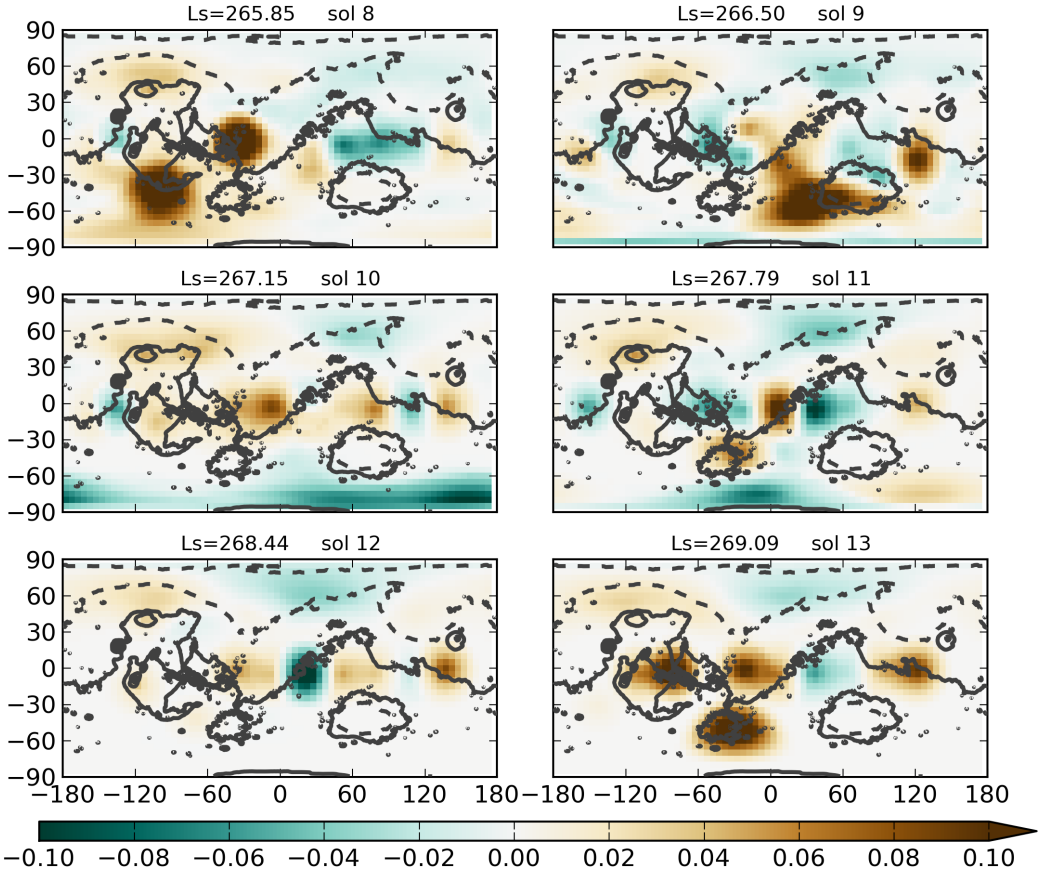

Figure 7.11 (continued).

During this precursor event, dust devil lifting appeared consistently to provide the background dust level, mostly in the southern hemisphere. On the other hand, dust lifted by the wind stress mechanism was found to be more strongly correlated with various identifiable centers of dust activity during the same period. Wind stress dust lifting was favored to inject dust into Alba Patera, the Acidalia-Chryse channel,

Xanthe Terra, Elysium Planitia and Noachis Terra. The dust increments introduced by the data assimilation scheme helped to "nudge" the numerical model towards the observed amount of dust, especially, when dust events were more active, and several dust centers formed during sols 10 to 13. Although intensive wind stress dust lifting events were simulated in sols 10 and 11, the injections of dust in multiple locations during sols 10 to 13 still needed to rely on dust assimilation increments, for instance, areas near Alba Patera, Isidis and Argyre, in order to match observations.

7.3.4. Maximum wind speed below 12 km

The Noachis dust events were consistent with the governing physics in the model, since the dust clouds were not predominantly injected by the assimilation scheme. The spatial maps of *tauref* from the reanalysis presented a clear trajectory of the Chryse dust storm that was consistent with visual images shown in the work of Wang and Richardson [2013]. This dust storm rapidly traveled from Chryse into the Noachis region in about 4 sols. Apart from the advection of dust, dust lifting was also active along the path of dust transport. The wind velocity in the reanalysis was also an indirect source of evidence to demonstrate the possible connection between the dust clouds of Chryse and of Noachis, not only for the results in our reanalysis, but also for supporting the observations based on visual images [Wang and Richardson, 2013].

Since the dust was readily transported horizontally with a vertical extension of more than 20 km, the maximum wind speeds below 12 km above surface were determined from the 2-hourly reanalysis and were then averaged between sols 0 and sol 3 (Figure 7.12). The dust storm traveled approximately 5000 km from Chryse to Noachis through Xanthe Terra. If the dust arrived at the Noachis region in sol 4, the average wind speed should be at least 14.5 $m \cdot s^{-1}$, and the average wind speed in the reanalysis

was obviously larger than 30 $m \cdot s^{-1}$ in Chryse and Noachis. Even though the wind speed decreased in Valles Marineris, the wind was still faster than 20 $m \cdot s^{-1}$ on average in the area. Based on their intermittent visual images, Wang and Richardson [2013] also claimed a higher wind speed (> 25 $m \cdot s^{-1}$) to establish the connection between the Chryse storm and Noachis dust events. The average maximum wind speed along the path of this precursor event was consistent with their assumption. However, Chryse should not be considered to be the only origin of the Noachis dust clouds, as the results in section 7.3.3 suggested that dust was not only lifted along with the movement of the dust storm, but also lifted in the areas in both the upwind and downwind directions.

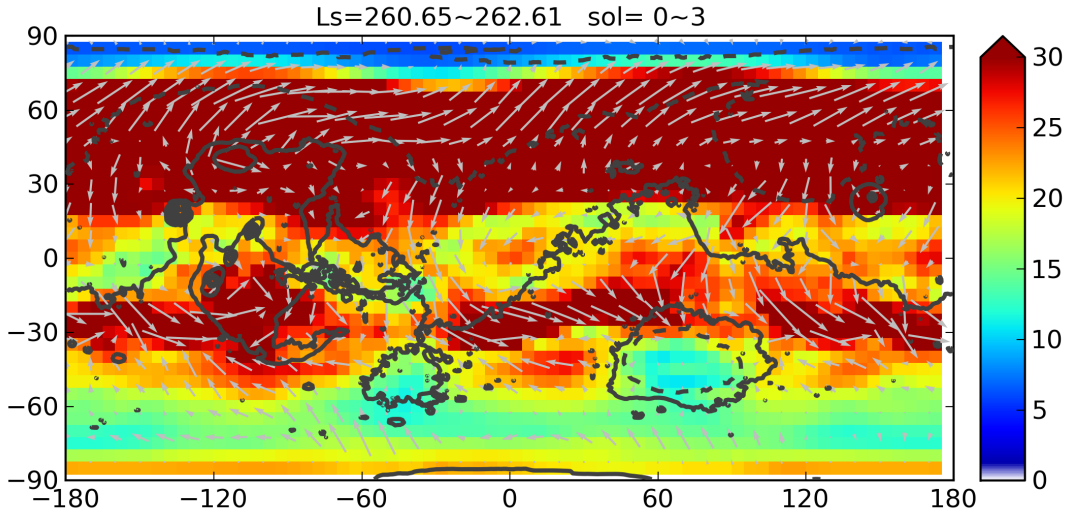

Figure 7.12 Average of maximum horizontal wind speed below 12 km above the surface during sols 0 ~ 3. The arrows are derived from the wind velocity at the first model level (~ 4 m) to indicate the prevailing wind direction in the period.

7.4. Evolution and impact of MY 28 GDS

7.4.1. Comparison of the reanalysis with observations

7.4.1.1. Validation against THEMIS dust data

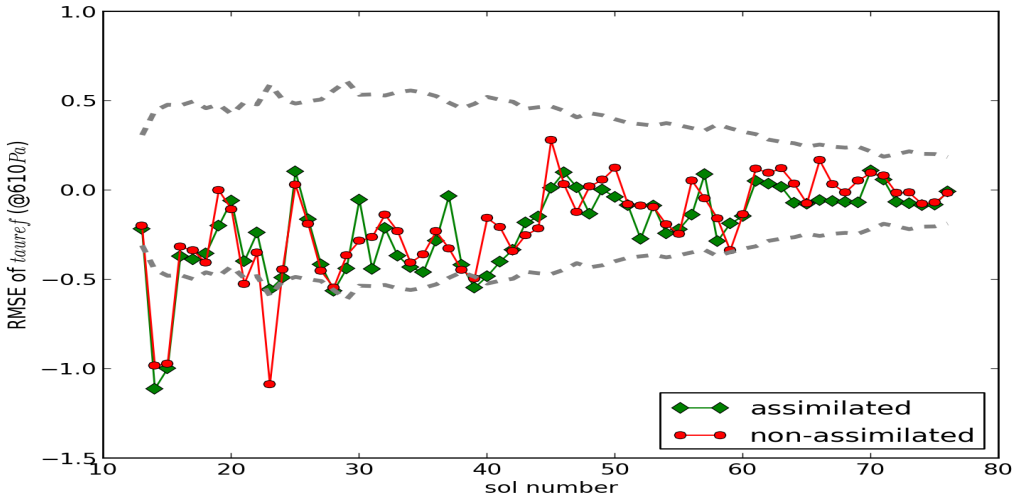

Figure 7.13 Same as Figure 7.5, but for the period between sol 14 and sol 78 ($L_s \approx 269.1° \sim 309.5°$).

During the MY 28 GDS, right after the precursor event, the reanalysis was validated against THEMIS data. THEMIS data had intensive coverage in the Southern Hemisphere during this GDS, although very few data were available to the north of the equator. Figure 7.13 shows the daily mean difference between dust opacities in the reanalysis and THEMIS data. The grey dashed lines represent the uncertainties of THEMIS data, chosen to be the larger value of 0.104 or 20% of the data values at visible wavelengths. The sol number is counted continuously from the beginning of the precursor event. Therefore, the study period of the MY 28 GDS extends from sol 14 to sol 78. It was evident that the reanalysis achieved reasonable agreement with the THEMIS datasets, even compared to the separated THEMIS dataset that was not assimilated. The differences between reanalysis and observations were in general smaller than the observational uncertainties.

Figure 7.14 shows the correlation of *tauref* between reanalysis and THEMIS data during this GDS. The reanalysis exhibited a slightly better correlation with directly assimilated data (Figure 7.14a) than with non-assimilated data (Figure 7.14b). During this intense storm, some of the observations had already reached opacity values of 6,

but the reanalysis tended to underestimate those large values (Figure 7.14a). The impact of the MY 28 GDS on the global dust distribution is studied in the following section by making comparisons with the corresponding distribution within the same time window in MY 29. Thus, the *taurefs* within the same time window of MY 29 ($269.1° \sim 309.5°$) are also compared to the THEMIS dust measurements (Figure 7.15). For MY 29, most of the dust measurements were within the range 0.2 – 0.6. The reanalysis produced fields of *tauref* in promising agreement with the THEMIS dust data, but with a small systematic underestimate compared with the whole dataset.

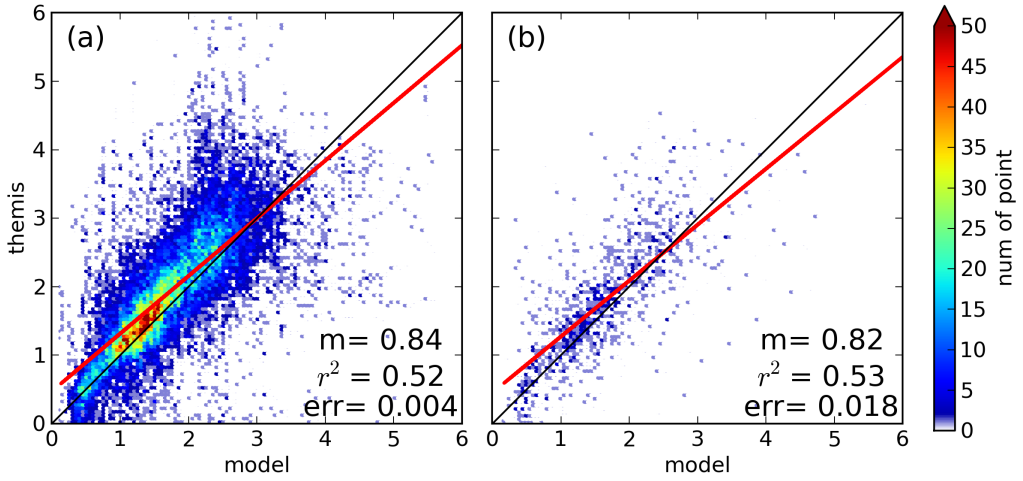

Figure 7.14 Same as Figure 7.6, but for the period between sol 14 and sol 78 ($L_s \approx 269.1° \sim 309.5°$).

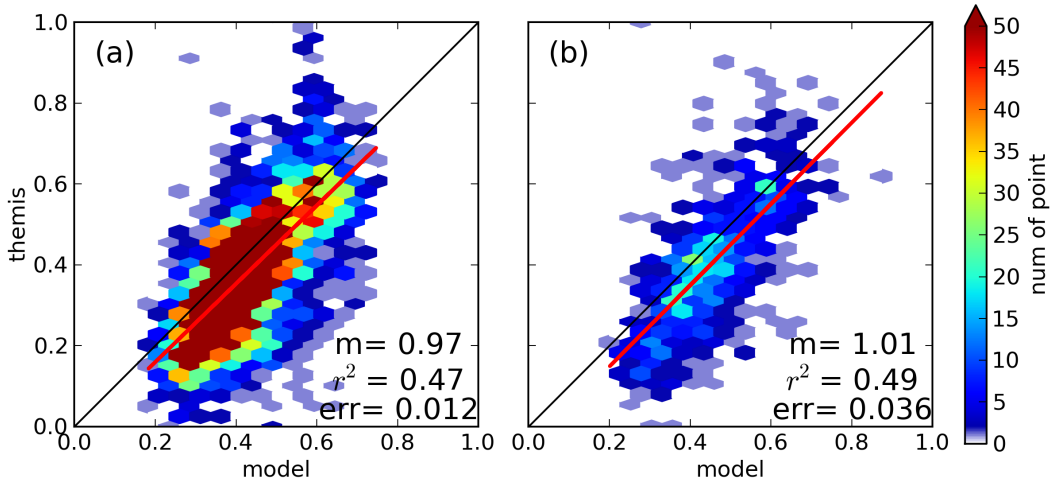

Figure 7.15 Same as Figure 7.14, but for the same period in MY 29 ($L_s \approx 269.1° \sim 309.5°$).

7.4.1.2. Validation against MCS dust data

The reanalysis is further validated against the MCS dataset in terms of the dust vertical distribution in units of km^{-1}. The reanalysis exhibited a similar performance during the MY 28 GDS in both assimilated (Figure 7.16a) and non-assimilated (Figure 7.16b) MCS data. The agreement of the reanalysis with THEMIS dust data varied with altitude. In the height range close to the ground (0-10 km), the reanalysis displayed large discrepancies due to the weak data constraint at these levels. The agreement was within or close to the observational uncertainties in 10-20 km and 20-30 km, but the discrepancy grew above altitudes of 30 km. These large discrepancies were the results of lacking MCS data in the Southern Hemisphere during the peak of the dust storm. Within the same time window of MY 29, the MCS dataset had significantly more data below 30 km than that of MY 28 (Figure 7.17). As a result, even within the 0-10 km interval, the reanalysis still exhibited promising agreement. The largest discrepancy for this period was at 30-40 km, and others were well within the observational uncertainties or very close to them.

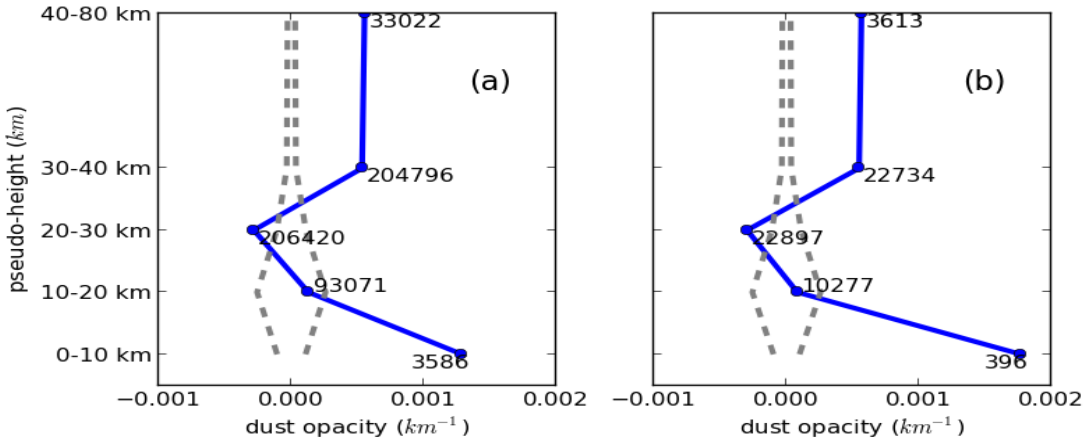

Figure 7.16 Same as Figure 7.7 but for the average difference between reanalysis and MCS data in sols 14-78 of the MY 28 GDS.

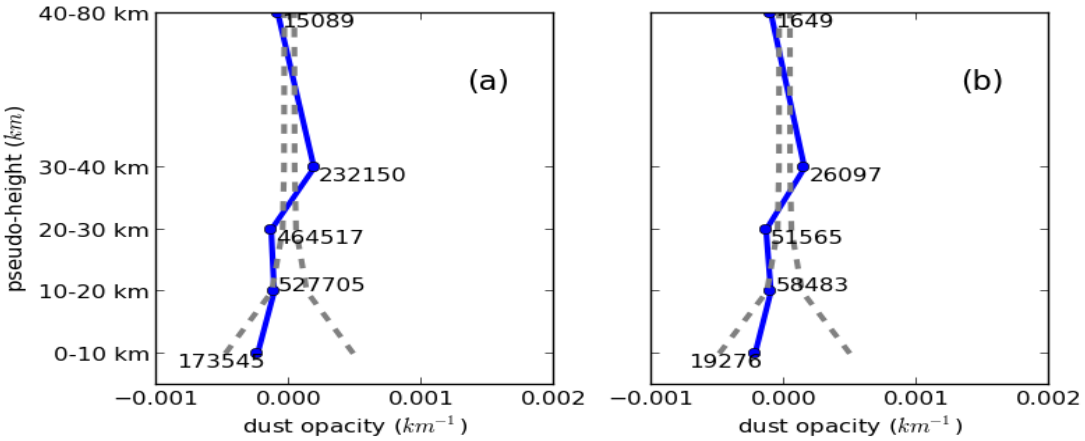

Figure 7.17 Same as Figure 7.16 but for the same period in MY 29.

7.4.1.3. Comparison with Mars Exploration Rovers' data

During the MY 28 GDS period and the corresponding time window of MY 29, ground based measurements were available in two locations from two independent rovers, i.e. "Spirit" and "Opportunity" [Lemmon et al., 2004]. They were operating at Gusev Crater and Meridiani Planum, respectively. The reanalysis dataset was validated against the Pancam data from these two rovers, as illustrated in both Figure 5.9 ("Spirit") and Figure 5.10 ("Opportunity"). In those figures, the blue lines represent rover data, and purple lines indicate the reanalysis. For both years, the reanalysis compares well with the "Spirit" dataset. Even though the rover datasets were not included in the assimilation, the latter still clearly reproduced the evolution of dust activity at Gusev Crater during $L_s \approx 269.1° \sim 309.5°$ of both years (Figure 5.9). At Meridiani Planum (Figure 5.10), the reanalysis has captured the evolution of the observations but underestimates the maximum in MY 28 and in the time window of MY 29.

7.4.2. Spatial maps of the dust distribution

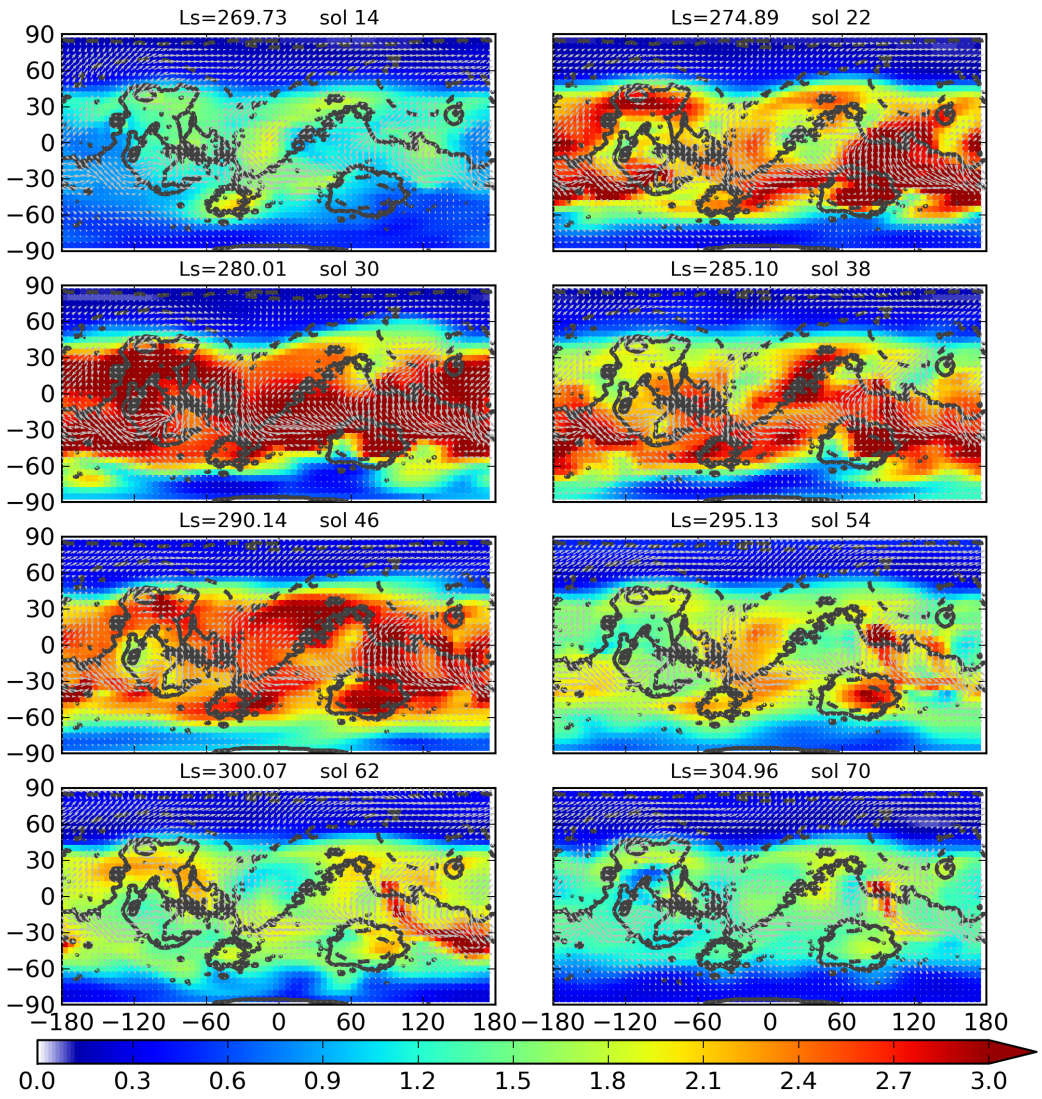

Figure 7.18 Similar to Figure 7.8, but showing spatial maps of daily-averaged *tauref* every 8 sols with a different color scale.

The measurements of dust from space-borne instruments are generally intermittent in time and space. Although the THEMIS team deliberately increased the density of measurements during the MY 28 GDS, the coverage of data was mainly restricted to the southern hemisphere and, even in southern hemisphere, the observations were still unable to capture complete and continuous maps of temperature or dust. The four-dimensional reanalysis is able to provide continuous information to be able to observe the evolution of the MY 28 GDS. It is also possible to study the impact of the MY 28 GDS on the global climate and circulation through diagnostics of the reanalysis

dataset. It was possible, of course, that the model might not always spontaneously produce dust events at the correct locations, but the dust increments from data assimilation might sometimes be the major factor in redistributing the dust in the model simulation. However, the dust distribution in the reanalysis was able to provide an unprecedented coverage that was seldom exceeded by the available observations.

Figure 7.18 shows the spatial maps of daily-averaged *tauref* every 8 sols during the evolution of the GDS. As in the section 7.3, the sol number here counts from the beginning of the precursor event. In sol 14, active dust centers are mainly located near Alba Patera, in the Xanthe-Meridiani and Argyre-Noachis regions, and in Arabia Terra and Elysium. The *tauref* values found at this time were up to ~ 2 in those active centers. In sol 22, the GDS had already intensified, raising *taurefs* values to > 3 in some places. The wind pattern was still broadly similar in form to that of sol 14, however. The strongest winds mainly blew from the Northern to the Southern Hemisphere down to latitudes ~ -45°, while the prevailing winds changed to an eastward dominated flow at ~ -30°. Although the storm intensity increased, the airborne dust was mainly restricted to within the latitudes -60° ~ 50°. Within the storm area itself, Tharsis Montes and part of the Meridiani-Arabia region remained relatively clear with *tauref* ~1.5. The most dusty region was around Hellas with opacity values of *tauref* > 3. The prevailing winds then blew from Elysium through Isidis into this region. By sol 30, the area between latitudes -60° and 50° were entirely covered by this GDS. During this time, the northern boundary of the storm remained the same as that of sol 22, and it was probably linked to a strong polar vortex. However, some of the dust lifted by the storm was already penetrating into the South Polar Region, and *tauref* reached values ~ 2 in those areas.

By sol 38, the GDS had started to dissipate. *tauref* near Alba Patera, and in Tempe Terra, Chryse Planum, Meridiani Planum and Elysium had then reduced to below 2. Intensive dust concentrations ($tauref > 3$), however, were still found near Arabia, Hellas and Daedalia. The GDS remained at similar strength in sol 46, and the dust was redistributed to cover the area more evenly. Although some places, e.g. Isidis and Arabia, had more dust cover at this time than they had in sol 38, *tauref* values near Hellas and Daedalia had obviously decreased to below 3. Dust finally started to settle down globally by sol 54, and the Chryse-Xanthe-Noachis and Isidis-Hellas regions now contained more dust than in other regions. *tauref* continued to decrease thereafter, and most regions were clearer than *tauref* ~ 2 by sol 62, including Meridiani Planum and Arabia Terra which appeared to be much clearer by this time, although a small dust storm was seen to travel along Isidis to Cimmeria. By sol 70, *tauref* in most of the areas had already dropped to below 1.5 and Tharsis Montes became almost completely clear with $tauref < 0.5$, even though additional dust clouds were still apparently being lifted within Isidis.

A set of comprehensive and truly continuous observations were not normally available for Mars, particularly for the period of the MY 28 GDS, and it is obviously intriguing to use this reanalysis to directly study the impact on the dust distribution across the planet due to the development of this GDS. In the following, we make a comparison of dust distributions with the following year that was without a major GDS (MY 29). The *tauref* maps were averaged over the same time window $L_s \approx 269.1° \sim 309.5°$ for both years, corresponding to an interval of 64 sols. It must be admitted that the dust distribution at this season in MY 29 was likely not to be wholly representative of a typical long-term average dust climatology. The comparisons here should therefore be seen as referring more specifically to the

conditions during MY 29. To some extent, however, the dust distribution on Mars during this year was more consistent with general trends seen for most MYs than in MY28. Therefore, this direct year-to-year comparison can still be regarded as revealing some of the influences of a major GDS compared with a typical state.

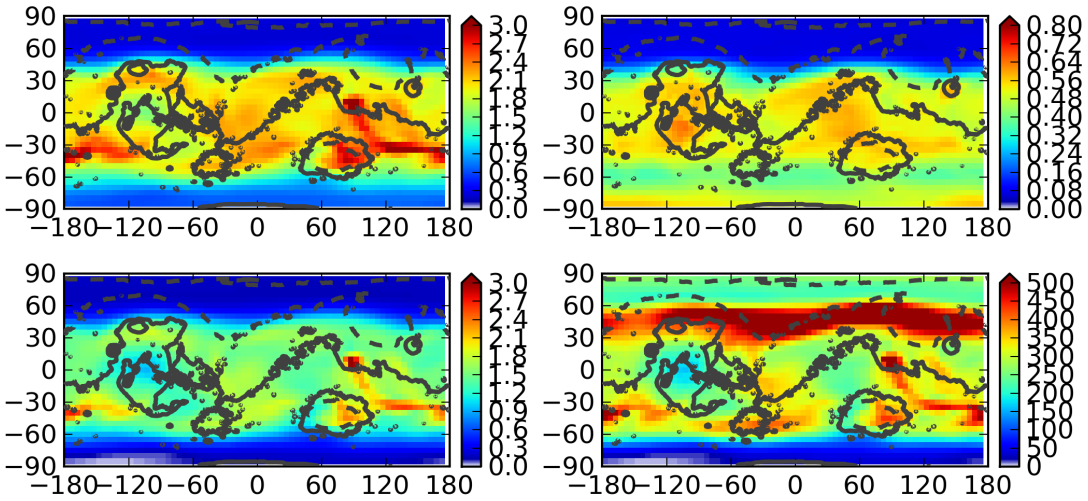

Figure 7.19 *tauref* averaged over the MY 28 GDS period ($L_s \approx 269.1° \sim 309.5°$, in total 64 sols; upper left panel), *tauref* averaged over same L_s time window in MY 29 (upper right panel). The difference was obtained by subtracting values during MY 29 from corresponding values in MY 28 (bottom left panel). Note the different color scales show the values of *tauref* in opacity. The bottom right panel is the percentage difference (%) in terms of *tauref* in MY 29.

Figure 7.19 shows maps of the value of *tauref* averaged over the MY 28 GDS, compared with the value of *tauref* averaged over the same period in MY 29, together with the differences between these two averages. In MY 28, the dust loading in the area between latitudes -60° and 45° was significantly larger than those in both polar regions. *tauref* was above 2 across in wide area during MY 28, and in some places had an average *tauref* larger than 3, mainly including Isidis, Tyrrhena, east of Hellas, Cimmeria and Sirenum. The area near -40° in the Southern Hemisphere was evidently more dust-active than other parts of the planet. In MY 29, the overall pattern of dust distribution at this season was quite different, with dust loadings and opacities that were significantly lower than in MY 28, in general remaining no higher than ~ 0.5

between latitudes -60° and 45°. The areas with relatively larger values of *tauref* were different from those in MY 28. They were found near Tharsis Montes, Cimmeria and the area between Arabia and Hellas. In this MY, dust was not obviously confined to the low and middle latitudes, and the Southern Polar Region was found to have similar dust loadings as in the low latitudes. The averaged values of *tauref* during MY 29 were subtracted from those values in MY 28 to show the influence of the GDS on the columnized dust distribution. Not surprisingly, dust opacities in MY 28 were globally larger than those in MY 29 (in general by > 1.5), as an active GDS injected large amounts of dust into the atmosphere. The active dust channel, from Isidis through Cimmeria to Sirenum, clearly shows the largest differences in opacity, in some places > 3. Between latitudes -60° and 45°, two major areas had differences smaller than 1.3, i.e. over Tharsis Montes and in the area between Arabia and Hellas. An interesting pattern could be noticed with regard to these two areas, however. These two areas were covered by relatively less dust compared to other areas between latitudes -60° and 45° in MY 28, while they were actually obscured by more dust in MY 29. The percentage difference suggests that the largest difference compared to MY 29 was found between latitudes 30° and 60° in the Northern Hemisphere, which corresponds to the boundary of polar vortex. Although the dust seemed to be confined between latitudes -60° and 45°, the percentage difference compared to MY 29 still showed more than a 2 times difference in the North Polar Region. In contrast, the South Polar Region surprisingly exhibited the lowest percentage differences (< 100%) compared to MY 29. Overall, the percentage difference in opacity between latitudes -60° and +45° was about 3 times the corresponding values in MY 29.

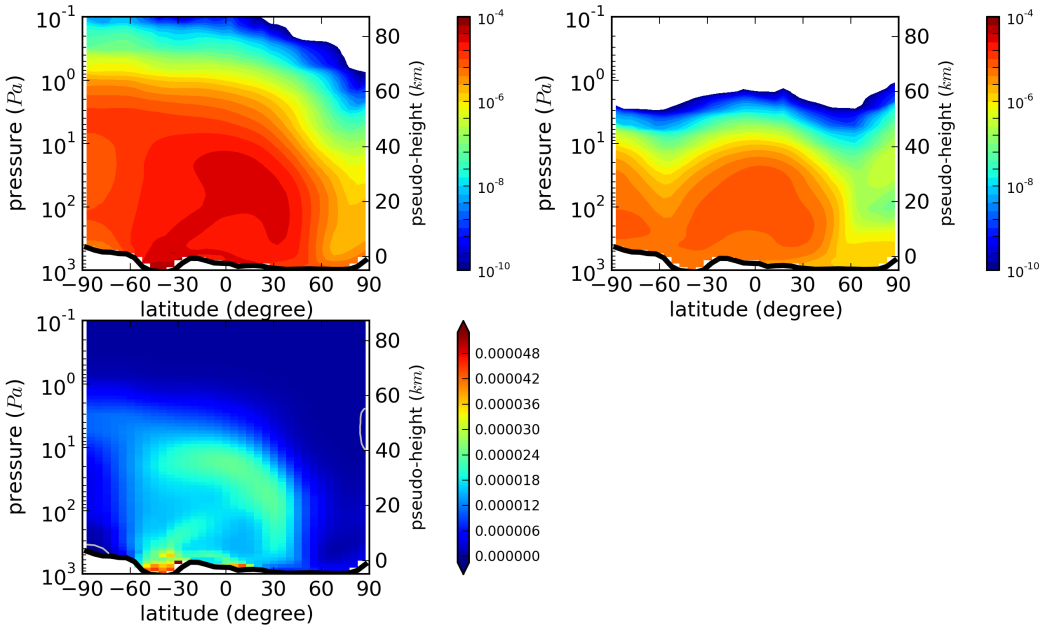

Figure 7.20 Log_{10} of the zonal average dust mass mixing ratio (kg·kg^{-1}) averaged over $L_s \approx 269.1° \sim 309.5°$ (a total of 64 sols). Upper left panel is for MY 28 and upper right panel is for MY 29. The bottom panel shows the difference between the two upper panels (MY 28 - MY 29) using a linear color scale; the grey lines show the negative differences. Note the log color contours for the two upper panels are shown every 0.2 log units. The black line indicates the approximate zonal mean topography.

7.4.3. Zonal vertical distribution of dust

Figure 7.20 shows latitude-height maps of the zonal and temporal averages of the dust mass mixing ratio in the time window of the MY 28 GDS during MY 28 and MY 29, respectively. The difference between the two years is also shown in linear color contours in Figure 7.20. In MY 28, the tops of the dusty layer (arbitrarily defined as mass mixing ratio 10^{-7} kg·kg^{-1} as in Chapter 6) mostly remained at a uniform height in the Southern Hemisphere, but started to be dramatically lower from latitude ~ 30° northward. Dust was seen to penetrate into the upper part of atmosphere (~ 70 km) from latitude 45° southward. In the North Polar Region, a moderate vertical dust penetration could be seen in the reanalysis (~ 40 km). A northward inclined "mushroom-like" maximum of dust mass mixing ratio was clearly apparent within the dusty region, starting from the bottom of Hellas (~ -45°) and pointing northward until

~ 40° and then upward to ~ 38 km. This was probably associated with the intensified Hadley circulation (discussed in section 7.4.4) during the main storm. The dust mass mixing ratios in both polar regions were comparably smaller than at lower latitudes. The dust mass mixing ratio in South Polar Region exhibited two maxima within the dusty region. One was near 15 km altitude, and the other was at about 45 km. In the North Polar Region, the dust mass mixing ratio decreased with height nearly all the way to the upper atmosphere.

In MY 29, the zonal mean vertical distribution of dust resembled the vertical dust distribution at $L_s = 270° \,\&\, L_s = 315°$ seen in the study of McCleese et al. [2010] using MCS data. Dust concentrations were obviously more in the summer hemisphere (i.e. Southern Hemisphere) than in the winter hemisphere (i.e. Northern Hemisphere). Dust mass mixing ratios reached their maximum values over the tropics (~ 100 Pa or 20 km). The dust-free air in the Northern Hemisphere extended into the North Polar region, and a maximum of dust mass mixing ratio was found aloft between altitudes of 25 km and 40 km over the North Pole. The dust extended to similar heights in the South Polar Region as in the tropics, but with a lower penetration height at ~ -60°. From latitude 45° southward, dust was transported to altitudes of ~ 40 km in the atmosphere, much lower than in MY 28 (~ 60 km).

The pattern of dust mass mixing ratio in MY 28 dominated in the interannual difference map of zonal average dust mass mixing ratio. The mixing ratios in MY 28 were generally much larger than those in MY 29, and in the extreme cases, differences could be up to 5 times larger. The mushroom-like distribution was still clear in this difference comparison, and this suggested that an intensified Hadley circulation was likely to have been the major contributor, given the amount of dust in the atmosphere was already increased by the MY 28 GDS.

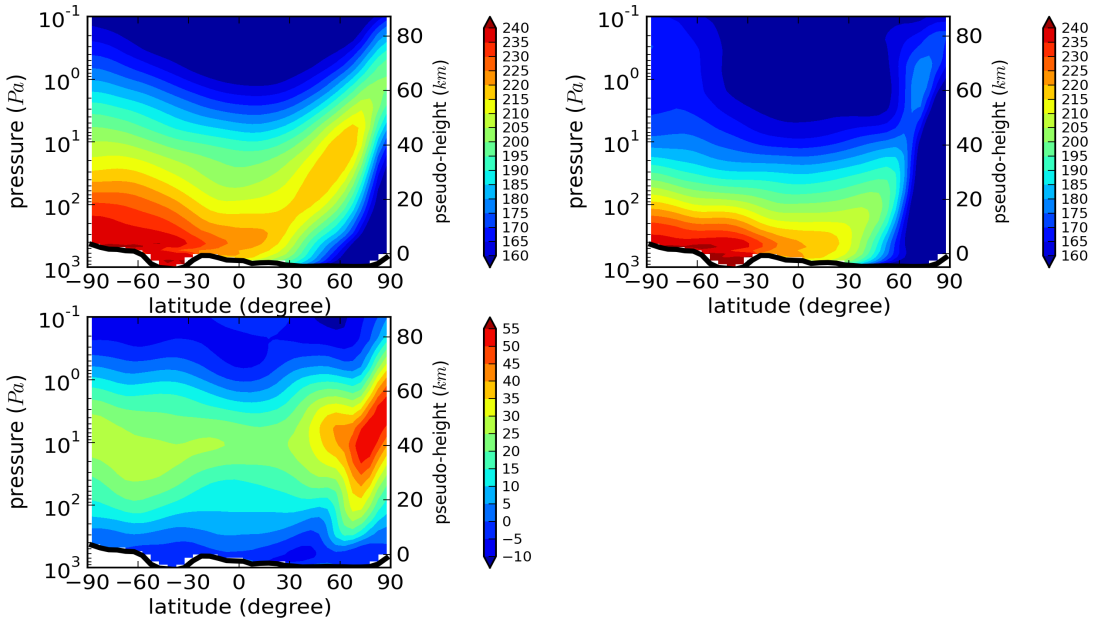

Figure 7.21 Zonal average of temperature (K) averaged over $L_s \approx 269.1° \sim 309.5°$ (a total of 64 sols). Upper left panel is for MY 28 and upper right panel is for MY 29. The bottom panel is the difference of the two upper panels (MY 28 - MY 29). The black line indicates the approximate zonal mean topography.

7.4.4. Zonal mean of temperature and intensified winter polar warming

Because of the thermal effects of suspended dust particles, temperature variations on Mars always show a strong correlation with the distribution of dust, especially under dusty conditions. As a result, a significant anomaly of dust distribution may make a considerable impact on the thermal state of the Martian atmosphere. Figure 7.21 shows the zonal and temporal averages of temperature in MY 28 and MY 29 over the same seasonal time window. The atmosphere during the MY 28 GDS was obviously warmer than it was in MY 29. Over the South Pole, the vertical temperature gradient below 100 Pa was bigger in MY 29. The 220 K contour already reached ~ 30 Pa in MY 28, while it only reached ~ 100 Pa in MY 29. For both MYs, the maximum temperatures (> 240 K) were both reached near latitudes -60° and -45° (the same latitude as the Hellas Basin). The maximum temperatures over the tropics were nearly the same for both MYs, but the atmosphere in MY 28 evidently had a smaller vertical temperature gradient. In MY 28, the polar warming in the Northern Hemisphere was

very strong, and it had a deep vertical extension (~ 150 Pa – above 0.1 Pa) and a wide latitudinal expansion even to the atmosphere over the tropics. A similar reversed (poleward) temperature gradient was seen in the Southern Hemisphere. Because the strongest direct solar radiation was located in the Southern Hemisphere during this season, this reversed temperature gradient should be associated with radiative effects instead of dynamical effects that are normally taken to be the main explanation for polar warmings [Kellogg and Schilling, 1951]. In MY 29, the polar warming in the Northern Hemisphere had a smaller vertical extension (~ 100 Pa – above 0.1 Pa) than that seen in MY 28, but was much weaker. The heating was dominant in the difference of zonal and temporal averages of temperature. Globally, the strongest heatings due to the MY 28 GDS (maximum > 50 K difference) were close to the top of the dust storm before the dust mass mixing ratio decreased (~ 10 Pa), and the coolings (leading to a maximum of > 10 K) were found above ~ 0.4 Pa and near the ground. These distributions of heating and cooling also coincided with the analysis of the zonal anomaly of a southward-moving dust storm in Chapter 6. The more intensive heating always happened near the tops of the dust storm, as the dust particles strongly absorbed the solar radiation. However, they also reduced the incoming solar radiation intensity into the lower atmosphere, so that as a result, the atmosphere near the ground was cooler. Similarly, the cooling above the dust layer top occurs because the thick dust layer also reduces the outgoing radiation due to the absorption of long wave radiation. The polar warming in the Northern Hemisphere (winter) could thus be intensified by over 50 K when it occurred between 20 Pa and 2 Pa. For comparison, the temperature in the Southern Hemisphere (summer) could be increased by 25 K during this intense GDS.

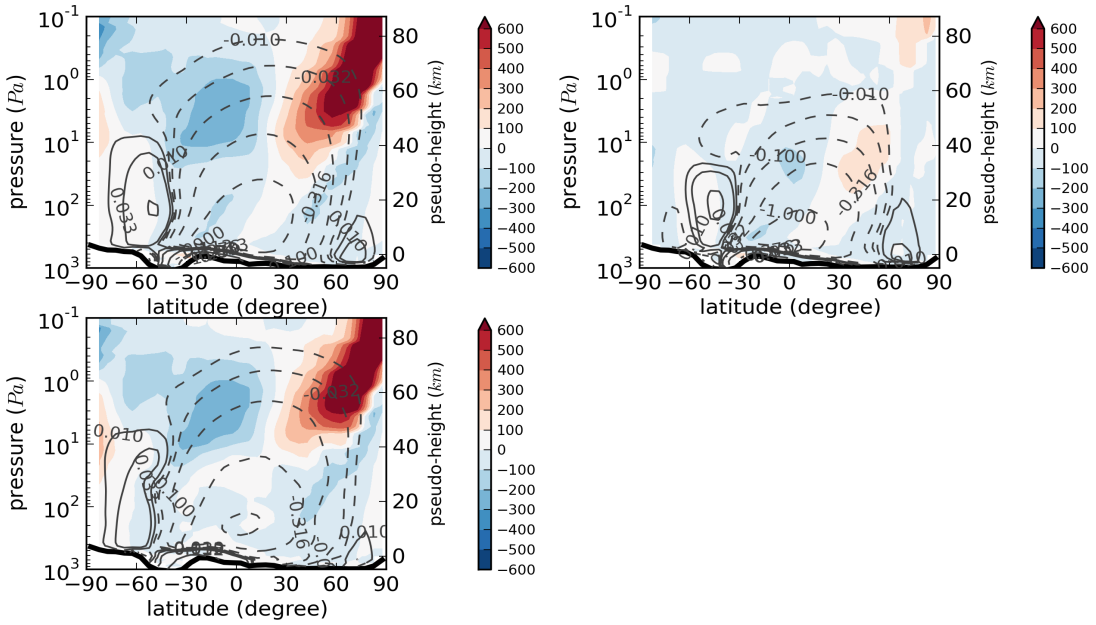

Figure 7.22 Zonally averaged mass stream function (10^{10} kg·s^{-1}; contour lines) and adiabatic heating rate (K·sol^{-1}; shaded color) averaged over the 64 sols of $L_s \approx 269.1° \sim 309.5°$. Upper left panel is for MY 28 and upper right panel is for MY 29. The bottom panel is the difference of the two upper panels (MY 28 - MY 29). Stream function contour intervals are logarithmic with negative values indicating clockwise circulation. The black line indicates the approximate zonal mean topography.

Polar warming over the winter pole was first explained in the theory by Kellogg and Schilling [1951], in which it was maintained dynamically through a thermal circulation with adiabatic heating taking place in the region of descent over the winter polar region. Various numerical experiments have since been conducted to study the Martian polar warming. Wilson [1997] used a MGCM to illustrate that the development of a thermally direct Hadley circulation could produce a polar warming phenomenon. In another numerical experiment designed by Medvedev and Hartogh [2007], the adiabatic heating, along with the extension of meridional transport, was demonstrated to play a more important role in magnifying the polar warming under dusty conditions than that of the direct solar (diabatic) heating of dust particles. Figure 7.22 shows the zonally averaged stream function and adiabatic heating rate during the GDS time window. For a non-GDS MY (MY 29 in this context), the adiabatic heating was dominant in the Northern Hemisphere (where the maximum

heating rate was 356 $K \cdot sol^{-1}$), while adiabatic cooling was dominant in the Southern Hemisphere (where the maximum cooling rate was 251 $K \cdot sol^{-1}$). The locations of the adiabatic heating in the North Polar Region were consistent with the polar warming in Figure 7.21. In a GDS year (MY 28), it was evident that the meridional circulation was strengthened during the MY 28 GDS, with a stronger extension vertically and poleward. The adiabatic heating rate in the North Polar Region also increased significantly with a maximum value of 1181 $K \cdot sol^{-1}$; a value that was more than 3 times that of MY 29. Apart from the thermal and dynamical impacts of the meridional circulation during the MY 28 GDS, the strong downward branch of the meridional circulation between 30°N and 60°N appeared to stop the further transport of dust into North Polar region, and instead, transported clearer air towards the equator near the ground. The stronger meridional circulation was therefore also responsible for generating the "mushroom" pattern of dust mass mixing ratio close to the equator (Figure 7.20).

7.4.5. Global average dust lifting rates

The dust events are undoubtedly always associated with dust liftings. Figure 7.23 shows the global average dust devil lifting rate and the global average of *tauref* in the same period of MY 28 and MY 29. In general, the strength of dust devil lifting was expected to be relatively consistent from year to year [Newman et al., 2002a]. After the outburst of GDS in sol 14, its global average intensity was smaller than that of the same period of MY 29. This suggested that the dust devil lifting was clearly suppressed by this intensive dust storm due to its negative feedback [Newman et al., 2002a]. On the contrary, the wind stress lifting rate was very variable and obviously increased during MY 28 GDS (Figure 7.24). It was found to have three phases of

changing. They were during the precursor events (sol 0-13), during the outburst of MY 28 GDS (sol 14-39), and before the final decay of MY 28 GDS (from sol 40 onward). The wind stress dust lifting displayed strong correlation with the global average dust loadings. This strong correlation should result from the positive feedback of the wind stress lifting [Newman et al., 2002a].

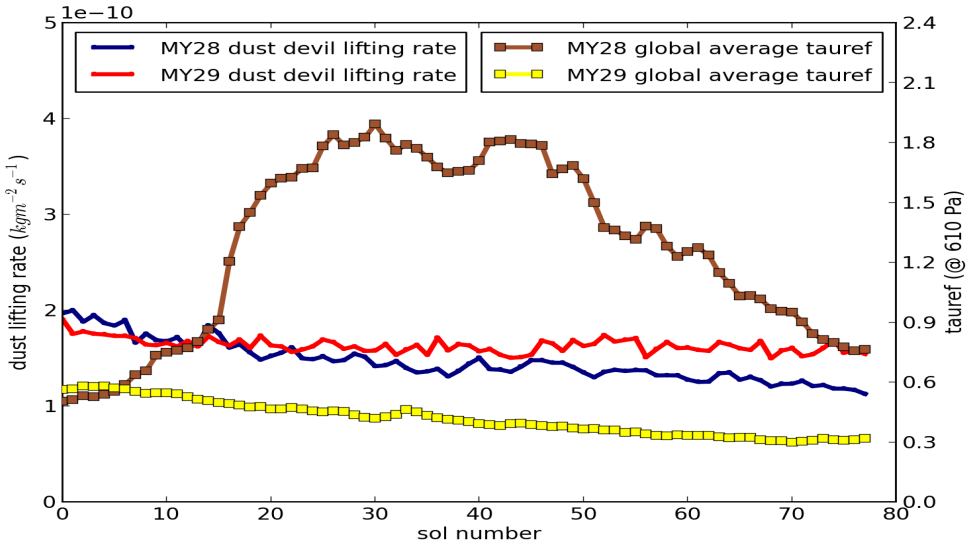

Figure 7.23 Global average dust devil lifting rate and *tauref* for the period from the start of precursor event (sol 0) to sol 78 ($L_s \approx 260.7° \sim 309.5°$) in both MYs.

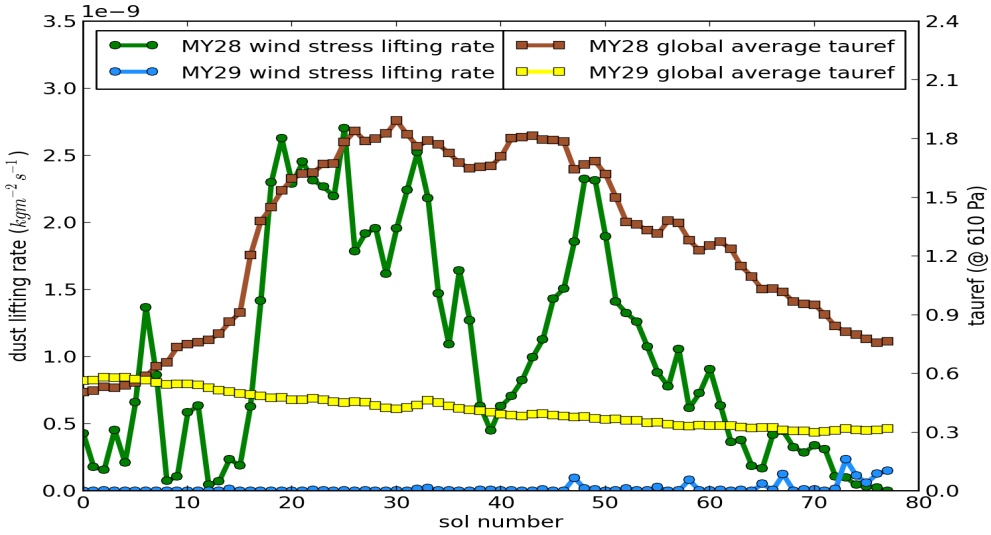

Figure 7.24 Same as Figure 7.23, but for the global average wind stress lifting rate.

7.5. Summary and discussion

In this chapter, the reanalysis was used to study both the precursor event and the related global and local impacts of the MY 28 GDS itself. The reanalysis was validated against various observational datasets for specific events. The correlations between reanalysis and THEMIS were shown to be strong. The comparisons with the MCS dataset suggested that the reanalysis was able to capture the dust vertical distribution above 10 km during the precursor event. The largest discrepancies often happened below 10 km in general or above 30 km during the height of the MY 28 GDS. They were always the result of weak data constraints. Nonetheless, the reanalysis exhibited very promising agreement with MCS data at all available heights during $L_s \approx 269° \sim 309°$ in MY 29.

The continuous reanalysis dataset was able to quantitatively depict the evolution of the sequence of dust events before the outburst of the MY 28 GDS itself. The columnized dust distributions were roughly consistent with the study of Wang and Richardson [2013] that was based on mosaics of intermittent visual images. Since the dust increments from the data assimilation process were not overwhelming along the path of this precursor event, it seems that the representation of physical processes (e.g., meteorology, dust transport, and dust liftings) within the UK-LMD MGCM was sufficient to produce quite realistic dust distributions. In the reanalysis, this precursor event did not only consist of a singular system, but also involved a series of separate dust events along its way to Noachis. Direct wind stress lifting appeared to be responsible for the initiation of the Chryse dust storm, while the dust devil lifting mechanism provided the background dust. The dust storm that occurred in Noachis was actually the joint result of the earlier Chryse storm and dust lifting along its path and local dust lifting in Noachis itself. The maximum average wind speed was also evidently strong enough to enable the Chryse dust storm to travel all the way to

Noachis, consistent with the condition discussed by Wang and Richardson [2013]. However, the UK-LMD MGCM failed to spontaneously generate the additional dust centers in the expansion of the precursor events. The build-up of those additional dust centers in the reanalysis relied mostly, therefore, on the dust injection due to the data assimilation correcting the dust distribution in the model.

The evolution of the atmospheric structure and meteorology during MY 28 was briefly described in this chapter, and the impact of the MY 28 GDS ($L_s \approx 269.1° \sim 309.5°$) was studied here by making a comparison with the same time window in MY 29, which did not support a GDS. Between latitudes -60° ~ +50°, the average difference in dust opacity between the two years during the MY 28 GDS could be more than three times larger than that of the same period in MY 29. During MY 28, the dust was obviously transported much higher into the atmosphere. The tops of the dust clouds could be as high as up to 70 km to the south of 45° latitude in MY 28, while they were only at about 40 km in MY 29. The vertical penetration decreased dramatically in association with the downward branch of the Hadley circulation, but it was much more obvious in MY 28, and actually formed a "mushroom" structure in the zonal mean dust distribution.

The polar warming in the Northern Hemisphere was much stronger during the MY 28 GDS by ~ 50 K on average compared to the equivalent period in MY 29. The vertical extension of the polar warming for the MY 28 GDS stretched from ~ 150 Pa to above 0.1 Pa, and was larger than that of MY 29. Among other studies of polar warmings in terms of realistic dust conditions, the study of Martin and Kieffer [1979] also discussed the north polar warming under the dusty condition of a realistic GDS. However, due to data limitations, their analysis only went down to the 50 Pa level. More recently, McDunn [2013] proposed a method of characterizing Martian polar

warmings, including the MY 28 GDS period, but they only considered the data above 10 Pa. The vertical extension reported in this chapter was notably lower than the reports from other studies of north polar warmings [e.g. Smith et al., 2001; Kleinbohl et al., 2009; Heavens et al., 2011b]. This is mainly because the polar warming can be intensified under GDS condition, and the reanalysis is able to provide detail insight to its thermal structure with consistent spatial and temporal coverage during MY 28 GDS.

In this study, the merdional circulation was demonstrated to intensify significantly during the MY 28 GDS. The pattern of adiabatic heating associated with downwelling was consistent with the location of the polar warming in the Northern Hemisphere (winter). During the MY 28 GDS, the maximum of the average adiabatic heating over Northern Polar Region (1181 $K \cdot sol^{-1}$) was 3 times that of the non-GDS MY 29 (356 $K \cdot sol^{-1}$). The magnitude of this adiabatic heating rate was actually much bigger than the value obtained in the model experiment conducted by Medvedev and Hartogh [2007]. This was probably because they simply superimposed artificially high dust loadings in the season of southern winter that was normally mild for dust. More importantly, the dust loadings used in their experiment were comparably smaller than encountered during the MY 28 GDS.

In addition, the intense dust had continually suppressed the dust devil lifting during MY 28 GDS. Although the wind stress lifting was clearly increasing during the GDS due to the positive feedback, based on this reanalysis, it is hardly to conclude that the wind stress lifting triggered the MY 28 GDS. It is entirely possible that the increase of wind stress lifting was the response of the increase of dust loadings due to the assimilation. Apart from showing what we observed in the reanalysis, this remains an unresolved question for this MY 28 GDS. To answer this, we need a sophisticated

way to separating the positive feedback of wind stress lifting due to the assimilation-injected dusts while the UK-LMD MGCM can still produce meteorological conditions before this MY 28 GDS that is close to what was observed in the reanalysis.

Chapter 8 Conclusions and Future Work

8.1. Semiannual oscillation on Mars

The first task involved in this thesis project was to investigate the possible existence of a semiannual oscillation (SAO) embedded in the zonal mean zonal wind on Mars. The dataset analyzed in this study was from a reanalysis (MACDA) in which measured temperature profiles and column-integrated dust opacities were assimilated [Lewis et al., 2007; Montabone et al., 2011b].

A Martian SAO, similar to that in the Earth's tropical stratosphere, was evident in the reanalysis not only in the tropics, but also extending to higher latitudes. Unlike on Earth, the SAO was found not always to reverse its zonal wind direction, however, but only manifested itself as a deceleration of the dominant wind at certain pressure levels and latitudes. Singular Systems Analysis (SSA) was further applied on the zonal mean zonal wind $u(t,p)$ in different latitude bands to reveal the characteristics of SAO phenomena at different latitudes. The second pair of principal components (PCs) was usually dominated by a SAO signal, though the SAO signal could be strong enough to manifest itself also in the first pair of PCs. The amplitude of the SAO signal was isolated by solely reconstructing $u(t,p)$ using the second pair of PCs; its amplitude could easily reach a maximum of 20 m/s or even greater.

A TEM analysis was applied on pressure-coordinates in the tropics to further elucidate the forcing processes driving the tendency of the zonal-mean zonal wind. The zonal mean meridional advection term was found to strongly correlate with the observed oscillations of zonal-mean zonal wind, and supplied the majority of the westward (retrograde) forcing in the SAO cycle. However, compared to the work of Kuroda et al. [2008], this forcing due to meridional advection displayed less asymmetry between the two SAO cycles during a year in this thesis study. Furthermore, the zonal mean vertical advection term was shown to mainly supply the eastward forcing in a strong annual cycle. The total wave forcing supplied forcing to the zonal mean zonal wind that was nearly the opposite of the meridional advection term above ~ 3 Pa, but it also partly supported the SAO between 40 Pa and 3 Pa. In contrast to the results of Kuroda et al. [2008], there was no consistent SAO signal in the forcings due to either total wave forcings or thermal tides. Moreover, the forcing due to transient waves was not negligible and supplied a similar strength of forcing to that of the forcing due to quasi-stationary waves. In addition, in the diagnostic results of Chapter 3, eastward Kelvin waves were found to mainly supply eastward momentum to the zonal-mean zonal wind, similar to their role on the Earth. This is consistent with the dissipation of their wave action. It is also evident that the westward forcing yielded by the eastward Kelvin waves in the work of Kuroda et al. [2008] is likely wrong.

Some distinctive features occurring during the period of the MY 25 global dust storm (GDS) were also notable. For instance, the meridional advection term supplied weaker westward momentum during the first half of MY 25 than before the onset of the MY 25 GDS in the second half of MY25, but substantially stronger eastward momentum and westward momentum were noticeable in the second half of MY 25

than those in other MYs. In addition, the forcings due to vertical advection, transient waves and thermal tides appeared to be stronger during MY 25 GDS. The intensified thermal tides most probably resulted from the enhanced solar heating effect due to increased dust loadings during the GDS. However, to establish any further link between those distinctive features and the trigger/response of a GDS still requires at least analyzing one other GDS event accordingly, for instance the MY 28 GDS observed in MCS mapping period. That may also improve the representation of tides in the current reanalysis, as MCS dataset extends higher in altitude than TES dataset.

8.2. Updated data assimilation system

The data assimilation system based on UK-LMD MGCM was updated in the work of this thesis in two aspects, 1) to include the activated dust lifting and transport schemes with the assumption of a single dust size distribution during the assimilation, and 2) to assimilate vertically resolved dust profiles in terms of layer-integrated dust opacity (LIDO). The new data assimilation system now overall consists of the assimilation of temperature profiles, and either the assimilation of column-integrated dust opacity (CIDO), LIDO or both simultaneously, together with activated dust lifting, deposition and dust transport.

The reanalysis from this joint assimilation of temperature profiles, CIDO and LIDO was demonstrated to converge quickly to become consistent with the data assimilated into this updated Mars data assimilation system to within observational uncertainties. The reanalysis was demonstrated convergence to displaying the observed features such as the elevated dust layers, as discussed in the context of MCS observations [Heavens et al., 2011a], that the free-standing model was unable to reproduce

unaided. Since Rafkin [2012] discussed the complication of producing this elevated dust layer in model simulations, especially in a relatively coarse resolution MGCM, the reproduction of these elevated dust layers in the reanalysis provides a valuable alternative means of investigating their characteristics and impact on the meteorology and atmospheric circulation.

The reanalysis was validated in Chapter 5 against separate (out-of-sample) THEMIS and MCS dust observations, as well as against the independent upward-looking MER data (using Pancam data from "Spirit" and "Opportunity" at 880 nm). The reanalysis was successfully able to reproduce the observed interannual and intraseasonal variability evident in the original THEMIS data, and generally improved the representation of the dust vertical distribution compared to free-running simulations. Since the systematic errors of MCS data are not well evaluated, the observational uncertainty presented with the MCS dataset could be smaller than the actual uncertainty of the data. The large differences below 10 km may not necessarily mean that the reanalysis had a poor representation of the "true" dust distribution. Although free-running simulations were able to simulate the pattern of dust loading during the "quiet" season, as seen in THEMIS data, it still failed to simulate the right amount of dust in the vertical direction. This might suggest that dust particles tend to accumulate in the atmosphere close to the ground where it is usually beyond the bottom of typical MCS retrieved dust profiles.

At the "Spirit" landing site in Gusev Crater, it was evident that the reanalysis captured the variability and intensity of dust opacity at that location in both "quiet" and dusty seasons. At the "Opportunity" landing site in Meridiani Planum, the reanalysis was able to capture variability of the dust opacity during the year, and improved the pattern of dust loading obtained during the dusty season compared to

free-running simulation. Compared to these surface observations at Meridiani Planum, persistent underestimates in the reanalysis as well as in the free-running simulation could be noticed, mainly during northern spring and summer (i.e. during the "quiet" season). Due to the assimilation of THEMIS data in this version of reanalysis, this discrepancy is likely to be associated with a systematic disagreement between the THEMIS and "Opportunity" data, as reported by Montabone et al. [2012]. As a result, the reanalysis produced in the work of this thesis is the best that can be done unless there is further explanation of similar disagreement between different measurements at Meridiani Planum among different observational datasets.

8.3. Evolution of a southward moving dust storm

An observed southward moving dust storm in MY 29, travelling through one of the three most climatologically favourable channels for such storms, was studied using the reanalysis produced in the work of this thesis. The reanalysis exhibited generally good agreement with the raw THEMIS and MCS datasets during this moving dust storm event, and reproduced the vertical dust distribution discernible in the ensemble of observed dust profiles within the area of influence of this dust event. The travel path and intensity of this long-lasting migrating dust storm were thereby quantitatively recorded in our study. It is evident that this reanalysis approach provides the potential for tracking the motion and evolution of various migrating dust storms, and perhaps generalizing the development of this kind of southward moving dust storm.

Because the wind stress dust lifting and the dust devil lifting were activated in the reanalysis, the possible physical sources of dust injection into the atmosphere were

explored to investigate how this migrating dust storm might have been generated. The initial disturbance of this dust storm was surprisingly found to be at least partly contributed by dust devil lifting. Dust devil lifting was evidently rather active near the origin of the storm and downwind from the area where it was initiated. Wind stress lifting seemed to be less important during the early stages of this event, and mainly supplied additional dust from outside of the chosen study domain. The relatively mild increments from the data assimilation system during this time suggest that the UK-LMD MGCM appeared to be simulating a physically reasonable evolution of this migrating dust storm, although the assimilation still needed to provide strong observational constraints to the UK-LMD MGCM at some critical points when significant changes happened to the intensity or the moving path of the storm.

In addition, the zonal anomaly of vertical dust distribution and thermal structure associated with this regional event were examined. The maximum of the zonal warm anomaly usually occurred near the top of the storm, as the dust at the top of the layer strongly absorbed the solar radiation. Along with the growing intensity of this storm, a cooling zone occurred beneath this dust storm, increasing to a ~ 2 K cold anomaly that was of a similar magnitude to what was found during the MY 25 global dust storm [Cantor, 2007]. Dust depletion was found above the tropics during this event, when the storm grew to a certain intensity. The strength of dust depletion displayed a correlation with the strength of the dust storm. However, more studies on regional dust storms are required to verify if this dust depletion always happens when the strength of the dust storm reaches a certain level, and furthermore to explain the cause of this depletion.

8.4. The MY 28 global dust storm

The last task reported in this thesis was to discuss the phenomena associated with the MY 28 GDS. The sequence of precursor dust events was first studied. Direct wind stress dust lifting was seen to be responsible for the initiation of the Chryse storm that was part of a sequence of precursor events of the MY 28 GDS, while dust devil lifting provided the background level of dust. A dust storm in Noachis that happened just before the outburst of the MY 28 GDS was found to be the joint result of the travelling Chryse storm, further dust lifting along its path, and local dust lifting at Noachis itself. The possible travelling of the Chryse storm towards Noachis Terra was evidently supported by the maximum average wind speed in the reanalysis, consistent with the condition discussed by Wang and Richardson [2013]. During this sequence of precursor events, the relatively gentle increments to the dust distribution from the assimilation of dust observations suggested that the dust-lifting physics embedded in the UK-LMD MGCM was sufficient to reproduce a realistic dust distribution. However, the reproduction of the rapid expansion of the GDS in the reanalysis still relied mostly on the assistance of dust assimilation.

The climatological impacts of the MY 28 GDS were studied by making a comparison with the same time window of MY 29, which did not support a GDS event. Between latitudes -60° and +50°, the average difference of columnized dust opacity between two years during the period of the MY 28 GDS could be more than three times larger than that of the same period in MY 29. During the MY 28 GDS, to the south of 45° latitude, the dust was obviously transported higher into the atmosphere (~70 km) than it was in MY 29 (~40 km). The north polar warming during winter was ~50 K stronger on average during MY 28 GDS than in the equivalent period of MY 29. The vertical extension of north polar warming reported in Chapter 7 of this thesis was as low as ~150 Pa, and this was much lower than the

reports from other studies [e.g. Smith et al., 2001; Kleinbohl et al., 2009; Heavens et al., 2011b]. Over the Northern Polar region, the pattern of adiabatic heating associated with the downward branch of meridional advection was consistent with the location of the observed north polar warming during winter. Under dusty conditions such as during a GDS, the maximum of the average adiabatic heating associated with this north polar warming was as high as 1181 $K \cdot sol^{-1}$, compared to 356 $K \cdot sol^{-1}$ in the non-GDS year MY 29. These adiabatic heating rates were much larger than that of a previous free-standing MGCM experiment (~150 $K \cdot sol^{-1}$) by Medvedev and Hartogh [2007], although that was carried out under unrealistic dusty conditions. In addition, the high dust loading appeared to suppress the dust devil lifting globally during MY 28 GDS. On the contrary, however, the wind stress lifting displayed a strong correlation with the global dust loading, and this significantly increased during the GDS. The trigger/response between wind stress lifting and high dust loading therefore still requires further attention to explain.

8.5. Discussion and future work

Following this thesis, much work could be done in near future to extend the use and techniques of reanalysis. Due to the limited time of this project, I was unable to extend the study of the driving processes of the SAO to latitudes outside of the Martian tropics. From an observationally-constrained dataset (MACDA), the SAO signal in the zonal-mean zonal wind was evident in the latitudes outside of the tropics (as demonstrated in Chapter 3 of this thesis). It would be of interest, therefore to find out what forcing processes dominate in producing the SAO of zonal-mean zonal wind

in those latitudes, and to establish if the dominant processes are the same as in the tropics or differ in a fundamental way.

Other work that should be conducted is to extend the new reanalysis to cover a longer period given reasonable coverage of observations. In the work of this thesis, the newly introduced reanalysis (from Chapter 4) was limited to between $L_s \approx 110°$ of MY 28 until $L_s \approx 330°$ of MY 29. The spacecraft-based measurements normally provide better coverage in space. TES, THEMIS and MCS datasets (as explained in Chapter 1) are currently the major spacecraft-based datasets that provide relatively uniform and consistent measurements during their operational periods. The availability of these spacecraft-based measurements is shown in Figure 8.1.

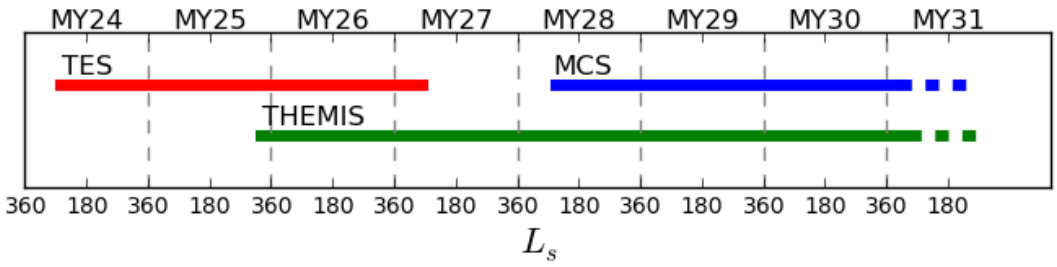

Figure 8.1 Time expansions of TES (red), THEMIS (green) and MCS (blue) datasets. The dashed lines means the instruments are still actively taking measurements.

Although the MACDA dataset used for the diagnosis of the SAO in Chapter 3 also assimilated the TES temperature profiles and CIDO, to extend the new reanalysis to include the period of operation of TES (from $L_s \approx 104°$ of MY 24 to $L_s \approx 82°$ of MY 27), I believe that the new reanalysis datasets will display more spatial and temporal variation than the MACDA. This is mainly because MACDA itself was produced without activating the dust lifting and dust transport schemes in the UK-LMD MGCM. Since the THEMIS dataset overlaps in time with the TES dataset, the additional information provided by the THEMIS dataset could also be used to further

constrain the dust distribution used in the model simulation during those periods. This is not included in the current version of MACDA used in Chapter 3.

The period between $L_s \approx 82°$ of MY 27 and $L_s \approx 110°$ of MY 28 only has the constraint of THEMIS data that can provide relatively consistent observations. Unfortunately, THEMIS data in general provides less intensive measurement coverage than TES. Thus, any reanalysis during this period may have fewer data constraints than in the TES period. Some other data may also be available during this period, however. For instance, the SPICAM (Spectroscopy for investigation of Characteristics of the Atmosphere of Mars) dataset [Montmessin et al. 2006] is available from the Mars Express mission, although the coverage of the data is generally quite sparse. SPICAM data are better able to discriminate between submicron particles and micron-sized particles [Montmessin et al. 2006]. For simplicity, the current version of reanalysis (introduced in Chapter 4) is only based on the assumption of one size of dust particle (1.5 μm, consistent with the estimates of mean effective radius), excluding the submicron dust particles. As a result, SPICAM data is not best suited to the current version of our Mars data assimilation system. However, the ability to assimilate SPICAM data should remain to be explored in a future version of the reanalysis.

I am also aware that a new version of MCS dataset (V4.3) just became available from January 2015 (personal communication) versus V3 used in the work of this thesis. The V4.3 MCS dataset improves the retrieval performance under high dust conditions, and it now has wider coverage than its V3 version. In addition, the dust opacities at high altitudes can also be retrieved in this later version. When the new reanalysis is extended to include the TES period, THEMIS-only period and MCS

period, it is also worth considering assimilating the latest version of MCS that may include more data in better accuracy than the previous versions.

If a continuous reanalysis, from the start of TES period extending nearly 8 MYs, becomes available following the work of this thesis, this extended reanalysis will include time-varying 3-D information on two major Martian GDS events (in MY 25 and MY 28). As a result, it will be possible to explore in detail the similarities and differences of these two GDS events. The impacts of a GDS on the horizontal and vertical distribution of atmospheric dust could then be studied and compared against the mean state of non-GDS years instead of the single non-GDS year (MY 29) compared in the present study. The reanalysis would also provide the opportunity to make a direct comparison of the intensified polar warmings during two GDSs. The relationship between the decay of each GDS and the termination of large-scale dust lifting should also be examined in both GDS events.

In Chapter 3, the features of different forcings to the zonal-mean zonal wind during MY 25 GDS were investigated. In the first half of the MY 25 GDS year, the zonal wind forcing due to meridional advection was clearly weakened, but due to the limitations of MCS data, the reanalysis introduced in Chapter 4 was not available until $L_s \approx 110°$ of another GDS year (MY 28), which inhibited further investigation of the possible link between the forcings and trigger/response of a GDS. Since another GDS year (including the MY 28 GDS) apart from MY 25 will then be completely included in the extended reanalysis, the outstanding questions concerning GDS events raised in Chapter 3 could be explored.

Among the further developments of the Martian data assimilation system that should be considered in the near future, is to enhance the complexity of the representation of the size spectrum of dust particles. In the current specification, a single size of dust

particles is assumed in the dust lifting and dust transport scheme. Although the chosen size is roughly consistent with estimates of the effective radius r_{eff} of observed dust particles [e.g., Pollack et al., 1995; Clancy et al., 2003; Lemmon et al., 2004], this uniform one-size representation is something of an oversimplification of the real dust in the atmosphere. Clancy et al. [2003], for example, found that r_{eff} could vary with time and space, although the majority of observational estimates were in the range of 1.5 ± 0.1 μm. Two methods of representing dust particles have been tested in newer versions of the free-running UK-LMD MGCM in the work of Mulholland [2012], i.e. an explicit multiple-size distribution and a two-moment scheme. It would be possible to explore the feasibility of a data assimilation system with either of these schemes in the next version of reanalysis. The extinction coefficient in nature varies slowly over most typical dust sizes, but it decreases dramatically for particles smaller than ~ 0.1 μm. The reanalysis often corrected the underestimate of the dust distribution in high altitudes in the free-running model (e.g. see Figure 5.7). Given that the submicron particles may actually be more populous at high altitudes, the assumption of a uniform distribution of 1.5 μm dust particles actually leads to an overestimate of the realistic dust heating rate in the reanalysis. With the implementation of a size-dependent representation of dust particles, I would expect that this may reduce the amplitude of at least some increments of temperature assimilation, potentially leading to the model-predicted temperature converging towards the observation faster than it does now. This impact may require verification. Moreover, the information obtained by the reanalysis with size-dependent dust transport should provide additional detailed insights into the variability of r_{eff}. More importantly, I hope that it may provide a base scenario to study the sustainability of the observed elevated dust

layers, given that the free-running MGCMs are unlikely to reproduce this feature until a sophisticated parameterization becomes available.

Bibliography

Andrews, D. G. and M. E. McIntyre (1978), Generalized Eliassen-Palm and Charney-Drazin Theorems for waves on axisymmetric mean flows in compressible atmospheres, *J. Atmos. Sci.*, *35*, 175-185.

Bagnold, R. A., The physics of blown sand and desert dunes, Methuen. New York, 1954.

Baldwin, M. P., L. J. Gray, T. J. Dunkerton, K. Hamilton, P. H. Haynes, W. J. Randel, J. R. Holton, M. J. Alexander, I. Hirota, T. Horinouchi, D. B. A. Jones, J. S. Kinnersley, C. Marquardt, K. Sato and M. Takahashi (2001), The quasi-biennial oscillation, *Review of Geophysics*, *39*, 179-229.

Balme M. R., P. L. Whelley and R. Geeley (2003), Mars: Dust devil track survey in Argyre Panitia and Hellas Basin, *J. Geophys. Res.*, 108(E8), 5086, doi: 10.1029/2003JE002096.

Barnston, A. G. and R. E. Livezey (1987), Classification, seasonality and persistence of low-frequency atmospheric circulation patterns, *Mon, Wea. Rev.*, *115*, 1083-1126.

Basu, S., M. I. Richardson and R. J. Wilson (2004), Simulation of the Martian dust cycle with the GFDL Mars GCM, *J. Geophys. Res.*, *109*, E11006, doi:10.1029/2004JE002243.

Basu, S., J. Wilson, M. Richardson and A. Ingersoll (2006), Simulation of spontaneous and variable global dust storms with the GFDL Mars GCM, *J. Geophys. Res. (Planests)*, *111*, E09004, doi:10.1029/2005JE002660.

Benson J. L., D. M. Kass and MCS Team (2011), Mars Climate Sounder observations of ice and dust layering in the Martian atmosphere, Fourth International Workshop on Mars Atmosphere Modeling and Obsevations, Paris, France, Feb. 2011.

Bohren, C. F. and D. R. Huffman, Absorption and scattering of light by small particles, Wiley Professional Paperback Series, Wiley-Interscience, New York, USA, 1998.

Cantor, B. A., P. B. James, M. Caplinger and M. J. Wolff (2001), Martian dust storms: 1999 Mars Orbiter Camera observations, *J. Geophys. Res.*, *106* (E10), 23653-23687.

Cantor, B. A (2007), MOC observations of the 2001 Mars planet-encircling dust storm, *Icarus*, *186*, 60-96.

Christensen, P. R., B. M. Jakosky, H. H. Kieffer, M. C. Malin, H. Y. McSween, K. Nealson, G. L. Mehall, S. H. Silverman, S. Ferry, M. Caplinger and M. Ravine (2003), The Thermal Emission Imaging System (THEMIS) for the Mars 2001 Odyssey mission, *Space Sci. Rev.*, *100*, 85-130.

Clancy, R. T., B. J. Sandor, M. J. Wolff, P. R. Christensen, M. D. Smith, J. C. Pearl, B. J. Conrath and R. J. Wilson (2000), An intercomparison of ground-based millimeter, MGS TES, and Viking atmospheric temperature measurements: Season and interannual variability of temperatures and dust loading in the global Mars atmosphere, *J. Geophys. Res.*, *105*(E4), 9553-9571.

Clancy, R. T., M. J. Wolff and P. R. Christensen (2003), Mars aerosol studies with the MGS TES emission phase function observations: Optical depths, particle sizes, and ice cloud types versus latitude and solar longitude, *J. Geophys. Res.*, *108*(E9), 5098, doi: 10.1029/2003JE002058.

Collins, M. and I. N. James (1995), Regular baroclinic transient waves in a simplified global circulation model of the Martian atmosphere, *J. Geophys. Res.*, *100*, 14421-14432.

Collins, M., S. R. Lewis, P. L. Read and F. Hourdin (1996), Baroclinic wave transitions in the Martian atmosphere, *Icarus, 120,* 344-357.

Collins, W. D., P. J. Rasch, B. E. Eaton, B. V. Khattatov and J. –F. Lamarque (2001), Simulating aerosols using a chemical transport model with assimilation of satellite aerosol retrievals: Methodology for INDOEX, *J. Geophys. Res.*, *106*, 7313-7336.

Conrath, B. J. (1975), Thermal structure of the Martian atmosphere during the dissipation of dust storm of 1971, *Icarus*, *24I,* 36-46.

Conrath, B. J., J. C. Peral, M. D. Smith, W. C. Maguire, P. R. Christensen, S. Dason and M. S. Kaelberer (2000), Mars Global Surveyor Thermal Emission Spectrometer (TES) observations: Atmospheric temperatures during aerobraking and science phasing, *J. Geophys. Res.*, *105*(E4), 9509-9519.

Daley, R., Atmospheric data analysis, Cambridge Univ. Press, Cambridge, UK, 1991.

Davies, H. C. and R. E. Turner (1977), Updating prediction models by dynamical relaxation: An examination of the technique*, Q. J. R. Meteor. Soc.*, *103*, 225-245.

Deming, D., M. J. Mumma, F. Espenak, T. Kostiuk and D. Zipoy (1986), Polar warming in the middle atmosphere of Mars, *Icarus*, *66*, 366-379.

Eluszkiewicz, J., R. A. Plumb and N. Nakamura (1995), Dynamics of wintertime stratospheric transport in the Geophysical Fluid Dynamics Laboratory SKYHI general circulation model, *J. Gerphys. Res.*, *100*(D10), 20, 883-20,900.

Euler, E. E., S. D. Jolly and H. H. Curtis (2001), The failures of the Mars Climate Orbiter and Mars Polar Lander: a perspective from the people involved, 24th annual AAS guidance and control conference, January 31-February 4, 2001, Brechenridge, Colorado, USA.

Fels, S. B. and R. S. Lindzen (1974), The interaction of thermally excited gravity waves with mean flows, *Geophys. Fluid Dyn.*, *6*, 149-191.

Fenton, L. K., and M. I. Richardson (2001), Martian surface winds: Insensitivity to orbital changes and implications for aeolian processes, *J. Geophys. Res., 106,* 32,885– 32,902.

Fisher, J. A., M. I. Richardson, C. E. Newman, M. A. Szwast, C. Graf, S. Basu, S. P. Ewald, A. D. Toigo, and R. J. Wilson (2005), A survey of Martian dust devil activity using Mars Global Surveyor Mars Orbiter Camera images, *J. Geophys. Res.*, *110*, E03004, doi:10.1029/2003JE002165.

Forget, F., F. Hourdin, R. Fournier, C. Hourdin, O. Talagrand, M. Collins, S. R. Lewis, P. L. Read and J.-P. Huot (1999), Improved general circulation models of the martian atmosphere from the surface to above 80 km, *J. Geophys. Res.*, *104* (E10), 24155-24176.

Garcia, R. R., T. J. Dunkerton, R. S. Lieberman and R. A. Vincent (1997), Climatology of the semiannual oscillation of the tropical middle atmosphere, *J. Gerphys. Res.*, *102*, 26019-26032.

Ghil, M. and K. Mo (1990), Intraseasonal oscillations in the global atmosphere. Part II: Southern Hemisphere, *J. Atmos. Sci.*, *48(5)*, 780-790.

Greeley, R. and J. D. Iversen (1985), *Wind as a geological process on Earth, Mars, Venus and Titan*, Cambridge Univ. Press.

Greeley, R., P. L. Whelley, R. E. Arvidson, N. T. Bridges, N. A. Cabrol, D. J. Foley, B. J. Franklin, P. G. Geissler, M. P. Golombek, R. O. Kuzmin, G. A. Landis, M. T. Lemmon, L. D. V. Neakrase, S. W. Squyres and S. D. Thompson (2006), Active dust devils in Gusev crater, Mars: Observations from the Mars Exploration Rover Spirit, *J. Geophys. Res. (Planets)*, 111:E12S09.

Greybush, S. J., R. J. Wilson, R. N. Hoffman, M. J. Hoffman, T. Miyoshi, K. Ide, T. McConnochie and E. Kalnay (2012), Ensemble Kalman filter data assimilation of Thermal Emission Spectrometer

temperature retrievals into a Mars GCM, *J. Geophys. Res.*, *117*, E11008, doi:10.1029/2012JE004097.

Guzewich, S. D., E. R. Talaat, A. D. Toigo, D. W. Waugh and T. H. McConnochie (2013), High-altitude dust layers on Mars: Observations with the Thermal Emission Spectrometer, *J. Geophys. Res. Planets*, *118*, 1177-1194, doi:10.1002/jgre.20076.

Hamilton, K. (1995), Interannual variability in the northern hemisphere winter middle atmosphere in control and perturbed experiments with the GFDL SKYHI general circulation model, *J. Atmos. Sci., 52,* 44–66.

Heavens, N. G., M. I. Richardson, A. Kleinböhl, D. M. Kass, D. J. McCleese, W. Abdou, J. L. Benson, J. T. Schofield, J. H. Shirley, and P. M. Wolkenberg (2011a), Vertical distribution of dust in the Martian atmosphere during northern spring and summer: High‐altitude tropical dust maximum at northern summer solstice, *J. Geophys. Res.*, *116*, E01007, doi:10.1029/2010JE003692.

Heavens, N. G., D. J. McCleese, M. I. Richardson, D. M. Kass, A. Kleinbohl, and J. T. Schofield (2011b), Structure and dynamics of the Martian lower and middle atmosphere as observed by the Mars Climate Sounder: 2. Implications of the thermal structure and aerosol distributions for the mean meridional circulation, *J. Geophys. Res.*, *116*, E01010, doi:10.1029/2010JE003713.

Hébrard, E., C. Listowski, P. Coll. B. Marticorena, G. Bergametti, A. Määttänen, F. Montmessin and F. Forget (2012), An aerodynamic roughness length map derived from extended Martian rock abundance data, *J. Geophys. Res.*, 117, E4, doi: 10.1019/2011JE003942.

Hinson, D. P., H. Wang and M. D. Smith (2012), A multi-year survey of dynamics near the surface in the northern hemisphere of Mars: Short-period baroclinic waves and dust storms, *Icarus*, *219*, 307-320.

Hoskins, B. J. and A. J. Simmons (1975), A multi-layer spectral model and the semi-implicit method, *Q. J. R. Meteorol. Soc., 101*, 637-655.

Hoffman, M. J., S. J. Greybush, R. J. Wilson, G. Gyarmati, R. N. Hoffman, E. Kalnay, K. Ide, E. J. Kostelich, T. Miyoshi and I. Szunyogh (2010), An ensemble Kalman filter data assimilation system for the martian atmosphere: implementation and simulation experiments, *Icarus*, *209*, 470-481.

Hourdin, F., F. Forget, and O. Talagrand (1995), The sensitivity of the Martian surface pressure and atmospheric mass budget to various parameters: A comparison between numerical simulations and Viking observations, *J. Geophys. Res., 100(E3),* 5501–5523, doi:10.1029/94JE03079.

Kahre, M. A., J. R. Murphy and R. M. Haberle (2006), Modeling the Martian dust cycle and surface dust reservoirs with the NASA Ames general circulation model, *J. Geophys. Res.*, *111*, E06008, doi:10.1029/2005JE002588, 2006.

Kahre, M. A., J. L. Hollingworth, R. M. Haberle and J. R. Murphy (2008), Investigations of the variability of dust particle sizes in the martian atmosphere using the NASA Ames General Circulation Model, *Icarus*, *195*, 576-597, doi:10.1016/j.icarus.2008.01.023.

Kahre, M. A. and R. M. Haberle (2010), Mars CO_2 cycle: Effects of airborne dust and polar cap ice emissivity, *Icarus, 201,* 648-653.

Kass, D. M., A. Kleinböhl, D. J. McCleese, J. T. Schofield and M. D. Smith (2014), Observations of large dust storms during the Martian dusty season, 5th International Workshop on Mars Atmosphere: Modelling and Observations, Oxford, United Kingdom, January, 2014.

Kellogg, W. W. and G. F. Schilling (1951), A proposed model of the circulation in the upper stratosphere, *J. Meteorology*, *8*, 222-230.

Kleinbohl, A., et al. (2009), Mars Climate Sounder limb profile retrieval of atmospheric temperature, pressure, and dust and water ice opacity, *J. Geophys. Res.*, *114*, E10006, doi:10.1029/2009JE003358.

Kok, J. F. and N. O. Renno (2008), Electrostatics in wind-blown sand, *Phys. Rev. Lett.*, *100*, 014501, doi:10.1103/PhysRevLett.100.014501.

Kuroda, T., N. Hashimoto, D. Sakai and M. Takahashi (2005), Simulation of the Martian atmosphere using a CCSR/NIES AGCM, *J. Meteorol, Soc. Jpn.*, *83*, 1-19.

Kuroda, T., A. S. Medvedev, P. Hartogh and M. Takahashi (2008), Semiannual oscillations in the atmosphere of Mars, *Geophys. Res. Lett.*, *35*, L23202, doi:10.1029/2008GL036061.

Lee, C., et al. (2009), Thermal tides in the Martian middle atmosphere as seen by the Mars Climate Sounder, *J. Geophys. Res., 114,* E03005, doi:10.1029/2008JE003285.

Lee, S. W. (1986), Regional sources and sinks of dust on Mars: Viking observations of Cerberus, Solis Planum, and Syrtis Major, in *Symposium on Mars: Evolution of Its Climate and Atmosphere, LPI Contrib. 599*, p. 57, Lunar and Planet. Inst., Houston, Tex.

Lemmon, M. T., M. J. Wolff, M. D. Smith, R. T. Clancy, D. Banfield, G. A. Landis, A. Ghosh, P. H. Smith, N. Spanovich, B. Whitney, P. Whelley, R. Greeley, S. Thompson, J. F. Bell III, S. W.

Squyres (2004), Atmospheric imaging results from the Mars exploration rovers: Spirit and Opportunity, *Science*, *306(5702)*, 1753-1756.

Lemmon, M. T., M. J. Wolff, J. F. Bell III, M. D. Smith, B. Cantor and P. H. Smith (2014), Dust, clouds, and the atmospheric optical depth record over 5 Mars years of the Mars exploration rover mission, 5th International Workshop on Mars Atmosphere: Modelling and Observations, Oxford, United Kingdom, January, 2014.

Leovy, C. and Y. Mintz (1969), Numerical simulation of the atmospheric circulation and climate of Mars, *J. Atmos. Sci.*, *26(6)*, 1167-1190.

Leovy, C. B., R. W. Zurek and J. B. Pollack (1973), Mechanisms for Mars dust storms, *J. Atmos. Sci.*, *30*, 749-762.

Lewis, S. R. and P. L. Read (1995), An operational data assimilation scheme for the martian atmosphere, *Adv. Space Res.*, *16(6)*, 9-13.

Lewis, S. R. and P. L. Read (2003), Equatorial jets in the dusty Martian atmosphere, *J. Geophys. Res.*, *108*(E4), 5034, doi:10.1029/2002JE001933.

Lewis, S. R. and P. R. Barker (2005), Atmospheric tides in a Mars general circulation model with data assimilation, *Adv. Space Res.*, *36(11)*, 2162-2168.

Lewis, S. R., P. L. Read, B. J. Conrath, J. C. Pearl and M. D. Smith (2007), Assimilation of thermal emission spectrometer atmospheric data during the Mars Global Surveyor aerobraking period, *Icarus*, *192*, 327-347.

Lewis, S. R., L. J. Steele and F. Forget (2014), High-altitude dust in the Martian atmosphere, 5th International Workshop on Mars Atmosphere: Modelling and Observations, Oxford, United Kingdom, January, 2014.

Lindzen, R. S. and S. S. Hong (1974), Effects of mean winds and horizontal temperature gradients on solar and lunar semidiurnal tides in the atmosphere, *J. Atmos. Sci.*, 31, 1421-1466.

Lorenc, A. C., R. S. Bell and B. Macpherson (1991), The meteorological office analysis correction data assimilation scheme, *Q. J. R. Meteor. Soc., 117*, 59-89.

Madeleine, J. –B., F. Forget, E. Millour, L. Montabone and M. J. Wolff (2011), Revisiting the radiative impact of dust on Mars using the LMD Global Climate Model, *J. Geophys. Res.*, *116*, E11010, doi:10.1029/2011JE003855.

Malin, M. C., B. A. Cantor, T. N. Harrison, D. E. Shean and M. R. Kennedy (2009a), MRO MARCI Weather Report for the week of 13 July 2009 – 19 July 2009, Malin Space Science Systems Captioned Image Release, MSSS-92, http://www.msss.com/msss_images/2009/07/22/.

Malin, M. C., B. A. Cantor, D. E. Shean, M. R. Kennedy and T. N. Harrison (2009b), MRO MARCI Weather Report for the week of 20 July 2009 – 26 July 2009, Malin Space Science Systems Captioned Image Release, MSSS-93, http://www.msss.com/msss_images/2009/07/29/.

Malin, M. C., B. A. Cantor, M. R. Kennedy, D. E. Shean and T. N. Harrison (2009c), MRO MARCI Weather Report for the week of 27 July 2009 – 2 August 2009, Malin Space Science Systems Captioned Image Release, MSSS-94, http://www.msss.com/msss_images/2009/08/05/.

Malin, M. C., B. A. Cantor, T. N. Harrison, D. E. Shean and M. R. Kennedy (2009d), MRO MARCI Weather Report for the week of 3 August 2009 – 9 August 2009, Malin Space Science Systems Captioned Image Release, MSSS-95, http://www.msss.com/msss_images/2009/08/12/.

Martin, T. Z. and H. H. Kieffer (1979), Thermal infrared properties of the Martian atmosphere 2. The 15-μm band measurements, *J. Geophys. Res.*, *84*, 2843-2852.

McCleese, D. J., J. T. Schofield, F. W. Taylor, S. B. Calcutt, M. C. Foote, D. M. Kass, C. B. Leovy, D. A. Paige, P. L. Read, and R. W. Zurek (2007), Mars Climate Sounder: An investigation of thermal and water vapor structure, dust and condensate distributions in the atmosphere, and energy balance of the polar regions, *J. Geophys. Res.*, *112*, E05S06, doi:10.1029/2006JE002790.

McCleese, D. J., et al. (2008), Intense polar temperature inversion in the middle atmosphere on Mars, *Nat. Geosci., 1,* 745–749, doi:10.1038/ngeo332.

McCleese, D. J., et al. (2010), Structure and dynamics of the Martian lower and middle atmosphere as observed by the Mars Climate Sounder: Seasonal variations in zonal mean temperature, dust, and water ice aerosol, *J. Geophys. Res.*, *115*, E12016, doi:10.1029/2010JE003677.

McDunn, T., S. Bougher, J. Murphy, A. Kleinböhl, F. Forget and M. Smith (2013), Characterization of middle-atmosphere polar warming at Mars, *J. Geophys. Res. Planets*, *118*, 161-178, doi:10.1002/jgre.20016.

Medvedev, A. S. and P. Hartogh (2007), Winter polar warmings and the meridional transport on Mars simulated with a general circulation model, *Icarus*, *186*, 97-110.

Mellor, G. L. and T. Yamada (1982), Development of a turbulence closure model for geophysical fluid problems, *Rev. of Geophys.*, *20,* 851-875.

Montmessin, F., E. Quémerais, J. L. Bertaux, O. Korablev, P. Rannou, and S. Lebonnois (2006), Stellar occultations at UV wavelengths by the SPICAM instrument: Retrieval and analysis of Martian haze profiles, *J. Geophys. Res.*, *111*, E09S09, doi:10.1029/2005JE002662.

Montabone, L., S. R. Lewis and P. L. Read (2005), Interannual variability of martian dust storm in assimilation of several years of Mars Global Surveyor observations, *Adv. Space Res. 36 (11)*, 2146-2155.

Montabone, L., S. R. Lewis, P. L. Read and D. P. Hinson (2006a), Validation of martian meteorological data assimilation for MGS/TES using radio occultation measurements, *Icarus 185 (1)*, 113-132.

Montabone, L., S. R. Lewis and P. Withers (2006b), Reconstructing the weather on Mars at the time of the MERs and Beagle 2 landings, *Geophys. Res. Lett., 33*, L19202.

Montabone, L., M. T. Lemmon, M. D. Smith, M. J. Wolff, F. Forget and E. Millour (2011a), Reconciling dust opacity datasets and building multi-annual dust scenarios for Mars atmospheric Models, 4th International Workshop on Mars Atmosphere: Modelling and Observations, Paris, France, February, 2011.

University of Oxford and The Open University. [Montabone, L.; Lewis, S. R.; Read, P. L.]. Mars Analysis Correction Data Assimilation (MACDA): MGS/TES v1.0, [Internet]. NCAS British Atmospheric Data Centre, 29 November 2011b, doi:10.5285/78114093-E2BD-4601-8AE5-3551E62AEF2B.

Montabone, L., F. Forget, E. Millour, R. J. Wilson, S. R. Lewis, B. Cantor, D. Kass, A. Kleinböhl, M. T. Lemmon, M. D. Smith and M. J. Wolff (2015), Eight-year climatology of dust optical depth on Mars, *Icarus*, *251*, 65-95.

Moudden, Y. and J. M. Forbes (2008), Effects of vertically propagating thermal tides on the mean structure and dynamics of Mars' lower thermosphere, *Geophys. Res. Lett.*, *35*, L23805, doi:10.1029/2008GL036086.

Mulholland, D. P. (2012), Martian dust lifting, transport and associated processes, D. Phil. thesis, St. Anne's College, University of Oxford, Oxford, United Kingdom.

Mulholland, D. P., P. L. Read and S. R. Lewis (2013), Simulating the interannual variability of major dust storms on Mars using variable lifting thresholds, *Icarus*, *223*, 344-358.

Murphy, J. R., J. B. Pollack, R. M. Haberle, C. B. Leovy, O. B. Toon, and J. Schaeffer (1995), Three-dimensional numerical simulation of Martian global dust storms, *J. Geophys. Res., 100(E12),* 26,357–26,376, doi:10.1029/95JE02984.

Navarro, T., F. Forget, E. Millour and S. J. Greybush (2014), Detection of detached dust layers in the Martian atmosphere from their thermal signature using assimilation, *Geophys. Res. Lett*., *41*, 6620-6626, doi:10.1002/2014GL061377.

Newman, C. E., S. R. Lewis, P. L. Read and F. Forget (2002a), Modeling the Martian dust cycle, 1, Representations of dust transport processes, *J. Geophys. Res.*, *107 (E12),* 5123.

Newman , C. E., S. R. Lewis, P. L. Read and F. Forget (2002b), Modeling the Martian dust cycle, 2, Multiannual radiatively active dust transport simulations, *J. Geophys. Res.*, *107(E12)*, 5124, doi:10.1029/2002JE001920.

Newman C. E. and M. I. Richardson (2015), The impact of surface dust source exhaustion on the martian dust cycle dust storms and interannual variability, as simulated by the MarsWRF General Circulation Model, *Icarus*, *257*, 47-87.

Nowicki, S. A. and P. R. Christensen (2007), Rock abundance on Mars from the Thermal Emission Spectrometer, *J. Geophys. Res. (Planets)*, 112:E05007.

Pike, E. R., J. G. McWhirter, M. Bertero and C. de Mol (1984), Generalised information theory for inverse problems in signal processing, *IEEE Proc.*, *131*(6), 660-667.

Pollack, J. B., M. E. Ockert-Bell and M. K. Shepard (1995), Viking lander image analysis of Martian atmospheric dust, *J. Geophys. Res. (Planets)*, *100(E3)*, 5235-5250, doi:10.1029/94JE02640.

Rafkin, S. C. R. (2012), The potential importance of non-local, deep transport on the energetics, momentum, chemistry, and aerosol distributions in the atmospheres of Earth, Mars and Titan, *Planetary and Space Science*, *60*, 147-154.

Read, P. L. and S. R. Lewis (2004), *The Martian Climate Revisited: Atmosphere and Environment of a desert planet*, Praxis Publishing Ltd, Chichester, UK, printed in Germany.

Reed, J. R. (1966), Zonal wind behavior in the equatorial stratosphere and lower mesosphere, *J. Gerphys. Res., 71,* 4223-4233.

Rennó, N. O., M. L. Burkett and M. P. Larkin (1998), A Simple Thermodynamical Theory for Dust Devils, *J. Atmos. Sci.*, 55:3244–3252.

Rennó, N. O., A. A. Nash, J. Lunine and J. Murphy (2000), Martian and terrestrial dust devils: test of a scaling theory using Pathfinder data, *J. Geophys. Res.*, *105(E1)*, 1859-1865.

Richardson, M. I. and R. J. Wilson (2002), A topographically forced asymmetry in the Martian circulation and climate, *Nature*, *416*, 298-301.

Rogberg, P., P. L. Read, S. R. Lewis and L. Montabone (2010), Assessing atmospheric predictability on Mars using numerical weather prediction and data assimilation, *Q. J. R. Meteorol. Soc., 136*, 1614-1635.

Sanchez-Lavega, A., An introduction to planetary atmospheres, Bilbao, Spain, 2011.

Schofield, J. T., D. M. Kass, A. Kleinböhl, D. J. McCleese, M. A. Allen, M. C. Foote, M. Jeganathan, F. Forget, A. Spiga, O. Talagrand, F. Lefèvre, A. Määttänen, T. Fouchet, N. Bowles, S. B. Calcutt, P. G. J. Irwin, P. L. Read, S. R. Lewis, J. R. Barnes, S. W. Bougher, R. M. Haberle (2011), The Exomars Climate Sounder (EMCS) investigation, Fourth International Workshop on Mars Atmosphere Modeling and Obsevations, Paris, France, Feb. 2011.

Schutgens, N. A. J., T. Miyoshi, T. Takemura and T. Nakajima (2010), Applying an ensemble Kalman filter to the assimilation of AERONET observations in a global aerosol transport model, *Atmos. Chem. Phys.*, *10*, 2561-2576.

Sekiyama, T. T., T. Y. Tanaka, A. Shimizu and T. Miyoshi (2010), Data assimilation of CALIPSO aerosol observations, *Atmos. Chem. Phys.*, *10*, 39-49.

Smith, D. E., et al. (2001), Mars orbiter later altimeter: Experiment summary after the first year of global mapping of Mars, *J. Geophys. Res.*, *106*(E10), 23,689-23,722.

Smith, M. D., J. C. Pearl, B. J. Conrath and P. R. Christensen (2000), Mars Global Surveyor Thermal Emission Spectrometer (TES) observations of dust opacity during aerobraking and science phasing, *J. Geophys. Res.*, *105*, 9539-9552.

Smith, M. D., J. C. Pearl, B. J. Conrath and P. R. Christensen (2001), Thermal Emision Spectrometer results: Mars atmospheric thermal structure and aerosol distribution, *J. Geophys. Res.*, *106*(E10), 23,929-23,945.

Smith, M. D., J. L. Bandfield, P. R. Christensen and M. I. Richardson (2003), Thermal Emission Imaging System (THEMIS) infrared observations of atmospheric dust and water ice cloud optical depth, *J. Geophys. Res.*, *108*(E11*)*, 5115, doi.10.1029/2003JE002115.

Smith, M. D. (2004), Interannual variability in TES atmospheric observations of Mars during 1999-2003, *Icarus*, *167*, 148-165.

Smith, M. D. (2008), Spacecraft observations of the Martian atmosphere, *Annu. Rev. Earth Planet. Sci.*, *36*, 191-219.

Smith, M. D. (2009), THEMIS observations of Mars aerosol optical depth from 2002-2008, *Icarus*, *202*, 444-452.

Smith, M. D., M. J. Wolff, R. T. Clancy, A. Kleinböhl and S. L. Murchie (2013), Vertical distribution of dust and water ice aerosols from CRISM limb-geometry observations, *J. Geophys. Res. Planets*, *118*, doi:10.1002/jgre.20047.

Spiga, A., J. Faure, J.-B. Madeleine, A. Määttänen and F. Forget (2013), Rocket dust storms and detached dust layers in the Martian atmosphere, *J. Geophys. Res. Planets*, *118*, 746–767, doi:10.1002/jgre.20046.

Steele, L. J. (2014), An investigation of the Martian water cycle and cloud radiative effects using data assimilation, PhD Thesis, The Open University, Milton Keynes, United Kingdom.

Stier, P., J. H. Seinfeld, S. Kinne and O. Boucher (2007), Aerosol absorption and radiative forcing, *Atmos. Chem. Phys.*, *7*, 5237-5261.

Strausberg, M. J., H. Wang, M. I. Richardson, S. P. Ewald and A. D. Toigo (2005), Observations of the initiation and evolution of the 2001 Mars global dust storm, *J. Geophys. Res.*, *110*, E02006, doi:10.1029/2004JE002361.

Szwast, M. A., M. I. Richardson and A. R. Vasavada (2006), Surface dust redistribution on Mars as observed by the Mars Global Surveyor and Viking orbiters, *J. Geophys. Res.*, *111*, E11008, doi:10.1029/2005JE002485.

Toon, O. B., J. B. Pollack and C. Sagan (1977), Physical properties of the particles composing the Martian dust storm of 1971-1972, *Icarus, 30,* 663-696.

Wang, H., M. I. Richardson, R. J. Wilson, A. P. Ingersoll, A. D. Toigo and R. W. Zurek (2003), Cyclones, tides, and the origin of a cross-equatorial dust storm on Mars, *Geophys. Res. Lett., 30(9)*,1488, doi:10.1029/2002GL016828.

Wang, J., U. S. Nair and S. A. Christopher (2004), GOES 8 aerosol optical thickness assimilation in a mesoscale model: Online integration of aerosol radiative effects, *J. Geophys. Res.*, *109*, D23203, doi: 10.1029/2004JD004827.

Wang, H. and M. I. Richardson (2013), The origin, evolution, and trajectory of large dust storms on Mars during Mars Years 24-30 (1999-2011), *Icarus*, in press.

White, B. R. (1979), Soil transport by winds on Mars, *J. Geophys. Res.*, 84, 4643-4651.

Wilson, J. and K. Hamilton (1996), Comprehensive model simulation of thermal tides in the Martian atmosphere, *J. Atmos. Sci.*, *53*, 1290-1326.

Wilson, R. J. (1997), A general circulation model simulation of the Martian polar warming, *Geophys. Res. Lett.*, *24*, 123-126

Wilson, R. J., S. R. Lewis, L. Montabone and M. D. Smith (2008a), Influence of water ice clouds on Martian tropical atmospheric temperatures, *Geophys. Res. Lett.*, *35*, L07202.

Wilson, R. J. et al. (2008b), Simulation of the 2001 planet-encircling dust storm with NASA/NOAA Mars general circulation model, Abstract 9023, Mars Atmosphere: Modeling and Observations Workshop, Williamsburg, VA.

Wilson, R. J. and M. A. Kahre (2009), The role of spatially variable surface dust in GCM simulations of the martian dust cycle, Mars Dust Cycle workshop, NASA/Ames Research Center, CA. USA.

Yumimoto, K., I. Uno, N. Sugimoto, A. Shimizu, Z. Liu and D. M. Winker (2008), Adjoint inversion modeling of Asian dust emission using lidar observations, *Atmos. Chem. Phys.*, *8*, 2869-2884.